Dynamics of single clusters in intense light pulses studied with ion spectroscopy and light scattering

vorgelegt von
Diplom-Physikerin
Leonie Flückiger
geb. in Bad Soden am Taunus

von der Fakultät II – Mathematik und Naturwissenschaften
der Technischen Universität Berlin
zur Erlangung des akademischen Grades

Doktor der Naturwissenschaften
– Dr. rer. nat. –

genehmigte Dissertation

Promotionsausschuss:
Vorsitzender: Prof. Dr. Mario Dähne
Gutachter: Prof. Dr. Thomas Möller
Gutachter: PD. Dr. Tim Laarmann

Tag der wissenschaftlichen Aussprache: 16. Juli 2015

Berlin 2015

to my friends and family

Abstract

The advent of x-ray free-electron lasers (FELs) has added a new twist to the field of interaction between ultrafast laser pulses and nanoscale matter. The vision to image non-crystalline targets in flight with atomic resolution in space and time is now within reach. This thesis explores the laser induced dynamics of clusters with extreme ultraviolet (XUV) radiation from the FLASH FEL in Hamburg as well as with infrared (IR) laser pulses from a Ti:Sapphire system. An infrared laser focusing unit and a motorized in-vacuum incoupling system were designed for the experiments in this thesis. IR and XUV pulses were guided into the interaction region where they intersect the cluster beam. Large single xenon clusters were produced in supersonic expansion under extreme conditions reaching a size range between 10 and 1000 nanometer in radius. A method of coincident single-shot single-particle imaging and ion spectroscopy was applied, which allows circumventing constrains of signal averaging due to cluster size distributions and FEL power density profiles. A set of filtering and sorting algorithms was developed to handle the large amount of collected data demanded by this method.

The laser-induced cluster evolution is highly dependent on quasi-free electron density and temperature. Nanoplasma dynamics were investigated dependent on cluster size and material composition as well as laser intensity and wavelength to gain insight into their correlation with experimental parameters. Astonishingly similar ion time-of-flight spectra were found for very different conditions, i.e. metal and rare-gas clusters as well as IR and XUV radiation. This reveals that very large clusters have universal dynamics in common: only the outermost atomic layers explode and strong recombination takes place in the inner core.

For time resolved investigation, a two color pump-probe technique was employed. The XUV irradiated cluster expanded to a density where the Mie resonance condition was matched and probed by the IR pulse. The average charge state created in clusters of well-defined size did not change with FEL intensity. Furthermore, the average charge state before recombination is derived from analytical calculations using the nanoplasma model.

In a reversed pump-probe scheme the IR-induced expansion was imaged. A plasma-driven surface melting could be traced in a decreasing scattering signal at large angle. The verification with basic 2D fast Fourier transforms revealed that the central part of the cluster stays intact on a picosecond timescale. A slow evolution of the cluster is also witnessed from ion signal with high kinetic energies, even a nanosecond after IR irradiation. A novel type of scattering patterns - speckles - traces a slowly expanding neutral core, driven by the hot electron gas in the nanoplasma. From the average speckle size the average cluster radius at the time of detection can be gained. A modulation of the speckle intensity envelope results from a density fluctuation inside the disintegrating cluster. The key features of the measured speckle pattern could be reproduced in scattering simulations using a numerical scalar approach.

Kurzfassung

Die Wechselwirkung von ultrakurzen Laserpulsen mit Nanoteilchen wird gegenwärtig intensiv untersucht. Freie-Elektronen-Laser (FEL) im Röntgenbereich erlauben seit kurzem völlig neuartige Untersuchungen. Durch ihre extrem intensiven Pulse wird es möglich werden nicht-kristalline Partikel mit räumlich und zeitlich atomarer Auflösung abzubilden. Im Rahmen dieser Dissertation wurden Cluster mit extrem-ultravioletter (XUV) Strahlung des FLASH-FEL in Hamburg abgebildet, sowie laserinduzierte Prozesse in der Probe mit infraroten (IR) Pulsen untersucht. Für die Experimente wurden ein Fokussier- und ein motorisiertes, vakuumtaugliches Einkoppelsystem entworfen und aufgebaut. In der Wechselwirkungszone wurden IR und XUV Pulse mit dem Clusterstrahl überlappt. Die Xenoncluster wurden in Überschallexpansion hergestellt und erreichten Größen von $10^5 - 10^{10}$ Atomen. Die Methode der Einzelclusterstreuung wurde mit Ionenspektroskopie kombiniert, wodurch eine Mittlung der Messsignale über die Clustergrößenverteilung und das Leistungsdichen-Profils des Lasers umgangen werden konnte. Um die enormen Datenmenge, welche mit dieser Methode einhergeht, zu handhaben, wurden eine Reihe von Filter- und Sortieralgorithmen entwickeln. Im Einzelnen wurden folgende Ergebnisse erzielt:

Die laserinduzierte Entwicklung des Clusters ist stark abhängig von der Dichte und Temperatur der quasi-freien Elektronen im Nanoplasma. Die Nanoplasmadynamiken wurden in Abhängigkeit von der Clustergröße und der Laserintensität, sowie des Clustermaterials und der Laserwellenlänge untersucht. Die detektierten Ionenspektren weisen erstaunliche Ähnlichkeit auf, was darauf hinweist, dass sich für sehr große Cluster die Dynamiken universal verhalten. Nur die äußersten Atomlagen explodieren vom Cluster ab, während im inneren Teil Elektronen und Ionen rekombinieren.

Für eine zeitaufgelösten Untersuchung wurde die Zweifarben Pump-Probe Technik angewendet. Der XUV bestrahlte Cluster wurde zu einer Dichte expandiert, bei der die Mie Resonanz auftritt, welche von dem IR Puls abgefragt wurde. In einer Clustergrößen-abhängigen Untersuchung konnte der mittlere Ladungszustand vor der Rekombination bestimmt werden.

Durch Umkehr der Pump-Probe Reihenfolge war es möglich die unterschiedliche Zerfallsstadien der IR induzierten Clusterexpansion mittels kohärenter Röntgenbeugung abzubilden. Aus einem Abnehmen der Streusignalintensität bei hohen Winkeln konnte ein Abschmelzen der Cluster-Oberfläche gefolgert werden. Das konnte mittels einfacher, schneller 2D Fouriertransformationen bestätigt werden, welche gleichzeitig zeigen, dass der zentrale Teil des Clusters auf einer Pikosekunden-Zeitskala intakt bleibt. Diese langsame Entwicklung des Clusterkerns wurde durch Ionensignal mit hohen kinetischen Energien bestätigt - selbst eine Nanosekunde nach Initialisierung der Expansion. Speckle-Muster in den Streubildern zeigen den langsam expandierenden neutralen Zentralpart, der in erster Linie durch einen Anstieg der Temperatur und nur zum geringen Teil durch Coulombkräfte auseinander driftet. Aus der mittleren Speckle-Größe lässt sich der mittlere Radius des Clusters zur Zeit seiner Abbildung bestimmen. Eine Modulation der Einhüllenden der Speckle-Intensität resultiert aus Dichte-Fluktuationen innerhalb des zerfallenden Clusters. Durch numerische Streusimulationen konnten die Hauptcharakteristika des gemessenen Speckle-Bildes reproduziert werden.

Contents

Chapter 1

Introduction

The human eye can perceive movies with mircosecond resolution. However, a laser-irradiated molecule takes only femtoseconds to disintegrate into single atoms. In order to make this dissociation process visible to the human eye, many single images taken with femtosecond exposure time and repetition rate need to be played back in a time-laps movie. The realization of such a molecular movie has been far from reach for a long time. Only in this century, with the invention of ultrafast, highly brilliant x-ray free-electron lasers (FELs), imaging of nanoworld objects became feasible approaching atomic resolution in space and time [1, 2]. First proof-of-principle experiments on solid targets were performed at the FLASH facility in Hamburg [3, 4]. Soon, they were followed by many others (e.g. [5, 6]) and the field of femtosecond coherent diffraction imaging and holography evolved. While high-resolution imaging of fixed solid-state targets was previously possible at synchrotron sources by averaging scattering patterns over a long time range, the imaging of single, free, unsupported, and thus naturally-grown and non-reproducible samples is a ground-breaking novelty [7]. From the diffraction patterns it became possible to map the shape and geometry of nanoparticles [8, 9, 10, 11, 12]. Also, fingerprints of ultrafast electronic excitation during femtosecond exposure could be read from the scattered light [10].

However, one single image still does not make a movie. A sequence of independent single-shot still pictures is needed to resolve atomic motion. In a pioneering x-ray pump / x-ray probe experiment, the *fastest movie in the world* was recorded by superimposing two subsequent x-ray holograms from the same sample on one detector [13]. These were later disentangled in post processing and resolved the sample at consecutive times. The experimental setup and reconstructed images are presented in figure 1.1 a. A different approach has to be used to circumvent the complicated process of disentanglement and to gain an extended time-series of more than two 'photographs'. In an optical pump / x-ray probe setup, the initiated evolution of separate identical copies of the sample could be captured in individual pictures at different delay times [14], as presented in figure 1.1 b. With this dynamic imaging method, ultrafast transient states in small particles can be directly recorded. They can contribute to a detailed understanding of molecular motion and chemical reactions.

Imaging nanoobjects by femtosecond x-ray scattering can thus not only reveal the geometry and shape of the sample, but also give access to the light-induced dynamics on the

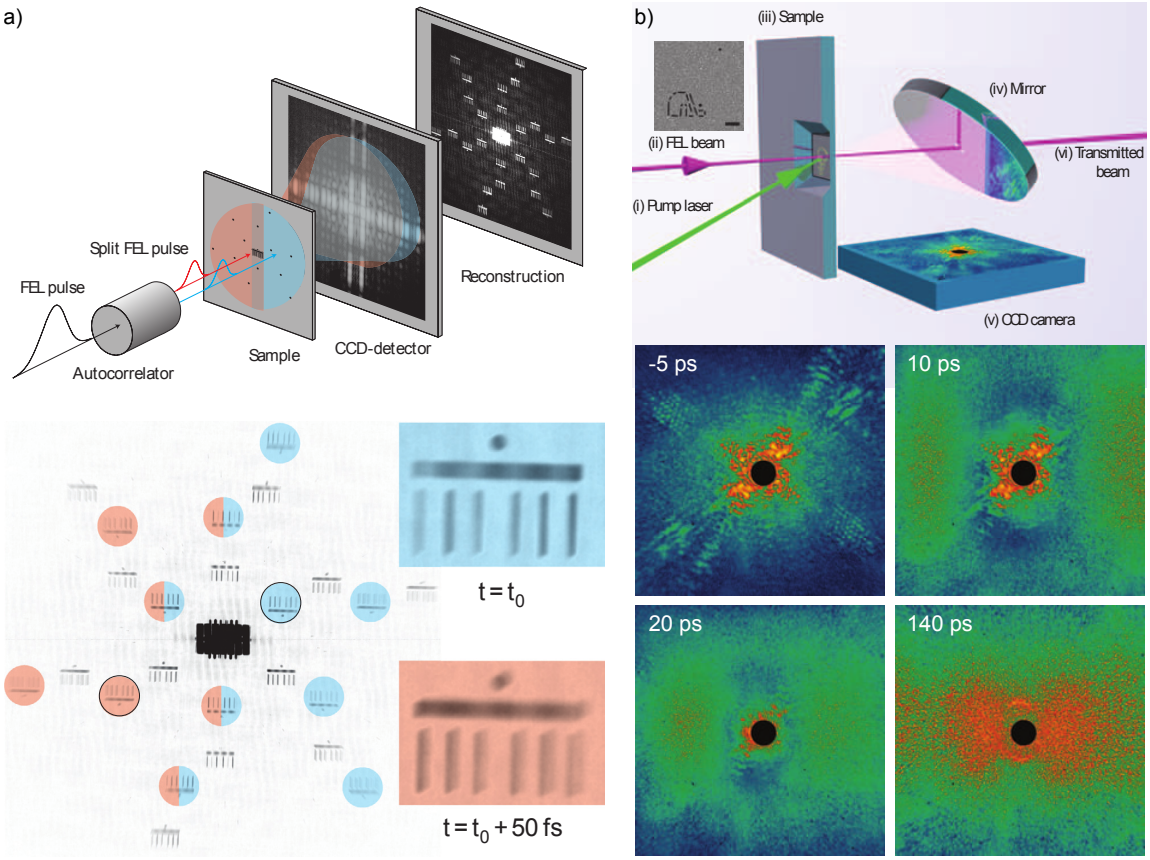

Figure 1.1: Experimental design and scientific results of two pioneering dynamic imaging experiments on solid targets. a) In x-ray pump / x-ray probe setup (blue and red pulse) two holograms from the same target are overlapped on one detector and disentangles in post-analysis. From [13]. b) In optical pump / x-ray probe setup (green and violet beam) a series of scattering patterns is recorded from different targets with the same shape at varying delay times. From [14].

timescale of atomic motion. However, dynamic imaging experiments become increasingly complicated on unsupported particles. Therefore, this thesis contributes to this field by investigating electronic excitation and ionic motion of free nanosamples and developing the experimental techniques required. As object of investigation clusters were chosen. Clusters are well established as nano-labs for laser interaction with finite targets. Due to their simple electronic and geometric structure, they are intriguing research objects for both theorists and experimentalists. Intra- and interatomic processes can be identified and contributions from surface and bulk atoms disentangled by tuning the cluster size from several tens to millions of atom. Time-resolved laser-cluster interaction is studied in this thesis by investigating the interplay of single large xenon, argon and silver clusters with ultrafast infrared (IR) and extreme ultraviolet (XUV) pulses. Ultrafast electron excitation, plasma formation and recombination processes are addressed with elastic light scattering and ion spectroscopy. To investigate atomic movement on a picosecond timescale, a pump probe scheme is applied.

The text is organized as follows. The second chapter gives a quick introduction into the basics of cluster generation, light scattering on nanoobjects, and dynamics arising from

cluster-light interaction. In chapter 3 the experimental setup is described, focusing on the laser pump-probe setup, the cluster source, and the ion and scattering detectors. The major part of this thesis is dedicated to the data analysis and results, presented in chapter 4. Ion spectra and diffraction patterns are examined for insight into nanoplasma dynamics. Theoretical calculations and simulations strengthen the physical interpretations gained from the analysis. A short summary and outlook on possible future experiments is subject to chapter 5.

Chapter 2

Theoretical concepts and previous experiments

A comprehensive introduction of the theoretical background of laser-cluster interaction and an overview of state-of-the-art experiments will be given, to provide a framework for the investigations of this thesis. First, the mechanism to produce rare-gas clusters in a supersonic expansion, semi-empirical scaling laws, and the time characteristics of a pulsed cluster jet are described in chapter 2.1. The key to understanding the functions and characteristics of particles often lies in their structure which can be resolved by imaging with x-ray scattering. The scattering processes fundamental for coherent diffraction imaging are addressed in chapter 2.2. Imaging samples by means of x-ray scattering always induces ionization and plasma formation. The nanoplasma evolution and expansion dynamics are the main topics investigated in this work. Initial ionization and subsequent dynamic processes occurring within the cluster are subject to chapter 2.3.

2.1 Generation of large clusters in supersonic expansions

Clusters, i.e. aggregates consisting of a finite number of atoms, are well established in contemporary studies of laser-matter interaction. They bridge the regime between single atoms and extended solids, since they show solid-like behavior while atomic effects are still relevant. They allow to research physical and chemical properties as a function of size and with varying surface to bulk ratio by tuning their size from a few to several millions of atoms. Rare-gas clusters are often favored in experiments due to their uncomplicated generation in supersonic nozzle expansion.

Section 2.1.1 focuses on cluster growth processes. The dependence of the cluster size on experimental parameters and corresponding prediction of cluster size via scaling laws is subject to section 2.1.2. Since the clusters investigated in this thesis were produced in a pulsed source, the temporal evolution of a cluster beam in a pulsed expansion is addressed in 2.1.3.

2.1.1 Free jet flow and cluster growth

Rare-gas clusters are produced in a supersonic expansion of atomic gas into vacuum. Since rare-gas clusters have small binding energies E_{bind} in the order of only several meV, low temperatures T_0 are needed ($k_B T_0 < E_{bind}$) to produce stable clusters. From a reservoir with low T_0 and with high background pressure p_0, the gas expands through a nozzle with diameter d into a vacuum reservoir with significantly lower pressure. In the high pressure reservoir the thermal atom motion is randomly directed and atom velocities are Boltzman distributed. The mean free path for an ideal gas is given by

$$\lambda = \frac{k_B T_0}{\sqrt{2} \cdot p_0 \cdot \sigma} \tag{2.1}$$

with Boltzmann constant k_B and collision cross-section σ. The atomic beam becomes aligned along the expansion direction by the adiabatic expansion of the gas through a narrow orifice. If the mean free path is smaller than the nozzle diameter d, the beam into vacuum is supersonic ($\lambda < d$)[1], which means that the mean velocity v is higher than the speed of sound c. The random thermal energy is transformed into directed kinetic energy. Faster atoms transfer parts of their energy to slower atoms via collisions. The resulting relative velocities of the atoms are small, which is equivalent to a strong adiabatic cooling of the beam. In the cold atomic beam, the atoms aggregate and clusters will form [15].

The ratio of stream velocity v to local speed of sound c is also referred to as the Mach number $M = v/c$. In the area behind the nozzle the Mach number is larger than one ($M>1$), e.g. the expansion velocity is faster than the speed of sound. This area is called the 'zone of silence', as indicated in figure 2.1. Outside this zone, shock waves are formed which reflect the expansion. They are thin non-isentropic regions of large gradients of velocity, pressure, temperature, and density. To the sides of the supersonic beam they are referred to as barrel shock. Downstream, the so-called Mach disk delimits the zone of silence of the gas jet. Its distance from the nozzle exit is given by [16]

$$d_M = \frac{2}{3}\sqrt{\frac{p_0}{p_{back}}} \cdot d. \tag{2.2}$$

It marks the transition from supersonic flow ($M>1$) back to subsonic flow ($M<1$) and destroys the generated clusters. A differential pumping stage can be used in order to lower the background pressure and therefore shift the Mach disk further away from the cluster source. Conical skimmers with sharp and narrow edges are often used to guide the cluster beam from one pressure stage to the next. The position of the skimmer has to be chosen carefully. On the one hand, the skimmer needs to be close enough to the nozzle, to be located within the zone of silence [17]. On the other hand, the skimmer transmission increases with distance as the mean free path decreases. Therefore, the skimmer needs to be far enough away from the nozzle, so that $\lambda > d_{Skimmer}$.

In microscopic description, the cluster growth process in the supersonic gas jet starts with three-body collisions. Two atoms are sticking together and the third one takes the binding energy away:

$$\mathrm{A} + \mathrm{A} + \mathrm{A} = \mathrm{A}_2 + \mathrm{A}^*. \tag{2.3}$$

[1] For $\lambda > d$ the beam is effusive.

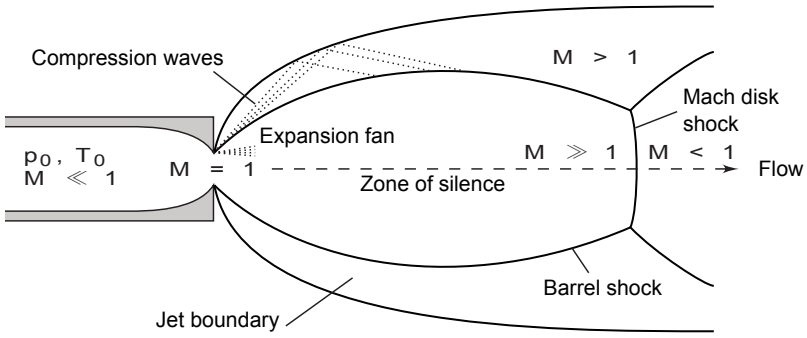

Figure 2.1: Scheme of the supersonic expansion of a free jet, adapted from [16]. Randomly directed atoms are forced through a nozzle behind which the beam gets directed, relative velocities are low, and clusters can form. Shockwaves and the Mach disk form a boundary to the vacuum background. Within the 'zone of silence' clusters can travel without getting destroyed.

The newly formed dimer is further used as nucleation seed growing by subsequent monomer addition. The inner energy of the cluster increases with every monomer attached and atoms evaporate off the cluster to reach thermal equilibrium. The number of atoms in the beam decreases with ongoing cluster growth, which leads to a lower probability for monomer addition. Instead, further down the beam, the growth process is taken over by cluster-cluster coagulation.

The size of the clusters produced is determined by the number of collisions. More specifically, the growth process dependent on the probability of the collisions and on the duration of the timespan at which collisions occur. Those are dependent on three parameters: the backing pressure p_0, the gas temperature T_0 and the shape of the nozzle. Higher backing pressure leads to a higher number of collisions in the beam and therefore to more and larger clusters. A higher temperature leads to a higher beam velocity which results in a lower collision frequency and therefore leads to smaller clusters [18]. The shape of the nozzle used for the supersonic expansion is important. Small nozzle orifices lead to a divergent beam with low collision rates. Less divergent beams have higher directed densities which favors the nucleation process, so that larger nozzle diameters result in larger cluster sizes. Throughout the years several nozzle geometries were proposed and examined for efficient cluster generation. Sonic, laval, conical, and trumpet shaped nozzles were used most commonly (see e.g. [19, 20]). The geometry determines the flow field gradients. If it is chosen such that the gas flow is constricted in transversal direction, the local pressure is higher and the probability of collision increases [19]. Also the on-axis beam flux is higher [20], which is especially important for experiments using a skimmer.

Due to the statistical formation process, the final size of the clusters exhibits a broad distribution. The shape of the size distribution shows an exponential decay at small average sizes where the production process is dominated by monomer addition. For large average sizes resulting from the coagulation of larger clusters, the size distribution further evolves to a log-normal shape. It follows the formulation [21]

$$f(n) = \frac{1}{\sqrt{2\pi}\sigma N} e^{-\frac{(\ln N - \mu)^2}{2\sigma^2}} \tag{2.4}$$

where σ is the logarithm of the geometric standard deviation and μ is the logarithm of the geometric mean.

2.1.2 Cluster size estimation by semi-empirical scaling laws

The size of the produced clusters is determined by the applied gas stagnation pressure p_0, the gas temperature T_0, and the geometry of the nozzle. These parameters together define the condition for the gas flow and therefore the condition for atom condensation [22]. Semi-empirical scaling laws were established in order to predict the mean generated cluster size $\langle N \rangle$ in dependence on these parameters. The first scaling laws were developed by Hagena for mono-atomic rare-gas clusters [22] and were later transformed for metals [23]. It was shown that these simple laws can also be applied to hydrogen-bonded molecular systems if the correct values of the degrees of freedom f were used[2].

A dimensionless scaling parameter Γ was introduced to correlate different initial expansion conditions, which result in the same cluster size for the same gas [24]. The scaling parameter combines the applied gas stagnation pressure p_0, the gas temperature T_0, and the nozzle diameter d:

$$\Gamma = p_0 \cdot T_0^{(q/4-3/2)} \cdot d^q. \tag{2.5}$$

The variable q was determined in various experiments and changes for different materials. For monoatomic gases it holds $q = 0.85$ [24].

Developing the correlation further, in order to be able to compare cluster sizes from particles of different gases, a reduced scaling parameter Γ^* was defined. It includes the characteristic variables $r_{ch} = \sqrt[3]{m/\rho}$ and $T_{ch} = \Delta h_0^0 / k_B$, where m is the atomic mass, ρ is the density of the solid, and Δh_0^0 is the enthalpy of sublimation at 0 K:

$$\Gamma^* = \Gamma \cdot r_{ch}^{(q-3)} \cdot T_{ch}^{(q/4-3/2)}. \tag{2.6}$$

The parameter Γ^* is a measure of the degree of condensation in the beam. Therefore, cluster beams produced from different materials under different conditions but with the same Γ^* should have the same mean cluster size $\langle N \rangle$. In simplified form it can be rewritten as [25, 26]

$$\Gamma^* = K_{ch} \cdot \frac{p_0 \cdot d^q}{T_0^{(5/2-q/4)}} \tag{2.7}$$

with p_0 in mbar, d_{eq} in µm, and T_0 in K. The factor K_{ch} is called specific gas constant and combines all material specific values:

$$K_{ch} = \frac{100 \cdot (10^{-6})^q}{k_B \cdot r_{ch}^{(q-3)} \cdot T_{ch}^{(q/4-3/2)}}. \tag{2.8}$$

The K_{ch} values for rare gases are listed in table 2.1. The increase of the specific gas constant from helium to xenon implies a higher clustering probability.

Table 2.1: Calculated specific gas constants K_{ch} for the rare gases helium, neon, argon, krypton and xenon, from [25]. A high clustering probability is mirrored by a high K_{ch} value.

	He	Ne	Ar	Kr	Xe
K_{ch}	3.85	185	1646	2980	5554

[2] For monoatomic gases $f = 3$ and for diatomic gases $f = 5$.

The orifice diameter d needs to be replaced with the so-called equivalent nozzle diameter d_{eq} in equation 2.7, to account for different nozzle geometries. The half opening angle α of the cone is taken into account for conical nozzles. The equivalent nozzle diameter is then given by

$$d_{eq} = G \cdot \frac{d}{\tan \alpha}. \tag{2.9}$$

The factor G is dependent on the type of gas. For monoatomic gases f $G = 0.736$ [22]. For arbitrary gases it can be calculated by [21]

$$G = 0.5(f+1)^{-(f+1)/4} A^{f/2} \tag{2.10}$$

with f the degrees of freedom for the gas and the constant $A = 3.22$ [27]. In the experiments performed throughout this thesis a conical nozzle with $d = 200\,\mu\text{m}$ and $\alpha = 4°$ was used, corresponding to an equivalent nozzle diameter of $d_{eq} = 2105\,\mu\text{m}$.

The mean number of atoms per cluster $\langle N \rangle$ is deduced from the reduced scaling parameter Γ^* by [23]

$$\langle N \rangle = C \cdot \left(\frac{\Gamma^*}{1000} \right)^B. \tag{2.11}$$

The values for the parameters C and B change for different size regimes (see table 2.2). Throughout this thesis only large clusters are addressed[3] which fall in the regime $10^4 < \Gamma^* < 10^6$.

In the basic assumption that large rare-gas clusters exhibit spherical shape, the mean radius $\langle R \rangle$ of the produced clusters can be gained from the mean number of atoms $\langle N \rangle$ in the cluster by

$$\langle R \rangle = \left(\frac{3 m_a \langle N \rangle}{4\pi\rho} \right)^{1/3} \tag{2.12}$$

with atomic mass m_a and solid density ρ. The expression reduces to $\langle R \rangle = \sqrt[3]{\langle N \rangle} \cdot 0.24\,\text{nm}$ for xenon clusters with $\rho = 3.781 \cdot 10^3\,\text{kg/m}^3$ and $m_a = 131.293 \cdot 1.660 \cdot 10^{-27}\,\text{kg}$. Figure 2.2 shows the average cluster radii for xenon clusters in dependence on stagnation pressure and gas temperature, produced with the nozzle applied in the experiment. The vapor pressure curve is indicated by a white dotted line. Clusters produced from experimental conditions above the curve are expanded from the liquid phase. If too low temperatures are applied and the stagnation pressure exceeds the vapor pressure, the gas freezes in the nozzle and cluster production is disturbed [25]. While the generation of small rare-gas clusters is mostly uncomplicated, the production of large clusters in a size range of several ten to hundred nanometer in radius is more challenging. The high stagnation pressure

Table 2.2: Values for the parameters C and B in equation 2.11. In different sizes range Buck and Krohne (small) [26], Hagena (medium) [23], and Dorchies (large) [28] found the listed values.

	$350 < \Gamma^* < 1800$	$1800 < \Gamma^* < 10^4$	$10^4 < \Gamma^* < 10^6$
C	3.84	33	100
B	1.64	2.35	1.8

[3] $p_0 = 9.8\,\text{bar}$, $T_0 = 180\,\text{K}$, $d_{eq} = 2105\,\mu\text{m}$, $\Gamma^* = 2.472 \cdot 10^5$.

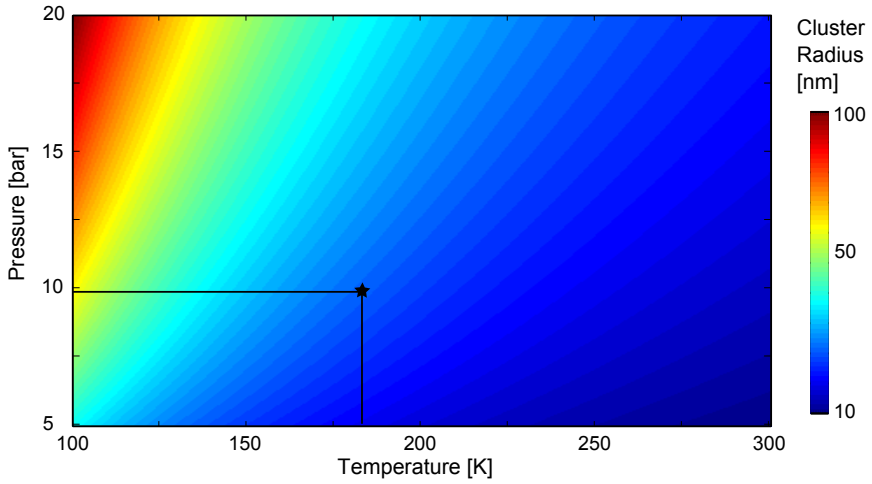

Figure 2.2: Average cluster radius in dependence on gas temperature and backing pressure for a nozzle with equivalent diameter of $d_{eq} = 2105\,\mu m$ and xenon gas, as calculated from equation 2.11. With backing pressure the average size increases, while it decreases with higher temperature. The experimental condition for the experiments described in this thesis is indicated by a star.

needed to produce large clusters leads to poor vacuum. In order to keep the background pressure low, strong vacuum pumps are needed and cluster generation is often performed in a pulsed jet instead of a continuous jet.

2.1.3 Temporal profile of a pulsed cluster jet

In a pulsed cluster jet, the concentration of the beam changes in time and space. Good knowledge of the temporal profile of the cluster jet is necessary to predict the generated cluster size. Up to date, two major studies investigated the temporal profile of pulsed jet [29, 30] and will be introduced in the following.

In the first study [29], the cluster flow of ensembles of xenon clusters in a pulsed expansion were investigated with the Raleigh scattering method for three different source geometries. One configuration had no reservoir between valve and nozzle and the other two had a small ($15\,mm^3$) and a large ($38\,mm^3$) reservoir respectively. As presented in figure 2.3 a, the time resolved spectra from xenon clusters show one plateau for the source without reservoir and two peaks for the geometries with reservoir. The second peak presumably results from larger clusters forming late in the pulsed beam. Apparently large clusters mainly grow if a preroom is present. It was interpreted by the authors that the gas remaining in the preroom after valve closing can serve as condensation nuclei upon a second reopening of the valve.

In the second study [30], a similar temporal behavior was found but a different explanation for the underlying physical processes was used. In an experimental setup similar to the one presented in this thesis in chapter 3, single large xenon clusters were investigated with x-ray scattering method allowing to precisely determine the radius of every detected cluster. The size of the preroom in the source was kept constant but the expansion conditions were varied from large clusters (case A), over medium sized clusters (case B), to atomic

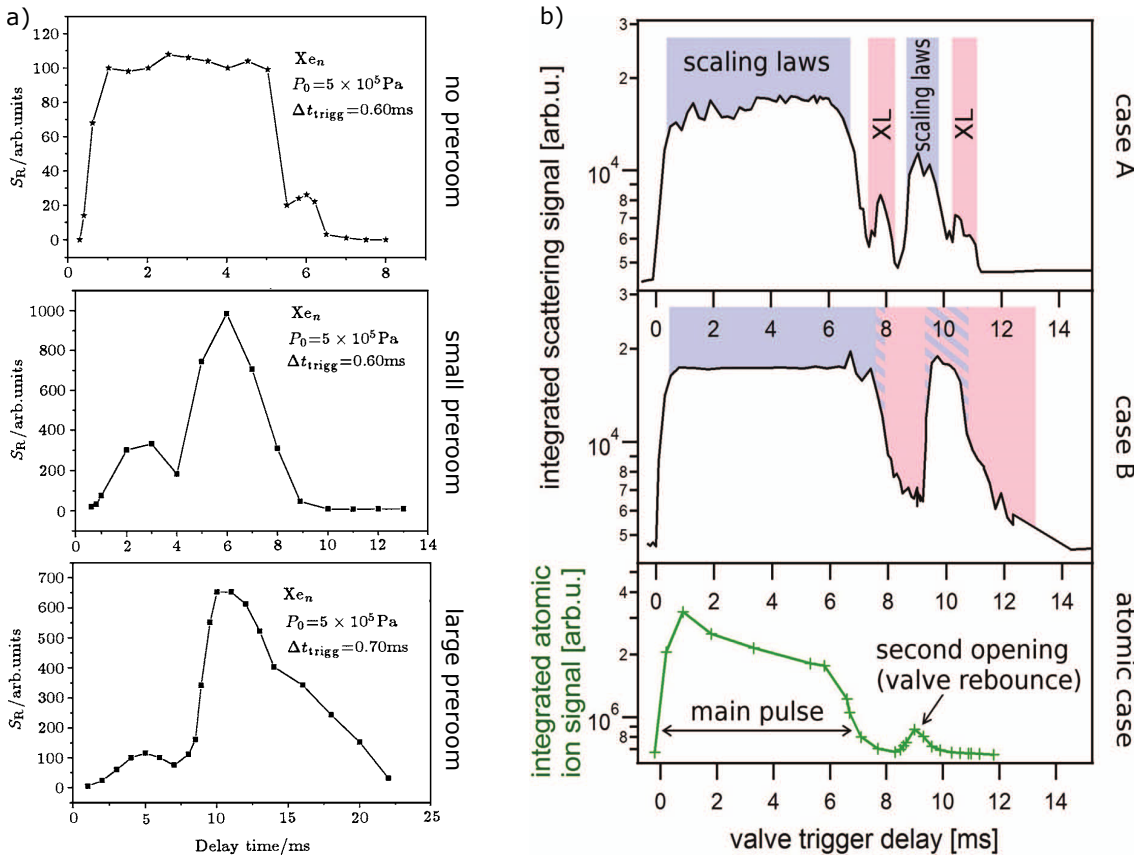

Figure 2.3: a) Temporal jet profile for ensembles of xenon clusters produced in sources with different preroom (reservoir between valve and nozzle) sizes. From [29]. The Rayleigh scattering signal gives information about the size and amount of xenon clusters in the beam. Two plateaux are visible in the graph taken with a large and small preroom respectively, while the spectrum taken with a source without preroom shows only one plateau. b) Temporal jet profile for single xenon clusters. From [30]. The second plateau in the atomic case hints towards a valve rebounce. The large cluster size at the end of each plateau in case A and B respectively, indicate that the cluster size is independent of the rebounce but results from the closing of the valve.

beams. The temporal profiles presented in figure 2.3 b show a broad plateau followed by a pronounced peak for all three cases. The second peak in the atomic case identifies that the valve opened twice due to a rebounce, since here the second peak cannot result from large clusters late in the beam.

In case A, two additional small peaks are present following the plateau and the major peak. The scattering experiment on single clusters makes it possible to determine the cluster size directly. It shows that in these small peaks only large clusters are present, e.g. that they appear late in the beam before the closing of the valve. A pressure shock wave arising from the valve closing might shift the initial expansion conditions towards much more extreme values, leading to larger clusters. Condensation in the preroom seems to be rather unlikely, as the gas temperature in front of the nozzle throat is still high. Hence, the large clusters detected at late times in the temporal profile can also appear if the valve does not exhibit a rebounce.

2.2 Basic concepts and previous results for light scattering on clusters

For the investigations in this thesis, clusters of different size and shape were illuminated by highly intense laser pulses. For a profound understanding of the underlying processes, this chapter gives an introduction to light propagation in matter. In section 2.2.1, the fundamentals of absorption and refraction are discussed. This approach is complimented by the microscopic treatment of light scattering. The basic concepts of elastic light scattering are for simplicity firstly described by scattering on free electrons and electrons bound to atoms. The formalism is later extended to multi-atomic particles. Afterwards, coherent diffraction on finite targets is introduced, distinguishing between optically thick and optically thin objects. The second part (chapter 2.2.2), concentrates on diffraction and scattering from spherical particles. Starting with Fraunhofer diffraction from a single aperture, the system is subsequently extended to arbitrary two-dimensional shapes. Then, Mie theory for three-dimensional spheres is highlighted shortly, including properties of matter. Finally, in section 2.2.3, several previous experiments using light scattering on clusters are reviewed. They have made use of this method in order to study the geometry and light-induced dynamics of clusters.

2.2.1 Fundamentals of light propagation

This section gives a short introduction into the fundamentals of light propagation. For a more detailed description the reader is referred to the literature [31, 32, 33]. Light propagation is described by the Maxwell's equations which are expressed in differential form as [34]

$$\begin{aligned} \nabla \cdot \boldsymbol{D} &= \rho \\ \nabla \cdot \boldsymbol{B} &= 0 \\ \nabla \times \boldsymbol{E} &= -\frac{\partial \boldsymbol{B}}{\partial t} \\ \nabla \times \boldsymbol{H} &= \boldsymbol{J} + \frac{\partial \boldsymbol{D}}{\partial t} \end{aligned} \tag{2.13}$$

where $\boldsymbol{D}$ is the electric displacement, $\boldsymbol{B}$ is the magnetic induction, $\boldsymbol{E}$ is the electric field vector, and $\boldsymbol{H}$ is the magnetic field vector. ρ and $\boldsymbol{J}$ are the free charge density per unit volume and free current density per unit area respectively. Monochromatic solutions to the Maxwell equations are plane harmonic waves. The electric field amplitude of a linearly polarized, electromagnetic plane wave is expressed as [33]

$$\boldsymbol{E}(\boldsymbol{r}, t) = \boldsymbol{E}_0 e^{i(\boldsymbol{k}\boldsymbol{r} - \omega t)} \tag{2.14}$$

where $\boldsymbol{r}$ indicates the position, ω the light frequency, and t the time. The wave vector $\boldsymbol{k}$ is related to the wavelength λ by $|\boldsymbol{k}| = 2\pi/\lambda$. The amplitude of the wave oscillates sinusoidally and the phase of the wave $\phi = \boldsymbol{k}\boldsymbol{r} - \omega t$ indicates the instantaneous state of this oscillation at point r.

In free space in the absence of any charges, e.g. in vacuum, the Maxwell equations can be rearranged to derive the homogeneous wave-equation for the electromagnetic field in scalar

form [35]

$$\nabla^2 \boldsymbol{E} - \varepsilon_0 \mu_0 \frac{\partial^2 E}{\partial t^2} = 0. \tag{2.15}$$

The permittivity of free space ε_0 and the magnetic permeable μ_0 can be expressed in terms of the phase velocity for propagation in vacuum, e.g. the speed of light, as $c = 1/\sqrt{\mu_0 \varepsilon_0}$.

Wave propagation in medium - index of refraction

If a wave is propagating through a medium instead of vacuum, the materials' refractive index n has to be taken into account[4]. In this case, the phase velocity is $v_p = c/n$, or in terms of the wave frequency $v_p = \omega/k$, which leads to the dispersion relation $k = \omega n/c$. The complex refractive index describes refraction and absorption of a material and is often written as [33]

$$n = (1 - \delta) + i\beta. \tag{2.16}$$

The real part accounts for the change in phase velocity of the propagating wave compared to that in vacuum and the imaginary part accounts for the attenuation of the wave propagating through medium. Based on the electric field amplitude of an electromagnetic wave in vacuum (2.14), the plane wave solution for the Maxwell equations in dielectric isotropic medium holds

$$\boldsymbol{E}(\boldsymbol{r}, t) = \boldsymbol{E}_0 e^{i(\boldsymbol{kr} - \omega t)} e^{i(1-\delta)\boldsymbol{kr} - \beta \boldsymbol{kr}}. \tag{2.17}$$

This solution consists of a superposition of two plane waves, one in vacuum and one in the medium of the refractive index n.

In a medium, due to **absorption** the wave amplitude decreases exponentially with increasing distance in the direction of propagation. The decay of intensity is described by the Lambert-Beer law as $I = I_0 \cdot e^{-\mu d}$ with I_0 the incident beam intensity, μ the linear absorption coefficient, and d the thickness of the material. The imaginary part of the refractive index is related to the linear absorption coefficient via $\mu = 2k\beta = 4\pi\beta/\lambda$. The intensity decreases by a factor of e over a distance [33]

$$l_{abs} = \frac{1}{\mu} = \frac{\lambda}{4\pi\beta} \tag{2.18}$$

also denoted as penetration depth into a thick material.

The refractive index of a medium is dependent on the light frequency. Close to atomic resonance frequencies the imaginary part β is larger, which implies that the attenuation is stronger there, due to an increased absorption probability. For optical light, n is typically larger than 1, while in the extreme ultraviolet regime it is usually close to but slightly smaller than 1. On the microscopic level, a photon absorbed by an atom transfers its energy to an electron, which in turn is transferred into an excited bound state or a free state above the ionization potential. If the photon is not absorbed it is either transmitted or scattered. Therefore, even though they are different processes, absorption and scattering are not independent and the factors δ and β are related[5].

[4] Note that in vacuum $n = 1$.

[5] The real and imaginary part of the refractive index delta and beta are connected by the Kramers-Kronig-relations (see for example [35]), relating the processes of absorption and scattering.

If a free propagating wave impacts on an interface to a medium, the wave is scattered at many scatterers within the material. The superposition of all scattered waves gives the **reflected** wave. It is moving with phase velocity v_p towards one direction, given by the Snells law: $\cos\alpha = n\cos\alpha'$, where α and α' are the incident and the refracted angle [33]. In all other directions the scattered amplitudes result to zero. Hence, the real part of the refractive index relates the angles of incidence and refraction when the plane wave is refracted at the interface between free space and medium.

A scattered wave exhibits a relative phase shift respective to the incoming wave given by [32]

$$\Delta\phi = \frac{2\pi\delta}{\lambda}\Delta r. \tag{2.19}$$

If $(1-\delta)>1$, the incoming and outgoing waves are in phase. If the the real part of the refractive index is smaller than unity, both waves are not in phase and the phase velocity inside the medium is larger than the speed of light[6]. This leads to the phenomenon of total internal reflection. In a scattering experiment, however, the phase cannot be detected, since only the scattered intensity is recorded, which is the modulus squared of the electric field amplitude

$$I = |E(\boldsymbol{r},t)|^2. \tag{2.20}$$

Elastic wave scattering

In this section the scattering probability of free electrons will be acquired. In a classical approach an impacting electromagnetic wave forces a **free electron** to oscillate. The electronic charge accelerates in the external field and its oscillating motion can be described by the Lorentz force $-e\boldsymbol{E}$. An electric dipole is produced. Upon its vibration the electron acts as a source and radiates a scattered wave. The electron acceleration is derived by Newtion's equation of motion $m_e\boldsymbol{a}(\boldsymbol{r},t) = -e\boldsymbol{E}(\boldsymbol{r},t)$, where m_e is the electron mass. With this and Maxwell's equations (2.14), the radiated field is deduced to [35]

$$\boldsymbol{E}(\boldsymbol{r},t) = -\frac{e^2}{4\pi\epsilon_0 m_e c^2}\frac{1}{r}\boldsymbol{E}_0\sin\theta e^{i(\boldsymbol{kr}-\omega t)} \tag{2.21}$$

with scattering angle θ and the classical electron radius $r_e = \frac{e^2}{4\pi\epsilon_0 m_e c^2}$.

For linearly polarized light, the intensity distribution of the scattered wave from the dipole induced by the oscillating electron dipole is depicted in figure 2.4. It is doughnut-shaped with a central hole in direction of the oscillation. A measure to characterize the strength of the scattered field is the total scattering cross-section σ. It is defined by the ratio of the average total power radiated by an oscillating electron $\bar{P}$ to the average incident power $\bar{\boldsymbol{S}}$:

$$\sigma = \frac{\bar{P}}{|\bar{\boldsymbol{S}}|}. \tag{2.22}$$

For a single free electron it holds $\sigma = \frac{8}{3}\pi r_e^2$, which is also denoted as Thomson cross-section.

The amplitude of the light scattered by a **single atom** can be given in fractions of the scattering amplitude of a single free electron. The ratio of scattering amplitude of an atom

[6] The group velocity however is still smaller than c.

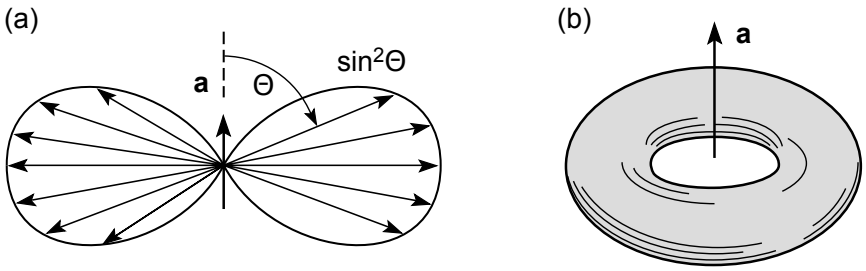

Figure 2.4: Donought-shaped intensity distribution of the radiation from a dipole which is induced by an electron oscillating in an electric field. From [32]. The central hole lies in direction of the oscillation a.

to the scattering amplitude of a free electron is given by the complex atomic scattering factor $f(\boldsymbol{q},\omega)$. It is dependent on the light frequency and the scattering vector $\boldsymbol{q} = \boldsymbol{k}_{out} - \boldsymbol{k}_{in}$ with $|\boldsymbol{q}| = 2|\boldsymbol{k}|\sin(\theta/2) = 4\pi/\lambda \cdot \sin(\theta/2)$. In spherical coordinates the scattering vector is composed of [36]

$$\begin{aligned} q_x &= q \cdot \cos(\theta/2)\cos(\varphi), \\ q_y &= q \cdot \cos(\theta/2)\sin(\varphi), \\ q_z &= -q \cdot \sin(\theta/2) \quad (\pi \geq \theta \geq 0; 2\pi > \varphi \geq 0) \end{aligned} \tag{2.23}$$

The atomic scattering factor accounts for the fact that the electrons in the atom are bound and have different contributions to the scattering signal. It introduces binding forces and damping and is composed of a real and an imaginary part $f(\boldsymbol{q}) = f'(\omega) - f''(\omega)$, where $f'(\omega)$ accounts for the binding of electrons to the atom and $f''(\omega)$ for the absorption of photons. The field radiated from an atom is given by [33]

$$\boldsymbol{E}(\boldsymbol{r},t) = -\frac{r_e}{r} f(\boldsymbol{q},\omega)\boldsymbol{E}_0 \sin\theta e^{i(\boldsymbol{kr}-\omega t)}. \tag{2.24}$$

Hence the total scattering cross-section for an atom is $\sigma = \frac{8}{3}\pi r_e^2 |f(\omega)|$ [33].

One topic of this thesis is the light interaction with **clusters, composed of many atoms**. In principle, in a system with several atoms, the wave scattered from one atom can be scattered by a second atom and so on. However, if this multiple scattering is neglected, the scattering amplitude from an object consisting of N atoms is simply calculated as the summation of the scalar electric fields from an arrangement of N point scatterers [36]:

$$A(\boldsymbol{q},\omega) = \sum_{j=1}^{N} \xi_j(\boldsymbol{q},\omega) e^{-i(\boldsymbol{q}\boldsymbol{r}_j - \omega t)} \tag{2.25}$$

where $\boldsymbol{r_j}$ is the central position of the jth atom, and $\xi_j(\boldsymbol{q},\omega)$ is the specific scattering efficiency for each scattering atom. It contains the atom specific form factor $f_j(\boldsymbol{q},\omega)$, the distance between particle and detector L, and the differential Thomson cross-section $\frac{d\sigma}{d\Omega}$ of a free electron: $\xi_j(\boldsymbol{q},\omega)^2 = |f_j(\boldsymbol{q},\omega)|^2 (\frac{1}{L^2}) \frac{d\sigma}{d\Omega}$ [36]. The scattered wave is a superposition of dipole radiations, building a spherical wave front.

Real and imaginary part of the atomic form factor f can be expressed in terms of the real and imaginary part of the refractive index n, to connect microscopic and macroscopic

description [33]

$$f'(\omega) = \frac{2\pi}{n_a r_e \lambda^2}\delta \quad , \quad f''(\omega) = \frac{2\pi}{n_a r_e \lambda^2}\beta. \tag{2.26}$$

Here n_a is the particle density and r_e the electron radius.

Diffraction in the far-field

If the wavelength of the light is larger than the irradiated object, the outgoing wave is best described by scattering, as it is the case of atoms in extreme ultraviolet (XUV) light or clusters in infrared (IR) light. For clusters in XUV light, the obstacle is larger than the wavelength. Here the outgoing wave is best described by diffraction. For objects with complicated geometry exact solutions of Maxwell equations are mostly not available, therefore approximations need to be used. The detector distance L is much larger than $\pi R^2/\lambda$ for all experiments performed in this work, which means that the experiments are in the far-field limit [32]. In this Fraunhofer regime the scattered waves can be approximated as scalar functions, which behave asymptotically like plane waves.

In the small-angle scattering limit $|\boldsymbol{q}| << k$, the relation of complementarity holds, which is also known as Babinet's principle. It states that diffraction from an obstacle can be treated as diffraction from an equally shaped aperture in an infinitely extended screen. Additionally, the far-field scattering pattern, which holds the geometry information of the scatterer, can be described by the 2D Fourier transform of the object's electron density projected onto a plane perpendicular to the incoming wave propagation direction [33]

$$I = \left|\boldsymbol{E}(\boldsymbol{r},t)\right|^2 = \left|\frac{e^{ikr}}{r}\int \rho(\boldsymbol{r}) e^{i\boldsymbol{q}\boldsymbol{r}} d^3\boldsymbol{r}\right|^2. \tag{2.27}$$

This becomes evident in the definition of the atomic form factor as the integral over the electron density of the atom $\rho(\boldsymbol{r})$, which gives the probability that an electron is positioned at a certain position $\boldsymbol{r}$ of the atom [33]

$$f(\boldsymbol{q}) = \int_{Atom} \rho(\boldsymbol{r}) e^{i\boldsymbol{q}\boldsymbol{r}} d^3\boldsymbol{r}. \tag{2.28}$$

Comparing equations 2.27 and 2.28 clearly shows that the atomic scattering factor is simply the Fourier-transform of the atomic electron density. Therefore a simple and effective method to estimate the **two-dimensional outline of a particle** shape from its small-angle far-field scattering pattern is to compare the Fourier transform of estimated particle shapes with measured scattering distributions as done in several experiments (c.f. [11] and chapter 4.3.1).

Only for small scattering angles, e.g. where the projection vector $\boldsymbol{n_p}$ is approximately parallel to $\boldsymbol{k_{in}}$, the assumption is valid that just a single projection plane is recorded in the scattering pattern. If a large angle range is detected, several projection planes under various angles are contained in the diffraction patterns, as schematically depicted in figure 2.5 b. If also large angles are detected in a 2D scattering pattern, the **three-dimensional shape of a particle** is encoded. The 2D information can be extended to a 3D object by accounting for the object depth with a multislice method [12].

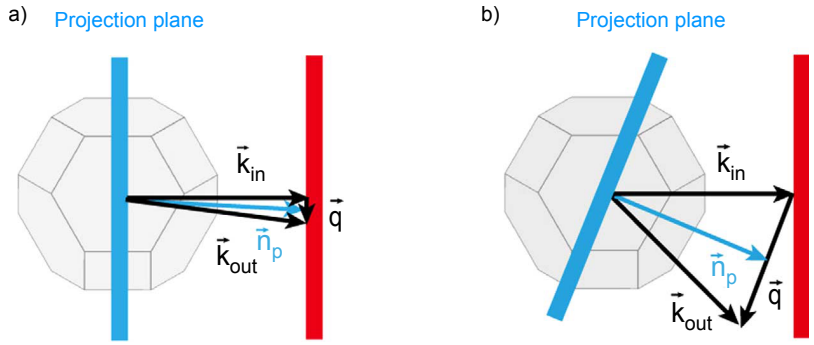

Figure 2.5: Schematics of small and wide angle scattering. From [12]. a) In small-angle scattering geometry the spatial information in beam propagation direction is not resolved, because the scattering vector $\boldsymbol{q}$ and the projection plane are oriented perpendicular to the beam. The projection vector $\boldsymbol{n_p}$ is approximately parallel to $\boldsymbol{k_{in}}$. b) In wide-angle scattering geometry 3D information is contained in the pattern because the projection plane is rotated considerably.

To simulate a wide-angle scattering pattern, the 3D object is subdivided into a stack of 2D binary arrays with their normal vectors $\boldsymbol{n_p}$ oriented parallel to the direction of wave propagation, which contain the particle electron density $\rho(x, y, z_{=j})$ at the respective slice of number j. The phase ϕ of each object slice, accounting for the speed and direction of light propagation, is given by [12]:

$$\phi_j(x, y) = (\sqrt{k^2 - (x^2 + y^2)} - k) \cdot j \tag{2.29}$$

where k is the wave vector. Subsequently, the Fourier transform is performed independently for each array. Finally all Fourier transforms are phase corrected and summed up to one final pattern [12]

$$F = |\mathcal{F}(\rho(x, y, z_{=j}))| + e^{i(\phi_j + \phi_{slice})}. \tag{2.30}$$

In contrast to small-angle scattering patterns, the wide-angle images are often not point-symmetric. This is owed to the fact that the Fourier transform of a symmetric function is always real, while the Fourier transform of an asymmetric function is imaginary [33]. In the diffraction patterns itself this behavior is manifested in a transition from broken point-symmetry to point-symmetry from large to small angles [12] (see also figure 2.8).

2.2.2 Diffraction and scattering from spherical objects

Rare-gas clusters grown by monomer-addition and by coagulation[7] are often round in shape (cf. section 2.1). For the simple case of spherical objects one can state precise calculations which will be highlighted in the following.

As stated earlier, due to Babinet's principle, the far-field diffraction pattern from a circular disk is equal to the one from a **circular aperture**. The latter is the well known Airy pattern. The intensity distribution in the far-field of an aperture with radius R is given by [33]

$$I = I_0 \cdot \left| \frac{2J_1(kR\sin\theta)}{kR\sin\theta} \right|^2 \tag{2.31}$$

[7] if the cluster is still warm enough and not frozen in an intermediate state.

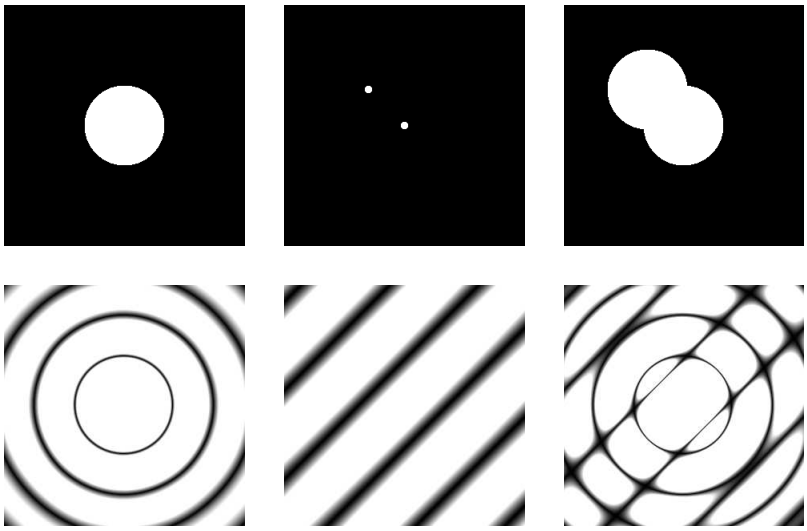

Figure 2.6: Binary array with one circular object. The corresponding ring-shaped diffraction pattern is called Airy pattern. The diffraction pattern from two point objects exhibits fringes. Two circular objects lead to a diffraction pattern with an Airy pattern amplitude which is in itself modulated by a set of interference fringes.

where J_1 is a first order Bessel function. The position of the first minimum θ_{min} is found at $k \cdot R \cdot \sin(\theta_{min}) = 3.83$. With this relationship the radius of a spherical cluster R can in simple approximation be deduced from the angle of the first minimum in the recorded scattering pattern as [32]

$$R = 0.61 \cdot \frac{\lambda}{\sin(\theta_{min})}. \tag{2.32}$$

In this formula the material dependent absorption or phase shift are not accounted for, even though they have an additional influence on the position of the minimum. Nevertheless, for the scope of this thesis equation 2.32 is of sufficient accuracy and has therefore been used in the analysis in section 4.1.1 to determine the radius of the clusters to study the size dependence of light-cluster interactions.

As introduced in section 2.1.1, clusters not only grow by monomer addition but from a certain size onwards also by coagulation. Thereby they sometimes freeze and build dumbbell-shaped twin clusters, triple clusters, and so on, up to hailstone-shaped nano-particles. The projection of these objects can be described by **multiple circular apertures** arranged on a flat screen. A set of apertures c_m, which all have the same radius and are not in contact with each other, build an overall aperture function $\rho(x, y) = \sum_m c_m(x, y)$. The diffracted amplitude from this system is given by the Fourier transform of the aperture function [37]

$$F(k_x, k_y) = \mathcal{F}(\rho(x, y)) = \int\int \rho(x, y) e^{i(k_x x + k_y y)} dx dy \tag{2.33}$$

The diffraction amplitude from the individual opening, defined as $C_0(k_x, k_y) = \mathcal{F}(c_0(x, y))$, is the above introduced Airy pattern. With the addition theorem of the Fourier transforms the diffraction amplitude from all aperture openings becomes $F(k_x, k_y) = \sum C_m(k_x, k_y)$. Taking the shifting theorem $C_m(k_x, k_y) = C_0(k_x, k_y) e^{i(k_x x_m + k_y y_m)}$ into account, the overall

diffracted amplitude can be expressed as [37]

$$\begin{aligned} F(k_x, k_y) &= C_0(k_x, k_y) \sum_{m=1}^{N} e^{i(k_x x_m + k_y y_m)} \\ \rightarrow \mathcal{F}(\rho(x,y)) &= \mathcal{F}(c_0(x,y)) \sum_{m=1}^{N} e^{i(k_x x_m + k_y y_m)} \end{aligned} \tag{2.34}$$

This equation expresses that the total scattering pattern comprises of the Airy pattern amplitude which is in itself modulated by a set of interference fringes, as visible from figure 2.6. The appearance of the fringes is determined by the arrangement of the single aperture positions. The pattern becomes increasingly complicated with increasing aperture number.

Mie theory

The elastic scattering from a **three-dimensional sphere** has been described by Gustav Mie in the context of his research on small gold colloids [38]. Based on the Maxwell equations (see set of equations 2.14), the Mie theory describes exactly the interaction between a plane electromagnetic wave and a homogeneous, dielectric, spherical particle, independent of distance of detection, and detected angle range. The scattered wave depends on the ratio of particle radius to light wavelength and the refractive index of the particle. It becomes possible to determine the radius and the refractive index of the particle by fitting radial profiles of experimentally recorded scattering patterns with Mie calculations. The entire derivation of the solution is complicated and described in detail in several books [39, 40, 41]. Here, only a short introduction and illustration of the main principles are given.

In vector form the fields inside and outside the object are described as superposition of partial waves. All partial waves have to be solutions of the wave equation which directly follow from the Maxwell equations. As boundary condition the energy at the surface needs to be conserved. The scattering field $\boldsymbol{E}_s$ in matrix form as a function of the incoming field $\boldsymbol{E}_i$ is written as [39]

$$\begin{pmatrix} E_{\parallel s} \\ E_{\perp s} \end{pmatrix} = \frac{e^{i\boldsymbol{k}(r-z)}}{i\boldsymbol{k}r} \begin{pmatrix} S_2 & S_3 \\ S_4 & S_1 \end{pmatrix} \begin{pmatrix} E_{\parallel i} \\ E_{\perp i} \end{pmatrix} \tag{2.35}$$

with angular scattering functions S_1, S_2, S_3, and S_4 and wave vector $\boldsymbol{k}$. For fully polarized light $S_3 = S_4 = 0$. The remaining scattering functions are infinite series. For computations, a cutoff at a certain degree m[8] yields good approximations [39]:

$$S_1 = \sum_m \frac{2m+1}{m(m+1)}(a_m \pi_m + b_m \tau_m) \quad , \quad S_2 = \sum_m \frac{2m+1}{m(m+1)}(a_m \tau_m + b_m \pi_m) \tag{2.36}$$

where a_m and b_m are scattering coefficients and π_m and τ_m are angular functions of the respective degree.

[8] To avoid confusion, it is necessary to note that in the book of Bohren and Huffman [39] the refractive index is denoted m and the degree of the series is denoted n, while in this thesis they are named the other way around. This denotation was chosen because in most literature like e.g. [32, 33] n is used for the refractive index.

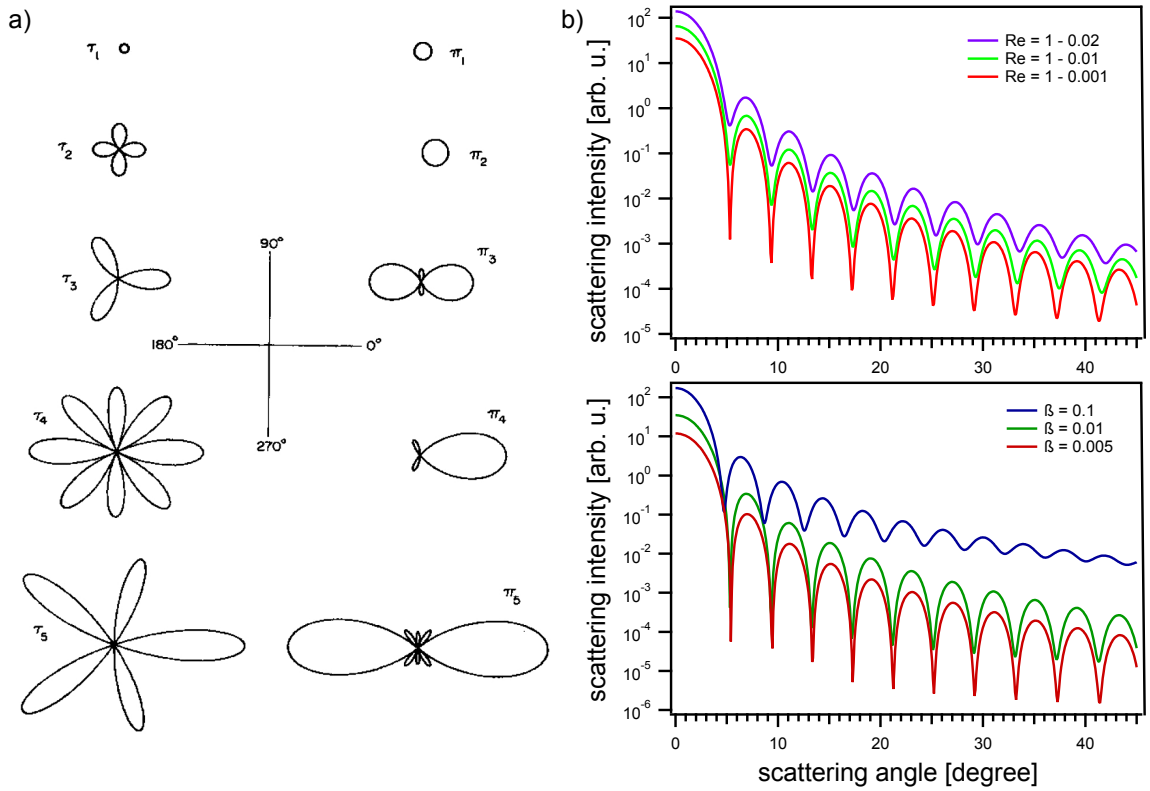

Figure 2.7: a) First five angular functions parallel and perpendicular to the propagation direction of the incoming beam. From [39]. With higher orders the lobes shift towards forward direction. b) Mie profiles of a 50 nm radius sphere exposed to 13.5 nm light. Their dependence on the real and imaginary part of the refractive index are depicted. With increasing real part $1-\delta$ (phase shift) the minima shift towards higher scattering angles (from red to blue). With increasing imaginary part β (absorption) the minima get shallower (from red to blue).

The scattering coefficients depend on spherical Bessel functions J, H and its derivatives J', H' and are calculated by [39]

$$a_m = \frac{nJ_m(nx)J'_m(x) - J_m(x)J'_m(nx)}{nJ_m(nx)H'_m(x) - H_m(x)J'_m(nx)} \quad , \quad b_m = \frac{J_m(nx)J'_m(x) - nJ_m(x)J'_m(nx)}{J_m(nx)H'_m(x) - nH_m(x)J'_m(nx)}.$$

The angular functions π_m and τ_m are defined as [39]

$$\pi_m = \frac{P_m}{\sin\theta} \quad , \quad \tau_m = \frac{dP_m}{d\theta} \tag{2.37}$$

with P the Legendre polynomial. The first five modes are plotted in figure 2.7 a.

The number of degrees calculated before truncation is dependent on the particle size in respect to the wavelength of the incoming light. With increasing order, the maximum scattered light shifts forward and the scattering lobes become finer. With increasing sphere size higher orders become increasingly important. For spheres with larger radius the first minimum shifts towards smaller angles, as already evident from the Airy pattern equation 2.32. In the scope of this thesis, Mie theory is used to determine the average radius of a cluster if the first minimum is not detected and therefore the Airy equation is not applicable.

The index of refraction influences the depth of the fringe minima, as depicted in figure 2.7 b. For spheres with a diameter of 100 nm irradiated with 13.5 nm wavelength light the following effect becomes visible for the diffraction pattern in forward direction: With increasing real part - e.g. phase shift - the minimum shifts towards higher scattering angles, while with increasing imaginary part - e.g. absorption - the minimum gets shallower. Mie theory includes sharp boundary conditions, since the refractive index for the object's material is taken to be constant and changes abruptly at the surface layer between vacuum and obstacle. It is a static theory which neglects dynamic effects like e.g. light-induced changes in the electronic structure or the density of the sphere. Therefore, even though Mie theory gives exact solutions for an ideal, homogeneous and spherical particle, the values gained from Mie fits for the refractive index can only serve as an estimate.

2.2.3 XUV scattering experiments on large clusters

Several single-shot single-cluster experiments have been performed at free-electron lasers up to date [42, 10, 11, 30, 12, 43, 44]. Their main goal was to investigate

- the cluster morphology, which gives indication about the cluster growth process,
- light induced ultrafast electron dynamics, imprinted in the scattering pattern by modifying the optical constants, and
- light induced cluster ionization and fragmentation dynamics.

XUV scattering experiments on xenon clusters of about 50 nm in radius produced in a supersonic expansion from the gas phase have identified two coexisting pattern geometries: concentric ring patterns and fringe patterns with underlying substructures [11]. Scattering simulations, using the Fourier transform of particle 2D projections, identified that these images result from spherical particles and more complex shaped obstacles like dumbell-shaped twin clusters. Figure 2.8 a shows outlines of twin clusters in various degrees of coalescence and the resulting scattering pattern simulations, matching experimental results. In a second experiment, even triple clusters and more complicated hailstone-like particles were found for larger clusters up to a micron radius [30]. From these final cluster shapes, new aspects of the cluster growth process became comprehensible. While small clusters arrange in monomer-addition, larger clusters grow in coagulation and, depending on their temperature, can freeze out in intermediate states, resulting in complex geometries.

In more advanced scattering simulations based on scalar theory and using the Born approximation, even three-dimensional particle information was extracted from the recorded images of multiple clusters in the interaction region [11]. Not only the particles' size but also their relative position, orientation, and distance within the focal volume was evaluated.

The structure of free silver clusters produced in a magnetron sputtering source was captured in another XUV scattering experiment [12]. The highly symmetric patterns, as reprinted in figure 2.8 b, point towards particle shapes of regular polyhedra. Broken point-symmetry in some of the wide-angle scattering patterns reveals that 3D information is encoded (see section 2.2.1). With multi-slice Fourier-transform simulations the orientation towards the beam axis and the full 3D shape of the individual particles was assigned.

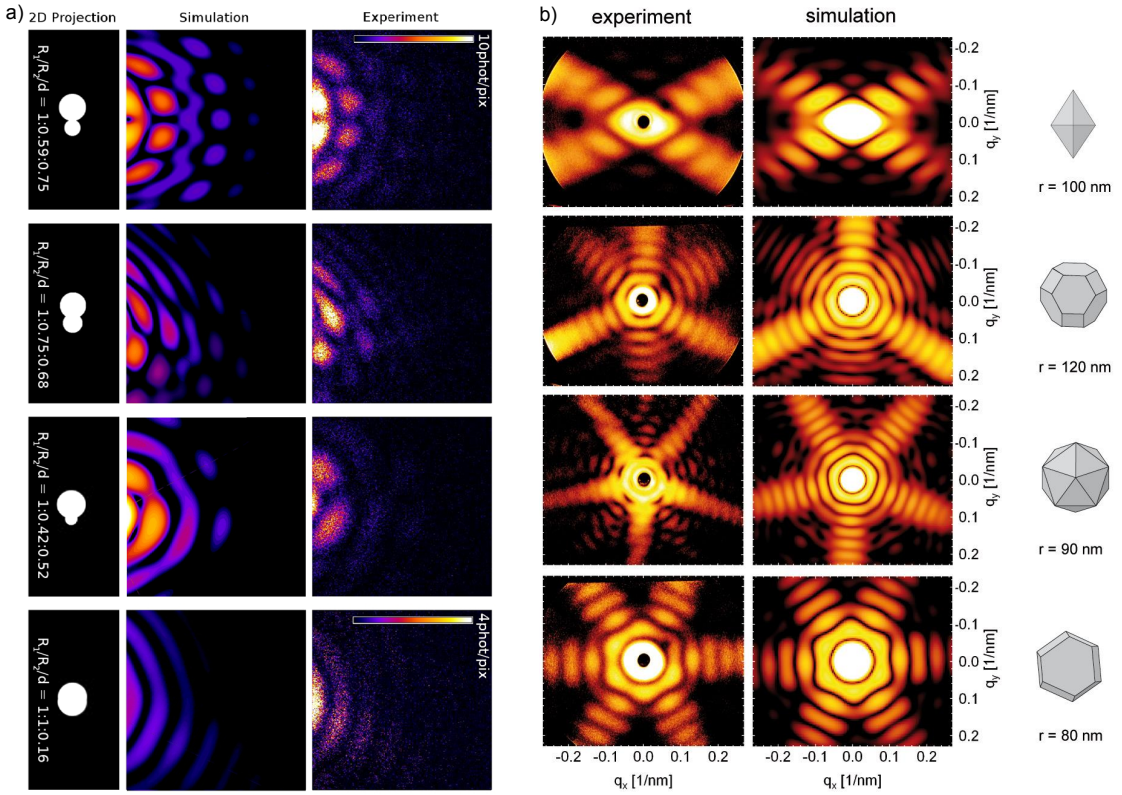

Figure 2.8: a) Measured scattering patterns from xenon twin clusters of different geometries. From [11]. Scattering simulations by FFTs of 2D masks illustrate the various degrees of coalescence. b) Measured wide-angle scattering patterns from free silver clusters. From [12]. Some patterns exhibit broken point-symmetry which indicated that three dimensional information about the cluster structure is contained. The particles architecture and orientation in space was determined with multi-slice Fourier transform simulations.

Theoretically predicted energetically preferred equilibrium shapes - like truncated octahedra - were identified as well as morphologies already known from deposition studies - like decahedra. Apart from these shapes, around hundred nanometer sized silver clusters with icosahedral and flat hexagonal (truncated twinned tetrahedra) shape were identified. Hence, XUV scattering is currently the only method to reveal, that silver clusters with metastable geometry exist in way larger sizes than previously expected.

The modulation in the profile along the azimuth over a fixed polar angle, contains information about the particle symmetry. Information about light-induced cluster dynamics are encoded in the intensity profile along one polar axis. This fact was used in a scattering experiment on single xenon clusters, to investigate the ultrafast (10 fs) sample response dependent on the laser power density [10]. It was found that for low laser focal flux, the envelope of the intensity profile followed a $(qR)^{-4}$ dependence, known as Porods law in small-angle x-ray scattering (see figure 2.9 a). With rising power densities the envelope increasingly deviated from this law, which was explained by an increase in the imaginary part of the refractive index. This showed directly, that the impact of the laser beam can change the electronic configuration within the cluster and therefore the ultrafast ionization processes in the particle.

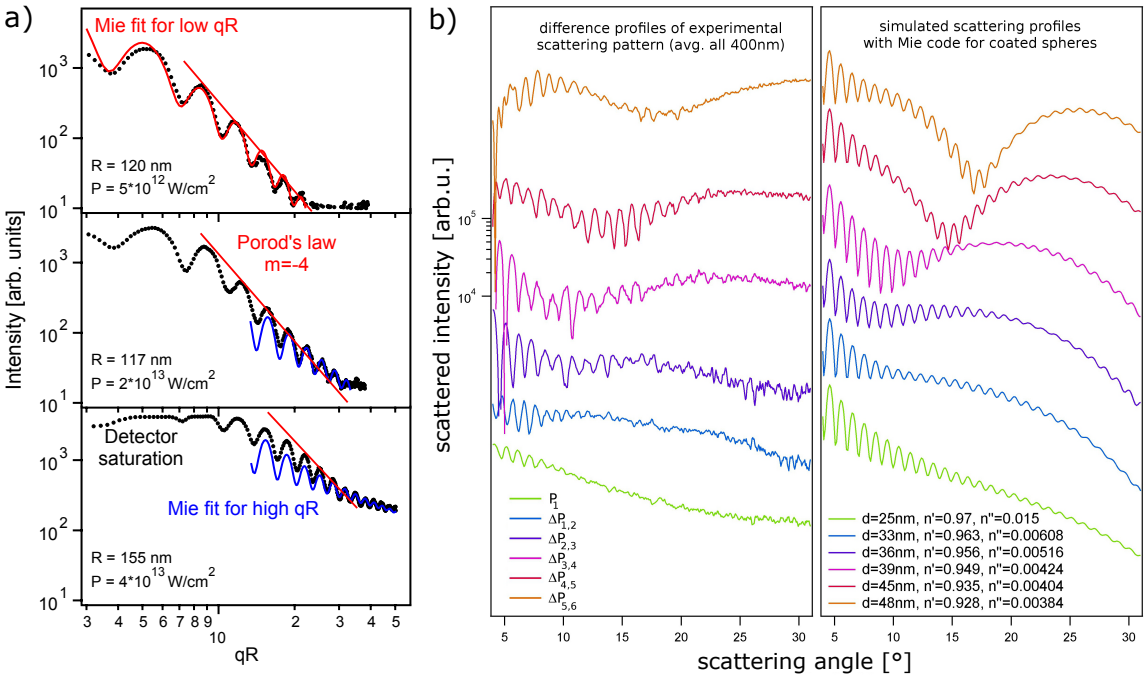

Figure 2.9: a) Scattering profiles from clusters irradiated with different power densities reveal information about the particles refractive index. From [10]. b) An overmodulation in scattering profile difference spectra points towards an internal refractive core-shell system within the cluster. From [45].

Within 10 fs, the atomic form factors change with increasing degree of ionization, evident from a deformation of the scattering amplitude envelope [10]. Using longer XUV pulses of 100 fs, a supermodulation of the fringe pattern appears. It gives evidence of a refractive core-shell system in the cluster. This is probably caused by sharp resonances of xenon ions at 91 eV photon energy, which lead to the formation of a core and a shell region with different refractive indices inside the cluster [45]. Difference spectra of radial profiles from clusters irradiated with increasingly bright light pulses are shown in figure 2.9 b. The supermodulation minimum shifts to larger angles with laser flux which indicates that a possible shell-region becomes increasingly thicker.

On an even longer time scale of several picoseconds, the scattering pattern vanishes completely as demonstrated in a recent IR-pump / x-ray-probe experiment [46, 43] (see also section 4.3.1). It was shown that with increasing pulse delay time the scattering signal decreases gradually from high to low scattering angles. This signature is attributed to a softening of the single particle surface, due to the explosion of highly charged ions gradually evolving from the cluster surface towards the cluster center.

2.3 Cluster dynamics induced by highly intense laser pulses

Since the advent of highly intense optical lasers in the sixties, many experimental and theoretical studies were performed in order to gain a profound understanding of laser-matter interaction. Already introduced in sections 2.1 and 2.2, clusters can serve as convenient

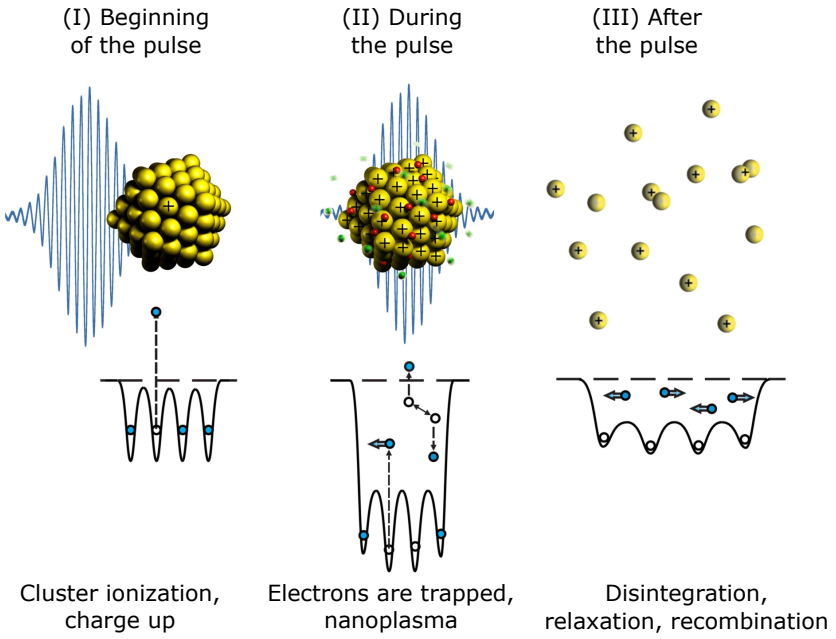

Figure 2.10: Exemplification of the three-phase model for a cluster in XUV light, adapted from [52, 45]: (I) Initial ionization of a neutral cluster in the rising edge of a laser pulse. Onset of nanoplasma formation. (II) Laser-electron and electron-electron interactions in the cluster nanoplasma during the laser pulse. (III) Energy redistribution and relaxation after the pulse is gone. Lowering of cluster density by disintegration.

nano-labs. In the optical regime ensembles of small clusters are well studied. Comprehensive reviews for the optical regime can be found in literature [47, 48, 49, 50]. With free-electron lasers emerging at the beginning of this century, coherent light pushing into the sub-nanometer regime in ultrashort pulses became available. The new possibilities sparked many studies on clusters in x-ray light. Work on light-cluster interaction in the XUV domain has been recently reviewed [51, 52].

These studies show that the interaction response of matter and light strongly depends on several properties. The **cluster component** determines ionization potentials, resonant transitions, as well as binding energies and different fragmentation dynamics are found for homo- or heteronuclear samples [53, 54, 55, 56]. With increasing **cluster size** bulk effects start to dominate surface effects. Several factors are of importance for the laser beam: the **photon energy** especially determines the mechanism of initial ionization, while the **intensity** of the field accounts for the amount of deposited energy in the system. The **pulse length** affects ionization and resonances and a **spatial and temporal chirp** may influences ion energies [57]. This chapter intends to give an introduction on the manifold dynamics taking place with emphasis on the interaction of rare-gas (especially xenon) clusters with highly intense (10^{12} - 10^{15} W/cm^2) XUV and IR pulses in the 100 fs duration range.

For a comprehensive illustration of the complex processes occurring in laser-cluster interaction it is useful to follow a three-phase model as often applied in literature [58, 59, 49, 50]. The interaction is partitioned in three steps independent of the exact experimental parameters. These are schematically depicted in figure 2.10 on the example of irradiation with XUV light. The outline of this chapter follows those phases:

(I) In the rising edge of the laser pulse, individual atoms are initially ionized and the cluster charges up, developing a deep Coulomb potential (see 2.3.1).

(II) During the pulse, electrons get trapped in the cluster potential. Further energy

transfer from laser to cluster as well as energy transfer within the cluster takes place. The different mechanisms are introduced in 2.3.2.

(III) After the energy absorption from the laser field ends, energy is still redistributed within the cluster. The particle expands and finally disintegrates, as will be discussed in section 2.3.3.

2.3.1 Initial ionization mechanisms and cluster charging

Upon irradiation of a neutral cluster with the rising slope of a laser pulse, the light couples to the compound atoms mostly as if they were isolated. This is especially the case for rare-gas clusters, where electrons are strongly localized, and also in the case of core electrons in metal clusters [49]. Instantaneously photon energy is absorbed and atoms get initially ionized. Several excitation mechanisms - either directly via single photon absorption or in non-linear processes - are possible dependent on the impacting laser power density and photon energy. The electronic configuration of the atoms plays an important role in the case of resonant excitation transitions. In this first phase the cluster environment is of minor importance, hence for simplicity several mechanisms are introduced on the example of atoms, following the reviews in [60, 61, 62, 50]. Finally in the context of the cluster environment a nanoplasma is build up, which is described in the last part of this section.

Initial ionization of single atoms

Single-photon ionization takes place if the photon energy $\hbar\omega$ exceeds the ionization threshold E_{ip} so that electrons are directly emitted into the continuum, as illustrated in figure 2.11 a. This is for example the case for rare-gas atoms in extreme ultraviolet (XUV) and x-ray light. In metal and water clusters, however, lower photon energies as in the vacuum ultraviolet (VUV) regime are sufficient. Light sources with high photon energies in the order of several tens of eV to one keV ionize mainly the inner electronic shells. They are subsequently filled by Auger decays leading to multiply charged ions upon absorption of a single photon (**multiple single-photon ionization**). During the pulse the instantaneously refilled inner shells can be ionized many times. **Multi-photon ionization** can take place via virtual states for energies smaller than the ionization potential ($\hbar\omega < E_{ip}$), promoting a bound electron over the vacuum level (see figure 2.11 b). This mechanism proceeds over many laser cycles of the rapidly oscillating field.

At high laser intensities and low laser frequencies the strong laser field leads to a deformation of the potential combined from ionic and laser field. If the bending is strong enough and the laser frequency sufficiently slow, an electron can escape the potential by tunneling through the barrier leading to **tunneling ionization** (see figure 2.11 c). The weakest bound electrons exhibit the highest ionization probability. For even stronger fields the potential bending is so strong that the barrier is suppressed below the bound state. No tunneling is needed and **above threshold ionization** takes place (fig. 2.11 d).

The interaction of atomic electrons with electromagnetic radiation can be split in two domains: the **photon dominated regime** where the field can be treated quantum mechanically as an ensemble of photons and the **field driven regime** where as many photons

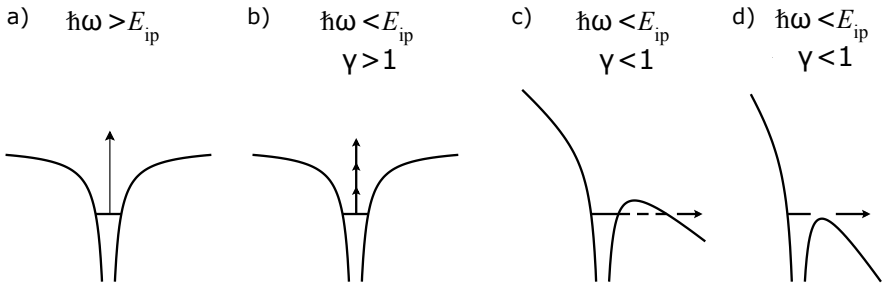

Figure 2.11: Schemes of photon dominated (a + b) and field driven (c + d) atomic ionization in a laser field. From [63]. a) If the photon energy $\hbar\omega$ exceeds the ionization potential E_{ip} single photon or multiple single photon ionization occurs. b) Multi-photon ionization takes place if $\hbar\omega < E_{ip}$. c) Tunnel ionization can occur if the laser field bends the atomic potential strongly. d) If the barrier is suppressed below the bound state above-threshold ionization takes place.

participate that light is treated as classical field. Which regime is the prevailing depends on the laser field strength and wavelength as indicated in figure 2.12. Here also the lasing regimes reached by optical and free-electron lasers are indicated.

Both regimes can be quantitatively separated by the dimensionless Keldysh parameter $\gamma = \omega/\omega_t$ [65]. It is introduced as the ratio of laser frequency ω to tunneling rate ω_t. The latter is given by [65]

$$\omega_t = \frac{eE_0}{\sqrt{2m_e E_{ip}}}, \tag{2.38}$$

where e is the elementary charge, E_0 is the laser field strength, m_e the electron mass, and E_{ip} the ionization potential. If the tunneling rate exceeds the laser frequency ($\gamma \leq 1$) the electron may leave the Coulomb potential by tunneling through the barrier and therefore the interaction is in the optical field ionization regime. For $\gamma \gg 1$, in the so-called perturbative regime occurring at high photon energies and low intensities, bound electrons get excited by single or multi-photon absorption.

It is also useful to express the Keldysh parameter by the ponderomotive potential, which is the cycle-averaged kinetic energy of a freely oscillating electron driven in an external laser

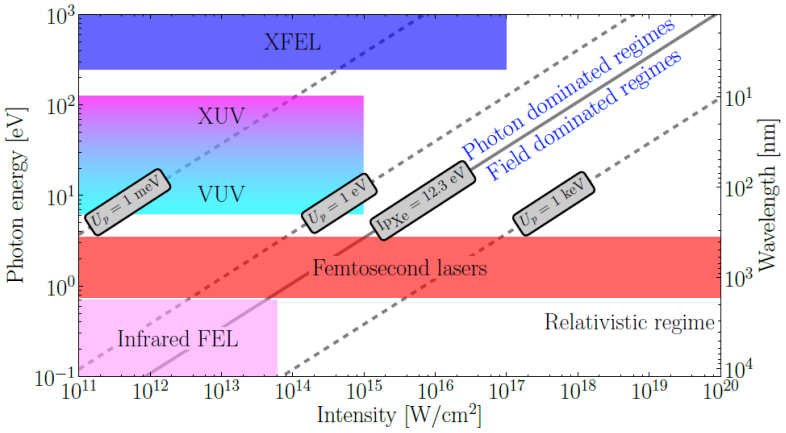

Figure 2.12: Photon energy over power density, illustrating the photon and field dominated regimes with indicated regions reached by optical and free-electron lasers. From [64].

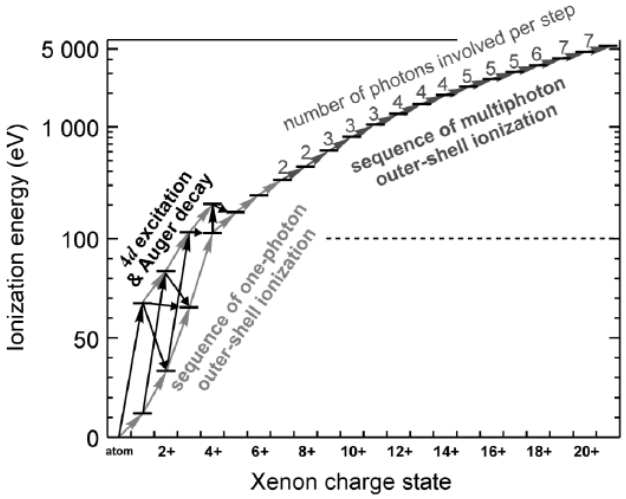

Figure 2.13: Excitation steps and ionization channels in xenon atoms irradiated by 93 eV photons. From [66].

field [60]

$$U_{pond} = \frac{e^2 E_0^2}{4 m_e \omega^2} = \frac{e^2 I}{2 \epsilon_0 c m_e \omega^2} \tag{2.39}$$

with $I = c\epsilon_0 E_0^2/2$ being the power density of the laser, ϵ_0 the vacuum permittivity and c the speed of light. Several values of the ponderomotive potential are indicated in dependence of photon energy and power density in figure 2.12. The transition between both regimes approximately occurs where $2 \cdot U_{pond} = E_{ip}$, as seen from the **Keldysh parameter** when expressed as [60]

$$\gamma = \frac{\omega}{\omega_t} = \sqrt{\frac{E_{ip}}{2 \cdot U_{pond}}}. \tag{2.40}$$

In the experiments performed for this thesis, ultrashort XUV pulses with 13.6 nm wavelength (= 91 eV photon energy) are used. They exhibit a maximum power density of about $4.1 \cdot 10^{14}\,\mathrm{W/cm^2}$ in the focal volume. With an ionization potential of $E_{ip} = 12.13\,\mathrm{eV}$ for xenon atoms [67], a Keldysh parameter of 29 can be calculated using equation 2.40. Therefore, the xenon-XUV interaction in this experiment is in the photon dominated regime. In this regime the electronic structure of the target material significantly influences the absorption efficiency. Depending on the electronic energy levels resonant excitations can occur. For the applied photon energy of 91 eV the so-called **giant resonance** appears in atomic xenon [66, 68]. The ground state configuration of xenon is: Xe = [Kr] $4d^{10}$ $5s^2$ $5p^6$. Around 100 eV resonant $4d$ - ϵf transitions with proceeding Auger decays lead to an enhanced ionization with cross-sections from 23 Mbarn for neutral xenon up to 1000 Mbarn for Xe^{6+} [69, 70]. While for the first few charge states atoms are multiply and singly ionized with only one photon, two photons are needed for ionization from Xe^{7+} onwards and three from Xe^{10+} onwards by stepwise absorption of single photons, as schematically depicted in figure 2.13.

Additionally, IR pulses with 800 nm wavelength are used in the experiments for this thesis. With a power density of $1.1 \cdot 10^{14}\,\mathrm{W/cm^2}$, the IR-xenon interaction is in the field-driven regime, as can be estimated from a Keldysh parameter of 0.9. Earlier experiments on

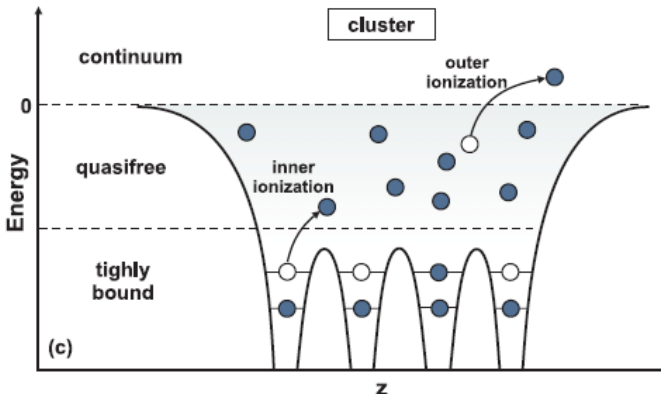

Figure 2.14: Concept of inner and outer ionization of excited electrons in the deepened cluster potential. From [50]. If an electron is released from an ion but does not overcome the ionization potential, it is quasi-free and called inner ionized. An electron leaving the cluster compound into the continuum is called outer ionized.

atomic gas with these parameters yielded charge states up to Xe^{3+} in 200 fs pulses [71], while in a later one Xe^{1+} was the highest charge state observed with pulses of 20 fs [72]. This comparison reflects the non-negligible influence of the laser pulse duration and resulting intensity and photon flux in the field driven regime.

Nanoplasma formation in clusters

The cluster environment is negligible for the initial ionization of a neutral cluster since the atoms act as they are independent. However the cluster compound plays an increasingly important role in the advancing processes. The liberation of each electron from the cluster - either direct or via tunneling as in single atoms - leads to a deepening of the cluster Coulomb potential. The individual potentials merge and atoms start 'feeling' each other as depicted in figure 2.14. Electrons released from an ion which do not have sufficient kinetic energy to overcome the potential are trapped. The efficient trapping of photoelectrons often starts a few fs after irradiation and therefore already in the leading edge of the pulse [50]. They trapped are referred to as **inner ionized** [58] or quasi-free. Together with the ion background the cloud of quasi-free electrons forms a **nanoplasma** [47]. A dense charged electron-ion system is created.

When ionized to that point, noble gas clusters become metallic since these electrons are not bound to an ionic core but delocalized across the whole cluster. While for rare-gas clusters a nanoplasma has to be created by inner ionization upon light irradiation, quasi-free electrons are inherent to the system in metal clusters already in the ground state. Quasi-free electrons in a cluster can absorb further energy during the light pulse. If they absorb enough energy to overcome the potential, they subsequently get emitted and are then denoted **outer ionized** [58]. With every expelled electron the potential barrier to overcome gets higher and the energy span between inner and outer ionization grows. As depicted in figure 2.10, the first phase is completed with the initial charging of the cluster. In the next phase other processes dominate these initial processes, which are subject to the next section.

2.3.2 Nanoplasma dynamics

Clusters are able to absorb energy from laser pulses more efficiently than atomic gas. This effect was found in several laser-cluster experiments investigating the emission of x-rays [73], highly energetic ions [74], neutrons from fusion [75], and highly energetic electrons [76]. The enhanced energy absorption in clusters compared to pure atomic gas results from processes mainly occurring in the second phase, indicated in figure 2.10. Here, the laser pulse interacts with an already charged cluster, where often a dense nanoplasma is present.

Like initial ionization procedures, nanoplasma dynamics can also be dependent on laser wavelength and strength as well as on cluster size. Bound and quasi-free electrons in a nanoplasma can absorb and exchange energy and get inner- and outer-ionized by several different effects [48, 77, 50]. As in the atomic case, some plasma dynamics can be differentiated in effects mostly driven by the laser field and in single-photon and multi-photon effects. Additionally, also regime independent effects are possible, which are mainly determined by the intensity of the space charge and the amount and energy of the quasi-free electrons. In most laser-cluster interaction scenarios many of these processes interact and are highly linked to each other. Several reviews and books give a good introduction into the complex mechanisms in the IR [47, 49, 62, 61] and in the XUV regime [50, 51, 78]. It has to be stressed, that many concepts in literature are valid for cluster sizes smaller than the wavelength. This is neither the case for several 10 nm radius clusters in XUV light nor for µm sized clusters in IR light, as both studied in this thesis. Still most models and ideas are applicable to the experimental data in good approximation.

Plasma coupling regimes

In plasmas, electrons coherently driven by the external laser field give rise to collective processes. But due to collisions of these electrons the collective motion can be destroyed and random thermal motion takes the lead [77]. Which of these processes is dominant during laser-cluster interaction, strongly depends on the temperature and density of the plasma and can be deduced from the Debye number

$$N_D = \frac{4\pi}{3} n_e \lambda_D^3 \tag{2.41}$$

where n_e is the electron number density and λ_D the Debye length [79]. The latter determines the length over which charge fluctuations are screened by the electron plasma. It is defined as

$$\lambda_D = \sqrt{\frac{\epsilon_0 k_B T_e}{n_e e^2}} \tag{2.42}$$

with k_B the Boltzman constant and T_e the electron temperature [79]. The number N_D gives the amount of electrons which contribute to the local screening. In a warm, dense, **strongly coupled** plasma, where $N_D \lesssim 1$, the electron-ion interaction strength is large and many collisions take place. For $N_D \gg 1$, corresponding to hot temperature and low density, the plasma is **weakly coupled** and collective motions are preserved.

A plasma can be characterized in two regimes, according to its particle density with respect to the incoupling laser wavelength. The plasma frequency at which electron waves oscillate

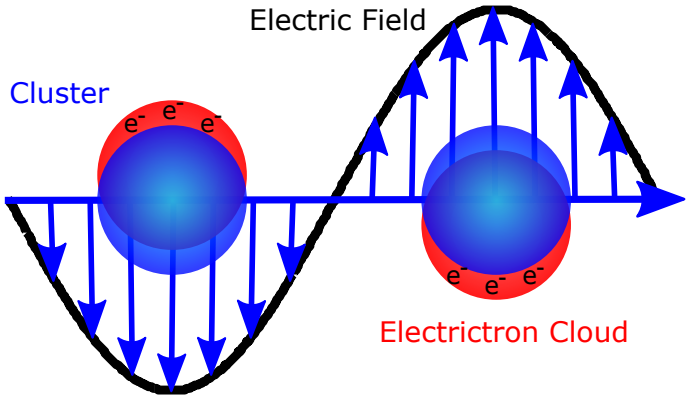

Figure 2.15: Cluster driven by an electric field in resonance with the eigenfrequency of the electron cloud motion. From [81]. In this state the nanoplasma receives a strong thermal excitation, which leads to a maximized energy absorption from the laser.

in a plasma is given by [61]

$$\omega_p = \sqrt{\frac{n_e e^2}{\epsilon_0 m_e}}. \tag{2.43}$$

If the laser frequency exceeds the plasma frequency ($\omega \geq \omega_p$), the plasma is **underdense**. For xenon with a particle density n_e of $1.7 \cdot 10^{28}\,\mathrm{m}^{-3}$ and therefore a plasma frequency of $7.4 \cdot 10^{15}\,\mathrm{Hz}$, this is the case in 13.5 nm light (XUV) with $\omega = 2.2 \cdot 10^{16}\,\mathrm{Hz}$. The plasma is **overdense** for 800 nm radiation (IR) corresponding to $\omega = 3.7 \cdot 10^{14}\,\mathrm{Hz}$, where $\omega \leq \omega_p$. If the plasma is weakly coupled, e.g. exhibits hot temperature and low density, the laser and plasma frequencies can be matched which results in an enhancement of collective electron motion.

Collective processes

The **Mie resonance** plays a major role in the ionization of overdense nanoplasmas ($\omega \leq \omega_p$) [49]. The natural collective oscillation frequency of an electron cloud is given in equation 2.43. Additionally, the quasi-free electrons are driven by the laser electric field, as depicted in figure 2.15. With a light-induced expansion of the cluster (as subject to section 2.3.3), the particle density drops and ω_p is lowered. Eventually the eigenfrequency of the electron motion matches the laser frequency [50]:

$$\omega_{Mie} = \frac{\omega_p}{\sqrt{3}} = \sqrt{\frac{\rho_e e}{3\epsilon_0 m_e}} \tag{2.44}$$

with ρ_e the quasi-free electron density. Here the energy absorption from the laser is maximized due to the strong thermal excitation of the nanoplasma. This resonant collective electron excitation was first experimentally demonstrated for small rare-gas cluster in IR light [80]. Since this effect only applies for overdense plasmas it is photon energy dependent and does not occur in clusters excited with XUV light. Apart from a strong wavelength dependence, the effect of the Mie resonance is also highly influenced by cluster size.

In the approximation of the cluster as a uniform density sphere and an ionic motion with

constant velocity, this resonance is reached after a resonance time [80]

$$\tau_{res} = \frac{R}{v}\left[\left(\frac{n_0}{3n_{crit}}\right)^{1/3} - 1\right]. \tag{2.45}$$

Here R is the initial radius, v the expansion velocity, n_0 the initial density, and n_{crit} the critical density. For metal clusters and small rare-gas clusters this resonance can be probed with a sufficiently long single laser in the range of femtosecond to nanaosecond duration. But for larger rare-gas clusters in fs-pulses, a dual-pulse pump-probe scheme is required to match the timescale of cluster expansion. During the expansion, the cluster density has radial dependence. Hence, the critical density reaches different parts of the cluster at different times. For large clusters the simple model was extended. It shows that the resonance is moving inwards from surface to the cluster center with time [82].

Collisional processes

Other energy-exchanging processes are **electron-ion** and **electron-electron collisions**. Fast quasi-free electrons transfer their kinetic energy to bound electrons and either promote them to an excited state by inelastic scattering or ionize them by electron-impact ionization [49, 50]. The corresponding cross-sections can be calculated from the empirical Lotz formula [83]. Due to scattering of hot electrons on other quasi-free electrons, a local quasi-equilibrium distribution establishes. This is the major mechanism leading to electronic thermalization and giving rise to an Maxwellian electron temperature distribution. The importance of collision processes rises with cluster size, as in larger clusters bulk processes become more prominent [84]. Collisions between ions can usually be neglected due to the slow ionic motion, which usually exceeds the timescale of a femtosecond-laser pulse.

Collisions of laser-driven electrons with plasma ions - referred to as **inverse bremsstrahlung heating (IBS)** - is a highly photon energy dependent process. Inner ionized electrons gain momentum in the laser field and transpose it to thermal energy by scattering on bound electrons. As a result the plasma gets heated. The averaged energy gain with time interval dE/dt scales with $\lambda^{8/3}$ [85]. Therefore, it is most significant in the IR regime but also has relevance in the VUV range. A IBS contribution was calculated for a wavelength of up to 62 nm [86]. However, this value could not be validated in experiments [87]. For XUV fields the oscillations are too fast for electrons to gain sufficient velocity and IBS is negligible.

Cluster size effects

As the last paragraph already indicated, many nanoplasma dynamic effects change in significance with cluster size and too simple models loose their accuracy. While for small clusters the charges can be treated as homogeneously distributed, this does not hold for larger clusters. Here, electron screening gains importance with increasing size. Trapped electrons migrate to an energetically favorable state in the cluster center where the cluster potential is deepest. The charge of the atomic ions is highest at the cluster boundary and declines towards the middle. The electron cloud screens the ionic background and for a

temperature T close to zero a fully net-neutral core is established up to a radius of

$$R_{el} = R \cdot \left(\frac{Q_{el}}{Q_{ion}} \right)^{1/3} \tag{2.46}$$

with Q_{el} and Q_{ion} the overall charge of the electrons and ions respectively [51]. This non-equilibrium plasma is maintained during the entire laser-matter interaction period. The time to reach a balanced state by electron-electron collisions is in the order of picoseconds and therefore exceeds the pulse length for femtosecond lasers [62].

Experimentally this non-homogeneous charge distribution was revealed in ion spectra of Ar-Xe core-shell clusters [56]. Xenon atoms building the cluster core were surrounded by an argon shell. While argon charges 4+ and higher were detected, highly charged xenon ions were virtually absent. This behavior was described by thermalization of the quasi-free electrons and a subsequent recombination of the plasma core (see also 2.2.3).

Explicit treatment of the electromagnetic wave propagation is negligible for small clusters and microscopic processes, such as collisions and plasma microfields, are of major importance. The electrostatic approximation breaks down for larger cluster sizes in the range of the wavelength. Here the so-called **propagation regime** is entered [79] where clusters opacity plays an increasingly important role and the plasma penetration depth δ_p has to be taken into account. For an overdense plasma with frequency ω_p it is given by [32]

$$\delta_p = \frac{c}{\omega_p}. \tag{2.47}$$

Throughout this thesis clusters composed of xenon, argon, and silver atoms are investigated. The corresponding penetration depth into the clusters with solid density is about 40 nm for xenon, 25 nm for argon, and 7 nm for silver particles.

2.3.3 Energy redistribution and disintegration of excited clusters

In the final stage of the three-phase-model (fig. 2.10), the light pulse goes to zero and no more energy absorption takes place. The energy inside the highly excited cluster is redistributed by charge transfer. Radiative and non-radiative relaxation and recombination events take place and fluctuations in charge states even out. Due to repulsive forces and hydrodynamic pressure the sample disintegrates on a timescale of picoseconds [43] and beyond [88]. The expansion of the ionic background results in adiabatic cooling of the electron cloud. Eventually the cluster fragments and reaches a final state, which can be measured in electron and ion spectra. Due to the dynamics in the previous stages, cluster ions exhibit higher kinetic energies than ions from atomic gas.

Cluster disintegration

Ionic motion might start already during laser-cluster interaction. After the laser pulse has gone and energy deposition into the cluster has stopped, the cluster disintegrates. Initial cluster ionization and subsequent energy transfer in the cluster (e.g. the charge of the cluster), the number of trapped electrons, and their temperature determine the expansion dynamics. There are two limiting cases: (i) explosion due to repulsive Coulomb forces

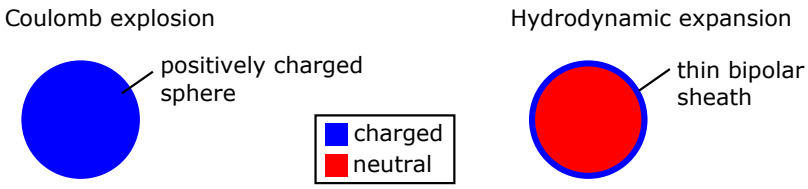

Figure 2.16: Schematic depiction of the cluster state determining the rivaling expansion mechanisms, adapted from [89]. (i) A net-positively charged cluster results in Coulomb explosion. (ii) A net-neutral cluster with a thin ambiploar shell leads to hydrodynamic expansion.

between ions and (ii) expansion by hydrodynamic pressure of the hot electron gas in a plasma. A sketch of the charge distribution in the cluster before disintegration in both regimes is presented in figure 4.27 a and b respectively. Intermediate regimes can occur in non-homogeneously charged clusters.

If the net charge of the cluster is positive due to previous outer ionization of electrons, unneutralized ions repel each other and are driving the cluster apart in a **Coulomb explosion**. Hence, the intensity of the laser field needs to be high enough to strip at least one electron from an atom before ionic motion sets in [61]. The timescale on which the cluster expands depends on the average charge state q. In a homogeneous expansion the sample doubles its radius during the time [50]

$$t_{Coul} = 2.3 \cdot \frac{\sqrt{2\pi\epsilon_0 m_i r_s^3}}{e \cdot q} = \sqrt{\frac{m_i}{n_i q^2 e^2}} \tag{2.48}$$

with m_i denoting the ion mass, r_s the Wigner-Seitz radius, and n_i the atom density. For xenon with $r_s = 0.24\,\text{nm}$ the time holds $t_{Coul} = 190\,\text{fs}/q$. The ions fly apart very quickly in the electric field of their own space charge, holding high kinetic energies. Coulomb explosion mostly occurs for smaller clusters [49], while for larger clusters a different mechanism is dominant.

In a cluster where most electrons are inner ionized and a dense nanoplasma is formed, the cluster can be highly charged but still being almost net-neutral due to the screening of quasi-free electrons in the sample. The cluster is driven apart by the thermal energy of the activated, hot electrons instead of repulsive inter-particle Coulomb forces. If the electron cloud is treated as an ideal gas with temperature T_e and electron density n_e, its hydrodynamic pressure of $p_{hydr} = n_e k_B T_e$ [47] is forcing the nanoplasma to drive apart in a **hydrodynamic expansion**. In this regime, the time a spherical cluster with initial cluster radius R needs to double in size is given by [48]

$$t_{hydr} = R \cdot \sqrt{\frac{m_i}{q k_B T_e}}. \tag{2.49}$$

The timescale is slower than in a Coulomb explosion and therefore the released charge ions hold lower kinetic energies.

The experimental determination in which of both regimes the cluster is fragmenting is not trivial. In early experiments on ensembles of clusters, it was proposed to identify the dominating regime by the dependence of the kinetic energy on ion charge [90, 91]. It was claimed that while in the Coulomb case the final kinetic energy scales quadratically with

the charge state ($E_{kin}(q) \sim q^2$), it scales linearly for the quasi-neutral case ($E_{kin}(q) \sim q$). Experiments on water clusters however indicate that this method is often ambiguous [55]. A theoretical study showed, that this behavior is only valid for the average charge state [92], e.g. for Coulomb explosion $\langle E_{kin}(q)\rangle \sim \langle q^2\rangle$ and for hydrodynamic expansion $\langle E_{kin}(q)\rangle \sim \langle q\rangle$. This was validated in an experiment on single clusters for the hydrodynamic case [44].

A different theoretical study suggested that ion energy spectra are not well suitable for the identification of the expansion mechanism [52]. This study also gives a more reliable measure for the regime in which the excited cluster disintegrates: the so-called **frustration parameter** [52]

$$\alpha = \frac{n_{tot}}{n_{out}}. \tag{2.50}$$

It is defined as the ratio of all (inner and outer) ionized electrons n_{tot} to outer ionized electrons n_{out}. In [52] the ionization is calculated in the photon-dominated regime with $n_{tot} = I\tau\sigma N/(\hbar\omega)$, where I is the laser power density, τ the laser pulse length, σ the atomic cross-section for the dominant ionization channel, and N the number of atoms in the cluster. The number of outer ionized electrons is calculated by [52]

$$n_{out} = \frac{4\pi\epsilon_0}{e^2} R \cdot (\hbar\omega - E_{ip}). \tag{2.51}$$

For $\alpha \leq 1$ the cluster is strongly charged and Coulomb explosion takes place, while for $\alpha \gg 1$ the majority of electrons is trapped and the major expansion mechanism is hydrodynamic expansion.

In many cases the expansion is a combination of both limiting mechanisms. As soon as there is a plasma the cluster will always expand in a hydrodynamic expansion due to screening by quasi-free electrons. But the shell will explode in a Coulomb explosion since the outer ions remain unscreened after electron migration towards the cluster center [93, 94]. In a laser wavelength dependent theoretical study on small argon clusters it was shown that there is a smooth transition from a more hydrodynamic to a predominantly Coulombic regime with increasing photon energy [52].

Recombination and relaxation processes

After the laser pulse is gone, the inner-ionized electrons relax either in three-body [95] or in many-body recombination [96]. An electron is captured by an ion in the vicinity of a second or more electrons respectively. The number of recombinations N_R is dependent on the ion density N_i, on the electron density N_e, and on the electron Temperature T_e. For $N_i = N_e = N_0$, the number of recombinations evolving with time t can be expressed as [97]

$$N_R(t) = N_0 \cdot \left(1 - \frac{1}{\sqrt{1 + t/\tau_r}}\right). \tag{2.52}$$

The recombination time is defined as $\tau_r = 1/(2\alpha_r N_0^2)$ with the electron temperature dependent factor $\alpha_r = 8.75 \cdot 10^{-27} T_e^{-4.5}\,\mathrm{cm^6 s^{-1}}$. Recombination is most effective when the nanoplasma is dense and cold.

The evolution of electron relocalization with cluster expansion is subject of a theoretical study [98]. Small ($N = 923$) xenon clusters in ultrafast (30 fs), XUV (92 eV) pump-probe

pulses were investigated with molecular dynamic (MD) simulations. It was found that three-body recombinations mainly take place in the early stage of cluster expansion, and are suppressed for long delays. The pump pulse generates a warm and dense nanoplasma which cools down during cluster expansion, as depicted in figure 2.17. These results prove evidence for the findings in an experimental study [99]. The number of recombination processes is also highly dependent on the location within the cluster nanoplasma. Shell-dependent recombination probabilities were found which are most efficient in the cluster center.

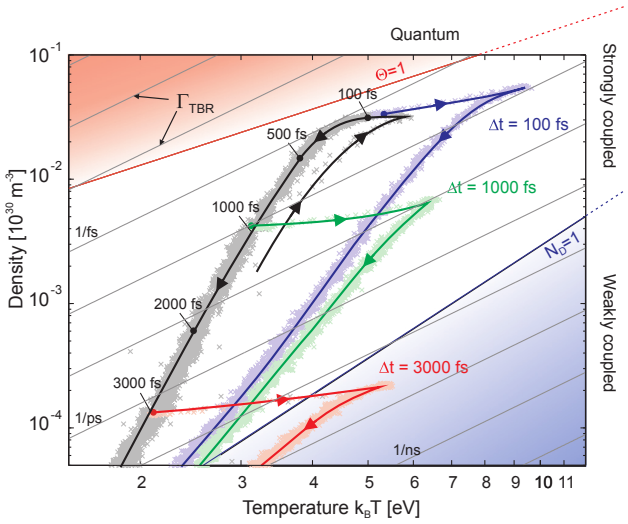

Figure 2.17: Evolution of nanoplasma density and temperature in a pump-probe setting calculated with MD simulations. From [98].

Fluorescence spectroscopy is a versatile tool to resolve charge states before recombination, which are hidden in ion spectra. Ion spectra from clusters consisting of a xenon core and an argon shell illuminated by an XUV pulse revealed a highly charged outer layer but only little charged ions from the recombined core [56]. Corresponding fluorescence spectra resolved multiply charged xenon ions from the inner cluster part, revealing that these were initially as highly activated as shell atoms [100]. This experiment proofed that the charge states generated during the laser-cluster interaction might significantly differ from the final charge state distribution, due to strong recombination.

However, recombination processes can also be efficiently suppressed, for example during ionization heating. This was demonstrated with 800 eV photons by using a new experimental approach [101]. Ion spectra and scattering patterns were recorded simultaneously from one single cluster in the interaction region. With this method, signal averaging over the cluster size distribution due to statistical cluster growth process and the focal intensity profile was ruled out. The striking observation in this paper is that exclusively highly charged atomic ions were detected from high laser intensities of about 10^{16} W/cm^2 onwards. The absence of low charge states is attributed to inefficient electron-ion recombination in a initially hot nanoplasma. Since this effect occurs only for the highest intensities it could not be resolved for experiments on ensembles of clusters. There, most particles are hit in the focal wings with low intensities.

Large clusters in IR and XUV light

Up to date, many experiments and theoretical studies were performed for small rare-gas and metal clusters in laser light, consisting of up to a few 10000 atoms. Those experiments helped to develop a fundamental understanding of the underlying dynamics. Less experimental and theoretical data is available for larger clusters from 10^5 atoms onwards, since in this size range sample generation becomes increasingly challenging and calculations com-

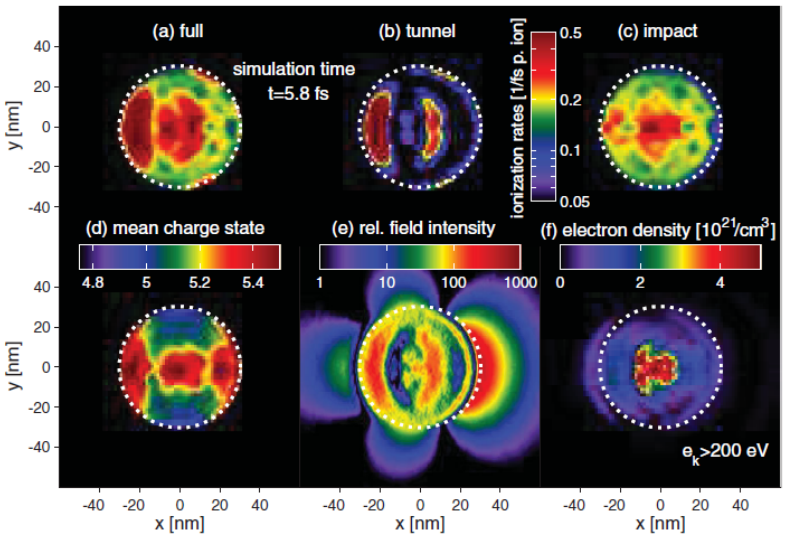

Figure 2.18: Microscopic particle-in-cell simulation for a 30 nm radius xenon cluster irradiated with an 800 nm laser pulse. From [102]. Shown are the calculated spatial distributions of total (a), tunnel (b) and impact ionization (c) rates, as well as mean charge states (d), electric field intensity (e) and fast electrons (f) at the point of resonance condition. Laser-induced plasma waves are responsible for the inhomogeneous distributions.

putationally costly. Nevertheless, also in this domain some experiments were performed, which could shed light on several aspects of laser-cluster interaction. This section tries to give a short introduction to the current understanding of phenomena occurring in large clusters from 10^5 atoms onwards and to point out the topics which are still under discussion. The focus is on the interaction of large xenon and argon clusters with IR and XUV light.

Dynamics of large clusters at 800 nm: The photon energies in the infrared regime (1.55 eV at 800 nm wavelength) are for most rare-gases too low for laser-cluster interaction to be in the photon-dominated regime. Clusters are initially ionized by tunnel or above-threshold ionization in sufficiently intense laser fields (see section 2.3.1). Subsequently inner ionization occurs 'from top to bottom', i.e. from outer to inner atomic levels. The plasma dynamics are dominated by the oscillating external laser field which drives the quasi-free electrons back and forth over a long range within the sample. Electrons are repeatedly forced to recollide with ions leading to inverse bremsstrahlung heating. Initially the plasma frequency is much higher than the laser frequency. Upon cluster expansion the plasma density drops and eventually Mie resonance is reached. This results in an enhanced energy absorption and increased ionization. For large clusters, the critical density is expected to be reached after picoseconds. Therefore, a dual-pulse experiment is needed to probe the resonance condition with femtosecond-laser pulses. Eventually the cluster fragments due to ionic motion. Large clusters usually disintegrate in a Coulomb explosion of the outer shell and a hydrodynamic expansion of the inner part, due to electron migration towards the center where a screened core is built.

From energy spectra the electron temperature can be deduced, like in an experiment performed on ensembles of Xe_{150000} clusters irradiated with $5 \cdot 10^{15}\,W/cm^2$ intensity Ti:Sa pulses [55]. A temperature of 600 eV was fitted to the electron kinetic energy distribution. An enhancement of electron emission in the Mie resonance with shift to higher kinetic energies, and therefore more efficient heating, was observed. The emission spectra show high angular dependence due to asymmetric barrier lowering parallel to the laser polarization.

A computational study with a microscopic particle-in-cell code (MicPIC) investigated the

resonant Mie plasmon excitation of a R = 30 nm preionized xenon cluster in 800 nm light with moderate laser intensities of $< 10^{14}\,\mathrm{W/cm^2}$ [102]. It was revealed that during the probe pulse attosecond plasma-waves are generated by hot electrons. Those waves recollide with the cluster surface and subsequently migrate to the cluster center where they collide with each other. Non-homogeneous electric field fluctuations arise, which exceed the driving laser intensity by more than 2 orders of magnitude (see figure 2.18). This results in an enhanced impact ionization creating charge states up to Xe^{10+}.

A one-color dual-pulse experiment with intensities of $5 \cdot 10^{15}\,\mathrm{W/cm^2}$ on large argon clusters (up to $R = 5\,\mathrm{nm}$) investigated the disintegration after irradiation [103]. In ion kinetic energy spectra after single-pulse excitation a cluster size dependency was revealed in an increase of the maximum energy proportional to the 1.6 power of the cluster source backing pressure. This leads the authors to the conclusion that the cluster explodes in a Coulomb explosion, because the kinetic energy of nanoplasma-expelled ions should be independent of the cluster size.

The anisotropy in ion emission was calculated for a R = 17.5 nm argon clusters with PIC code [104]. It shows that anisotropy is less important for large clusters because electron collisions become more relevant. They also investigate resonant heating. The resonance appears when the period of an energetic electron in the confining electrostatic potential matches the laser frequency. The electron oscillation period, however, depends on the laser intensity. Therefore, a threshold intensity in the order of $10^{15}\,\mathrm{W/cm^2}$ has to be reached for this resonance. This is not the case in the experiments performed for this thesis and can therefore be ruled out.

Dynamics of large clusters at 13.5 nm: Cluster dynamics in short-wavelength pulses differ fundamentally compared to the optical regime. The laser field is oscillation fast compared to the tunneling time of an electron. Tunnel and above-threshold ionization are negligible in the XUV regime. Also IBS heating is ineffective in the XUV regime due to a low ponderomotive potential. Additionally, the plasma is underdense from the beginning such that resonant collective heating cannot occur. Unlike in IR pulses, cluster ion charges do not exceed atomic ion charges. Instead, the sample is initially ionized in direct single-photon absorption. Subsequent Auger cascades fill the inner-shell vacancies and further electrons are ejected. The nanoplasma is heated via ionization heating [105, 52]. Higher charge states are generated by electron-collision ionization or multi-photon absorption. At 90 eV collisional cross-sections for 5s and 5p states are higher (500 Mbarn) than photoionization cross-sections (20 Mbarn) [106]. An experiment on small xenon clusters revealed that the electron energy distribution shows two major peaks: one from directly photoionized electrons and one from plasma electrons with a temperature of about $T_e = 20\,\mathrm{eV}$ [42].

The first experiment on single, giant (R = 30 - 600 nm) xenon clusters in single-shot mode at 13.6 nm light revealed new insights into energy redistribution processes and cluster explosion [45]. The data is depicted in figure 2.19. The newly developed method of photon imaging coincident with ion time-of-flight spectroscopy allowed to sort single cluster data for their size (deducted from the spacing of the rings in scattering patterns, see fig. 2.19 a) and subsequently to arrange ion spectra according to exposed power density (fig. 2.19 b). The central kinetic ion energy, extracted from the time-of-flight spectra, scales linearly

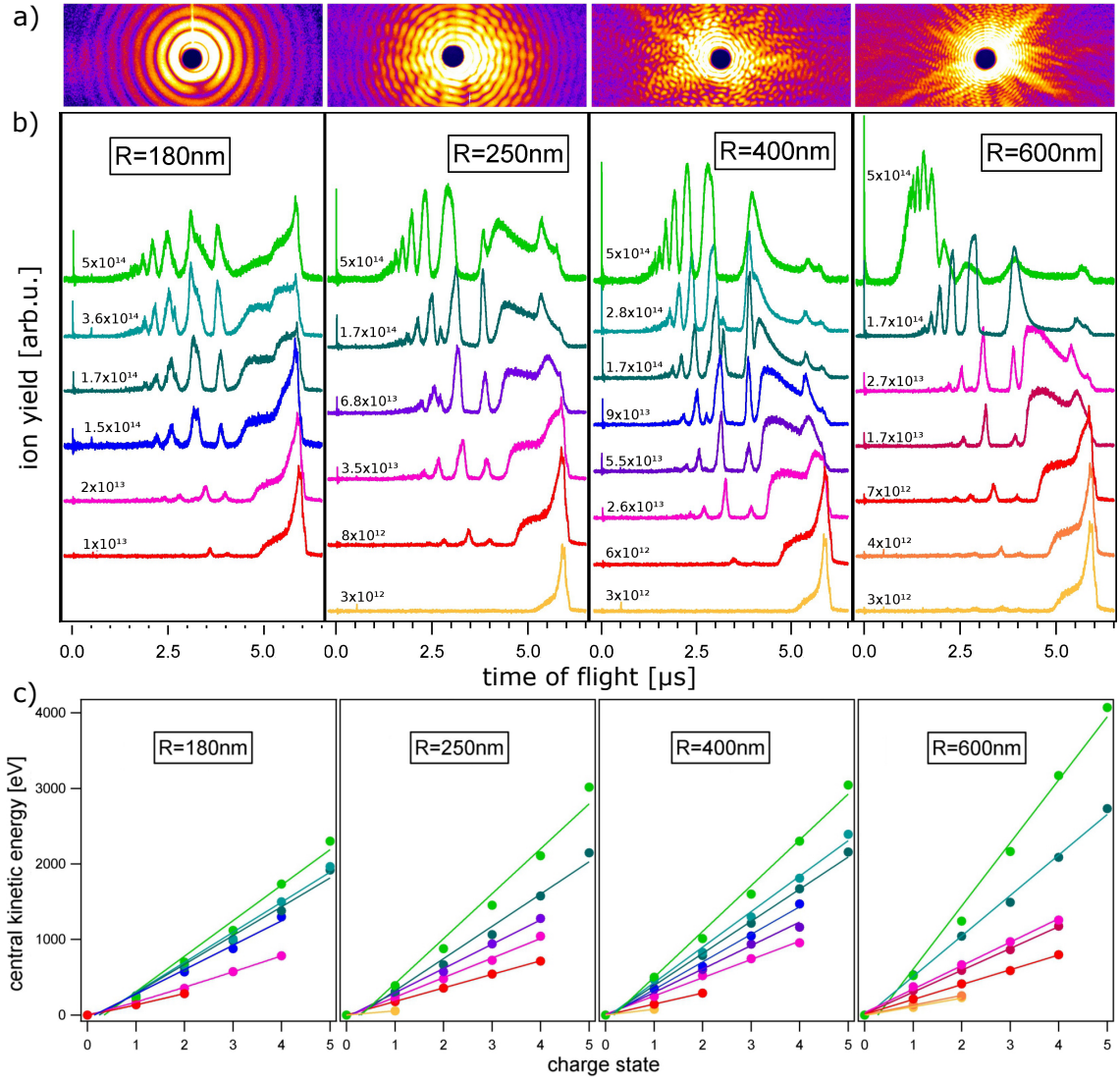

Figure 2.19: Data taken in single-cluster single-shot experiments on giant xenon clusters with 13.6 nm pulses. From [45]. (a) Scattering patterns of clusters with different radii encoded. (b) Ion spectra sorted for size and exposed power density. With increasing intensity higher charge states rise and shift towards shorter flight times. (c) Corresponding kinetic energies deduced from the flight times plotted over charge state reveal a linear dependency and an increase in energy with cluster size.

with charge state (fig. 2.19 c). For all four size ranges an increase in power density from approximately $3 \cdot 10^{12}$ to $5 \cdot 10^{14}\,\mathrm{W/cm^2}$ results in an increase in charge states by a factor of 3 to 4. With increasing cluster radius (by factor 3.3 from 80 to 600 nm) the ion kinetic energy per charge state grows only by a factor of 1.7. Apparently the laser focal power density has more impact on the laser-induced cluster dynamics than the particle size.

Charge state resolved kinetic energy distributions reveal a narrow energy distribution and missing low kinetic energies [44] (not shown in fig.2.19). This behavior was interpreted as indicator for strong recombination in agreement with theoretical MD calculations on small argon clusters [52]. From a calculated frustration parameter of $6 \cdot 10^5$ deep in the nanoplasma regime and narrow ion kinetic energy distributions for all charge states, the

conclusion was drawn that for large clusters a thin outer shell comes off in hydrodynamic expansion and the nanoplasma core recombines to full neutrality.

Short summary at present understanding

In laser-cluster interaction, the influence of many parameters (sample matter, and size; laser intensity, pulse length, and photon energy) on complex processes in the cluster make it hard to foresee the outcome of an experiment. General trends are a smooth transition from mainly hydrodynamic to Coulomb expansion with increasing laser wavelength and intensity as well as with decreasing cluster size. However, the assignment of process dominance from experimental data proves to be nontrivial. Ruling out cluster size distribution and focus averaging gives better access to underlying dynamics such as recombination frustration and enables a charge state resolved analysis of ion kinetic energies.

Up to date not all processes during and after cluster irradiation are completely understood. The key questions are:

- How and how fast does ultrafast ionization proceed and is a plasma built-up upon irradiation?
- How fast is the energy redistributed inside? What is the role of collision and recombination processes?
- How and on which timescale does the fragmentation of an irradiated particle proceed? What is the role of screening and recombination in the context of cluster disintegration?

This thesis tries to contribute to answering these questions by investigating large, single xenon, argon, and silver clusters in ultrafast, highly brilliant IR and XUV pulses.

Chapter 3

Experimental Setup

This thesis provides new insights into the dynamics of very large, individual xenon clusters induced by ultrashort, highly intense light pulses. This chapter gives an overview of the components used in the experiment and collection of raw data. The experiments were performed in August 2011 at the **F**ree-electron **Las**er in **H**amburg (FLASH) at DESY in Germany. FLASH provides ultrabright laser pulses of very short wavelength.

A schematic drawing of the setup is presented in figure 3.1. Femtosecond pulses of infrared (IR) and extreme ultraviolet (XUV) light were coupled into the experimental chamber and guided into the interaction region by a set of stray light apertures. Here, the pulses were intercepted with single clusters, produced in supersonic expansion. Upon irradiation clusters

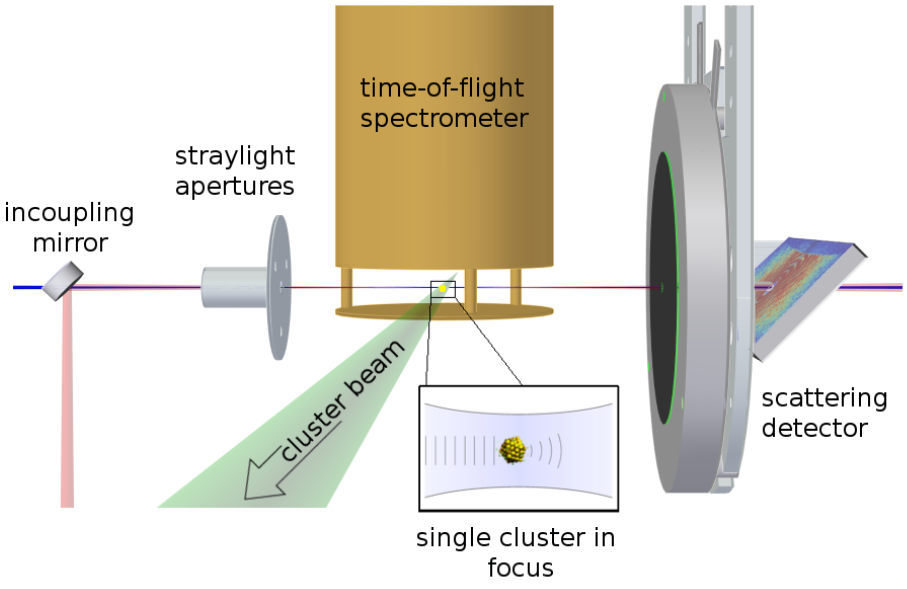

Figure 3.1: Scheme of the experimental setup. From left to right: XUV and IR beams from the FLASH facility are colinearly coupled into the vacuum chamber. Straylight apertures guide the beams into the interaction region. Here, they are intercepted with single large clusters. The resulting ionized fragments are recorded with a time-of-flight spectrometer. Diffraction patterns are captured by a scattering detector.

are turned into a nanoplasma. The morphology and transient electronic states are captured by XUV scattering. Fragments of the exploding clusters are recorded simultaneously with an ion time-of-flight (TOF) spectrometer.

In a pump-probe setup, XUV and IR pulses initiate and probe the dynamics, expansion, and disintegration of the xenon clusters. A detailed overview of the free-electron and optical laser properties and the layout is given in section 3.1. The vacuum system, cluster source, and detector systems are described in detail in section 3.2.

3.1 Generation of XUV and IR pulses

Research in the field of laser-matter interaction drastically increased with the emerging of lasers, providing mono-energetic radiation with high coherence. Over the last decades table-top lasers developed to become shorter in pulse length (down to attoseconds) allowing to study processes with atomic resolution in time. Table-top Higher Harmonic generation sources even reach the x-ray regime necessary to investigate matter with almost atomic spacial resolution [107]. However, their peak brilliance is not sufficient for many experiments involving imaging of individual nanoparticles. Accelerator-based synchrotron sources deliver highly brilliant x-ray beams, but cannot compete with lasers when it comes to pulse length. Free-electron lasers (FELs) opened up new possibilities by combining all three characteristics, pushing into the x-ray regime with ultrashort pulses and additionally providing high intensities [7].

In the experiments performed for this thesis, XUV laser pulses from the FEL where combined with IR pulses from a table-top laser system in a pump-probe setup. A quick introduction to the generation process of FEL pulses is given in section 3.1.1. The IR laser was provided at FLASH and the system is described in section 3.1.2. For two color pump-probe experiments, a good temporal and spacial overlap is critical. The setting and determination of the spacial and temporal overlap of the two individual pulses are explained in more detail in section 3.1.3.

3.1.1 XUV pulse generation at the free-electron laser facility FLASH

For portraying individual non-crystalline nanoparticles by diffraction imaging, several requirements need to be fulfilled by the illuminating light source [35]. A high photon flux is crucial to gain a good signal-to-noise ratio from scattered photons. The light needs to be monochromatic with a wavelength smaller than the particle, being in the XUV to x-ray regime for nanometer sized targets. The length of the light pulse must be shorter than the timescale of atomic vibrations and rotations in molecules and other targets which is in the range of 10^{-12} s [108]. Sufficient coherence is important since interference of diffracted waves is required. Presently, all of the above requirements combined are only fulfilled by a short-wavelength FEL pulse.

FELs are fourth generation accelerator-based light sources using the principle of synchrotron radiation generation by sending a beam of relativistic electrons through a magnetic structure referred to as Doppler frequency up-shifting of emitted radiation. Up to date there are four FELs in user operation worldwide lasing in the XUV up to x-ray regime:

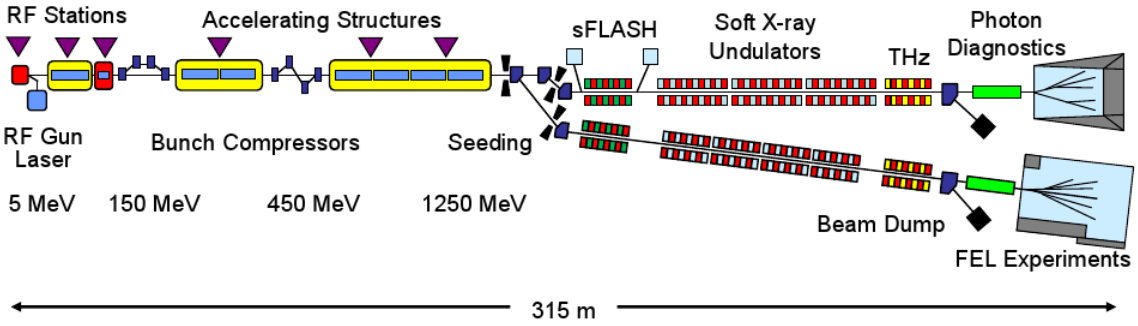

Figure 3.2: Schematic drawing of the current FLASH I and planned FLASH II setup, depicting the constituent components required to generate a FEL beam [109]. See text for detailed description.

FLASH [110, 111, 112] where the experiments for this thesis took place, the Linac Coherent Light Source (LCLS) in the US [113], the SPring-8 Angstrom Compact free-electron laser (SACLA) in Japan [114], and the free-electron laser for multidisciplinary investigations (FERMI) in Italy [115]. Development and planing are ongoing for further x-ray FEL facilities like the European x-ray free electron laser (XFEL) [116], the SwissFEL [117], the PAL XFEL in Korea [118], and for extensions of FLASH and LCLS. Detailed descriptions and derivation of the theory behind FELs are found in literature (e.g. [119, 120, 121, 122, 123]) and a good illustration of the machine operation mode and setup at DESY is given in [124]. A short introduction into the principle of FEL radiation generation will be given here on the basis of the FLASH layout depicted in figure 3.2.

The main components of a FEL are an electron injector, a particle accelerator, and a magnetic undulator as seen from left to right in figure 3.2. Free electrons are produced with 10 Hz repetition rate in a Radio-Frequency (RF) gun by illuminating photocathodes with short ultraviolet (Nd:YLF) laser pulses. The photoemitted electrons are rapidly accelerated to relativistic energies by radio-frequency fields. This cancels the repelling electric forces between the equal charges by the attractive magnetic forces between the parallel currents. The electron beam is further accelerated close to speed of light in superconducting linear accelerators. The electrons are driven in klystrons by electromagnetic alternating fields of more than 15 MV/m. Between the accelerating structures bunch compressors are shortening the electron pulses in length by two orders of magnitude. Here, the leading electrons of the bunches gain less energy than the trailing ones. Forced through a magnetic chicane the tail electrons travel a shorter distance and hence catch up.

The actual lasing process takes place in six undulator modules of 4.5 m each (sketched in alternating green and red in fig. 3.2). Forced by a long arrangement of dipole magnet pairs with alternating polarity, the electrons follow a wavelike orbit and emit photons with each turn. The wavelength of the emitted light is dependent on the spacing of the magnets (undulator period λ_U), the magnetic field B, and the energy of the electrons. Continuous tuning of photon energy is realized at FLASH by adjusting the electron beam energy. Electron beam and radiation co-propagate along the undulator interacting with each other. The electron beam is bundled along its direction of propagation when the undulator period λ_U is chosen such that the radiation field propagates (or slips) through the electron pulse at one fundamental wavelength per undulator period, as sketched in figure 3.3. The electrons are now emitting photons coherently [120]. At FLASH the

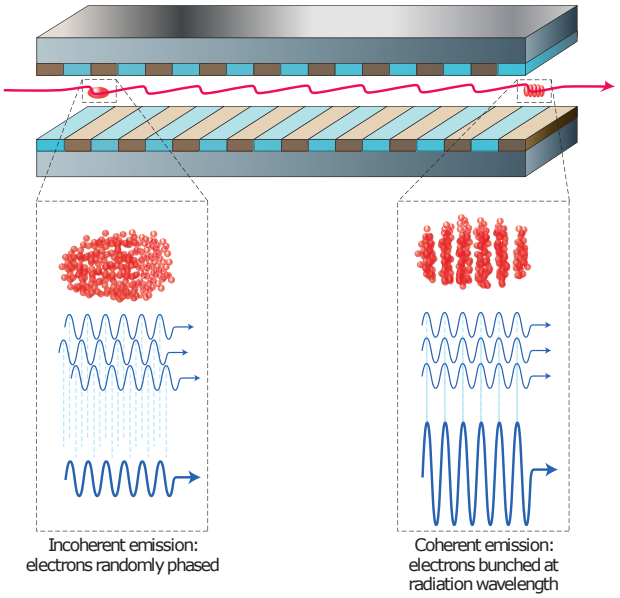

Figure 3.3: Schema of FEL radiation emission from relativistic electrons and microbunching by velocity slipping in an undulator [123]. a) When the electrons enter the undulator their phases are randomly distributed and radiation is emitted incoherently. While passing the undulator the electrons start bundling by velocity slipping and eventually start to radiate cohernently, if the electrons are bunched at the radiation wavelength.

beam is spatially fully coherent across the entire focus diameter [125]. The temporal coherence length holds a few femtoseconds [126]. The intensity of the emitted light scales quadratically with the undulator period $I \approx N^2$. The radiation power grows exponentially until saturation sets in.

FLASH is a so-called SASE laser, which stands for **s**elf **a**mplified **s**pontaneous **e**mission. Here, the lasing starts from shot noise and hence the spontaneous undulator radiation is amplified at the beginning of the undulator. Due to the statistical process the photon energy fluctuates. A different approach is to stimulate the lasing process with a monochromatic x-ray beam. The lasing process is then seeded. Due to the controlled FEL radiation generation the pulses have well-defined profiles and bandwidths, leading to higher brilliance. Additionally, there is no temporal jitter with respect to the seeding laser. A seeded FEL in operation is the FERMI FEL in Trieste [115].

At FLASH the electron beam is deflected behind the undulators by a magnet and dumped. Downbeam the light axis follows a photon diagnostics section (indicated by a green box in fig. 3.2), where each shot is characterized in non-invasive measurements. The fluctuations in wavelength - due to the statistical SASE process - are recorded with a variable line spacing grating spectrometer (VLS). Four gas monitor detectors (GMD) determine the position and the intensity of each pulse. Two filter wheels for attenuation of the beam are installed. Additionally, a gas attenuator can provide continuously variable intensities.

The beam is delivered to the user's experimental endstations through a photon beam transport system with gracing incidence carbon and nickel mirrors operating under high vacuum conditions to prevent light absorption in air. At beamline 3, where the measurements were

Table 3.1: FLASH is a user facility since 2005 and has been upgraded several times. Listed are the state-of-the-art radiation parameters in 2014 [127] and values of the 2011 experiment.

Parameter	**Current**	**2011**
Wavelength	4.2 - 45 nm	13.6 nm
Average Single Pulse Energy	10 - 500 µJ	140 µJ
Pulse Duration (FWHM)	< 50 - 200 fs	100 fs
Photons per Pulse	10^{11} - 10^{13}	10^{13}
Spectral Width (FWHM)	0.7 - 2 %	1 %
Peak Power (from av.)	1 - 3 GW	-
Average Power (example for 5000 pulses/s)	up to 600 mW	-

performed, tight focusing is established with ellipsoidal mirrors of 2 m focal length, resulting in a focus of $r = 10\,\mu\text{m}$ in radius [111]. For XUV pulses centered around $\lambda = 13.6\,\text{nm}$ wavelength (corresponding to 91 eV) with $t = 100\,\text{fs}$ pulse length and $E = 140\,\mu\text{J}$ pulse energy, this leads to a power density I in the focus of

$$I = \frac{E}{2\pi r^2 t} = 4.1 \cdot 10^{14}\text{W/cm}^2. \tag{3.1}$$

3.1.2 IR pulse generation at FLASH

The FLASH facility provides amplified Titanium:Sapphire (Ti:Sa) pulses which are temporally synchronized with the FEL pulses for the performance of two color pump-probe experiments. A detailed overview of the optical femtosecond laser system is given in [128]. The major components used for the experiments in this thesis are shortly introduced here. A schematic drawing of the setup in the laser hutch is presented in figure 3.4.

The infrared laser pulses with a central wavelength of $\lambda = 800\,\text{nm}$ and bandwidth of 50 nm are generated by a Ti:Sa ultrashort pulse oscillator (*Kapteyn & Murnane Laboratories*, Model MTS). To perform well defined pump-probe experiments the oscillator is synchronized to the FEL master clock with a jitter of under 70 fs root mean square (rms). The oscillator seeds two amplifiers: a burst-mode optical parametric amplifier (indicated in yellow in fig. 3.4) and a single-pulse chirped-pulse amplifier system (indicated in red in fig. 3.4). In the experiments performed for this thesis only the latter was used. It consists of a regenerative and a 2-pass amplifier (*Coherent*, Hidra-25). The maximum output power is 20 mJ at 50 fs pulse duration. For safe beam transportation the pulse is stretched and later shortened with a compressor, leading to a pulse duration of 80 fs for the experiment [129].

With temporal instabilities from the amplifier, the beam transport line, and the FEL pulse jitter the overall temporal fluctuation between FEL and Ti:Sa adds to a total of 250 fs rms [130, 131]. It is constantly monitored by a streak camera (*Hamamatsu*, C5680) which records the arrival time of the optical laser pulse and the synchrotron radiation pulse, radiated when the electrons are bent to get dumped. The relative jitter between both pulses is saved in the data acquisition (DAQ) system. This enables to trace random fluctuations and drifts in timing difference on-line and in post-analysis. The temporal separation between FEL and IR pulses can be altered with a computer controlled delay

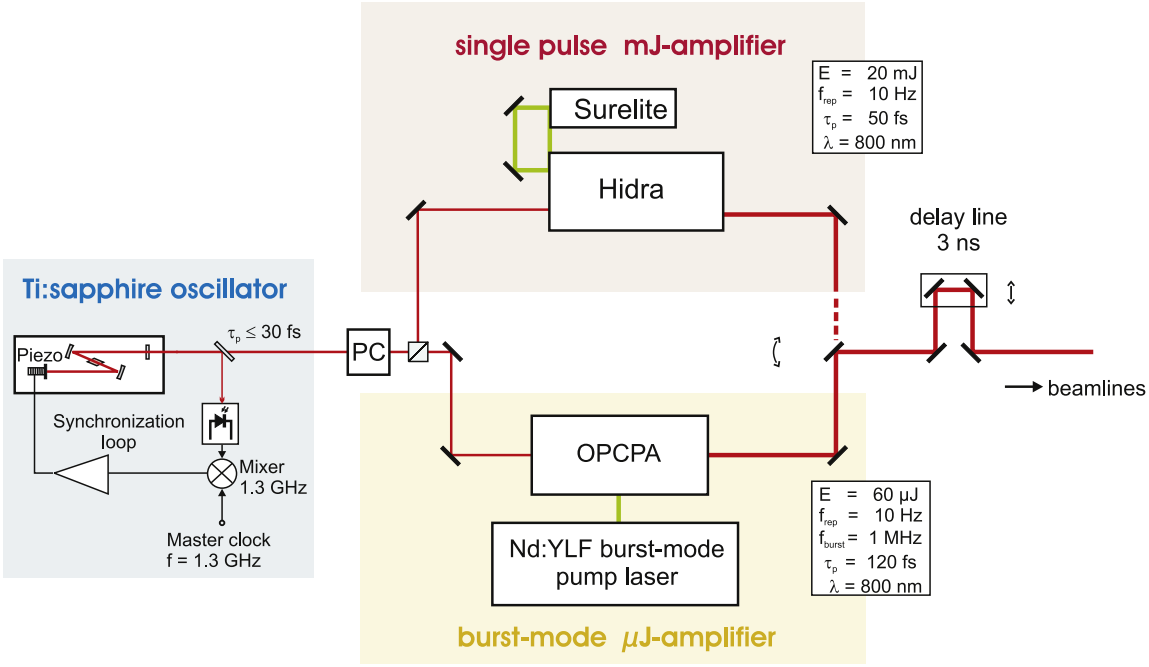

Figure 3.4: Layout of the optical laser system at FLASH [128]. For the experiments in this thesis only the single pulse amplifier was used.

state within a 3 ns range in steps of 10 fs. The position of the stage is linked to the bunch-ID and also saved in the DAQ system. The optical pulses, delivered via a beamline system to the experimental endstations, exhibit a beam diameter of 16 mm FWHM.

To couple the beam into the vacuum chamber and to focus it onto the interaction region is in the responsibility of the users. Therefore, an optical setup was designed and implemented on a breadboard positioned between vacuum chamber and beamline. The beam was transported to the height of the optical setup with a periscope. For maximum transmission, 2 inch diameter mirrors (*Newport*) were used. The IR beam entered the vacuum system through a CF60 window flange. To achieve good spatial and temporal overlap in pump-probe configuration (see next section) and due to the detector setup (see chapter 3.2.3), the incoupling geometry of the IR was collinear with the XUV beam. The Ti:Sa pulses were reflected into the interaction region via a mirror in the FEL beam path, which had a centered hole of 2 mm diameter to allow the FEL beam to pass. The mirror was placed in a CF60 cube in the vacuum system and fixed on motorized in-vacuum stages for full movement in all directions (three linear states with 8 mm hub (*Mechonics*) and two angular stages (*Newport*) for pitch and tilt motion).

The focal length was chosen such that the power density in the interaction region was maximum. Therefore, three aspects had to be taken into account:

- the focal length had to be short in order to get a tight focus,
- the divergence had to be small for the beam to fit through the detector hole, and
- the beam diameter had to be large on the hole of the incoupling mirror to keep the power loss low.

Table 3.2: IR radiation parameters of the optical laser system in the laser hutch [128] and at the experimental endstation in 2011.

General Parameters	Value	In Experiment	Value
Central Wavelength	800 nm	Focal length	750 mm
Max Pulse Energy	20 mJ	Pulse energy in focus	0.8 mJ
Min Pulse Duration	<50 fs	Pulse Length	80 fs
Beam Diameter (FWHM)	16 mm	focal diameter	90 µm
Repetition Rate	10 Hz	Focal power density	$1.1 \cdot 10^{14}$ W/cm^2
Energy Stability	3 % rms		

To fulfill all three aspects, a clano-convex lens (*Thorlabs*, N-BK7) with focal length of 750 mm was chosen, resulting in a spot size of 5.5 mm diameter on the holey mirror, of 90 µm in the focal region, and of 1.4 mm at the detector hole. For focal spot positioning along the beam axis, the lens was mounted on a linear stage (*Thorlabs*, 2 inch travel) which was placed outside the vacuum due to the long focal length. In front of the vacuum chamber the IR beam had a power of 1.4 mJ, which was reduced at the holey mirror by 40 %. The power behind the interaction region was measured to hold $E = 0.8$ mJ, resulting in a focal power density of $I = 1.1 \cdot 10^{14}$ W/cm^2 with central wavelength $\lambda = 800$ nm, pulse length $\tau = 80$ fs, and estimated focal spot size $d = 90$ µm (see equation 3.1).

3.1.3 Spatial and temporal overlap in pump-probe setup

The pump-probe scheme is one of the most promising concepts to examine dynamic processes on a picosecond time scale. While the pump pulse initiates the reaction of the sample, the probe pulse observes the induced changes. In order to ensure that both pulses hit the target, a reliable spacial overlap between IR and XUV pulse is required. In the interaction region, the IR beam with focal spot size of 90 µm was overlayed onto the 20 µm FEL beam with the help of a yttrium-aluminium-garnet (YAG) screen and a microscope. The screen was moved into the interaction region with an UHV manipulator. While the FEL focal position was fixed, the Ti:Sa focus was moved with two mirrors located on the breadboard outside the vacuum. The beam profiles were imaged with a resolution of 7 µm by a CCD camera (*Basler*) combined with a zoom-objective (*Edmund*, VZM 450i). This setup succeeded in establishing a spacial overlap with a precision of about 10 µm in x- and y-direction and about 300 µm in z-direction [132].

After setting the spacial overlap, the temporal overlap between IR and FEL pulses was established in three steps. First, it was roughly set with a resolution of 100 ps by irradiating a coaxial cable placed in both focal volumes. Upon impact the photons induced a current in the inner conductor, which is sensitive to a broad photon energy range and exhibits a fast rise time of 100 ps. The pulses induced by both laser beams are monitored with a fast oscilloscope (*LeCroy*) and brought to overlap by movement of the IR delay stage in the laser hutch.

In a second step, the temporal overlap was established more precisely with a resolution of 1 ps, using molecular nitrogen (N_2) as demonstrated in [133]. Via a metering valve the vacuum chamber was flooded with gaseous nitrogen up to a pressure of $p = 4{\cdot}10^{-7}$ mbar. By

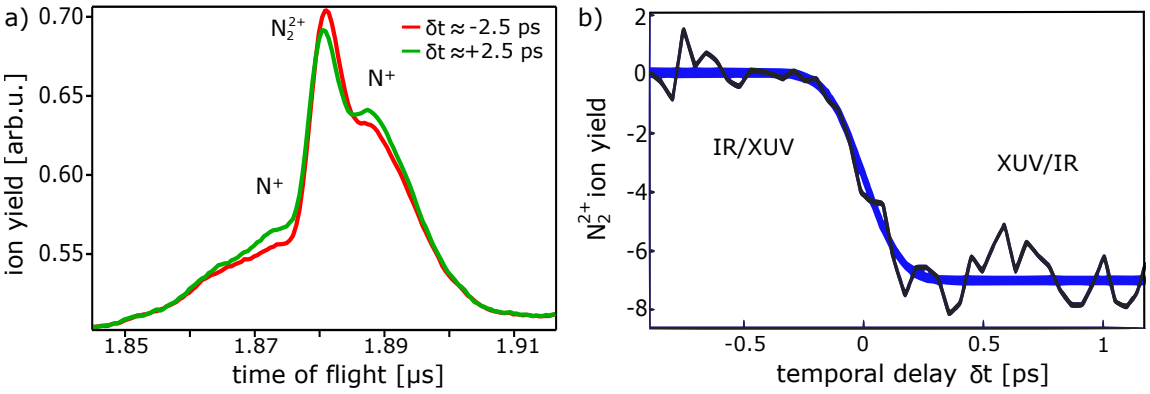

Figure 3.5: Temporal overlap determination with precision of one picosecond, adapted from [132] and [133]. a) If the gaseous nitrogen is hit by an XUV beam it gets ionized and a high N_2^{2+} signal can be detected in ion TOF spectra (red curve). If a strong IR beam follows the XUV beam, the XUV generated N_2^{2+} dissociates into N^+ leading to a decrease in N_2^{2+} signal (green curve). b) Tracking the N_2^{2+} ion yield over pump-probe separation time δt shows the isochronous arrival of both laser pulses, where the Gaussian error function fit (blue line) decreases to half of the maximum N_2^{2+} signal.

pumping the gas with the XUV beam the molecular nitrogen was turned into molecular nitrogen dications (N_2^{2+}) due to core-level ionization and subsequent Auger relaxation. As depicted in figure 3.5 a (red curve), a high N_2^{2+} signal was detected in the ion TOF spectrometer. When probing the XUV-ionized nitrogen molecule with the IR pulse, it dissociates due to the intense optical field. As a result, the N_2^{2+} signal decreases (see green curve in fig. 3.5 a). To establish the temporal overlap, the IR delay stage was scanned. The central N_2^{2+} peak intensity was plotted over delay time and fit with a Gaussian error function. The delay stage was positioned where the fit function decreased to the half maximum (see blue curve in fig. 3.5 b).

Once the temporal overlap was established on a picosecond timescale, it was possible to employ a third method as described in [134]. Here, the short-lived transient ion signal of Xe^{3+} is indicating the isochronous arrival of both pulses with a resolution of 400 fs. Via the cluster source gaseous xenon was leaked into the chamber. Around 90 eV photon energy, xenon exhibits the 4d - ϵf giant resonance [66] introduced in section 2.3.1. Irradiation with one single XUV photon leads to double or triple charged xenon, due to 4d shell ionization and subsequent Auger decay leaving two or three electron vacancies in the outer 5p shell, respectively. The Xe^{2+} and Xe^{3+} ion TOF signals therefore scale linearly with the FEL intensity[1]. Long-lived intermediate states just below the Xe^{3+} threshold can be pumped by the IR pulse leading to a temporary increase in Xe^{3+} ion yield as evident from figure 3.6 a. The green curve shows a spectrum where the xenon gas is pumped with an IR and probed with an XUV beam. When reversing the pump-probe scheme (blue curve), an increase in Xe^{3+} ion yield exhibits the excitation of XUV generated Xe^{2+} states to Xe^{3+} states. In 500 TOF spectra taken at each delay time, the Xe^{3+} yield was integrated and normalized to the Xe^{2+} yield. Plotted over pulse separation time δt the half maximum of the Gaussian error function fit revealed the isochronous arrival time of both pulses with a

[1] In the production of higher charge states nonlinear processes like multiple-photon absorption are involved.

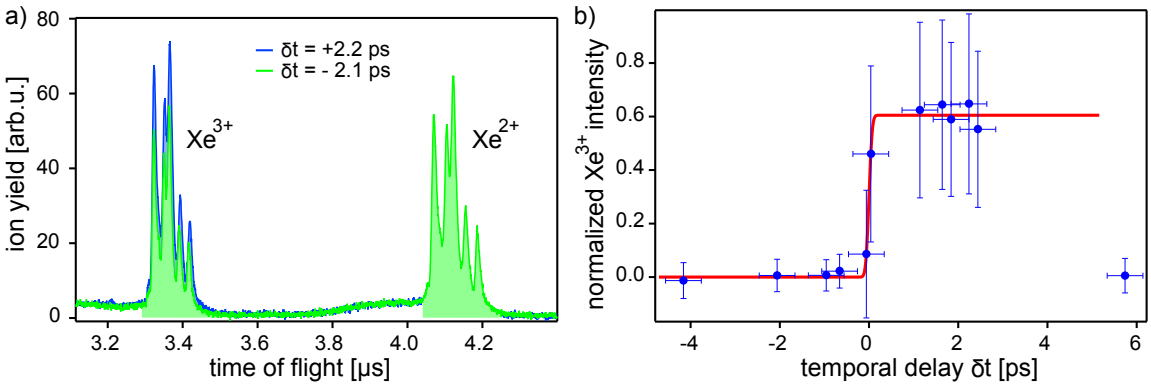

Figure 3.6: Fine temporal overlap between IR and XUV pulse established with xenon gas, adapted from [132]. a) Ion TOF spectra from xenon gas. Green curve: xenon is first exposed to IR and after to XUV beam. Xe^{2+} and Xe^{3+} ion yield scale linearly with FEL intensity. Blue curve: if the IR beam follows the XUV beam, XUV-excited intermediate states are pumped by the IR pulse leading to an increase in Xe^{3+} ion yield. b) Isochronous pulse arrival time is extracted from the half maximum of the Gaussian error function fit to the normalized Xe^{3+} ion yield plotted over pulse separation time δt.

resolution of 400 ps (fig. 3.6 b). Once both laser pulses are well synchronized in time and space, a good overlap with the cluster beam needs to be established as described in the next section.

3.2 Experimental chamber

The experiments were performed in an ultrahigh-vacuum (UHV) chamber. Here, the cluster beam was produced and laser-cluster interaction was detected. The requirements regarding the vacuum system are high, since cluster generation involves heavy gas loads and residual detection requires good signal-to-noise ratio, e.g. high vacuum. To match all needs the UHV chamber is separated into four parts, as described in detail in section 3.2.1.

The clusters were produced in a pulsed supersonic expansion (see 2.1). Large cluster sizes in the range of several ten to hundred nanometer could be obtained by cooling the source and applying high gas backing pressure. A key feature of this experiment is the ability to study individual clusters to rule out the blurring of signals due to measurements on an ensemble of clusters. Therefore, the jet was heavily skimmed such that only one single cluster was detected in the interaction region at a time. The cluster source used for the presented experiments is introduced in chapter 3.2.2.

A combined approach to simultaneously detect elastically scattered photons and fragmented cluster ions was applied to investigate light-matter interaction on different timescales. It is introduced in 3.2.3. The positively charged ions were collected with an ion time-of-flight spectrometer. A scattering detector recorded diffraction patterns and fluorescence photons of the disintegrating clusters shot by shot. The detected data was stored together in one file with an identifier from the FEL light pulse.

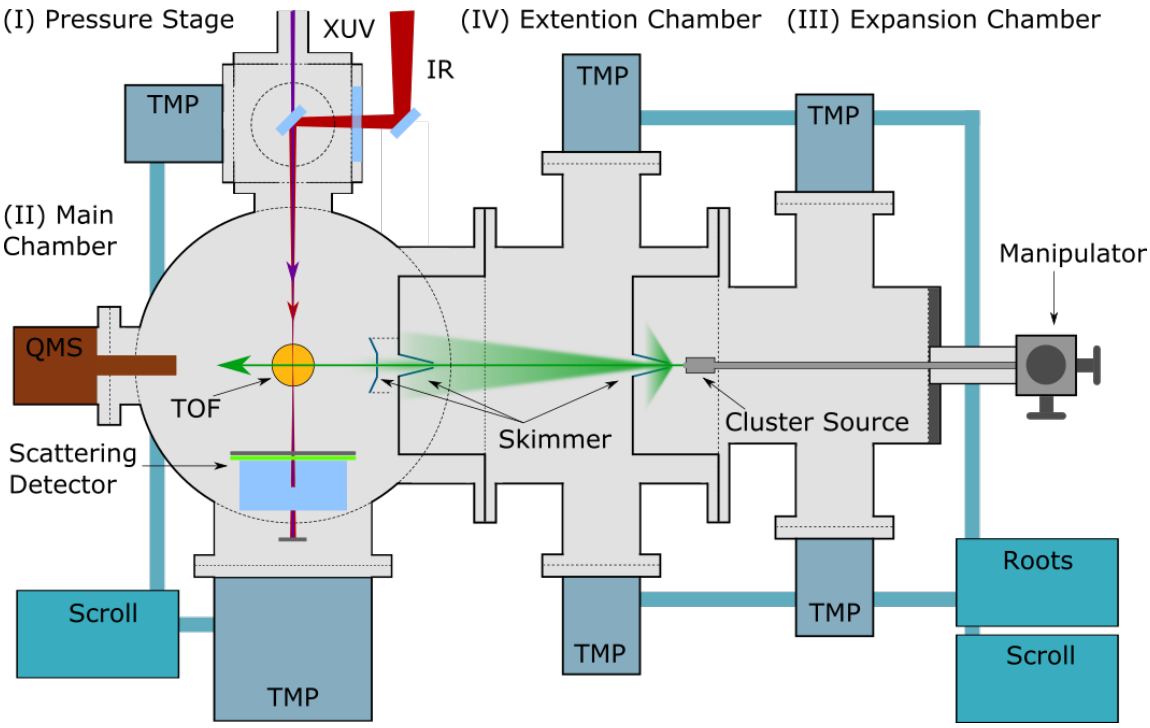

Figure 3.7: Schematic diagram of the vacuum apparatus, adapted from [132]. I) The pressure stage served as differential pumping stage between main chamber and beamline. II) In the main chamber the interaction region and the detectors were located. Here, the background pressure needed to be low in order to ensure a good signal-to-noise ratio in the measurements. III) In the expansion chamber the clusters were generated by supersonic expansion of high pressure gas into vacuum. Since the gas load under these conditions was heavy good vacuum pumps were needed. IV) The extension chamber separated main and expansion chamber and served as differential pumping stage. The gas throughput was kept low by two conic skimmers with small orifices of 0.5 and 1 mm diameter.

3.2.1 Vacuum system

Clusters were produced under heavy gas load in the same chamber where experiments under high vacuum conditions were performed. In order to keep undesirable background signal in the measurements low, a smart vacuum system was needed. Hence, the chamber was divided into four differentially pumped sections, as sketched in figure 3.7. A pressure stage (I) was located between beamline and main chamber (II) where the laser beams were intersected with the cluster beam and the scattering patterns and ion mass spectra were detected. The clusters were formed in the expansion chamber (III) which was separated from the main chamber by a set of small skimmers and a differentially pumped extension chamber (IV). The whole vacuum setup was pumped by a set of turbo-molecular pumps (TMP) and prevacuum pumps and constantly monitored with several pressure gauges (*Pfeiffer*, Full range gauges and Pirani gauges connected to a Maxi Gauge controlling unit). A safety system ensured controlled venting of the entire vacuum chamber, either manually, or automatically if an error occurred at any of the vacuum pumps.

The pressure stage (fig. 3.7 I) served as incoupling stage for the IR laser, as already introduced in section 3.1.3. Additionally, it ensured that the vacuum in the experimental

chamber was always better than in the beamline. This prevented residual carbon hydrates from migrating into the beamline where they could coat the mirrors. Both vacuum systems were separated by a pressured valve which automatically closed if the pressure in the pressure stage rose above the pressure in the beamline. Therefore, the valve was coupled to the signal of the pressure gauge in the pressure stage and could only be opened if the pressure was below $p_{\mathrm{I}} = 10^{-6}$ mbar. A TMP (*Pfeiffer*) was installed to achieve this pressure, reaching down to $p_{\mathrm{I}} = 10^{-8}$ mbar. The TMP was coupled to a scroll pump (*Franklin Electric*) providing a prevacuum of $p = 10^{-2}$ mbar.

In the main chamber (fig. 3.7 II) the jet of free clusters was channeled into the pulse trains of the XUV and IR laser. The detection of scattered photons and fragmented ions as residuals from the interaction demanded for low background pressure to ensure a good signal-to-noise ratio in the measurements. With a large TMP (*Pfeiffer*, TMU1000PC) background pressures of $p_{\mathrm{II}} = 10^{-9}$ mbar and $p_{\mathrm{II}} = 10^{-6}$ mbar were reached, without and with cluster source switched on respectively. The prevacuum system was coupled with the pressure stage. Gaseous residuals in the vacuum were analyzed with a quadrupole mass spectrometer (*MKS*, e-Vision 2) which was also used for the alignment of the cluster source, as described in section 3.2.2.

The clusters were generated in the expansion chamber (fig. 3.7 III) in supersonic expansion with 5 Hz and backing pressure of 9.8 bar (see next section for setup of the cluster source). Despite the heavy gas load, a background pressure of $p_{\mathrm{III}} = 10^{-4}$ mbar was reached due to two TMPs (*Leybold*, volume flow rate of 345 l/s) coupled to a strong prevacuum system. This prevacuum system consisted of a roots (*Oerlicon Leybold Vacuum*, WSU251) and a scroll (*Edwards*, XDS35i) pump, reaching a pressure of $p = 10^{-3}$ mbar without gas load [132]. The same system was used for two TMPs, which were pumping the extension chamber (fig. 3.7 IV) down to a pressure of $p_{\mathrm{IV}} = 10^{-5}$ mbar. The extension chamber was located between expansion and main chamber. All three chambers were only connected via two conical skimmers with orifice diameters of 0.5 and 1.0 mm respectively. These were not only used to keep the gas throughput low, but also to extract only the central part of the cluster beam, where the largest particles are present.

3.2.2 Cluster source for large xenon cluster generation

Large xenon clusters were generated in a cryogenic, pulsed cluster source, using the principle of supersonic expansion as introduced in the theoretical section 2.1. The main components of the source were a nitrogen cooled cryostat, a solenoid driven pulsed valve, and a conical nozzle. The commercial cryostat (*CryoVac*) was mounted on a flange with several feedtroughs for liquid cooling material, temperature sensors, heat and valve control, and gas inlet. The xenon gas was sent through a steel tube and cooled in a spiral around the cryostat. From there, it was sent through the valve which was housed by a gold shield where a temperature sensor and heat capacitors were located. The nozzle was directly attached to the valve with an indium gasket to minimize leakage while optimizing heat transport. To prevent clogging of the nozzle orifice, a sintered filter (*Swagelock*, 15 µm pore size) was installed in front of the gas inlet.

To enable imaging of the clusters by XUV scattering, the samples had to be larger than 25 nm in radius, corresponding to about 110000 atoms in a spherical xenon cluster (see

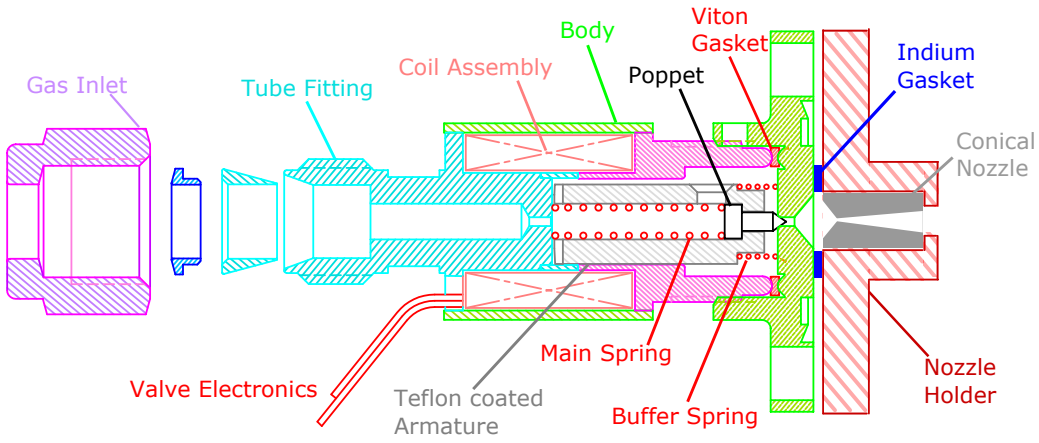

Figure 3.8: Schematic depiction of the cut through the solenoid pulsed valve and the conic nozzle, adapted from [135, 136]. The atomic gas enters the valve from the left and exits it on the right when the poppet in the armature is pulled back due to a magnetic filed induced in the coil assembly. The gas expands in a supersonic expansion through the conic nozzle and thereby clusters are formed.

equation 2.12). To generate such large particles the xenon gas was cooled to $T = 180\,\mathrm{K}$. A conic throat nozzle with an orifice diameter of 200 µm and a half cone angle of 4° was chosen for a relatively low but well directed gas flow. With a backing pressure of 9.8 bar the resulting average number of atoms per cluster should have been $\langle N \rangle = 210000$ according to empirical scaling laws [28] (see also equation 2.11). Since the producible cluster size is limited by the background pressure and pumping speed a pulsed valve was used to keep the gas load low. Pulsed operation has considerable advantages towards continuous jet flow:

- the stagnation pressure can be increased
- pumping requirements are reduced
- cleaner spectra with increased signal-to-noise ration can be detected and
- characterization of the velocity distributions in the jet is facilitated.

A schematic sketch of the solenoid valve (*Parker General Valve Corporation*, series 99) is presented in figure 3.8. The valve is sealed by a vespel poppet pushed into the valve orifice by the main spring. The poppet is located at the tip of a teflon coated, magnetic armature which is pulled back by the induced magnetic field of a coil assembly when current is applied. As long as the current is kept and the poppet is held back, the gas can flow freely through the valve. Upon switching the current off, the poppet is pushed back into the orifice by the main spring and the gas flow is stopped. The valve is controlled by a pulse driver (*Parker*, IOTA ONE) which initiates valve opening with a -28 V opening pulse and keeps it open with 250 mV holding voltage. An opening time of 5 ms was chosen for the experiments. A minimum opening time of 1 ms is needed for the generation of clusters as reported for similar experiments [137]. When the valve is closed between two pulses, the dead reservoir between valve and nozzle is exhausted by pumping through the nozzle.

The repetition rate of the valve was set to 5 Hz which was half the frequency of the laser pulses. For temporal synchronization of cluster beam and laser pulses the valve driver was

triggered with a TTL input from the FEL. The timing was controlled with a digital delay generator (*Stanford Research Systems*), which received the timing pulse from the DESY master clock and produced a preset beam duration after the desired delay. The XUV pulse arrived 24 ms after the master signal in the interaction region [138]. In order to record the temporal profile of the jet pulse, the delay was scanned between 0 and 14 ms after the light entered the interaction region. The temporal profiles for the atomic beam and the cluster beam are presented in figure 2.3 b. Atomic background spectra for reference and optimization procedures were taken in the rising edge at 0.5 ms delay.

In order to establish single-cluster mode, the cluster jet had to be skimmed down in front of the interaction region. The jet issuing from the cluster source was heavily skimmed by a set of two conical skimmers downstream of the nozzle with 1 mm and 0.5 mm orifice radius respectively. The shape of the skimmers is essential and follows the rules for skimmer design [17], which are introduced in section 2.1. The main part of the incoming gas remained in the expansion chamber and only the central beam part containing the largest clusters was guided into the interaction region. Precise adjustment of the cluster beam axis was necessary to establish a clear path through both skimmers and spacial overlap between cluster and laser beams. Therefore, the cluster source was mounted onto a mechanically translatable XYZ-manipulator and adjusted to a high dimer-to-monomer signal ratio in a quadrupole mass spectrometer (QMS) downstream of the skimmers (see [45, 132] for detailed description of the alignment procedure). The dimer signal indicates whether clustering is effective.

The narrow beam in the main chamber could additionally be cut with a skimmer slit which is continuously variable in size. By varying the width of the skimmer slit, the number of clusters in the focal volume was controlled. The slit consisted of two razor blades mounted onto a piezo-driven shutter system (*Piezosysteme Jena*). The shutter closed upon applying voltages up to 150 V. The resulting width varied between 0 and 1.5 mm. Reference values between 0 and 10 V are monitored and converted into slit opening d_{slit} by the following calibration relation

$$d_{slit} = a - b \cdot U + c \cdot U^2 \tag{3.2}$$

with $a = 1500\,\mu\text{m}$, $b = 227.2\,\mu\text{m/V}$, and $c = 7.3\,\mu\text{m/V}^2$ [132]. For single cluster experiments, the skimmer voltage was adjusted to a read-out value of $U = 8\,\text{V}$, corresponding to a slit width of $d_{slit} = 150\,\mu\text{m}$.

3.2.3 Coincident photon and ion detection

Once the cluster source and the laser beams were set correctly and all beams intersected in the interaction region, the residuals from the light-matter interaction were detected. A combined approach was used to investigate different time scales: during the interaction on a femtosecond timescale and after the pulse on a nanosecond timescale. With a scattering detector elastically scattered photons were collected, which contain traces of the change of the optical constants and therefore transient electronic configuration during the pulse. Complementary data was recorded with an ion time-of-flight spectrometer. After cluster explosion fragments were detected when ultrafast processes like electron collisions and recombination were already finished. For easy data post-processing, both datasets were stored coincidentally in one file [139], together with other information like e.g. laser parameters.

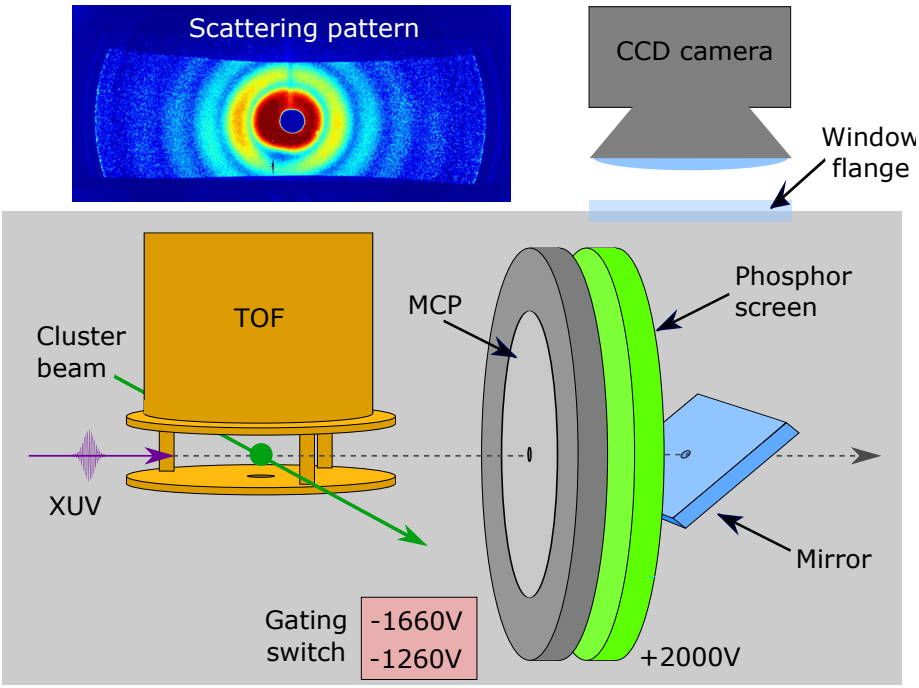

Figure 3.9: Scheme of the scattering detector setup, adapted from [132]. The elastically scattered and fluorescing photons hit the front of the MCP where they induce electron avalanches. The amplifies signal is converted into visible light by the phosphor screen. The out-of-vacuum CCD camera records an image of the back of the phosphor screen through the window via the mirror under 45 degrees. The camera trigger is synchronized to the FEL pulse. The TOF electrodes cast a shadow on the detector limiting the detected diffraction pattern in vertical direction.

Scattering detector

The scattering patterns were captured by a 2D area detector (*Photonis*), used in several previous experiments [42, 10, 30]. It is a robust and affordable solution which fulfills the requirements of spacial resolution, dynamic range, x-ray sensitivity, and fast read-out time. X-ray sensitive in-vacuum charge-coupled device (CCD) cameras are either extremely expensive [140] or have insufficient resolution or readout rate. The here applied detector uses an optical CCD-camera after conversion of the diffracted XUV light into visible light and redirection of the image out of the vacuum chamber. The detector assembly is composed of four major parts, as depicted in figure 3.9: (i) a multi-channel plate (MCP) stack which transfers the XUV photon signal into electronic signal, (ii) a phosphor screen which converts the electronic signal into visible green light, (iii) a mirror which reflects the diffraction pattern out of the vacuum chamber, and (iv) a triggered out-of-vacuum CCD camera to ultimately record the pattern. The first three detector components have a central hole to pass the direct laser beam through and protect the components from beam damage.

The large-area MCP stack consists of two MCPs twisted by 180 degrees to each other. Both have a sensitive area of 75 mm diameter and channels with 25 µm under 8 degrees to the surface. Due to this set-up, the detector has reduced detection probability at one spot of under 8 degrees scattering angle (see scattering pattern in figure 3.9). A voltage of

-1660 V was applied to the MCP front, facing the interaction region, in order to accelerate the electrons to the second MCP which was grounded on the back. Electrons produced in the interaction region were repelled by the negative charge. To prevent the MCP from detecting attracted ions, the voltage supply was gated by a fast high-voltage switch (*Behlke*) from -1660 V to -1260 V after photon impact.

With +2000 V applied to the phosphor screen close behind the MCP stack the electrons were accelerated towards the screen. Here the electronic signal was converted into green light with a wavelength around 550 nm. The screen consisted of a fiberoptical plate coated with P20-type phosphor. A mirror angled at 45 degrees reflected the diffraction image out of the vacuum chamber through a CF60 flange window. The images were detected shot-to-shot by an out-of-vacuum CCD camera (*Basler*, 1392 x 1040 pixel with 69 µm pixel size), triggered synchronously with the arrival of the FEL pulses. An IR filter was installed at the outcoupling window to protect the camera from direct IR light reflected in the mirror.

Great care needed to be taken to minimize stray light, originating from optical components in the beampath. One circular aperture was positioned in the FEL path upstream from the IR incoupling mirror. Additionally, a light baffle system for the IR path was constructed. It consists of three circular apertures of 2.0, 1.5, and 1.1 mm diameter placed at 90, 70, and 50 mm upstream from the interaction region respectively. Between the apertures the beams were covered by black tubes to prevent IR reflexes from the vacuum chamber walls.

With the scattering detector mounted at a distance of 61.6 mm from the interaction region, scattering angles from 4 degrees to a maximum angle of 31 degrees were covered. The corresponding maximal momentum transfer is $q = 4\pi/\lambda \cdot \sin(\theta/2) = 0.25\,\mathrm{nm}^{-1}$ (with $\lambda = 13.5\,\mathrm{nm}$), limiting the detection resolution to $2\pi/q = 25\,\mathrm{nm}$. In vertical direction, the maximum detected angle is limited to 11° due to a shadow originating from the TOF-spectrometer electrodes (see fig. 3.9).

Ion time-of-flight spectrometer

The ion mass spectra in this thesis were detected with an ion time-of-flight (TOF) spectrometer. The atomic and cluster ions created in the interaction region upon laser impact were accelerated and guided towards a detector using electric fields. A schematic depiction of the spectrometer principle is presented in figure 3.10 a. A difference in potential between two electrode plates, located around the ion starting point, generates a field that pushes the ions towards the time resolved detector. Between acceleration region (with length s) and detector lies the drift region (with length d) where the ions fly in a field-free environment. TOF spectrometers are based on the principle that the acceleration of a particle in a homogeneous electrical field depends on its mass-to-charge ratio (m/q) [141]. When the mass m is known the charge q of the ion and their initial kinetic energy is determined by the flight time t_{TOF} elapsing between creation and detection. The flight time is given by

$$t_{\mathrm{TOF}} = \sqrt{\frac{m}{q}} \left(\sqrt{\frac{2 \cdot s \cdot s_1}{U_1}} + \sqrt{\frac{d \cdot s_1}{2 \cdot U_1 \cdot s}} \right) \tag{3.3}$$

where U_1 is the repeller voltage.

The ion TOF spectrometer applied in this thesis is equipped with a bipolar detector and introduced in detail elsewhere [93]. In principle it can detect both, ions and electrons,

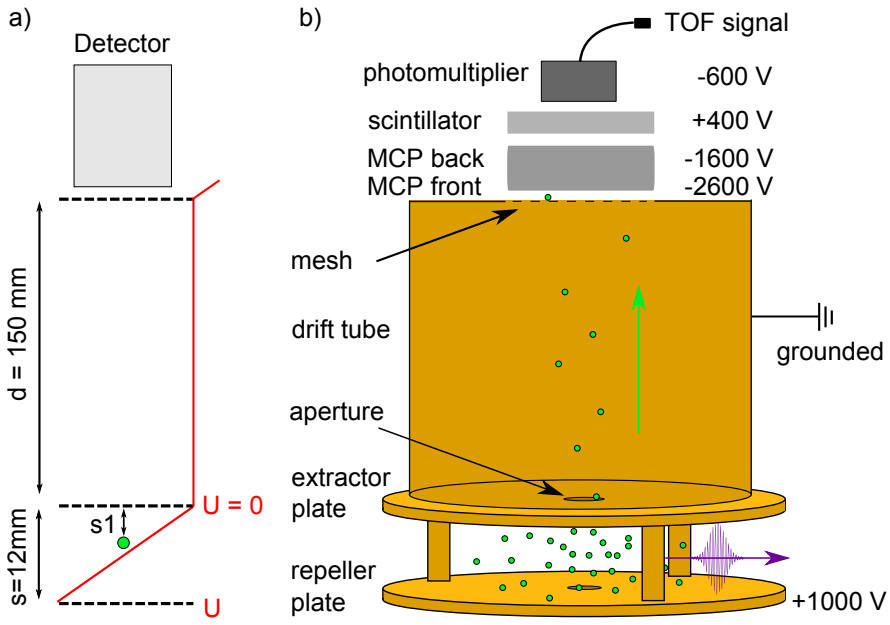

Figure 3.10: a) Scheme of the TOF-spectrometer principle with measures of the used spectrometer, adapted from [139]. Ions are accelerated upwards in the electric field around the interaction region. They fly field-free in the drift region until they get post-accelerated toward the detector behind the mesh. b) Depiction of the TOF design with voltages applied in the experiment, adapted from [132].

depending on how voltages are applied. It consists of a repeller plate for acceleration of particles and an extractor-plate. The extractor plate has a limiting aperture of 3.5 mm diameter, so that only ions originating from the interaction region are collected and the residual gas spectrum is cut out. Behind the repeller plate is a grounded drift tube made out of μ-metal[2]. It is covered with a mesh in order to keep the inner tube field-free, and a detector. The measures of the spectrometer are indicated in figure 3.10 a. Behind the drift tube is a commercial detector (*Burle Industires*). It is composed of a MCP for signal amplification, a scintillator crystal which converts the electronic signal into photons, and a photomultiplier which enhances and reconverts the optical into electronic signal. The voltages[3] applied during the experiment are indicated in figure 3.10 b.

The spectrometer is non-Wiley-McLaren [142] and can therefore also resolve initial ion kinetic energies. Ions with higher momenta are faster and recorded earlier in the flight-time spectrum. For the conversion of flight time into kinetic energy the exact spectrometer geometry needs to be taken into account. Xenon cluster flight-time spectra for the spectrometer design were modeled with SIMION in [45]. The resulting simulated conversion function is linear

$$E_{ini} = 1.8 \cdot 10^{-8} \cdot t^{-2} - 444 \cdot q \tag{3.4}$$

with t the flight time and q the charge. As plotted for the first five xenon cluster ion charge states in figure 3.11 a, the kinetic energy is reciprocal to the squared flight time.

[2] μ-metal is a nickel copper alloy which effectively shields magnetic fields.
[3] With different voltages applied also electrons can be detected with this system.

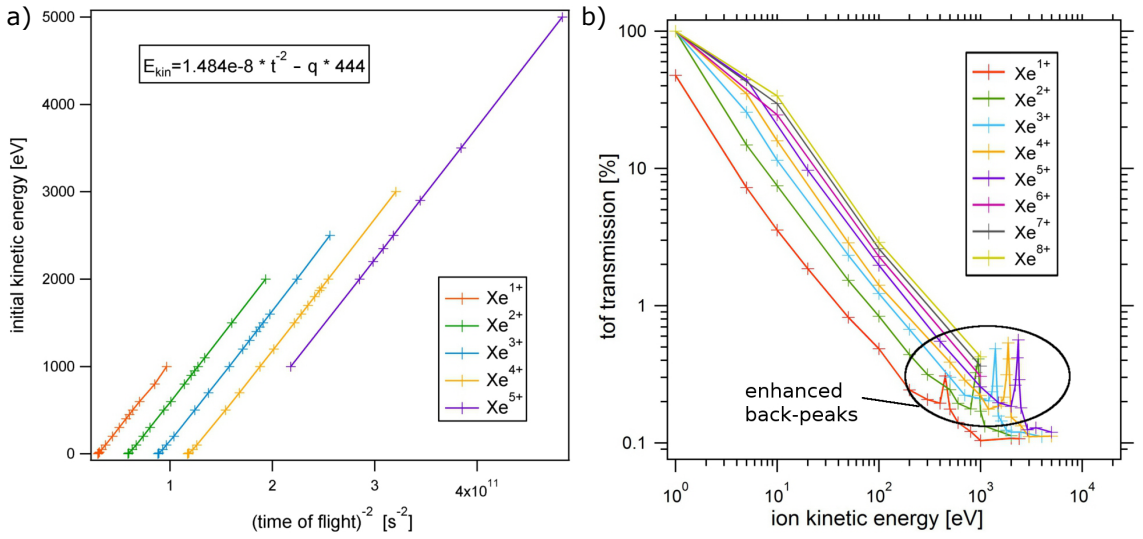

Figure 3.11: a) Time-to-energy conversion curves for the first five charge states and b) transmission function for the first eight charge states of xenon clusters simulated with SIMION [45].

When analyzing the TOF spectra for signal intensities, the spectrometer transmission has to be taken into account. The transmission is dependent on the emission angle, charge state, and momentum of the ions. The simulated transmission functions of the TOF spectrometer for the first eight charge states are plotted in figure 3.11 b [45]. For ions with low kinetic energies the detection probability is higher than for high kinetic energy ions. The latter are thus underrepresented in the TOF spectra. Additionally higher charge states are transmitted better, since their trajectories are stronger influenced by the electric field. A prominent feature in the transmission function spectra are sharp peaks at high kinetic energies. They result from an artifact owed to the detector geometry. In the TOF spectra back-peaks are present, originating from ions which are initially ejected away from the detector but later pushed towards it by the electric field of the repeller electrode. A small aperture in the repeller plate distorts the field and leads to a lens effect, efficiently focusing high energy ions onto the detector. Therefore, their transmission is high and strong contributions from back-peaks can be found in TOF spectra of strongly excited clusters.

Chapter 4

Results: Cluster evolution in intense XUV and IR pulses

The power of the approach of measuring matter-light interaction of single, free clusters lies in the access to phenomena which are hidden when averaging over an ensemble of clusters [42, 10]. Together with the combined approach of elastic-light-scattering detection and coincident ion spectroscopy, complementary aspects and different time scales of laser-cluster interaction are accessed in unprecedented detail [101, 44]. Precise morphological characterization of non-periodic, nanoscale particles and analytical examination of the individual degree of laser impact become possible with this method [11, 12]. The great wealth of recorded information holds the potential for extensive examinations. However, it also demands for the design of new data-processing tools and filtering routines [143]. Their development and implementation are subject to the first part of this chapter (section 4.1).

Cluster disintegration as a consequence of laser impact is the main topic of this thesis. Single-pulse measurements with changing parameters are studied in detail in section 4.2 to disentangle the particular influence of different materials and laser characteristics on the particle evolution. Distinctions and analogies in cluster disintegration for varying particle sizes and chemical components, as well as for tuned laser intensities and wavelengths reveal interesting correlations in nanoplasma dynamics on the femto- up to picosecond timescale.

To trace the cluster ion motion, the experiment has been pushed further to an extended timescale of up to nanoseconds by applying a pump-probe scheme (fig. 3.1). Single large xenon clusters have been exposed to intense, extreme ultraviolet pulses to initiate an expansion process, which is topic of chapter 4.3. The simultaneous imaging of the clusters upon pump-pulse impact allowed for good characterization of the initial particle condition. The subsequent gradual dilution of the sample was tracked with an infrared pulse by probing the time of collective quasi-free electron motion driven by the laser field.

Finally, the disintegrating cluster was directly imaged in a reversed pump-probe setup. A strong IR pulse triggered nanoplasma formation and evolution. It was followed by a delayed XUV pulse, which recorded structural changes at consecutive points in time. The emerging 'movie' presents a variety of insights into different expansion states. Simulations based on scalar theory of light scattering manifest the survival of large clusters on long timescales (section 4.4).

4.1 Filtering and processing single-shot single-particle data

Single-shot single-particle measurements open up a wide range of new possibilities to precisely explore laser-induced nanoplasma dynamics on well-characterized systems. Up to date most experimental studies of cluster-light interaction are performed on *ensembles* of clusters (cf. [47, 59, 144]) - while almost all theoretical investigations deal with calculations for *single* clusters (cf. [48, 49, 50]). This discrepancy often complicates a simple comparison between measured and simulated data [145]. On the one hand, data from a cluster ensemble exhibits spreading due to a size distribution resulting from the statistical growth process of clusters (see section2.1). On the other hand, the Gaussian distribution of laser intensity in the focal area adds further averaging of measured signals. This is caused by the fact that clusters are hit in different places within the focus and therefore experience different power densities.

Both resolution-lowering distributions are circumvent with the imaging of single particles by XUV photon scattering, in contrast to experiments on cluster ensembles. Every individual shot is stored together with its FEL-allocated bunch-ID, giving the opportunity to combine each hit with its corresponding pulse characteristics data in post analysis, as introduced in section 3.2.3. The amount of photons scattered at one particle increases with the amount of impinging photons. It therefore gives information about the imposed laser power density (see 4.1.1). Additionally, the size of each individual target is precisely recorded in its diffraction pattern. As consequence, size distribution averaging can be ruled out which opens the possibility to study radius-dependent effects in great detail. Pioneering experiments on individual xenon clusters displayed a vast amount of target sizes and shapes [146, 11]. A different experiment was able to reveal the change of optical constants dependent on laser intensity completely independent of size effects [10] and just recently shock waves were observed in nanoplasmas [147]. These publications impressively prove the necessity of single-particle detection to gain access to information concealed in ensemble measurements.

A tremendous gain in information lies in the combined approach of collecting scattering patterns and ion time-of-flight (TOF) spectra from the same sole sample. While nanoplasma processes occurring on a *femtosecond* timescale are imprinted in CCD images, ion spectra contain information about expansion mechanisms taking place *picoseconds* after illumination (discussed in 4.1.2). Unexpected details about cluster fragmentation and electron recombination were revealed in the first experiment using this composite practice [101]. This method allows to uncover previously hidden processes, but also demands for the collection of a large amount of data to reach significant statistics with meaningful assertion. Novel filtering and analyzing procedures for efficient, automated, and unsupervised sorting are inevitable to process these huge amounts of data [143].

All measurements investigated in the scope of this thesis were taken at two different beamtimes at the free-electron laser FLASH in Hamburg. The first took place in 2011 and the second a year later in 2012. All together over two Terabyte of data containing about a million single shots were recorded to fulfill the needs of good statistics. In the first beamtime, large xenon clusters were investigated with 13.6 nm wavelength FEL pulses and 800 nm wavelength Ti:Sa pulses - either separate or consecutive in pump-probe configuration. In one 16 h shift a total of 180 runs containing almost 100000 shots were recorded. By measuring all data in one single shift it was ensured that all xenon clusters were produced

under very similar conditions and that laser specifications stayed relatively constant over the whole experimental period. In the following year, only XUV pulses were used. This time, additionally to xenon clusters, also silver and argon clusters were inspected. Due to remodeling of the vacuum chamber by installing different cluster sources, the data was collected over several days. With over 100000 shots recorded for each cluster component meaningful statistics were gained to ensure a significant characterization of the studied processes. During the course of this thesis, I wrote a whole set of filtering routines in MATLAB [148] for handling of this massive amount of data. The three main filters are sorting for

- cluster size, determined by fringe spacing from the scattering patterns,
- intensity of the CCD image, and
- high kinetic energies in ion TOF spectra.

The filters will be presented in the subsequent two sections.

4.1.1 Filtering by CCD image

Imaging in single-cluster mode was reached by cutting the cluster beam such that the majority of shots in which clusters are hit by a laser pulse comprises only one single cluster. A piezo-driven slit (see section 3.2.2) was set to the position where the minority of the produced clusters gets through to achieve this condition. In this configuration, the target beam was diluted so strongly that a vast amount of shots actually contained no cluster but only atomic residual gas in the interaction region. Images resulting from pure atomic signal in the focus had to be sorted out for analysis of laser-cluster interaction.

Four exemplary raw CCD images are shown in figure 4.1: the first two images, a and b, show photons fluorescing and scattered from xenon and residual gas, hit by either an XUV or by an IR pulse respectively. The hole which protects the detector from the direct laser beam is visible in the center of the subfigures. In the first image (a), the high circular signal around the hole arises from XUV photons secondarily scattered at the focusing mirror in the beamline. In the second image (b), only little stray-light signal is seen to the left side of the hole since the IR laser is focused by a lens (see section 3.2). Only IR light falling directly through the hole of the detector can be detected since the detector MCP is insensitive to the IR wavelength. The diffuse signal on the lower left side originates from a reflection at the outcoupling window. The second set of images (c and d) depicts single clusters hit by either an FEL or a Ti:Sa pulse respectively. Here, the shade from the TOF-spectrometer electrodes falling on the round scattering detector becomes clearly visible. The pattern from the XUV irradiated cluster (c) exhibits characteristic diffraction rings due to strong forward scattering. In the last image (d), heterogeneous scattering signal from the long-wavelength infrared in combination with fluorescence is visible. Under an angle of 8 degrees the detector sensitivity is lowered due to the detector configuration as introduced in section 3.2.3. All images exhibit a few dead camera pixels which do not affect the analysis and are therefore ignored. Above the detector hole a stripe with low detection signal is visible. It is attributed to a local degradation effect. It results from ionized background gas in the chamber which is repelled from the lower TOF spectrometer electrode (compare section 3.2.3).

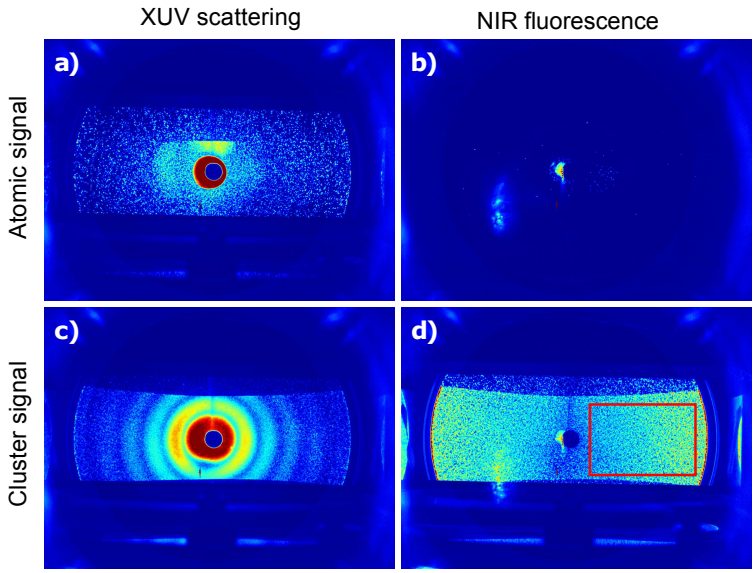

Figure 4.1: CCD camera images showing scattered and fluorescing photons from xenon gas as well as residual gas irradiated by a) an XUV pulse with maximum power density of $4 \cdot 10^{14}\,\mathrm{W/cm^2}$ and b) an IR pulse with with maximum power density of $1 \cdot 10^{14}\,\mathrm{W/cm^2}$. c) Scattering pattern from a single xenon cluster hit by the XUV beam with minor fluorescence contribution. d) Fluorescence from a xenon cluster irradiated the IR beam. Note that the MCP of the detector is insensitive to elastic scattering in the IR wavelength regime. The red box indicates the region used to identify the average scattering and fluorescence intensity.

The sum of pixel intensities over a suitable area of the detector (as indicated by a red box in figure 4.1 d) was calculated for every shot in order to sort out 'atomic pictures'. Images with intensity values falling under a certain threshold were rejected for further analysis. All remaining images were cut to the scattering region to save memory and speed up filtering algorithms.

After assuring that only patterns from clusters were left, a different type of image was sorted out: patterns which result from more than one cluster in the interaction region. The are often referred to as 'newton rings' [11]. Here, three-dimensional information is encoded in the 2D images (introduced in section 2.2.3). These types of images constitute a whole interesting field of its own. Since they are not subject to this thesis they were sorted out and neglected in the analysis.

Determination of cluster size from radial profiles

For spherical clusters the radius of the object is encoded in ring patterns of XUV photons scattered, like the size of an aperture is contained in its airy disk [31]. For this thesis an algorithm was developed for automatized extraction of the sample radius from each image and is described in the following. The intensity value at each pixel is divided by a factor of $\cos^3(\theta)$ to account for the flat detector [10, 149]. First, the radial profile was generated by averaging intensity values over scattering angle θ. The evaluated area was restricted to a sector of the image to avoid including detector artifacts. In figure 4.2 four characteristic scattering patterns and corresponding azimuthally integrated profiles are presented. In a

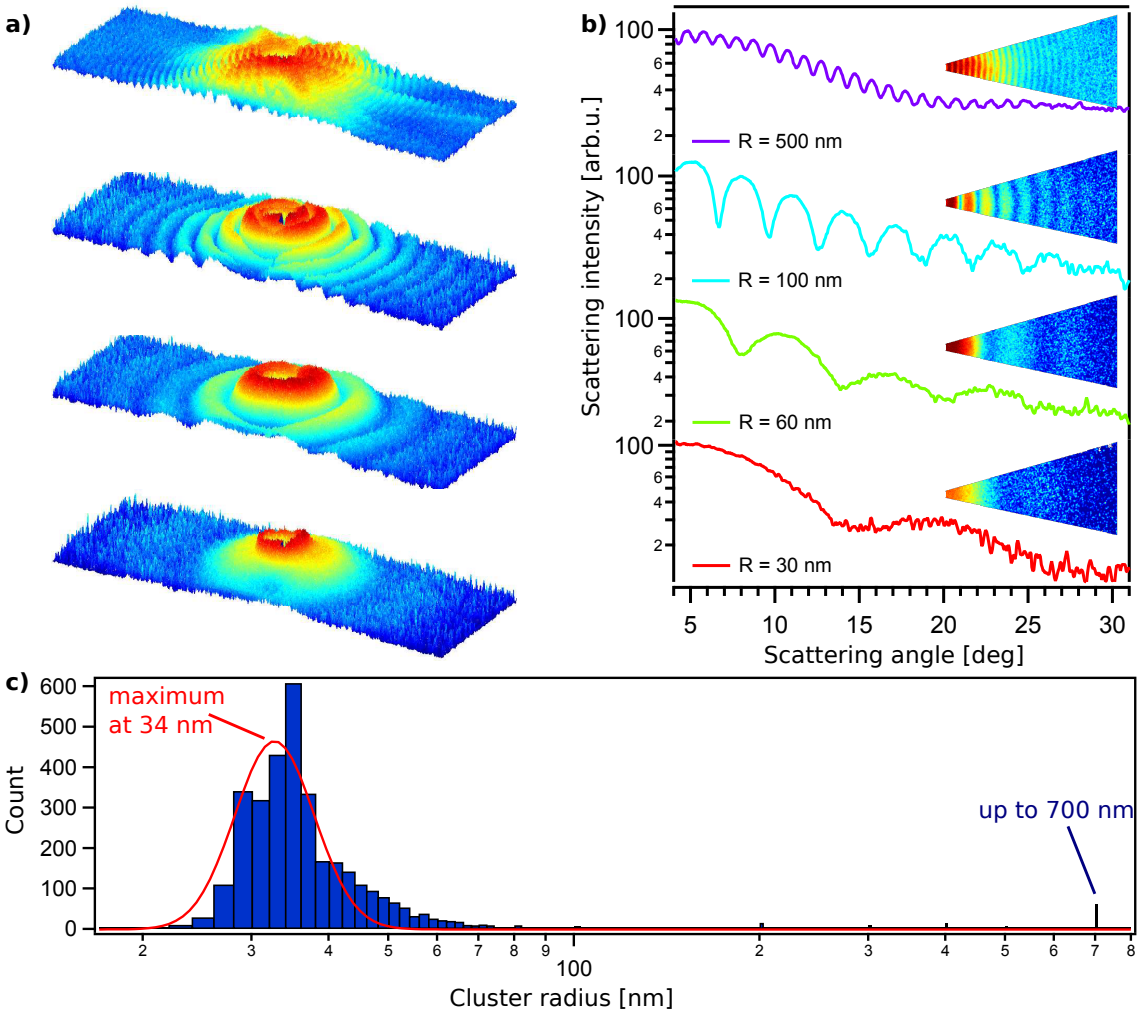

Figure 4.2: a) 3D plots of XUV scattering patterns from spherical xenon clusters with different sizes and b) their corresponding radial profiles plotted over scattering angle θ. The respective cluster size is determined from the angle of the first minimum for small clusters and from fringe spacing for large clusters. c) The histogram of cluster radii reveals a log-normal distribution with maximum at 34 nm radius and several very large clusters up to 700 nm radius.

second step, local minima and maxima of the profile were identified and their separation was determined. If the first minimum was detected the radius was simply estimated by the relation [31]

$$R = \frac{1.22 \cdot \lambda}{2 \cdot \theta_{min}} \tag{4.1}$$

with θ_{min} the angle of the first minimum. A different approach was applied if the imaged target was so large that the first minimum is overlaid by stray light or disappears in the detector hole. Profiles were generated in Mie simulations for several radii ranging from 100 up to 700 nm. Subsequently, measured data was assigned to the simulated profiles by the distance of profile minima. For cluster sizes above 700 nm radius, the interference fringes were too fine to get resolved due to the detector spacial resolution. In line with recent findings [44], smaller particles are round in shape reflected by circular scattering patterns (fig. 4.2 a bottom). Particles of larger sizes exhibit a rough surface, since they freeze out in

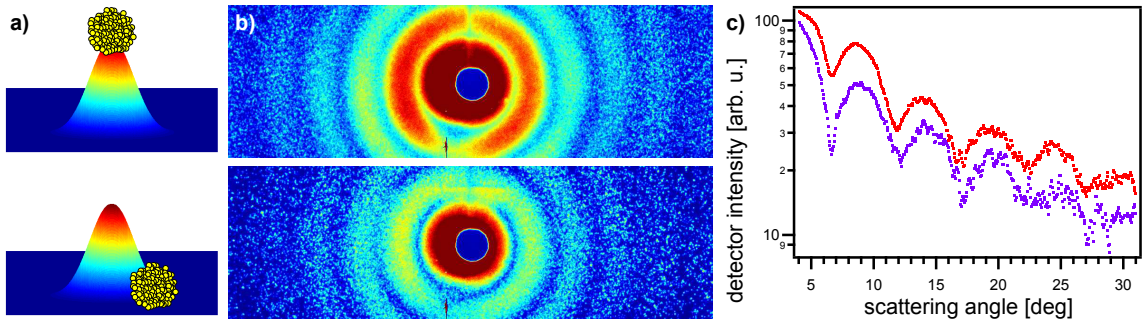

Figure 4.3: a) Illustration of a Gaussian focal density distribution with FWHM of 20 µm. Clusters in the size range of several ten to hundred nanometer can be exposed to varying positions within the focal volume. b) Scattering patterns of equally sized clusters exhibit various amounts of scattered photons. c) Radial profiles of both patterns set in direct comparison reveal a difference in intensity of scattered photons by a factor of 1.5.

non-spherical shapes during their growth by coagulation (fig. 4.2 a, see also section 2.2.3).

For xenon clusters measured in the 2011 experiment, the radii of all single clusters were determined from XUV only and XUV/IR pump-probe data. They are depicted as histogram in figure 4.2 c. A log-normal distribution with maximum of 34 nm radius was fitted. This result corresponds well with pertinent scaling laws [28]. Xenon clusters of 34 nm radius consist of $N \approx 2.6 \cdot 10^6$ atoms while the scaling law predicts $\langle N \rangle = 2.0 \cdot 10^6$ for the expansion conditions applied in the experiment ($p = 9.8$ bar, $T = 180$ K, $d_{eq} = 2105$ µm). Extraordinarily large sizes with radii of several hundreds of nm originate from valve closing in pulsed cluster generation as stated in 2.1.3 [44]. Due to the missing detector resolution the size of clusters larger than 700 nm cannot be resolved and are indicated in the histogram (fig. 4.2 c) as 700 nm radius clusters.

As a matter of course this procedure only works for patterns recorded from particles irradiated with a short-wavelength pulse. For IR data the radius cannot be extracted due to missing minima in forward scattering direction. All experiments were performed in one long experimental run with stable cluster source conditions, switching back and forth between laser settings to ensure that the cluster size distribution is alike for data taken with IR pulses only or in IR/XUV pump-probe configuration.

Experienced power density dependent scattering intensity

The clusters range in a size scale of several tens to hundreds of nanometers. In comparison, the focus spot of the FEL beam was about 20 µm FWHM [111]. Hence, each cluster experiences a different power density dependent on its position within the laser focus (see figure 4.3 a).

The exposed power density a cluster experiences was $4.1 \cdot 10^{14}$ W/cm^2 in the focal maximum of the FEL pulse. It drops to zero outside the wings. The main quantity of the clusters are hit in the sides [97]. Exemplary two CCD images with equal ring spacing from clusters of same radius are presented in figure 4.3 b. The slopes of both patterns are set in direct comparison in figure 4.3 c. They reveal a disparity in signal intensity by a factor of 1.5. The

difference in brightness is a direct indication for the discrepancy in scattered photons due to the different extend of irradiation. A direct determination of absolute power densities from an averaged detector intensity is not possible since clusters of different size scatter with varying strength. Additionally, the electronic configuration within the cluster changes with FEL impact, which results in a change in the scattering-profile slope [10]. The overall amount of scattered photons increases with higher exposure power density value. Therefore, the method of filtering for sample radius and subsequently for detector intensity has proven to be a versatile tool to investigate cluster-size and power-density dependent nanoplasma dynamics [101, 45].

This method is not applicable for images recorded from particles irradiated with 800 nm light only. The CCD images exhibit homogeneously distributed fluorescence instead of ring patterns (see figure 4.1 d). Still the screen intensity gives a hint about the rage of the size of exposed cluster and impacted laser intensity. An earlier experiment with photonenergy-sensitive pnCCD detectors revealed that with raising power density of an infrared laser, the fluorescence yield increases due to higher ionization and subsequent radiative decay [46]. Furthermore, larger clusters scatter more intensely. Therefore, the assumption is justified that the brightest CCD images result from very large clusters hit in the focal center.

4.1.2 Filtering by ion time-of-flight spectrum

Ion TOF spectra from atomic gas and from clusters differ significantly. In figure 4.4 three exemplary ion spectra of xenon irradiated by XUV pulses only are shown. Single-shot atomic data is plotted in figure 4.4 a. It exhibits pronounced peaks which are even isotope resolved. Singly ionized xenon is almost not detected due to Auger processes and missing recombination as already discussed in section 2.2.1. Charge states up to Xe^{9+} are detected for a focal power density of $4.1 \cdot 10^{14}\,W/cm^2$. Cluster spectra are presented in figure 4.4 b and c. The peaks are broadened towards shorter flight times from accelerated cluster ions which override the residual gas peaks. The assignment of single charge states becomes difficult because the peaks merge into each other. For a cluster hit in the focal wing Xe^{1+} is the most pronounced peak (fig. 4.4 b), while for a strongly exposed cluster the distribution is shifted to higher charge states (fig. 4.4 c). Sorting according to ion yield at flight times where no atomic signal is detected (indicated by the light red areas in fig. 4.4) is a very reliable filter to distinguish cluster data from atomic data.

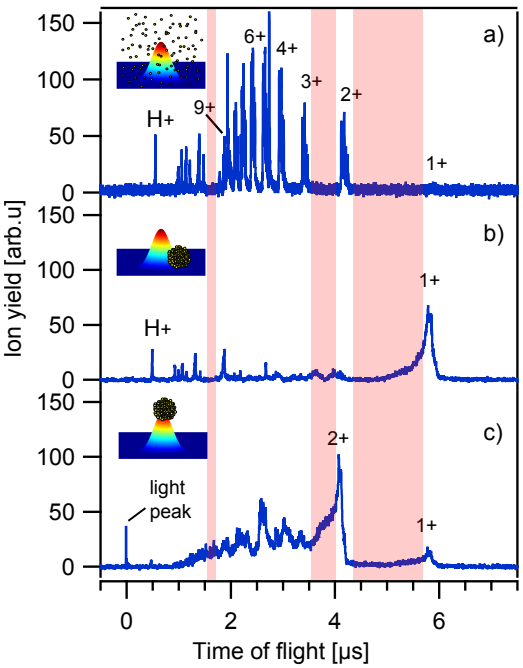

Figure 4.4: Single-shot ion time-of-flight spectra of (a) xenon atoms and (b+c) single xenon clusters exposed to a 91 eV FEL pulse. Spectra differ significantly. By filtering on characteristic features ($E_{kin} \gg 0$, areas marked in red) atomic and cluster data can be reliably separated.

In addition to ions, scattered light under 90 degrees was collected by the MCP of the TOF spectrometer causing a *light peak* in the spectrum. Compared to the ions arriving at the detector on a nano- to microsecond timescale, the light is detected almost instantaneously. It was therefore used for calibration of the spectra to zero flight time. Further, the light peak yield can be utilized to measure how well the cluster was hit in the focal area of the laser pulse. Graph 4.4 b from a cluster exposed to the focal wing does not show a light peak. However, a light peak is present in the spectrum of a cluster encountering the focal center (4.4 c). While the scattering detector detects light from a broad region in the experimental chamber, the TOF spectrometer only collects photons originating from the interaction region, due to a small aperture in the drift tube. Since it is a time-resolved signal the light peak also shows a fluorescence tail, especially in pump-probe data taken at late delay times (cf. chapter 4.4). This helps to distinguish scattering and fluorescence signal, which is not possible with the scattering detector.

4.2 Universal dynamics in large cluster nanoplasmas

The previous chapter explains how single-shot single-particle data was prepared and sorted for further analysis. Based on that, this chapter focuses on the complicated dynamics of clusters induced by irradiation with an ultrafast and highly brilliant laser pulse. With the method of single-cluster imaging with coincident ion spectroscopy, it became possible for the first time to disentangle the contributions from various experimental parameters to laser-cluster interaction with unprecedented detail. In this chapter, several comparative analyses focus on the expansion mechanism of single, large clusters. First, insights into the affect of cluster size and laser intensity are given by the analysis of a single-shot experiment on extremely large xenon clusters excited by 13.6 nm light discussed in section 4.2.1. Subsequently, in section 4.2.2 the material response is compared for xenon, argon, and silver clusters of similar diameter under similar laser conditions by investigating their ion kinetic energies. In a third study, the influence of the laser photon energy is examined in detail in section 4.2.3, by means of ion spectroscopy on xenon clusters in single XUV and single IR pulses respectively.

4.2.1 Ionization and ionic motion in XUV irradiated xenon clusters

The affect of laser intensity and cluster size on the laser-matter interaction is in principle identified from theoretical models [49, 50] as introduced in chapter 2.3. With increasing cluster size and laser intensity hydrodynamic expansion becomes more probable, while with smaller cluster size and laser intensity the clusters are more likely to disintegrate in Coulomb explosion [52]. Which of the two is the prevailing expansion mechanism can be estimated by the frustration parameter α (see equation 2.50). It is given by the ratio of photoactivated n_{tot} to photoionized n_{out} electrons [52]. In the case of xenon clusters in XUV light, where the photon energy exceeds the ionization threshold, cluster atoms are photoionized and field driven effects are either not present or negligible.

In this section, large xenon clusters exposed to 91 eV laser pulses will be analyzed in size and focal intensity resolved manner. As introduced in section 4.1, examined cluster sizes are ranging between 25 and 1000 nm and the peak FEL pulse power density holds

$4.1 \cdot 10^{14}\,\mathrm{W/cm^2}$. Upon XUV photon impact the amount of outer-ionized electrons before frustration n_{out} is calculated with equation 2.51 in the *photon dominated regime*. The maximal kinetic energy is hereby not defined by the difference between photon energy and ionization potential ($\hbar\omega - E_{ip}$), but by the Auger electrons with $\approx 32\,\mathrm{eV}$ [42, 52]. Therefore, we get

$$n_{out(\mathrm{photon})} = 32 \cdot \frac{4\pi\epsilon_0}{e^2} \cdot R = 22.22 \cdot R\,[\mathrm{nm}] \tag{4.2}$$

For the entire cluster-size range, n_{out} varies between ≈ 550 and ≈ 22200 electrons. Note that secondary processes like ionization heating, electron thermalization, and electron-impact ionization are neglected in this calculation. The total amount of outer ionized electrons most probably exceeds the values calculated here.

The amount of overall (outer- and inner-) ionized electrons n_{tot} can be determined by absorption cross-sections with equation 2.51 introduced in chapter 2.3.3. However, in 13.6 nm wavelength light very large clusters are optically thick and the laser cannot penetrate the entire particle. The absorption length of xenon is $l_{abs} = \lambda/(4\pi\beta) = 24\,\mathrm{nm}$ (see equation 2.18) with $\beta = 0.0445$. Therefore, a simple calculation via atomic absorption cross-section might give misleading results. Instead, n_{tot} can be simply approximated by geometric cross-sections. It is estimated that every atom is charged twofold by photoionization with succeeding Auger excitation, as long as the number of photons impacting on the laser is larger than the number of atoms in the cluster [66]. This is the case for a laser pulse with focal power density of $4.1 \cdot 10^{14}\,\mathrm{W/cm^2}$ where the number of photons is estimated as $n_{Photon} = 1.7 \cdot 10^{10}$ [45]. The number of atoms in a xenon cluster of solid state density is calculated by

$$N = \frac{4\pi\rho R^3}{3m_a} = 72.67 \cdot (R[\mathrm{nm}])^3 \tag{4.3}$$

with $\rho = 3.781 \cdot 10^3\,\mathrm{kg/m^3}$ and $m_a = 131.293 \cdot 1.660 \cdot 10^{-27}\,\mathrm{kg}$ for xenon clusters (compare equation 2.12). This results in $N = 1 \cdot 10^6$ and $N = 7 \cdot 10^{10}$ for clusters with 25 and 1000 nm radius respectively. Only a very small fraction of all excited electrons leaves the cluster. The frustration parameter is calculated as

$$\alpha = \frac{n_{tot}}{n_{out}} = \frac{2N}{n_{out}}. \tag{4.4}$$

For the experimentally detected cluster-size range the frustration parameter results between $\alpha \approx 2000$ and $\alpha \approx 3 \cdot 10^6$. It is deep in the nanoplasma regime ($\alpha > 100$) and therefore the expansion is expected to be far in the hydrodynamic limit for all data analyzed in this section.

While the nanoplasma model was established for clusters exposed to infrared laser light, it also holds for clusters in the XUV regime. This was demonstrated in earlier experiments [93, 150] and theoretical calculations [52]. The majority of activated electrons resides quasi-free in the cluster compound as the approximation above shows. These charges redistribute to lower the total energy stored in the clusters [56, 151]. The electrons move towards the center of the sample where they screen the positive cluster charges while at the surface the ions stay partially unscreened. Thus a net-neutral core with a highly charged surface is built.

The dense, cold nanoplasma in the net-neutral core allows for recombination via many-body collisions. At the same time hydrodynamic expansion takes place upon the pressure

of the energetic quasi-free electrons. The cluster expansion starts at the outer surface and proceeds layer-wise towards the cluster center [52]. While an ion at the cluster surface is strongly accelerated during dissociation, an ion at the center is screened by the surrounding electrons and hardly obtains kinetic energy. Therefore, the kinetic energy distribution, detected e.g. in ion TOF spectra, mirrors the spacial distribution of the ion within the cluster [151]. Recombination processes are manifested in TOF spectra by a missing of low kinetic energy contributions in higher charge states, as well as by a strong contribution of lower charge states. While these features predicted by theory are washed out in ion spectra detected on ensembles of clusters, they are evident from single-cluster ion spectra as will be demonstrated in the following section.

Expansion signatures in size and intensity characterized single-cluster ion spectra

Here, an extended analysis of scattering patterns and ion TOF spectra from very large, single xenon clusters in highly intense, ultrashort (100 fs) XUV pulses with 91 eV photon energy is presented. A similar study was performed and analyzed in previous work [45]. It gives a good description on how to analyze single-shot coincident measurements. The results of this study are the fundamentals for further investigation in this thesis and its understanding is a prerequisite for the following sections. Data analysis methods developed in [45] were applied to the data set collected for this thesis and are presented in the following.

After determining the cluster-size distribution (see section 4.1.1), single clusters in a size range between 100 nm and 1 µm radius were picked for further investigation. They were grouped in three categories with radii of (200 ± 100) nm, (500 ± 200) nm, and larger than 700 nm. Three representative scattering patterns revealing the size of the investigated clusters are presented in figure 4.5 a. Within the three groups all shots were sorted according to the intensity of the recorded scattering pattern. It gives an indication of the sample position within the Gaussian focal distribution of the laser pulse and therefore the exposure power density (see section 4.1.1). Ion spectra were sorted accordingly and several selected single-cluster ion spectra are shown in figure 4.5 b.

Several features in the sorted single-cluster ion TOF spectra illustrate power density and cluster size dependent effects in nanoplasma dynamics. Within one cluster-size range a redistribution from lower to higher charge states takes place with rising exposure power density (fig. 4.5 b). The ion charge-state peaks shift towards shorter flight time and become narrower for similar laser intensity but increasing target radius. This indicates that the kinetic energy of the ions rises and develops towards an increasingly mono-energetic distribution. The kinetic energy is a fingerprint of the ion position within the cluster [151]. Therefore, a narrow flight time distribution for one charge state is a strong indication that these ions originate from a rather narrow cluster shell. Peak truncations at short flight times - thus lower kinetic energies - point towards recombination processes taking place in the dense cluster nanoplasma [52].

However, charge-state abundance and kinetic energy are not directly resolved in TOF spectra. Accounting for spectrometer transmission and conversion to energy scale are necessary to directly extract kinetic-energy distributions from the recorded TOF spectra.

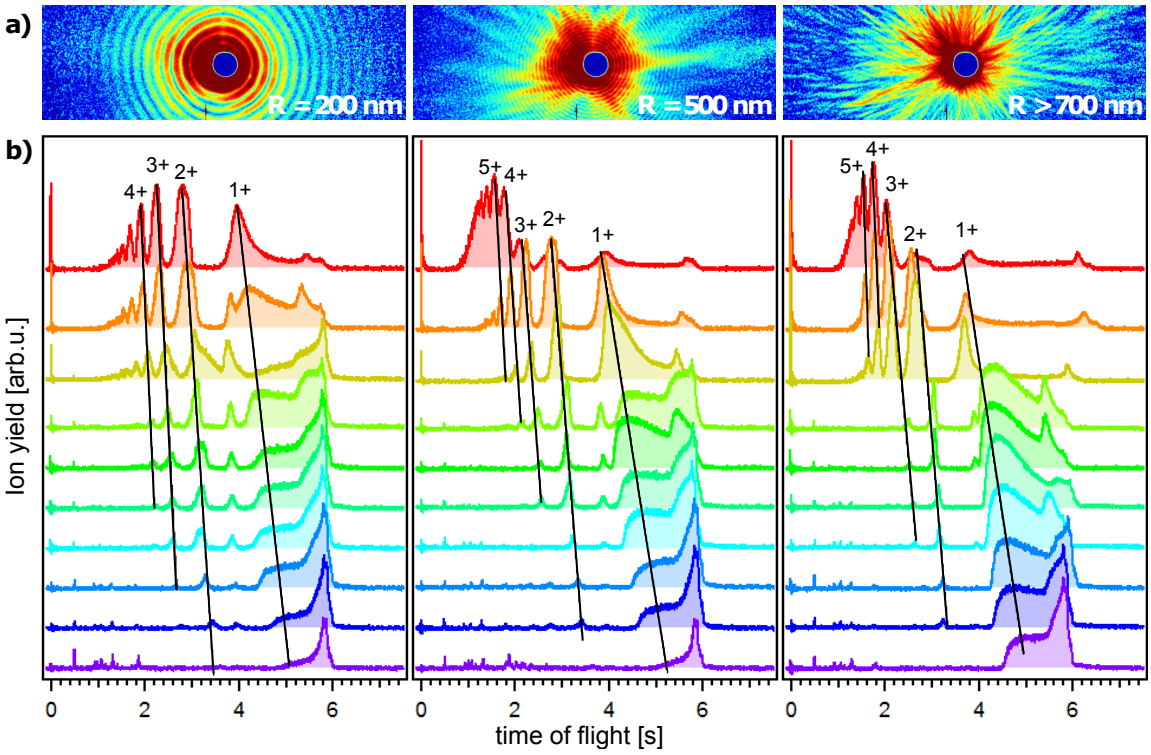

Figure 4.5: a) Single-cluster scattering patterns of single xenon clusters with about 200 nm and 500 nm radius, extracted from the fringe spacing in the pattern. in the last image the fringes are too fine to be resolved due to the detector resolution. This indicates that the cluster is larger than 700 nm in radius. b) Ion time-of-flight spectra sorted first on cluster size and within one range to assigned laser power density. The peak power density in the beam is $4.1 \cdot 10^{14}$ W/cm^2. While higher charge-state yields rise dramatically with intensity the influence of the change in size is relatively small.

A full characterization of the spectrometer used for this thesis is given in literature [152, 45]. In principle, every single ion spectrum needs to be simulated for a full charge-state resolved kinetic-energy distribution. This procedure is extremely time consuming while the information gain is relatively small. Instead, only the central kinetic energy in dependence on the charge state is investigated here. The central kinetic energy is extracted from every TOF spectrum depicted in figure 4.5 by polygon fits and subsequent adjustment to the transmission function of the spectrometer as described in [45]. Plotted over charge state in figure 4.6, a linear dependence is prominent for all shots.

Up to date there is an ongoing debate how the correlation of kinetic energy and ion charge can contribute to distinguish between both limiting expansion scenarios: Coulomb explosion and hydrodynamic expansion. It is often claimed that the mean kinetic energy $\langle E \rangle$ scales linear with the ion charge in the case of hydrodynamic expansion, but quadratic for Coulomb explosion:

$$\langle E_{Hydro} \rangle \propto q \quad , \quad \langle E_{Coul} \rangle \propto q^2. \tag{4.5}$$

Several experiments on ensembles of clusters used this dependency to explain their explosion mechanics [90, 91, 55, 93]. However, from Monte Carlo classical particle-dynamics simulations of a cluster undergoing Coulomb explosion, a quadratic dependence was only

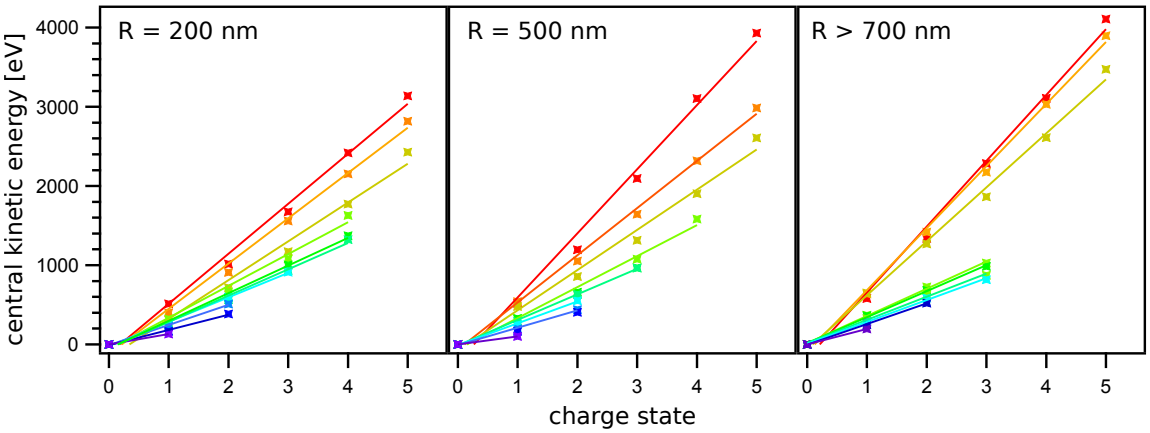

Figure 4.6: Central kinetic energies over charge state extracted from the TOF spectra presented in figure 4.5. The color coding is maintained. With increasing exposed power density the central kinetic energies are increasing and higher charge states appear. A linear dependence is found for all spectra indicated by straight lines.

found for low charge states, while for higher charge states it was linear [92]. There, the quadratic behavior was attributed to an artifact from the laser focal averaging. More recent simulations using molecular dynamics calculations investigate single clusters [52]. The authors suggest that ion spectra from clusters undergoing Coulomb explosion and hydrodynamic expansion do not significantly distinguish if recombination processes are taken into account. However, the ion spectra contain only charge states up to 4+ and authors do not comment on the linear/quadratic behavior discussion.

With the single-cluster ion spectra presented in this chapter it becomes possible to attribute a linear correlation of mean kinetic energy and ion charge (fig. 4.6) to cluster in hydrodynamic expansion (estimated with equation 4.4) without influence of laser power density and cluster size averaging. Since the experiments performed here on very large clusters in the XUV regime reside deep in the nanoplasma regime, no comment can be given on the behavior for clusters undergoing Coulomb explosion. Therefore, single-cluster imaging experiments in coincidence with ion spectroscopy has to be performed on smaller clusters with higher photon energy, like it is available at the hard x-ray FELs, e.g. the LCLS or SACLA.

4.2.2 Relationship between material characteristics and ionization dynamics, studied in a comparison of xenon, silver and argon clusters

The electron temperature and density inside an XUV laser excited cluster is strongly influenced by the particle material. The excess energy, e.g. the remaining kinetic energy of a photoelectron after ionization, varies for different chemical components due to the respective electronic configuration. An attempt is made to understand the role of the electronic configuration for large clusters in XUV light. Therefore, the well studied ion spectra of individual xenon clusters are compared with TOF spectra from other materials, taken under the same free-electron-laser conditions (wavelength: 13.6 nm, photon intensity: 150 µJ, focal spot size: 20 µm and pulse length: 100 fs).

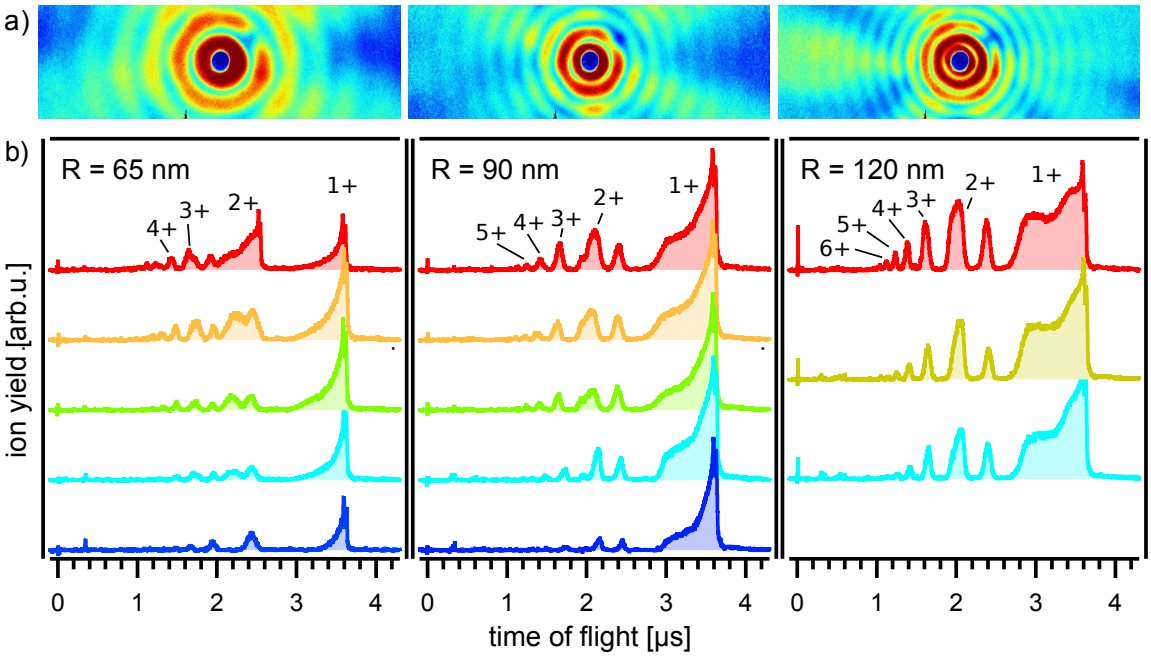

Figure 4.7: Ion time-of-flight spectra of silver clusters, sorted by particle radius (independent of the exact cluster shape) into groups of (65 ± 12.5), (90 ± 15), and (120 ± 15) nm. Within one size range spectra are arranged for exposed power density with a maximum of $4.1 \cdot 10^{14}\,\mathrm{W/cm^2}$. Characteristic features are prominent, like an increase of high charge-state yield with laser focal power (bottom to top) and a narrowing of charge-state flight-time distributions with cluster size (left to right).

Xenon is a special case for 91 eV photon energy because of its $4d$ giant resonance resulting in high photoionization cross-sections (see chapter 2.3.1). The initial ionization proceeds from inside out, starting in the $4d$-shell followed by the $4s$, $5s$, and $5p$ shell [66]. Argon is chosen for comparison since it is also a rare-gas and clusters are grown under similar conditions. It is likewise Van-der-Waals bound, but has a different electronic configuration and therefore no resonant energy absorption at 91 eV photon energy. The electron excess energy in argon ($E^* = 22\,\mathrm{eV}$) is higher than in xenon ($E^* = 20\,\mathrm{eV}$) [42]. This leads to a higher electron temperature and lower quasi-free electron density within the cluster. Contrary to xenon, argon is ionized outside in. Another juxtaposition is made with silver because it has metal bonding and already delocalized electrons in the ground state. In comparison with xenon it has similar energy levels, leading to similar electron temperatures. Ionization proceeds likewise from inside out. Xenon, argon, and silver clusters are expected to have a different response to the light pulses because of different photoionization cross-sections and atomic electron levels.

In a collaboration with the group of Prof. Meiwes-Broer from the University of Rostock first scattering [12] and ion spectroscopy experiments were performed on large silver clusters at FLASH. Due to a different cluster generation mechanism [153], the silver particles are smaller than the xenon clusters and statistics are low for largest clusters. Like with xenon in the previous section, silver shots are sorted according to sample radius and within one size bucket sorted on intensity as presented in figure 4.7. Spectra are shown for radii ranging between 65 and 120 nm and exposure power densities up to $4.1 \cdot 10^{14}\,\mathrm{W/cm^2}$. Comparison

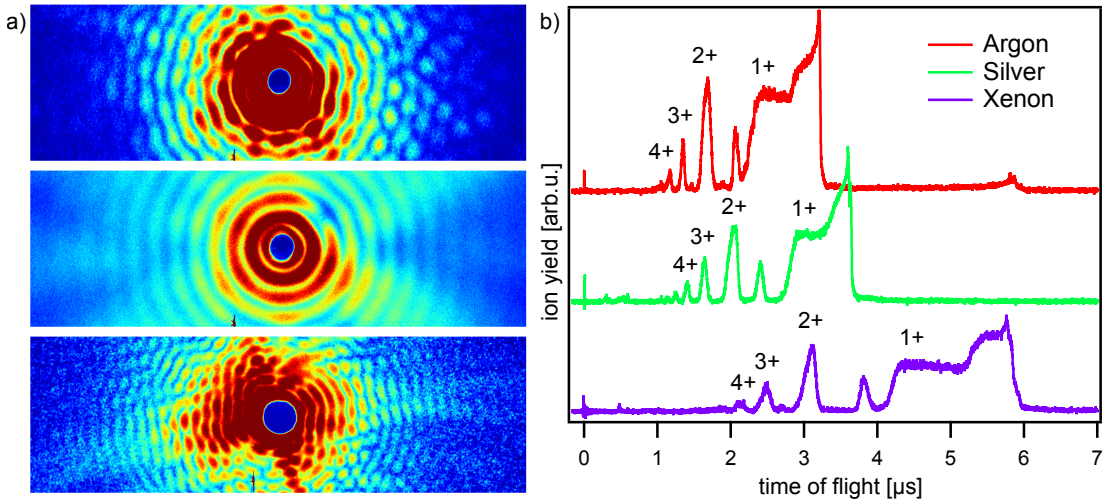

Figure 4.8: (a) Scattering patterns from single argon (R = 160 nm), silver (R = 120 nm) and xenon (R = 280 nm) clusters exposed to a 100 fs XUV pulse. (b) Corresponding single-cluster ion time-of-flight spectra. Despite different flight times due to particle mass, all three spectra exhibit similar features. Charge states up to 5+ are detected and peak widths for higher charge states are rather narrow.

of the spectra in figure 4.5 and 4.7 reveals that ion spectra are different for xenon and silver particles, but the overall size and intensity dependence is similar. With increasing cluster radius charge state peaks get narrower and more pronounced and higher charge-state yields increase. Within one size range, the charge-state distribution shifts towards higher values with increasing exposure power density. The fact that these characteristics are equal for xenon and silver targets points towards very similar ionization processes taking place independent of the bond type, the target geometry, and exact ground state electron configuration.

Another juxtaposition is made with argon clusters. For argon, size and intensity resolved analysis is disregarded for redundancy reasons. Rather a single ion TOF spectrum is set in direct comparison with a single spectrum from a xenon and a silver cluster. As presented in figure 4.8 all three images show comparable cluster radius and exposure power density. Flight times are slower for heavier particles, and therefore the time axis differs for varying materials, but the main features in the spectra are quite similar. All three particles are up to fivefold ionized and, apart from the first charge state, flight-time distributions of single charge-state peaks are rather narrow.

Since ion spectra mirror the final state after cluster fragmentation, no information about initial cluster charging can be directly extracted from the spectra. However, the cluster expansion dynamics and the resulting ion kinetic energies are determined by energetics of the nanoplasma, which itself results from the initial cluster charging process. Photoionization energies are different for xenon, silver, and argon (see table 4.1) and therewith the following absorption cross-sections and Auger-decay rates. While xenon atoms exhibit the 4*d* giant resonance around 91 eV, resulting in high absorption cross-section (23 Mbarn), photoionization processes in silver and argon are without any resonances. Their absorption cross-sections at 91 eV photon energy are correspondingly small as can be seen from the comparison in table 4.1.

Table 4.1: First three ionization energies (I_P in eV) [32] and absorption cross-sections at 91 eV (σ in Mbarn) for xenon, silver, and argon atoms respectively [154]. Clusters sizes extracted from figure 4.8 a respectively and corresponding total atom numbers N. Calculation of the amount of outer photoionized electrons n_{out} upon 91 eV pulse impact and the corresponding ratio from total atom number to outer photoionized electrons.

	E_{ip} [eV]	E_{ip}^{1+}	E_{ip}^{2+}	σ [Mb]	R [nm]	N	n_{out}	N/n_{out}
Xenon	12.1	21.0	31.1	23	280	$1.6 \cdot 10^9$	5200	$3.1 \cdot 10^5$
Silver	6.5	20.8	35.5	2.03	120	$4.2 \cdot 10^9$	800	$5.2 \cdot 10^6$
Argon	15.76	27.63	40.74	1.2	160	$7.7 \cdot 10^8$	2300	$3.3 \cdot 10^5$

Despite varying initial ionization, for all materials only a small number of electrons n_{out} gets outer ionized before photoionization frustration sets in as calculated from equation 2.51. The calculated numbers for clusters of the sizes presented in figure 4.8 are listed in table 4.1. Due to the very large cluster sizes initial ionization only contributes marginally to the overall ionization and nanoplasma effects take the lead. Ionization heating and electron impact ionization become dominant [105]. In a comparative paper where ionization of silver and argon is calculated [84], electron impact ionization effects play a major role. With increasing cluster size, the mean ionic charge number increases. Hence, for larger clusters the impact ionization is more efficient during the cluster expansion compared to smaller clusters. The ionization processeses in the nanoplasma have to have the same impact as final spectra (fig. 4.8 b) show a high resemblance. Many nanoplasma processes are independent of target material: electrons migrate to the cluster center, while an outer shell comes off since it remains unscreened. The narrow distribution of the charge states again hints on the explosion of a thin shell in hydrodynamic expansion. It seems that with increasing cluster size, the amount of trapped electrons plays a major role. Plasma dynamics become so dominant that the cluster dynamics become universal independent of the particle material. This behavior is known from large clusters exposed to laser pulses in the infrared regime [53]. Large xenon clusters in IR light will be the subject of the next section.

4.2.3 Multistep vs field ionization: XUV and IR irradiated clusters

Above, expansion dynamics were examined in dependence on laser focal power density, cluster size, and cluster component. In this section, cluster expansion is addressed regarding illumination with a laser pulse of different photon energy. Therefore, ion spectra from large xenon clusters exposed to near-infrared laser pulses ($\lambda = 800\,\text{nm}$, $I = 1.1 \cdot 10^{14}\,\text{W/cm}^2$, $\tau = 80\,\text{fs}$, see also section 3.2.2) are analyzed and set in comparison to the previously analyzed spectra from clusters excited by extreme-ultraviolet laser pulses ($\lambda = 13.6\,\text{nm}$, $I = 4.1 \cdot 10^{14}\,\text{W/cm}^2$, $\tau = 100\,\text{fs}$). In both cases cluster charging proceeds through different ionization processes. In contrast to 91 eV XUV photons, direct single-photon ionization of xenon atoms is not possible for IR photons of 1.55 eV photon energy. At least eight photons are necessary for multi-step ionization of a single neutral xenon atom. In the infrared regime, field driven effects like tunnel ionization are dominant.

To investigate the influence of initial ionization regime on cluster expansion, ion TOF spectra of clusters in XUV pulses are now compared with spectra from clusters in IR

pulses. As stated earlier, in contrast to data recorded upon XUV illumination, size and intensity resolved sorting is not possible for images and ion spectra upon IR excitation due to missing interference fringes in scattering patterns (compare figure 4.1 d). Nevertheless, the cluster size distribution should be equal to the one determined with XUV scattering - with radii between 25 and 1000 nm and maximum distribution at 34 nm radius - since xenon clusters are produced under the same expansion conditions (see figure 4.2 c for cluster size distribution upon XUV irradiation). The intensity of the scattering images only gives limited information. Images with moderate intensity might result from a large cluster hit in the focal wing as well as from a small cluster exposed to the focal center. Therefore, the most reliable filter is sorting for highest detector intensity which results from largest clusters located in the focal center.

To map the higher value ends of size and intensity distribution, the brightest 200 shots out of a total of 5000 shots are subdivided in five groups. Ion spectra coincidentally recorded with the 10 brightest scattering images are averaged for XUV and IR exposure respectively and plotted in figure 4.9 a. TOF spectra for decreasingly bright pictures are averaged and presented in graphs 4.9 b-e. With increasing photon detector intensity, the charge distributions shift towards smaller flight times in IR and XUV spectra. This indicates an increasing energy absorption independent of laser wavelength.

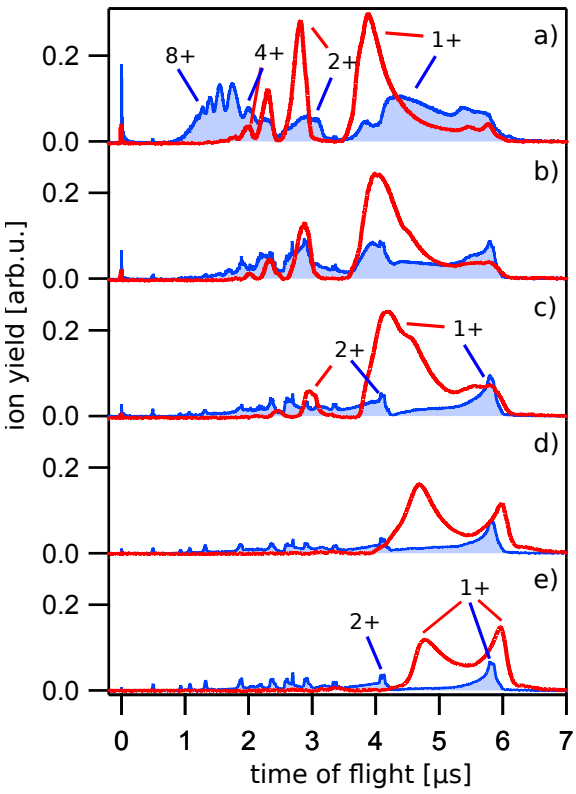

Figure 4.9: Averaged ion time-of-flight spectra from single xenon clusters, irradiated either with IR light (red graphs) or XUV light (blue graphs). Average of (a) 1 to 10, (b) 11 to 25, (c) 26 to 55, (d) 51 to 100, and (e) 101 to 200 brightest respectively. Cluster sizes can only be determined from corresponding single scattering patterns upon XUV radiation, but not upon IR irradiation.

Apart from this common effect, significant deviations between main features in graphs from XUV and IR excitation are prominent. Detected charge states are higher for XUV exposure. This is most likely a result from different initial cluster charging mechanisms, namely photoionization for 91 eV and tunnel ionization for 1.55 eV photon energy, as well as from different laser power densities ($I_{\mathrm{XUV}} = 4.1 \cdot 10^{14}\,\mathrm{W/cm^2}$ and $I_{\mathrm{IR}} = 1.1 \cdot 10^{14}\,\mathrm{W/cm^2}$). For IR spectra the Xe^{1+} peak is the most prominent. It exhibits higher kinetic energies than for the XUV spectra. For xenon clusters in XUV light ionization starts from inner shells proceeding to the valence levels via single photon absorption. The opposite holds for the infrared case, with ionization from the outer to inner levels. Therefore, lower charge states are produced first and higher charge states are generated by subsequent heating and particle collisions.

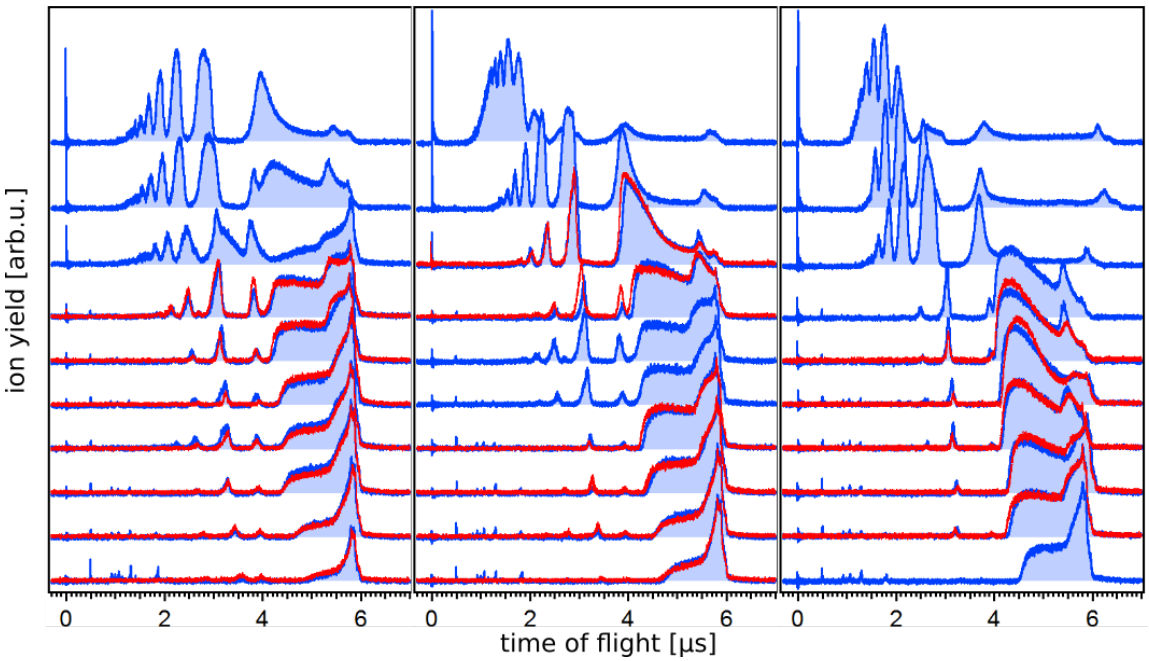

Figure 4.10: Blue graphs: Single-cluster ion time-of-flight spectra from xenon clusters irradiated with XUV pulses with peak power density of $I_{\mathrm{XUV}} = 5 \cdot 10^{14}\,\mathrm{W/cm^2}$, sorted for cluster size and exposed power density, as already presented in figure 4.5. Red graphs: Matching ion spectra from clusters exposed to IR pulses with peak power density of $I_{\mathrm{IR}} = 1 \cdot 10^{14}\,\mathrm{W/cm^2}$. Note that the size for the clusters in IR light is unknown.

Although sorting for cluster size and laser power density is not possible for single-cluster IR spectra, their investigation can uncover characteristics hidden in averaged spectra. Comparison with single-shot XUV spectra exhibits an unexpected similarity for several shots. Blue graphs in figure 4.10 present the size and intensity sorted single-cluster ion spectra from xenon clusters under XUV radiation already plotted in figure 4.5. With the help of a filter that compares all recorded spectra and subsequently sorts for similarity, spectra from IR excited clusters are plotted on top of the most similar spectra from XUV irradiated particles[1]. In direct comparison single spectra from clusters irradiated by XUV or IR pulses reveal astonishing resemblance. Even though the initial excitation mechanisms of the two pulses with different photon energies differ drastically, the overall deposited energy seems to be the same resulting in similar cluster expansion. Due to the alike appearance of the ion distributions, the linear increase in central ion kinetic energy over charge state is equal. This indicates that large xenon clusters in strong IR pulses likewise undergo hydrodynamic expansion of outer shell layers as predicted from earlier calculations.

The mechanism of initial ionization seems to be secondary, as long as a certain amount of quasi-free electrons is trapped inside the cluster and the major part of the cluster is turned into a nanoplasma. This is most likely the case for large clusters. Therefore, from a certain particle radius on the expansion dynamics might be dominated by the large cluster size instead of the laser photon energy. Independent of the regime of initial cluster charging, the outer particle shell blisters off in hydrodynamic expansion and a recombined center

[1] Note that for highest intensities no matching shots are found, which is due to the lower power density of the IR laser.

core remains. The detected ion distribution results in the same charge states with the same kinetic energy distribution.

To conclude, similar expansion dynamics were found for large xenon, argon, and silver clusters after the interaction with a strong XUV pulse. This suggests that the exact electronic configuration of the cluster seems to play a minor role for the particle evolution after nanoplasma formation. Similar dynamics were also found when large xenon clusters were irradiated with strong IR pulses. Independent of the initial ionization regime (photon dominated in XUV light and field driven in IR light), the dynamics seem to be mainly determined by the large cluster size and similar exposed power density ($I_{\mathrm{XUV}} = 4.1 \cdot 10^{14}\,\mathrm{W/cm^2}$ and $I_{\mathrm{IR}} = 1.1 \cdot 10^{14}\,\mathrm{W/cm^2}$). Therefore, it is not a single cluster or laser parameter that gives information about the final explosion process, but the ratio of outer to inner ionized electrons. Hence, light-matter interaction under strongly different initial situations can lead to astonishingly similar final results.

While recorded ion TOF spectra can give insight about the final state of the cluster after fragmentation, the plasma evolution in intermediate states stays unidentified. The cluster density is scanned in a dual-pulse experiment to trace the plasma disintegration step-by-step, which is subject to the next section.

4.3 Probing collective electron oscillations in pre-expanded clusters

Clusters are systems which exceed atoms and solids in efficient energy absorption from laser radiation [47]. This effect is further drastically increased in resonance condition. Here, the electron cloud inside a cluster is collectively oscillating driven by an external laser field as demonstrated in several experiments on rare-gas and metal clusters [80, 155, 156]. This so-called Mie resonance, introduced in chapter 2.2.2, is met when the frequency of the collective electron oscillation ω_P is close to the laser frequency ω_L [38]. The resonance Mie plasmon frequency is then given by $\omega_{Mie} = \omega_p/\sqrt{3} \approx \omega_L/\sqrt{3}$. Solid density xenon clusters in IR fields are overcritical. This means that the density dependent plasmon oscillations are faster than those of the driving laser field. Matching condition between laser and plasmon frequency is reached by reducing the particle density due to the laser-induced expansion of the cluster. For very large clusters, the evolution time until resonance condition with an infrared pulse is met often exceeds the ultrashort pulse length. In this case the powerful concept of the pump-probe technique can be applied to push the experiment to longer timescales.

Since the Mie resonance occurs for a certain cluster density, the delay time Δt at which it occurs gives information about the expansion speed of the disintegrating cluster. This fact is used here to further investigate the expansion behavior of large xenon clusters after XUV excitation. In dual-pulse configuration an FEL pulse ($13.6\,\mathrm{nm} \mathrel{\widehat{=}} 91\,\mathrm{eV}$, $100\,\mathrm{fs}$, $4.1 \cdot 10^{14}\,\mathrm{W/cm^2}$) formed a nanoplasma, induced plasmons, and triggered the free target expansion. With a temporally delayed Ti:Sa pulse ($800\,\mathrm{nm} \mathrel{\widehat{=}} 1.55\,\mathrm{eV}$, $80\,\mathrm{fs}$, $1.1 \cdot 10^{14}\,\mathrm{W/cm^2}$) the Mie resonance condition was probed. The particle's characteristic expansion time Δt_{char} required for frequency matching is radius dependent as introduced in chapter 2.2.2. The delay between the pulses was scanned in a wide range from $1\,\mathrm{ps}$ up to $1500\,\mathrm{ps}$ to

account for the large cluster size distribution with radii from 25 nm to 1 µm. The initial state of the single object was imaged by choosing XUV photons for the leading pulse. This enables extraction of cluster size and exposed focal flux information from the scattering patterns. This method opens the possibility to study the Mie plasmon resonance under well characterized sample conditions, utterly impossible in earlier studies on ensembles of clusters.

In this chapter, the resonance behavior is examined by means of highest charge-state yields from single-shot single-cluster ion TOF spectra, which were recorded simultaneously with scattering patterns. First, ion spectra from size-selected clusters are investigated as a function of laser pulse delay, revealing a pronounced characteristic pulse separation time for enhanced target ionization (section 4.3.1). Subsequently, the resonance behavior is revisited for several intensities of laser focal power and discussed in the context of charge-dependent cluster expansion (section 4.3.2). To conclude, in section 4.3.3, the influence of the cluster radius on field-driven collective electron motion is investigated and compared with hydrodynamic expansion theory. All results in this chapter were gathered together with Mario Sauppe within the scope of his master thesis [132].

4.3.1 Driving collective electron motion in xenon clusters

As described in detail in chapter 3.2, free-electron laser pulses delivered by the FLASH facility hold a peak power density of $I_{\mathrm{XUV}} = 4.1{\cdot}10^{14}\,\mathrm{W/cm^2}$, pulse length of $\tau_{\mathrm{XUV}} = 100\,\mathrm{fs}$, and a wavelength of $\lambda_{\mathrm{XUV}} = 13.6\,\mathrm{nm}$. The thereto synchronized Ti:Sapphire laser pulses hold $I_{\mathrm{IR}} = 1.1{\cdot}10^{14}\,\mathrm{W/cm^2}$, $\tau_{\mathrm{IR}} = 80\,\mathrm{fs}$, and $\lambda_{\mathrm{IR}} = 800\,\mathrm{nm}$. In this dual-pulse configuration several fluctuations influenced the outcome of the detected single shots. Apart from cluster sizes and exposed focal intensity varying from shot to shot, the laser beams exhibited spatial and temporal jitter with each other. While the temporal jitter in the order of 250 fs [130] is negligible in the time range examined, the spatial jitter has a larger impact. The 20 µm and 90 µm focus of XUV and IR vibrated against each other, such that for some shots the beams did not overlap completely. Therefore, a small amount of data was detected resulting from clusters hit only by one single laser pulse - either FEL or Ti:Sa respectively. This fact demands for accurate filtering routines. Scattering patterns from clusters only irradiated by the IR pulse do not contain any fringe signal, but only homogeneously distributed fluorescence. They are therefore easily recognizable as seen in figure 4.1 d. Scattering patterns from exclusively XUV excited clusters do only contain fringe patterns but only minor fluorescence and can be identified by the low signal at high scattering angles (see fig. 4.1 c). After precise sorting, data from single-pulse excited clusters was neglected which decreases the overall statistics. For the further analysis only pump-probe data was taken into account.

The previously introduced concept (see section 4.2.3) of basic filtering by investigating best hits with highest detector intensity leads again to large clusters with highly excited ions and large kinetic energies. This method is preferable for introducing approach since differences in ion spectra are most prominent for large clusters as seen in chapter 4.2.1. To make spectra comparable, highest excited clusters with 200 nm radius are chosen and the resulting ionization of the cluster is evaluated as a function of the time separation Δt between the pulses as depicted in figure 4.11. An increase of higher charge-state yield (between 1 and 2 µs flight time) is visible with up to 12 ps delay. At the same time the lower

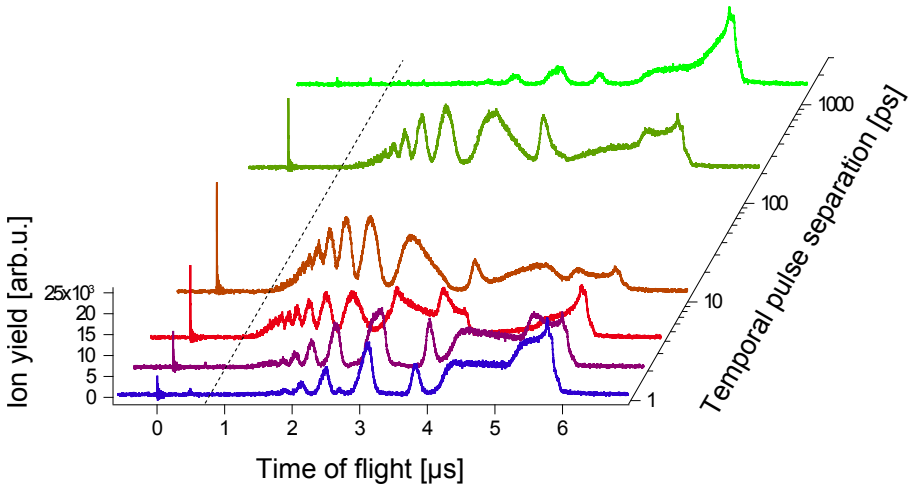

Figure 4.11: Single ion spectra of R = 200 nm clusters for different delays between leading XUV and following IR pulse. Enhancement of high charge-state yield and kinetic energies with delay up to 12 ps and subsequent decline hints on resonance feature. The same behavior is found for the light peak measured at 0 µs flight time [132].

charge states gain in kinetic energy, indicated by the peak shift towards shorter flight times. For longer delays, the ion distribution shifts back to lower charge states and the overall signal decreases. The same rise-and-fall behavior is found for the light peak measured at 0 µs flight time, consisting of scattered and fluorescence photons detected under 90 degrees. Due to the statistical growth process leading to a log-normal cluster size distribution (see fig. 4.2) statistics are very few for large clusters. No shots were found for R = 200 nm at pulse separations of 20, 50, and 100 ps resulting in a big gap between the ion spectra taken at 12 ps and 200 ps delay. Therefore, a qualitative analysis of the collective motion of quasi-free electrons in clusters in this size range is not possible from this limited dataset. Still the ion signals give strong evidence for resonant energy absorption in accordance with theoretical predictions [157, 158, 159, 49, 50].

For better statistics, a size range around the most frequently detected radius of 34 nm was chosen, from 27.5 to 40.5 nm, holding between 100 and 200 shots for each delay time. Since the photon detector is not energy resolved, the signals resulting from XUV and IR pulses respectively are hard to disentangle and sorting for exposed power density of both pulses becomes extremely challenging. Sorting for detector intensity was renounced to avoid misleading results by false assortment. All ion spectra measured for 34 nm xenon clusters were averaged for each delay and plotted in figure 4.12 a. Every averaged spectrum shows strong contribution from residual gas and uncondensed xenon atoms in the cluster beam. They originate from single shots by clusters hit in the low-intensity focal wing. Since those are the most frequently apparent their contribution is strongly prominent. In a small region around short flight times between 1 and 2 ps cluster and atomic signal is well separable. Averaged ion spectra at this high-charge-state region are set in comparison in figure 4.12 b.

To extract pure cluster signal, each single-shot spectrum is integrated for flight times where no background signal is detected as indicated by a red box in figure 4.12 b. In this region, ions with higher charge states and kinetic energies than from pure xenon atoms are measured. Subsequently, the single integrated values are averaged for each run. When

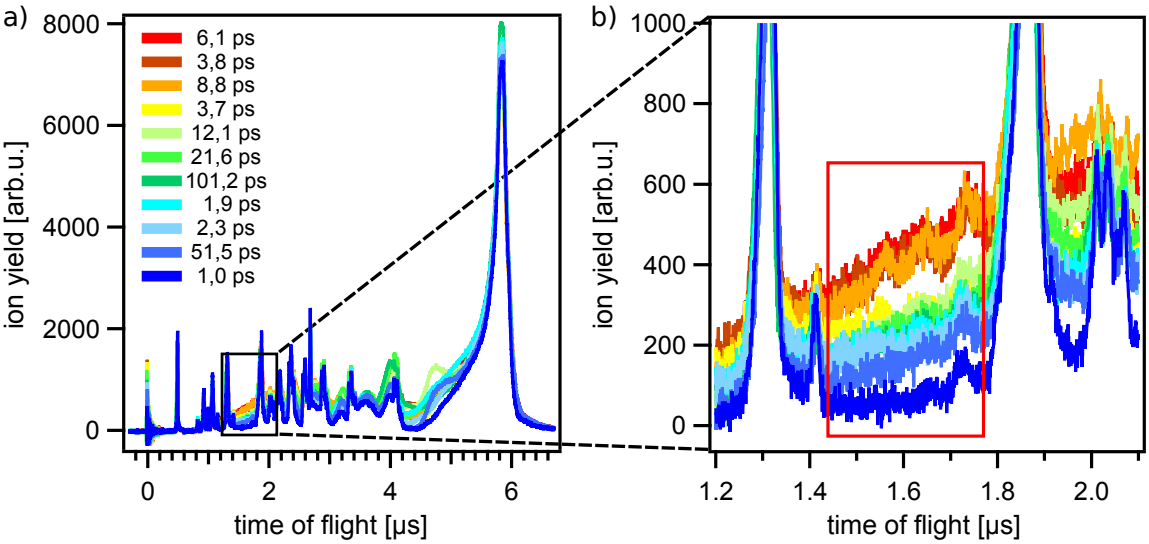

Figure 4.12: a) Averaged ion spectra for xenon clusters of 34 ± 6.5 nm radius taken with varying pump-probe delays. Despite large atomic background signal an enhancement of high charge states for certain delays is prominent. b) Zoom to the flight-time region where high charge states appear. The maximum ion signal is obtained in spectra recorded at a temporal separation of $\Delta t = 8.8$, 3.8, and 6.1 ps. The red box indicates the integrated high-charge-state region.

plotted over delay (figure 4.13 a) it clearly shows that the enhanced ionization is a function of temporal delay. The large error bars calculated by the standard deviation result from a strong fluctuation of the high charge-state yield on a shot-to-shot basis. Highest ion signals are detected at 6.1, 3.8, and 8.8 ps. This indicates that after these times the density of the cluster has dropped sufficiently to reach coincidence between the frequency of collective quasi-free electron motion in the cluster and the IR laser frequency. The delay time for maximum resonance condition is determined by a log-normal fit [80]

$$I = I_0 + A \cdot e^{-\left(\frac{ln(\Delta t/\Delta t_{char})}{W}\right)^2} \tag{4.6}$$

with initial intensity I_0, Amplitude A and full width at half maximum W. A value of 6.3 ps is found as indicated in figure 4.13 a.

The size of the expanded particle at point in time upon probing is disguised, even though in the recorded scattering patterns the initial cluster radius is imprinted. For the resonance condition, however, it can be calculated as demonstrated in the following. The so-called Mie surface-plasmon corresponds to collective oscillations of the quasi-free electron cloud against the ionic background. Its frequency is approximately given by [38, 50]

$$\omega_{Mie} = \frac{\omega_p}{\sqrt{3}} = \sqrt{\frac{e \cdot \rho_{ion}}{3\epsilon_0 m_e}} \tag{4.7}$$

with the electron mass m_e, the vacuum permittivity ϵ_0, and the ion density ρ_{ion}. A nanoplasma is generated by the leading XUV pulse. It the quasi-free electrons oscillate with the same frequency as the probing IR laser field ($\omega_L = 3.7 \cdot 10^{14}$ Hz), the energy absorption is enhanced. This leads to the direct acceleration of electrons and strong thermal excitation [160]. A critical ion density has to be reached to fulfill this resonance condition:

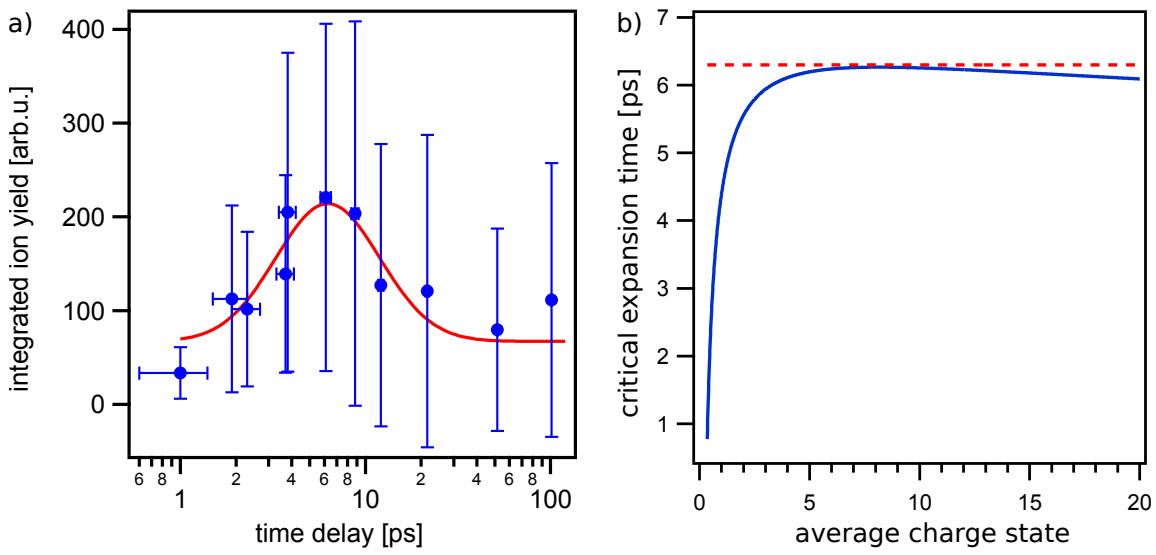

Figure 4.13: a) High charge-state yield of 34 ± 6.5 nm radius clusters integrated over the flight time range indicated by the red box in figure 4.12 b. Plotted over XUV/IR pulse separation time Δt an increase in ion yield by one order of magnitude becomes prominent. Fitted with a log-normal distribution the maximum appears at 6.3 ps. The maximum signal is accounted as evidence of resonant collective electron excitation. b) Expansion time calculated with the uniform density model over charge state. The initial radius is taken to be 34 nm and the electron temperature an 19.7 eV. The measured expansion time of 6.3 ps is indicated by a dotted red line.

$\rho_{ion} = 3\epsilon_0 m_e \omega_L^2 / e$. The leading FEL pulse excites the cluster and initiates its expansion by Coulomb and hydrodynamic forces. Accordingly the target density drops as a function of time due to an increase in cluster volume

$$\rho_{ion}(t) = \frac{N\langle q \rangle e}{V(t)} \tag{4.8}$$

with the number of atoms in the cluster N, the average charge state $\langle q \rangle$, and the time dependent cluster volume $V(t)$. The latter is given by

$$V(t) = 4\pi/3 \cdot R(t)^3. \tag{4.9}$$

When combining equations 4.7, 4.8, and 4.9, a critical radius is found where the resonance condition is matched [50]

$$R_{crit} = \left(\frac{e^2 \langle q \rangle N \lambda^2}{16\pi^3 \epsilon_0 m_e c^2} \right)^{\frac{1}{3}}. \tag{4.10}$$

For a cluster with $R = 34$ nm the number of atoms in the cluster is calculated to $N = 2.9{\cdot}10^6$ from equation 2.12. To fully determine the critical radius the average charge state $\langle q \rangle$ in the cluster is necessary.

Ion TOF spectra contain information about the final charge-state distribution of the disintegrated cluster. From the averaged ion spectrum measured at 6.1 ps time delay, which is closest to the fitted maximum resonance time, the average charge state was extracted. Furthermore, the flight-time was converted into mass-over-charge and the ion spectrum's center-of-gravity was determined to be $m/q = 92.8$ u. With a xenon mass of $m_{\mathrm{Xe}} = 131.3$ u

the average charge state can be derived as $\langle q \rangle = 1.4$. Note that the transmission function of the time-of-flight spectrometer for each charge state is not taken into account here, because single charge states are hard to disentangle in the averaged spectrum (see fig. 4.12). Since higher charges are better transmitted than lower ones, the value of $m/q = 92.8\,\mathrm{u}$ might be overestimated, e.g. the value of $\langle q \rangle = 1.4$ is probably underestimated. Additionally, this value has to be treated with care, because charge migration and recombination are taking place before the final state is reached, which is recorded in the TOF spectra. A comparison between ion and fluorescence spectra for similar xenon cluster and FEL properties demonstrated that higher transient charge states are hidden in ion spectra [100]. Therefore, the observed value of $\langle q \rangle = 1.4$ can only hold as a lower limit for the average charge state before expansion. An estimation of the average charge state before recombination can be calculated from the charge state dependent expansion time.

As presented in section 4.2.3, the expansion for large xenon clusters irradiated by a $10^{14}\,\mathrm{W/cm^2}$ infrared pulse resides deep in the hydrodynamic regime. Therefore, the time for a spherical cluster to expand to the critical radius can be calculated from the constant plasma sound velocity $v = \sqrt{\langle q \rangle k_b T_e / m_i}$ to be [48, 99]

$$t_{exp} = (R_{exp} - R) \cdot \sqrt{\frac{m_i}{\langle q \rangle k_b T_e}} \tag{4.11}$$

with electron temperature T_e. In an experiment on an ensemble of $N = 2000$ atoms xenon clusters in 90 eV FEL light with $5 \cdot 10^{14}\,\mathrm{W/cm^2}$ power density, the electron temperature was determined to be $T_e = 19.7\,\mathrm{eV}$ from electron TOF spectra [42]. With this temperature, an initial radius of $R = 34\,\mathrm{nm}$, and by combining equation 4.11 with equation 4.10, the critical expansion time was calculated for a range of average charge states and plotted in figure 4.12 b.

As seen from figure 4.12 b, for low charge states the expansion time is slow and rises drastically up to around $\langle q \rangle \approx 4$. From there it saturates and eventually decreases again slowly towards high $\langle q \rangle$ values. The maximum calculated value of 6.3 ps just matches the measured peak expansion time of 6.3 ps (see fig. 4.12 a). The corresponding charge state of $\langle q \rangle = 8.1$ is much higher than the earlier deduced value of $\langle q \rangle = 1.4$ predicted from the ion TOF spectra. In comparison with the highest charge state detected of $q_{max}>10$ (see figure 4.13), it seems to be a possible value for the cluster before recombination and expansion. However, it stays unclear which of the values is more realistic.

4.3.2 Relationship between exposed power density and resonance condition

In the previous section, laser-intensity effects were not directly addressed by averaging single ion spectra of one cluster size but for all exposed power densities. The previous calculations based on the hydrodynamic model suggest that the characteristic resonance time is almost independent of the charge state from a certain threshold onwards (see graph 4.13 b). For sufficient photon fluxes it is therefore independent of the laser intensity of the pre-expanding laser pulse. The model implies a homogeneous charge-state distribution and does not take into account any radial dependencies. However, the quasi-free plasma electrons migrate to the energetically preferred particle center and a shell-wise expansion takes place as introduced in chapters 2.2.3 and 4.2.1. This effect becomes increasingly

important with large cluster sizes. Therefore, the validity of the calculation in figure 4.13 b for the measured data needs to be revisited.

To examine the impact of the laser intensity on resonance condition, the size-selected data from the previous section was filtered further for detected photon signal. Since the employed scattering detector is not energy sensitive it is not possible to distinguish between FEL and Ti:Sa induced signal and hence to disentangle XUV and IR exposed power densities. Still the recorded frame intensity makes a reasonable filter if the signal is grouped in coarse enough fractions. The data was arranged in three intensity regimes with low (35 - 42 arb.u.), moderate (42 - 49 arb.u.), and high (49 - 56 arb.u.) photon signal. As in the previous section, filtered ion spectra were integrated and averaged over high charge states for each delay. The gleaned values are plotted in figure 4.14. It shows that for all pulse separation times Δt the integrated high-charge-state yields are largest for the data filtered for highest photon signal. This behavior is expected since a stronger scattering signal results from higher laser intensity. This leads to stronger cluster excitation resulting in higher ionization (cf. section 4.2.1).

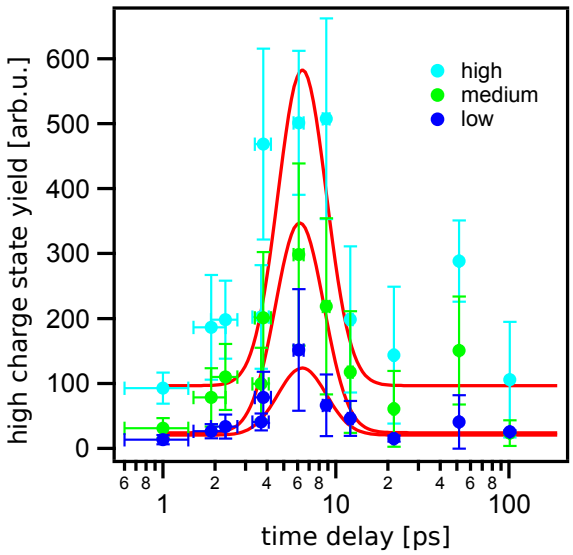

Figure 4.14: Integrated charge-state yields from ion spectra of 34 ± 6.5 nm radius clusters averaged for three detector intensity regimes exhibit resonance enhancement around the same laser pulse delay time. Laser peak power densities are $I_{\mathrm{XUV}} = 4.1 \cdot 10^{14}\,\mathrm{W/cm^2}$ and $I_{\mathrm{IR}} = 1.1 \cdot 10^{14}\,\mathrm{W/cm^2}$. Adapted from [132].

For all three intensity regimes a resonance enhancement in ion signal is observed around a similar probe delay time. For a more precise analysis all data sets were fitted with a log-normal distribution (equation 4.6). The resulting maximum values are 6.4 ps for high, 6.2 ps for medium, and 6.4 ps for low excitation respectively. No clear dependence on the laser intensity is found for the occurrence time of the Mie plasmon resonance. This observation stands in good agreement with the previous calculation, predicting a similar characteristic delay time for a wide range of average charge states, as soon as a certain threshold is exceeded. Apparently, the approximations of the basic hydrodynamic expansion model of a uniformly charged sphere are applicable in this case.

Non-homogeneous charge distributions in large clusters are reported to be reflected in a broad temporal resonance distribution [49, 50]. The uniformly-charged-sphere model predicts the enhanced absorption to be completed after a femtosecond interval [47]. In contrast, the resonance enhancement is calculated to be completed after several picoseconds when a radial quasi-free electron distribution is included in calculations [82]. The charge imbalance results in a non-uniform expansion of the cluster with faster outer side and slower interior. Therefore, only those electrons in the layer where the density has sufficiently dropped are collectively driven. This layer gradually moves from the outside to the cluster center over a long time period. In the experiment performed on $R = 34$ nm xenon clusters

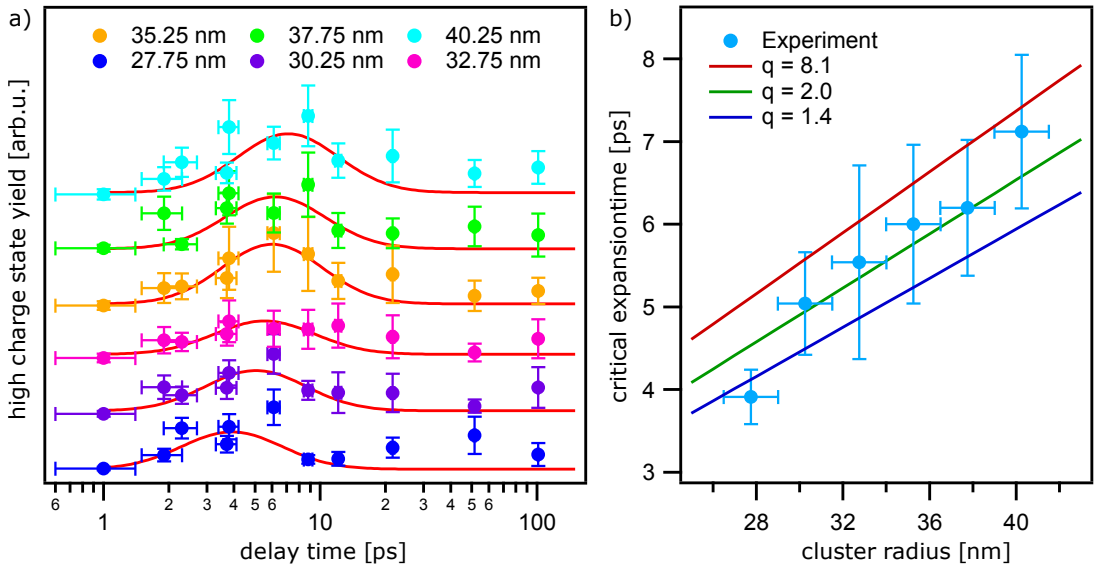

Figure 4.15: a) Integrated ion yield over pump-probe separation time Δt from averaged ion spectra of different cluster sizes. Red curves are log-normal fits, revealing the relative peak delay times. b) Peak resonance delay times (extracted from fits in (a)) over initial cluster radius. Calculated expected characteristic resonance delay times for three different average charge states are indicated by lines. Adapted from [132].

an enhanced resonance is detected between 4 and 9 ps with a fitted full width at half maximum of $W = 5$ ps for all three intensity ranges (figure 4.14). In earlier experiment on cluster ensembles [80], it was speculated that a broad resonance-time distribution might result from a large cluster size distribution. By investigating single-cluster spectra of size-selected particles, a size-average effect can be excluded here. Therefore, a broad resonance time can be attributed to an shell-wise expansion as theoretically predicted [82].

4.3.3 Cluster size dependent resonance development

As evident from equation 4.10, larger clusters require more time to expand to frequency matching condition. The data set from the previous section is split in six size regimes from 27.75 up to 40.25 nm radius to study the radius-dependent resonance excitation time. For better statistics and due to negligible influence it is refrained from intensity filtering. For each temporal pulse separation and cluster-size range the single-shot high charge-state yields are averaged and plotted in figure 4.15 a. Fitted log-normal distributions are indicated as red lines. From bottom to top the delay times of maximum signal enhancement shift towards higher values as expected for increasing particle size. While the size grows by a factor of 1.45 the characteristic time develops with a factor of 1.8.

In figure 4.15 b, the experimental values are plotted together with model calculations for different average charge states $\langle q \rangle$. A value of $\langle q \rangle = 1.4$, as extracted from averaged ion spectra in section 4.3.1, underestimates the characteristic expansion time (blue line). The calculated value of $\langle q \rangle = 8.1$ (red line) delivers times exceeding those of the experiment. The best compliance with the experiment is found for $\langle q \rangle = 2.0$ (green line). With this value the critical cluster radius R_{crit} for all cluster sizes can be calculated assuming an

Table 4.2: Initial cluster radius R_0 deduced from fringe spacing in scattering patterns. Critical expansion time t_{exp} extracted from figure 4.15 a. Critical cluster radius R_{crit} calculated with equation 4.10 and an average charge state $\langle q \rangle = 2.0$. Resulting plasma velocity v_{exp}, calculated with $v = \sqrt{\langle q \rangle k_b T_e / m_i}$ and $T_e = 19.7\,\mathrm{eV}$.

R_0 [nm]	t_{exp}[ps]	R_{crit} [nm]	v_{exp} [m/s]
27.75	3.9	52.2	6300
30.25	5.1	56.8	5200
32.75	5.5	61.6	5200
35.25	5.9	66.3	5200
37.75	6.1	71.0	5400
40.25	7.0	75.6	5100

electron temperature of $T_e = 19.7\,\mathrm{eV}$. Due to the knowledge of the initial radius before excitation the expansion speed of the critical cluster layer up to resonance condition can be calculated. The results are listed in table 4.2. For all initial sizes the speed was calculated to be similar, fluctuating around 5500 m/s. In earlier drift measurements on xenon clusters a velocity distribution with maxima at 3600 and 12000 m/s was detected [152]. This shows that the here deduced results are realistic. This indicates that the fitted value of 2.0 is a good estimate for the average charge state before recombination for clusters of $R = 34\,\mathrm{nm}$ in 80 fs IR pulses of $10^{14}\,\mathrm{W/cm^2}$.

To conclude, the method of single-cluster imaging in coincidence with ion spectroscopy allows to study the Mie plasmon resonance in unprecedented detail. By imaging the cluster initial state with the pump pulse, the particles can be well characterized for size and exposed focal flux. Independent of the latter, maximum ionization occurs 6.3 ps after XUV excitation for particles with radius $34 \pm 6.5\,\mathrm{nm}$. This indicates that the electron cloud is driven resonantly by the strong IR laser field. The broad resonance time distribution of 5 ps is a signature of the layer-wise cluster expansion, e.g. the electron density dropping to resonance condition shell-by-shell. In cluster radius-dependent observation larger initial cluster sizes lead to longer expansion times until the critical radius is reached. From the nanoplasma model an average charge state of $\langle q \rangle = 2.0$ can be fitted to the data. Derived from the thereby calculated critical radius the expansion speed of outer exploding shell is determined.

What stays unrevealed is the destination of the cluster core after shell explosion. As spectroscopy is blind to uncharged particles and therefore the recombined core, a different approached is needed for its investigation. Since imaging provides access to neutral matter the pump-probe setup is reversed in time. While the IR pulse initiates cluster expansion, snapshots of the disintegrating sample are recorded with the succeeding XUV pulse for several points in time. Combined they provide a movie of plasma evolution, subject to the next chapter.

4.4 Imaging IR induced explosion

In the previous section the cluster expansion was initiated by an FEL-pump pulse and the response was tracked with an IR-probe pulse. By examining of the characteristic time of

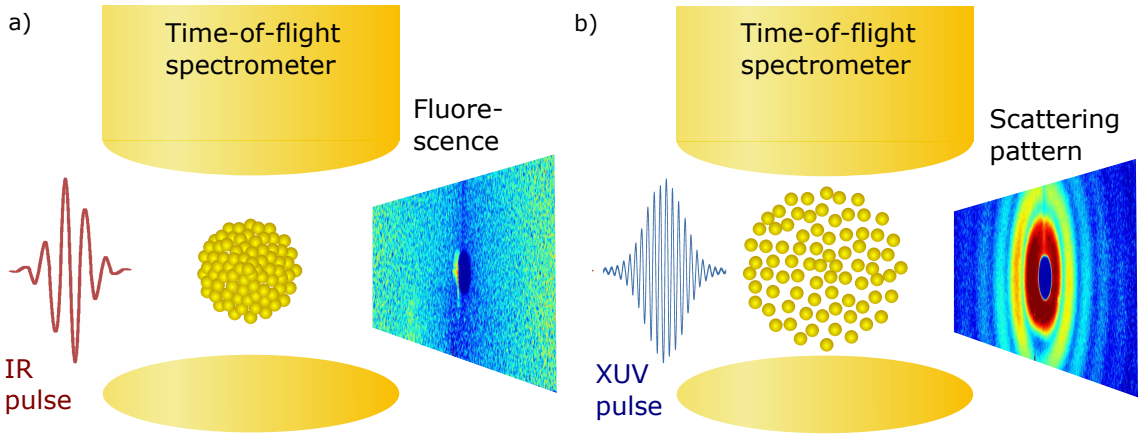

Figure 4.16: Experimental scheme of the excitation mechanism. a) An IR-pump pulse excites a single xenon cluster and induces a nanoplasma. The detected photon signal shows homogeneous scattering and fluorescence. b) A variably delayed XUV pulse directly images the state of cluster-electron distribution. By varying the arrival time of the pump pulse, the nanoplasma evolution is mapped on an extended timescale up to nanoseconds. While ion spectroscopy is blind to neutral cluster atoms, imaging gives access to investigate the recombined cluster core.

the ion-density dependent plasmon resonance the expansion speed was estimated. In this chapter, the temporal pump-probe scheme of the two laser pulses is reversed. Thereby their roles get interchanged: The IR pulse from the 800 nm Ti:Sa initiates cluster expansion and cluster fragmentation is examined with the 13.6 nm XUV pulse from the FEL. Some aspects of IR specific dynamics have been already discussed in detail in section 4.2.3. The electrons in the cluster are field driven by the IR-pump pulse. Quasi-free electrons are produced by inner field ionization processes, resulting in the build-up of a dense nanoplasma and a disintegration of the particle's outer ionic shell in a hydrodynamic expansion. At the same time the inner core recombines and stays intact on a supra-femtosecond timescale. The further development and the timescale of possible disintegration of the neutral core is unknown. Therefore, the last key issue of this thesis is to investigate how the shell disintegrates and what happens to the remaining core several pico- up to nanoseconds after the excitation. While ion spectroscopy is blind to neutral cluster atoms, imaging gives access to investigate the recombined cluster core. With the XUV as probe pulse snapshots of the disintegrating sample are directly imaged for a detailed examination of the nanoplasma evolution.

The pump-pulse delay with respect to the probe pulse was varied in 12 steps between 0.3 ps and 1.5 nanoseconds to analyze the cluster expansion with good resolution on an extended time range. 24000 scattering patterns and corresponding ion TOF spectra were recorded from individual xenon clusters. Those were produced under the same expansion conditions as stated in chapter 3.1, exhibiting a log-normal size distribution with the maximum at 34 nm radius and cluster radii up to 1 µm (see figure 4.2). In the previous section, the initial cluster condition was mapped on the CCD image but no information about the final state could be deduced from the scattering pattern. In this section, the setup is reversed as schematically depicted in figure 4.16. No details can be directly extracted about the size and shape of the cluster before excitation by the IR pulse. Only the state after expansion is retained in the CCD images. With increasing delay time the disintegration of the cluster

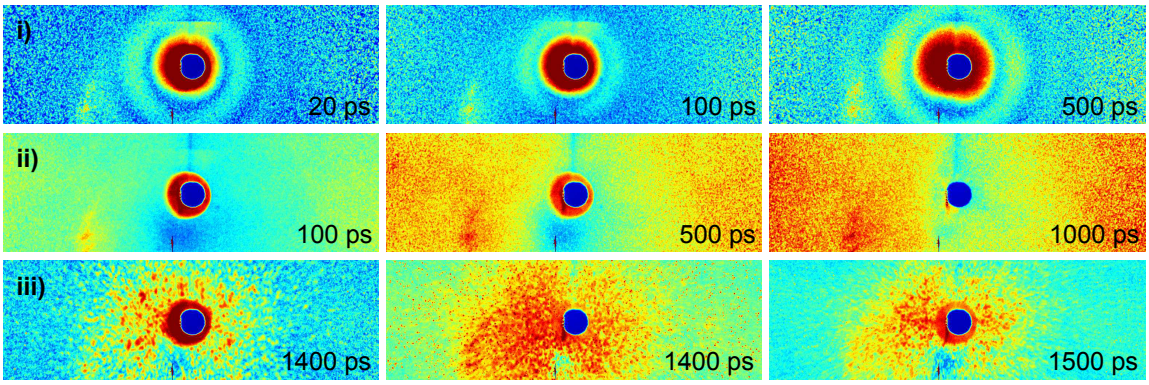

Figure 4.17: Three types of characteristic CCD images recorded from individual xenon clusters excited by an IR pulse and subsequently probed by an XUV pulse. i) Ring structures hinting on intact clusters. ii) Homogeneously distributed photon signal. iii) Speckle patterns. The respective pulse separation time is denoted in each image. For a detailed description of the detector artifacts visible in the scattering patterns see chapter 4.1.1 and figure 4.1.

should cause a dramatic change in scattering patterns due to IR induced electron-density deformation and plasma-profile evolution.

Snapshots of manifold expansion states

A vast variety of images was recorded. Therefore, careful inspection and filtering of the single-shot patterns had to be executed. A large amount of data exhibits shots where no cluster is hit by any of either laser pulses, because of heavy cluster beam skimming. Other data results from clusters hit exclusively by an FEL or an IR pulse respectively, due to missing spacial overlap. These datasets were filtered and neglected for further pump-probe investigations. Apart from those discarded shots three fundamentally different types of scattering images were recognized on different timescales. A characteristic assortment of the repertoire is depicted in figure 4.17. They are grouped in rows, depicting

(i) ring structures with additional fluorescence (fig. 4.17 i),

(ii) a rather homogeneously illuminated screen (fig. 4.17 ii), and

(iii) diffuse speckle patterns (fig. 4.17 iii).

These limiting cases mirror the different atom/ion-density distributions, present picoseconds after laser-cluster interaction. The discussion of the underlying physical principles, leading to these patterns will be the topic of this chapter. It will lead to an overall picture of the expansion dynamics taking place from a picosecond up to a nanosecond timescale.

The first characteristic type of scattering images appears over the entire time range from 0.3 ps up to 1500 ps delay time, though the vast majority is found at short delays. Due to the visible fringe structure they have high resemblance with patterns from intact clusters irradiated by an FEL pulse only. In addition they exhibit an enhanced background signal reminding of CCD signal from exclusive Ti:Sa irradiate particles. As investigated in section 4.2.3, interaction of giant clusters with a moderate IR pulse results in skinning of a rather

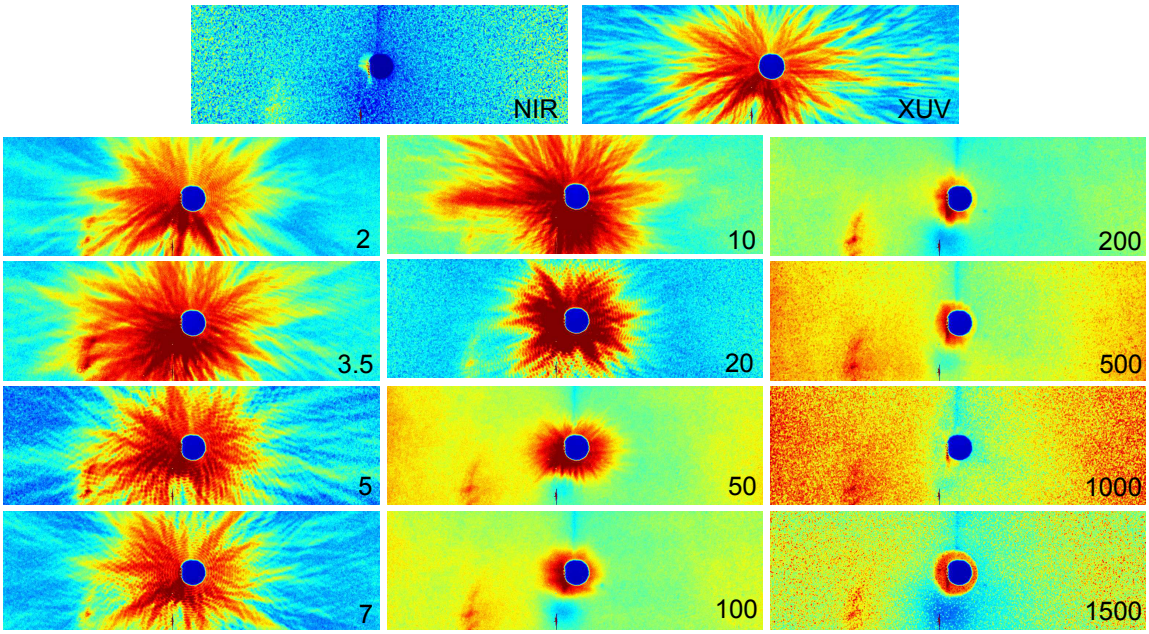

Figure 4.18: Brightest CCD images of different runs. First row: clusters were exclusively hit by an IR or XUV pulse respectively. Images below: clusters are imaged by the FEL pulse after Ti:Sa excitation at different temporal delays, increasing from top to bottom and left to right as indicated by the delay time in picoseconds. The gradual change in patterns mirrors the evolving cluster disintegration. With increasing probe delay time the scattering fringe signal decreases and fluorescence signal increases.

thin outer ionic shell and a remaining neutral nanoplasma which can efficiently recombine. The visible ring structure in the scattering patterns indicates that the cluster core is still to some extend intact, even picoseconds after the IR excitation. The timescale of the core continuance will be analyzed in detail in section 4.4.1.

The rather constantly illuminated screen in the second type of images (fig. 4.17 b) resembles data taken from clusters hit by an IR pulse only. For this reason they are hard to disentangle from those and the corresponding ion spectra are necessary for reliable filtering. A loss of information in the scattering pattern corresponds to a loss of order in the sample [161]. Hence, the absence of any fringes or speckles indicates an advanced destruction of the particle. Also the intensity of the signal rises with pulse separation times, which will be analyzed in more detail in section 4.4.2.

The third type of CCD images, as in the bottom row of figure 4.17, exhibits diffuse speckle patterns not resembling any images detected from unmaimed rare-gas clusters. They strikingly stick out from any patterns priorly presented and are very rare. They appear only from a nanosecond delay onwards. Such speckle patterns are known from other fields, such as particulate matter. They were detected from aggregates of spherical nanoparticles like soot and aerosols [8, 162] but never before from mono-atomic clusters. From an extended analysis in section 4.4.3, they can be understood as images of the slowly expanding neutral cluster core, which exhibits internal density fluctuations.

4.4.1 Imaging cluster surface ablation

Comparing the scattering patterns in figure 4.17, the question arises how the transition between those extreme, limiting cases takes place. From the basic observation that with delay time the amount of fringe patterns (as in fig. 4.17 i) decreases, while the quantity of 'homogeneously illuminated' patterns (fig. 4.17 ii) increases, the conclusion can be drawn that on a median timescale images of an intermediate state should be present. Indeed patterns with vanishing fringe signal are existent, but accounting those to a corresponding initial state and a matching final state is challenging, if not impossible.

Therefore, in figure 4.18 the most reliable assignment has been used to investigate on which time scale large clusters get destructed by an IR laser as explained in the following. All CCD images recorded for one delay time were filtered for the brightest photon signal. The assumption thereby is that largest clusters scatter most and cluster most centrally placed in both beam foci result in highest detector intensity. By this method it is ensured that the biggest and best hit clusters of each run are picked out. For every delay time the scattering pattern of those selected clusters are plotted in figure 4.18 in comparison with the most intense shot for single pulse excitation (IR and XUV only respectively). Pump-probe patterns at shorter delay times up to 20 ps show the familiar, fine fringe structures from giant, hailstone-shaped xenon clusters. For delay times up to 20 ps no major differences to patterns from clusters in exclusive FEL pulse imaging are observed, except from the varying target geometries. From 50 ps onwards the fringe pattern vanishes and a drastic increase in background signal becomes prominent at larger scattering angles. Whether this background arises from fluorescence, inelastic, or incoherent scattering cannot be determined since the detector is not energy resolved. However, ion time-of-flight spectra reveal an increase in fluorescence signal with delay time, as will be discussed later (see chapter 4.3.2 and figure 4.24). The drastic change in pattern appearance between 20 and 50 ps is most probably arising from the deformation of the atom/ion-density distribution which proceeds on a picosecond timescale.

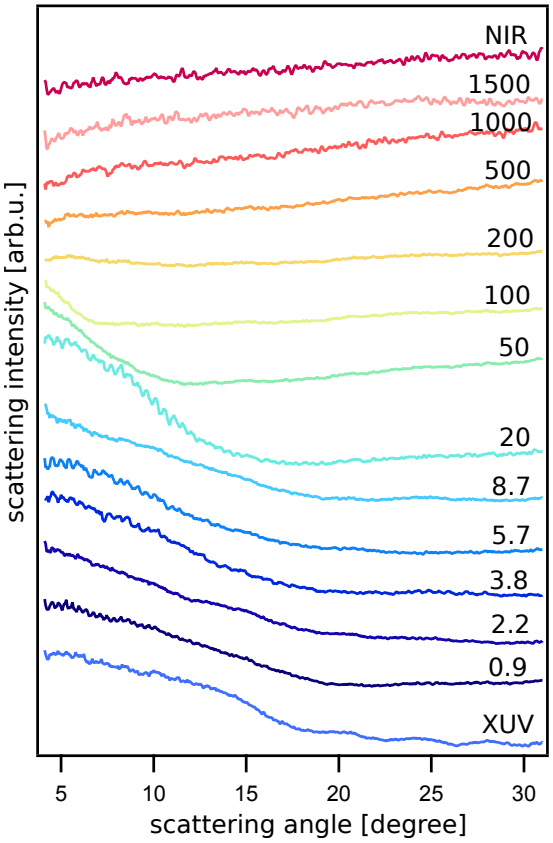

Figure 4.19: a) Azimuthally averaged scattering signal of the diffraction patterns shown in figure 4.18. For a juxtaposition the XUV only profile is at the bottom (blue), while the IR only one is at the top (red). Temporal delay increases from bottom to top as indicated by numbers in picoseconds. The arrows are a guide to the eye to trace the shift of envelope minimum towards smaller angles for increasing delay.

More detail is revealed by the azimuthally integrated scattering profiles as presented in figure 4.19 a. The fine fringes in the ring pattern are almost not resolved (compare with

figure 4.2) due to the very large cluster sizes and the detector geometry. However, the profile envelope is clearly visible. For the FEL-only-shot this envelope appears to change its slope around 20 degrees scattering angle. For the pump-probe hits this 'minimum' evolves towards smaller scattering angles with delay time, to around 7 degrees for the profile at 100 ps. On the same timescale the background signal at high scattering angles increases. Its origin is discussed further below. From 200 ps delay onwards no more fringe signal is detected. This leads to the conclusion that it has vanished to small angles below 4 degrees which are not recorded with this setup[2]. From 500 ps onwards the profiles remarkably resemble the ones recorded from clusters exposed to IR light only. However, the overall detector intensity is higher for pump-probe data. This phenomenon will be elaborated and interpreted in section 4.4.2.

Analysis of core melt-off by shell ablation

Previous single-shot XUV imaging experiments on xenon clusters demonstrated that ultrafast changes in electronic configuration - proceeding within femotseconds - are imprinted in the scattering signal [10]. Within 10 fs, the atomic form factors can change with increasing degree of ionization, evident from a deformation of the scattering amplitude envelope. Using 100 fs XUV pulses a supermodulation of the fringe pattern appears. This gives evidence of a *refractive core-shell system* in the cluster. It is probably caused by sharp resonances of xenon ions at 91 eV photon energy which lead to the formation of two regions with different refractive indices inside the cluster [45]. Both publications ([10, 45]) show that ultrafast electronic changes affect the pattern intensity distribution. However, the fringe structure itself, e.g. their spacing and radially integrated intensity distribution, is not drastically altered. In contrast to those single-pulse experiments, the dual-pulse configuration used in this work enters the timescales of atomic/ionic motion. Here, the changes in scattering signal are more drastic. From the evolution of the scattering signal with varying temporal pulse separation a precise conclusion about the evaluation of the nanoplasma profile can be drawn. This was consistently demonstrated in an experimental [46] and a theoretical study [163].

An IR-pump / x-ray-probe experiment on medium sized xenon clusters (20 nm in radius) was performed recently at the hard x-ray free-electron laser LCLS. It was shown that higher order scattering rings disappeared fast after a probe pulse delay time of only several hundred femtoseconds [46]. The particles were pumped by a highly intense Ti:Sa pulse with peak power density of $2 \cdot 10^{15}\,\mathrm{W/cm^2}$ (almost 20 times more intense than in the present experiment). The resulting high charge states exceeded Xe^{6+} by far. The fast stripping of electrons from their parent ions resulted in a Coulomb explosion of the repulsive ionic outer cluster layers and the cluster rapidly expanded. In small-angle Guinier-scattering simulations on electron densities with Gaussian-like distribution - as reported for plasma evolution in vacuum [164, 165] - the vanishing of fringe signal at larger angles was reproduced. Moreover, the cluster size before illumination by the IR pulse was simulated. A decrease of scattering signal at large angles by almost two orders of magnitude after 500 fs was attributed to a core melt-down of 50 %. Additionally, it was revealed that the scattering signal has completely blurred into background signal before complete destruction of the cluster.

[2]Detector hole and stray light cover the region from 0° to 4° scattering angle.

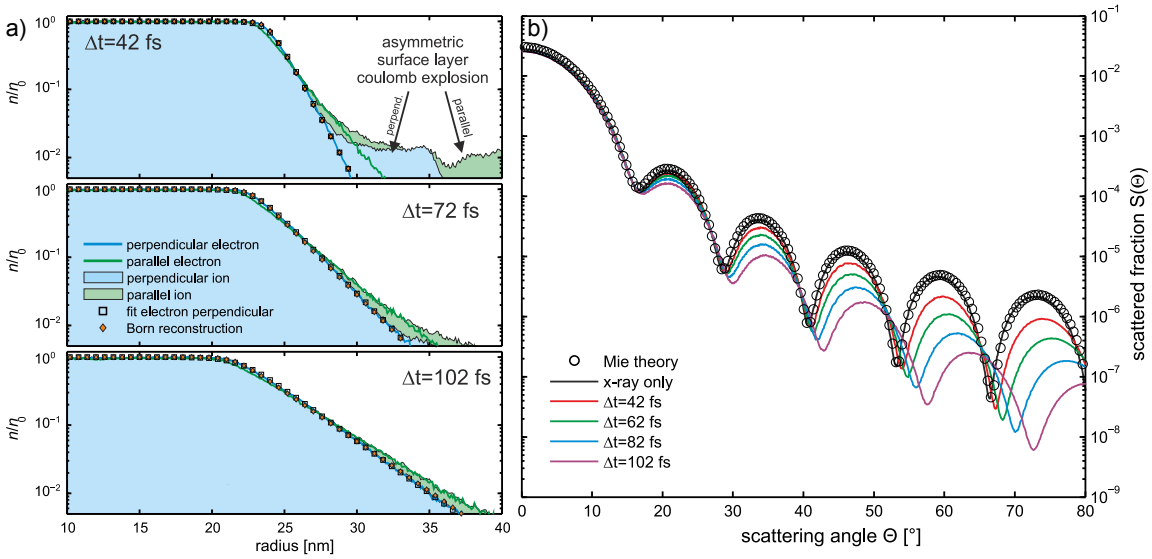

Figure 4.20: Adapted from [163]. a) MicPIC simulation for the electron and ion distribution of an initially 25 nm radius hydrogen cluster at tree different time steps after excitation with an IR pump pulse ($\lambda = 800\,\text{nm}$, $\tau = 10\,\text{fs}$, $I = 10^{15}\,\text{W/cm}^2$). b) Simulated corresponding scattering profiles generated by an XUV probe pulse ($\lambda = 10\,\text{nm}$, $\tau = 10\,\text{fs}$, $I = 10^{16}\,\text{W/cm}^2$) at several delay times after IR excitation. With increasing surface ablation higher order scattering maxima decrease in intensity.

This signal drop in scattering intensity at large angles with cluster expansion was already predicted by extensive theoretical calculations for hydrogen particles [163]. The evolution of the radial ion and electron density several femtoseconds after excitation was computed in MicPIC simulations on a hydrogen cluster excited by an IR pulse. Exemplary, results for a 25 nm radius hydrogen cluster are shown in figure 4.20 a. First, an unscreened surface layer bursts off the fully ionized particle in a Coulomb explosion. Eventually, the remaining screened core - where ion and electron density coincide - undergoes hydrodynamic expansion. At all time steps the simulated electron-density distribution was found to consist of a uniform volumic mass core and an exponentially decaying shell. In total, it follows the equation

$$\rho(r) = \frac{\rho_{Core}}{[\exp(\frac{r-r_C}{d \cdot s}) + 1]^s} \tag{4.12}$$

with the density of the cluster core ρ_{Core}, the distance from the cluster center r, the radius of the cluster core r_C, the decay length of the melting surface d, and a sharpness factor s, which ensures the correct transition between core and shell region [163].

In the same study, scattering patterns from an XUV pulse probing those density distributions were calculated by the scattering fraction of the scattered electric field. They are shown in figure 4.20 b where two major results are immediately visible. One the one hand, the higher order maxima decrease in intensity with broadening of the surface layer and smoothing of the edge between core and shell region. On the other hand, the minima shift towards larger angles with delay time due to a reduction of the core radius. Due to this behavior the amplitude envelope of the fringes gets steeper with surface ablation.

The results of this theoretical study were applied to the measured data presented in figures

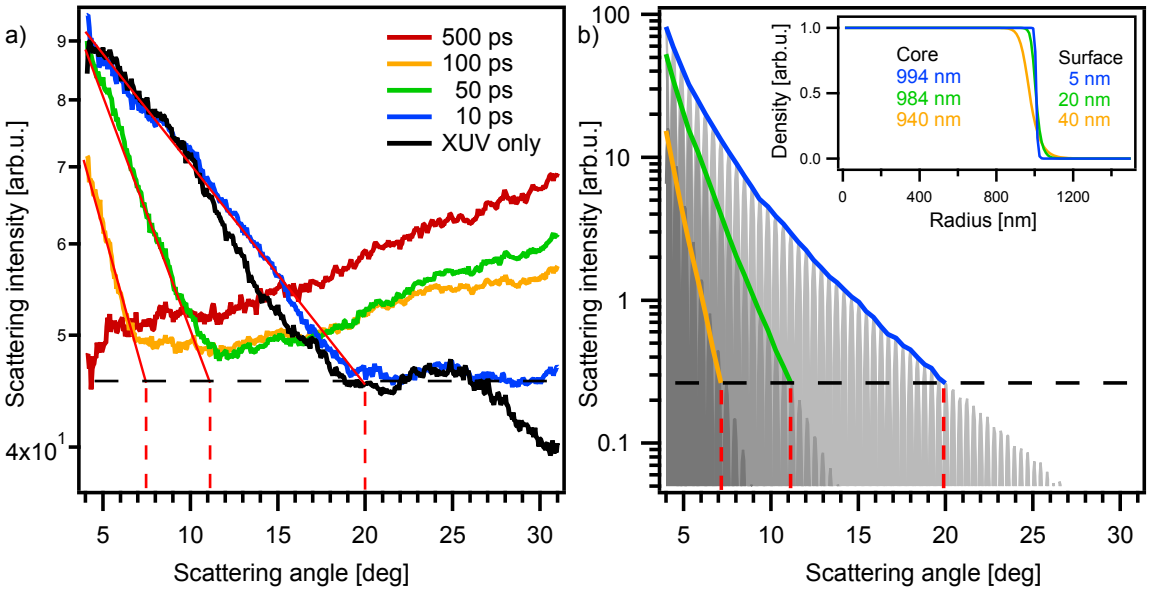

Figure 4.21: a) Azimuthally integrated scattering patterns of clusters irradiated exclusively by an FEL pulse or by an FEL pulse following a Ti:Sa pulse at different delay times respectively. Due to the large particle size (>700 nm radius) the fringes are not resolved. The background signal increases with delay and an intensity threshold is indicated by the black dotted line where fringe signal is overlayed. The envelope of the scattering pattern gets steeper with temporal separation between pump and probe pulse, as indicated by the red lines. Correspondingly crossing-points of intensity threshold and envelope shift towards smaller angles with nanoplasma evolution. b) Simulation of scattering patterns by 2D FFT of projected electron density arrays. Profile of an intact cluster of $R = 1000$ nm radius with hard edge is depicted by the light gray pattern. Where the blue envelope reaches an angle of 20 degrees an intensity threshold (black dotted line) is set. Profiles with envelopes crossing this line are matched for angels of 11.5 and 7.5 degrees fitting the measured data. Inset: Corresponding density profiles reveal the relatively small melted surface compared with the remaining core.

4.18 and 4.19. The steepness of the scattering profile envelopes was analyzed to investigate the change in electron-density distribution as function of expansion time. In figure 4.21 a the profile for the XUV only excited cluster is set in direct comparison with clusters imaged at 10, 50, 100, and 500 ps delay respectively. The two main tendencies observed are

- rising steepness of the intensity slope at low scattering angles with delay time and
- an arising of background signal at high scattering angles.

The second aspect is of minor interest for the understanding of the underlying physical aspects of cluster expansion and will be discussed here only briefly. A minor background arising from inelastic photon scattering is predicted by theoretical calculations [163], but with orders of magnitude lower in intensity than the intensity of the elastically scattered light[3]. A different publication reports on a previous dynamic pump-probe imaging experiment, where a strong background signal with intensities in the order of the elastic scattering intensities was also detected at high scattering angles and increasing with delay time [161]. However, this experiment was not performed on isolated targets, but on several

[3]Note that contribution by fluorescence is neglected in this calculation.

extended membranes with the same pattern etched into them. The increase in background signal with delay time was attributed to scattering from additional structure induced in the membrane by the pump-pulse. Since this cannot be the case for finite targets, as in the experimental data presented in figure 4.18 and 4.21 a, the background signal at high angles is attributed to a composition of fluorescence and inelastic scattering. However, it is not understood why it increases towards larger angles. Due to the high background signal, the fringe envelopes are superimposed by the background signal from a certain intensity threshold, indicated by the black dotted line in figure 4.21 a. Because the steepness of the envelope rises with delay time, the scattering angle at which the envelope crosses this threshold shifts towards smaller angles (indicated by the red dotted lines in fig. 4.21 a) until it vanishes towards angles lower than those detected.

To further analyze the underlying plasma evolution, measured envelope changes have been compared with theoretical simulations. In scattering profiles from pristine spherical clusters the envelope steepness is independent of the cluster size, evident from Mie theory [38], as demonstrated in figure 4.22. This observation enables a qualitative statement for the measured data without prior knowledge of the initial cluster radius before IR excitation and subsequent cluster expansion. Several electron-density distributions with increasing surface decay length and correspondingly shrinking core have been calculated to mimic the cluster shapes at several time steps after IR irradiation. They are displayed in the inset of figure 4.21 b. For their calculation the analytic expression proposed by MicPIC theory for nanoplasmas in hydrodynamic expansion [163] was employed (equation 4.12). In the present experiment, however, the initial cluster size is unknown. The profiles presented in figure 4.21 a originate from the largest clusters produced, which exceed a radius of 700 nm since the fringe spacing cannot be resolved (see section 4.1.1). Therefore, an estimated initial radius of $R = 1000$ nm was used in all calculations in figure 4.21 b. Again, note that the scattering envelope of a spherical particle is independent of the scatterer size. Therefore, any arbitrary initial radius is applicable to study the amplitude envelope changes.

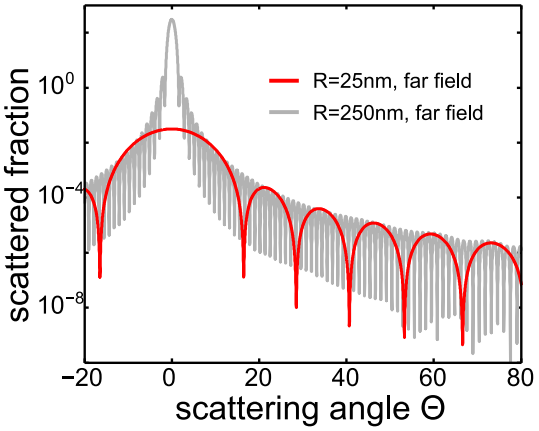

Figure 4.22: Scattering profiles of patterns calculated with Me's theory from a spherical cluster with 25 nm (red graph) and 250 nm (gray graph) radius respectively from [163]. Despite the different particle radius and resulting scattering fringe spacing, the profile envelope is the same.

In a simplified approach scattering profiles were simulated by 2D Fast-Fourier-transforms (FFT) of the electron-density distribution projected onto the scattering plane. Scattering fringes are plotted in gray in figure 4.21 b and envelopes are highlighted in color. The blue density distribution in the inset of figure 4.21 b is calculated for a cluster with a surface decay length of 5 nm and corresponding core of 994 nm. In order to make theory and experiment comparable, an intensity threshold was set in figure 4.20 b where the higher order maxima of the profile with blue envelope reach 20 degrees scattering angle. The scattering angle at which envelope and threshold level cross is used as reference point to find the matching density profiles. From density distributions with melting outer shells

(see inset in figure 4.21 b), profiles with envelopes crossing the background-threshold at 11.5 and 7.5 degrees were calculated, to simulate the data taken at 50 and 100 ps after IR excitation respectively. The parameters for the density were chosen such that the overall volume was kept constant. The resulting density distributions hold a cluster core of 984 and 940 nm with surface decay lengths of 20 and 40 nm respectively. With this basic simulation the general trend of **decrease in scattering yield at large angles with proceeding cluster melting** is well reproduced. It still is important to keep in mind that neither initial cluster radius nor absolute values of slopes and threshold can be deduced from the measured data in this experiment.

In conclusion, this simulation reveals that **a cluster is not necessarily completely destroyed when fringes are absent in measured scattering patterns**. This observation agrees with the earlier presented result (section 4.2.3) that for large clusters in infrared pulses only a thin cluster shell expands upon hydrodynamic pressure of the hot electron cloud. The remaining core recombines to full neutrality after electrons migrate to the energetically preferred cluster center. Information about the cluster evolution on large timescales up to nanoseconds is probably prevented due to fringes hidden below 4 degrees, where scattering signal is missing due to the experimental setup. Even though the decreasing core seems to be the major part remaining, its further fate is still unknown. In corresponding ion TOF spectra the further existence of the cluster is witnessed on the entire measured time scale up to 1.5 nanoseconds. TOF spectra are investigated in more detail in the following section to get insight into the cluster dynamics on this extended time scale.

4.4.2 Ionization of clusters under surface ablation

In this section, strongly (peak power densities of $1.1 \cdot 10^{14}\,\mathrm{W/cm^2}$) IR-excited clusters with a substantial fraction of the core melted down are analyzed on an extended timescale up to one and a half nanoseconds of pulse separation. Therefore, the data was filtered for

- shots where no diffraction rings are visible in the CCD images, but exclusively strong fluorescence and diffuse scattering signal are detected (as in figure 4.17 ii). And for
- shots where high kinetic energies are detected in ion TOF spectra, as indicated by red areas in figure 4.4.

From the analysis in the previous section it is concluded that the cluster surface is melted to a degree where the resolvable fringe pattern falls into the detector center region at small angles where residual stray light and the detector hole overlay the signal. Additionally, these shots were filtered for corresponding TOF spectra which show clear evidence of cluster signal, to ensure that data from pure atomic xenon was not taken into account.

Time evolution of detector intensity (scattered light and fluorescence)

For each remaining shot the averaged detector luminosity is plotted run-wise over temporal pulse separation between IR-pump and XUV-probe pulse in figure 4.23 a. The overall number of filtered images increases with delay time. A substantial quantity of hits exhibits low and moderate intensity, mirroring the fact that the biggest amount of shots are recorded

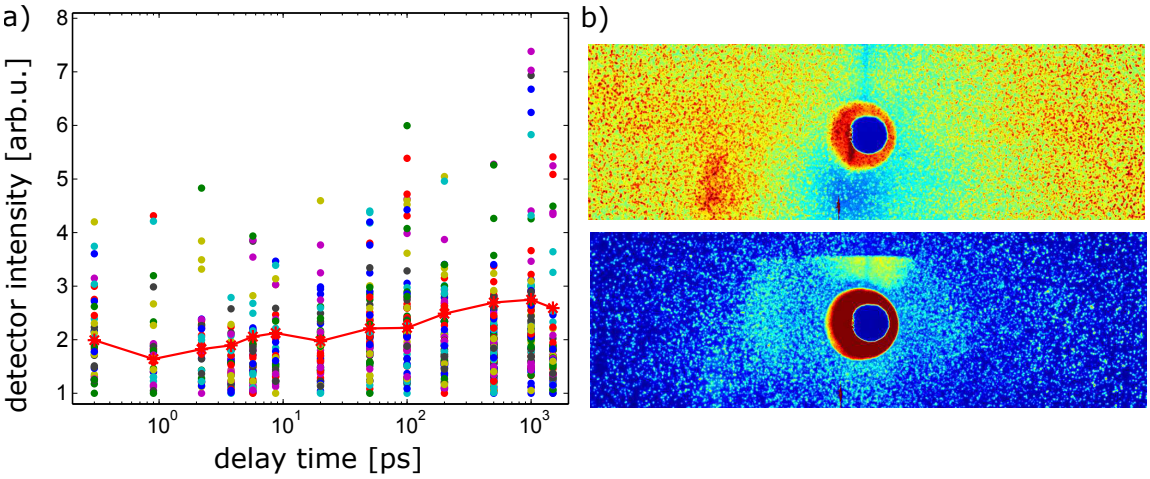

Figure 4.23: a) Integrated detector intensity for filtered shots in each run plotted over temporal pulse separation between IR-pump and XUV-probe pulses. Averaged values for one run are indicated by red stars. With increasing delay the high intensity shots gain in number and the maximum single-shot detector intensity rises. b) Filtered CCD images with highest (top) and one of the lowest (bottom) detector intensities respectively. The data was filtered on absence of scattering fringes and high kinetic energy tails of charge states in TOF spectra. Inhomogeneities in the images arise from residual scattering and detector artifacts as described in chapter 4.1.1 and figure 4.1.

from clusters hit in the focal wings and sides. The brightest images most probably result from large clusters hit in both beams focal centers. The peak intensity as well as the average luminosity increases with laser pulse delay time. Exemplary a high intensity and a low intensity CCD image are depicted in figure 4.23 b.

Two effects can explain the change in detector intensity with delay time:

- scattering contribution and
- fluorescence contribution.

On the one hand, shortly after laser excitation most probably only small clusters are melted to an extend where the scattering envelope has vanished towards small angles. Since the initial size of the cluster is unknown in this experiment it is very likely that larger clusters are filtered out by the special filter (no rings in scattering patterns, high kinetic energy ions in TOF spectra) at small Δt values because they are expected to need more time for substantial surface ablation. Bigger clusters lead to higher detector intensities as they scatter more strongly. However, as discussed in the previous section, with increasing delay time shell ablation proceeds. This results in a decrease in scattering signal at high angles and therefore to an overall decrease in detector signal.

On the other hand, in dense systems fluorescence is often suppressed due to quenching. Excited states which are available for radiative decay become depopulated by electron collisions. Upon particle expansion, these collisions become less probable and fluorescence frustration is abolished, leading to higher photon signal. Additionally, in a dense system photon reabsorption is frequent. Therefore, fluorescence is mostly collected from the cluster outer layers. As introduced in section 2.3.3, a recent experiment on Ar-Xe core-shell clusters revealed that fluorescence from the cluster core is emitted only from states with short lifetime, while fluorescence from the shell is emitted from many states and therefore

has a stronger contribution to the overall detected photon signal [100]. Since the ablation of the cluster evolves shell-wise on a long timescale, as analyzed in the previous section, there is continuously a new outer cluster layer and the fluorescence is expected to gradually increase until the process of shell ablation is completed.

Time evolution of ion TOF spectra (charge states and kinetic energies)

From the filtered scattering images where fringe signal is missing (cf. fig. 4.23 b and 4.17 ii) only little information can be drawn. However, in the corresponding ion spectra salient features mirror the nanoplasma evolution. The ion spectra averaged over every filtered shot for every pump-probe separation time are plotted in figure 4.24 a. Zooming in at zero flight time it shows that the light peak gains in height and width due to increased fluorescence. This behavior is in agreement with the increasing luminosity of the scattering screen described earlier. Looking at the entire TOF spectrum at short delay times (blue spectra), the Xe^{1+} peak is most prominent with large contribution from high kinetic ions. Towards later times it decreases and the distribution shifts towards higher charge states (red spectra). At latest delays Xe^{7+} and higher are protruding. The charge-state increase with Δt becomes most prominent when plotting the spectra's center-of-mass over delay time, as presented in figure 4.24 b. In this depiction the TOF transmission functions for each charge state are not taken into account due to the challenging assignment of charge states for ion yields in averaged spectra (see section 3.2.3). Therefore, it is expected that the average charge states in figure 4.24 b are slightly underestimated. However, the general trend of increasing average charge state with delay time is contained.

The shift towards higher charge states is a strong indication for recombination suppression. This finding was recently simulated with molecular dynamics simulations for an XUV/XUV pump-probe scheme on small xenon clusters [98]. Only in a dense, strongly coupled nanoplasma three-body recombinations are effective. Here, the hot electrons can release enough energy in collisions, so that recombination is possible. In a dilute plasma however, collisions are less probable and electrons cannot cool down and have too high energy to recombine. Therefore, in the late stages of cluster expansion the recombination is not possible which results in overall higher charge states detected.

The second main characteristic feature in the averaged ion spectra is that with proceeding delay time he overall spectrum resembles more and more an atomic one, irradiated exclusively by an FEL pulse. For comparison a spectrum from pure xenon gas is plotted at the top of figure 4.24 a. At large delay times, TOF peaks with high kinetic energies reveal that cluster components are still present. This gives evidence that the evolution of the excited nanoplasma lasts up to nanoseconds, even though not directly resolved in the corresponding diffraction images (compare fig. 4.21).

With increasing delay time the signal becomes more 'atom-like' because the cluster core becomes increasingly atom-like. While the cluster shell explodes off due to charge separation, the recombined neutral cluster core exhibits no large kinetic energy when hit by the probe pulse. An increasing 'atomization' of the ion signal reveals an increasing 'atomization' of the cluster core. This means that the neutral core disintegrates after bonds are breaking due to energy deposited in the cluster from the pump pulse.

The increase in light peak yield gives evidence that a transition from non-radiating recom-

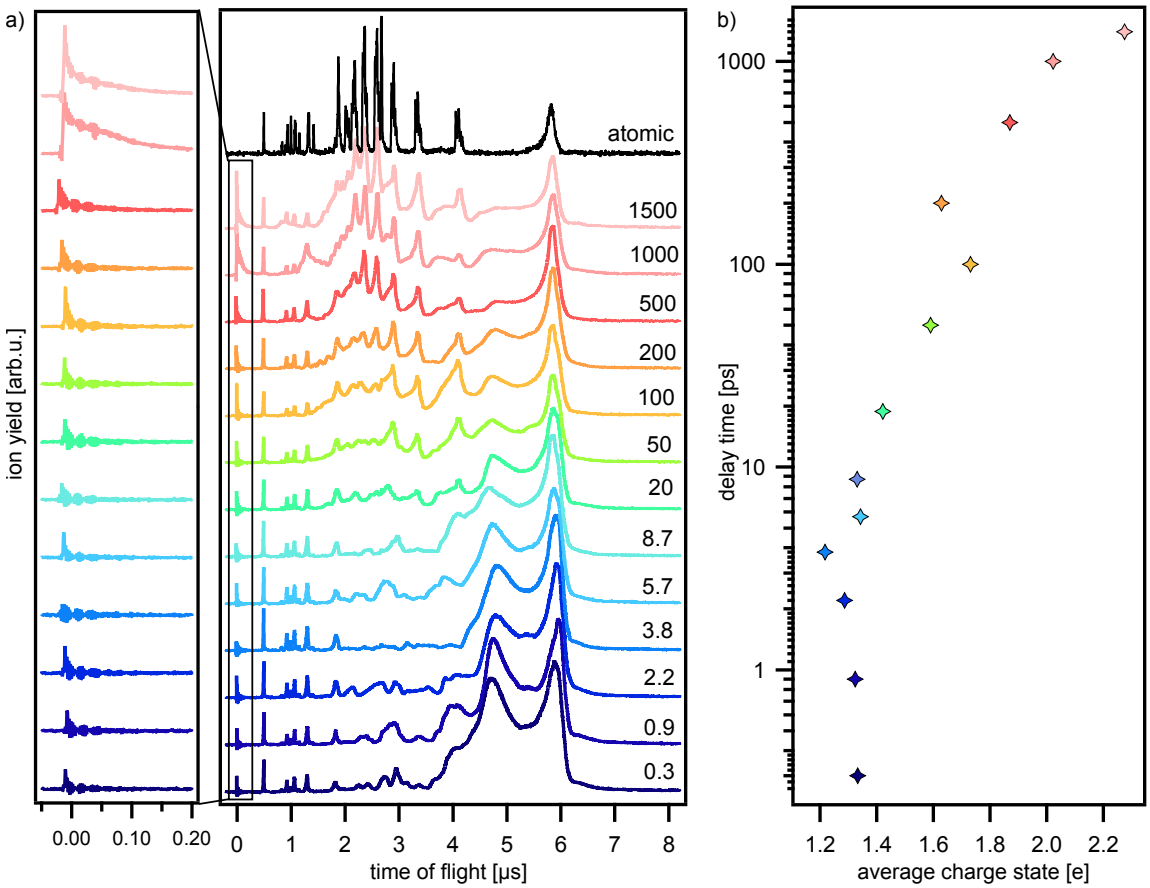

Figure 4.24: a) Filtered and averaged ion TOF spectra, taken in IR/XUV pump-probe configuration for varying delay times as indicated by numbers in picoseconds. The filter was set on absence of fringes in CCD images and high kinetic energy contribution in corresponding TOF spectra. Laser peak power densities were $1.1 \cdot 10^{14}\,\mathrm{W/cm^2}$ and $4.1 \cdot 10^{14}\,\mathrm{W/cm^2}$ for the IR and XUV pulses respectively. For comparison an atomic spectrum from xenon gas irradiated with an XUV beam only is included on top of the graph (black). b) Average charge state of each run, extracted from the averaged TOF spectra's center-of-mass. Note that the TOF transmission function is not taken into account here, due to the challenging assignment of charge states for the ion yield in averaged spectra.

bination and relaxation to radiative relaxation takes place. Strong shell ablation leading to images of the second category (compare figure 4.17 ii) results from clusters well hit by the pump IR pulse. A different picture arises for clusters less highly excited due to lower exposed power densities, which are subject of the next section.

4.4.3 Expansion of a neutral cluster core on the nanosecond timescale

One nanosecond after excitation by the pumping infrared pulse some xenon clusters feature a substantially new appearance. This is manifested in the third category of scattering patterns recorded, as introduced in figure 4.17 iii. They exhibit an unordered speckle structure - never before detected from spherical clusters. Some representative examples with azimuthally averaged intensity profiles are presented in figure 4.25. The fact that they appear earliest 500 ps after expansion initialization by the IR-pump pulse and the absence of

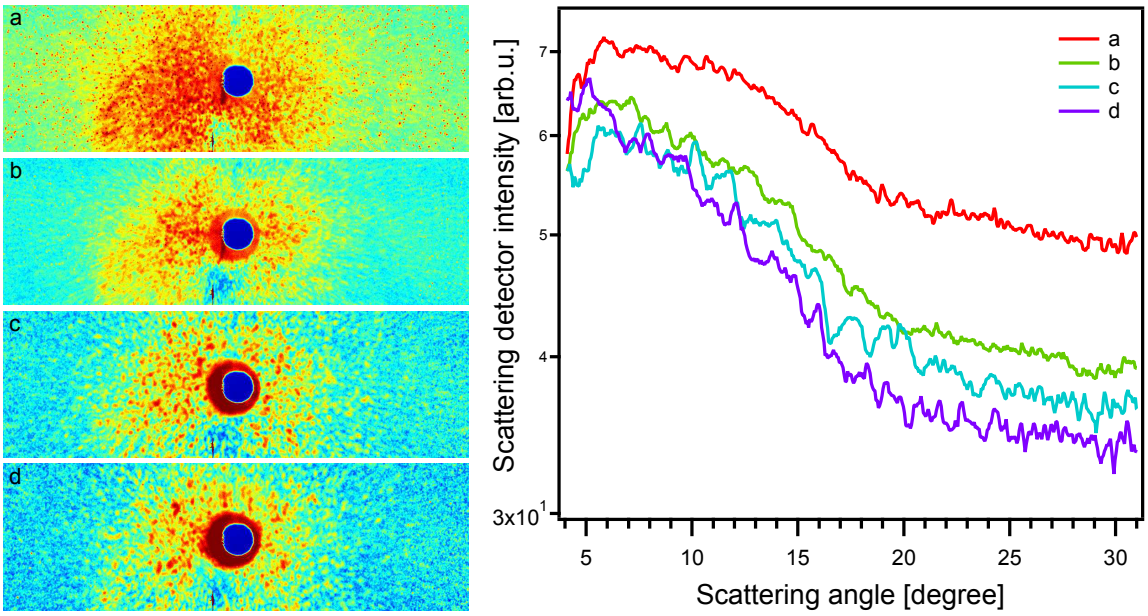

Figure 4.25: Several characteristic patterns with unsystematic speckle distribution, recorded upon XUV illumination 1.4 and 1.5 nanoseconds after IR excitation and their corresponding profiles of azimuthally integrated scattering intensity. The profile slopes exhibit an overmodulation with minima between 18 and 22 degrees scattering angle.

any ring structures indicates a different cluster evolution behavior than the above discussed surface melt-down (section 4.4.1). The question arises how exactly a cluster disintegrates after shell ablation and recombination of the cluster core to full neutrality.

The complexity of the speckle patterns prevents an exact retrieval of the disintegrating cluster shape. Nevertheless, as this section will show, pattern frequency and intensity envelope analysis allow to extract average parameters determining the particle appearance encoded in the scattering patterns. Comparison with Mie theory indicates how to interpret those speckle patterns. In ring-patterns from Mie calculations on spherical objects the oscillation of the pattern yields information about the particle size [38]. Additionally, the course of the amplitude is determined by the refractive index, which is directly coupled to the material density. This chapter will show that the same correlation is valid for speckle patterns. The shape and size of the speckles originate from the overall particle outline and average diameter while the amplitude modulation is a direct consequence of fluctuations in the particle density [166].

The arising of speckle appearance can be attributed to a ring break-up, originating from a significant drop in particle density. Small-angle scattering simulations (SAXS) were performed in three steps to visualize this behavior:

1. First, with the example of a linearly expanding dilute cluster with uniform density.

2. In a second step, this spherical cluster is subdivided in smaller units to account for the density fluctuations in the evolving recombined plasma. The radius of the sub-clusters in this model system exemplifies the size range of an internal cluster-density modulation.

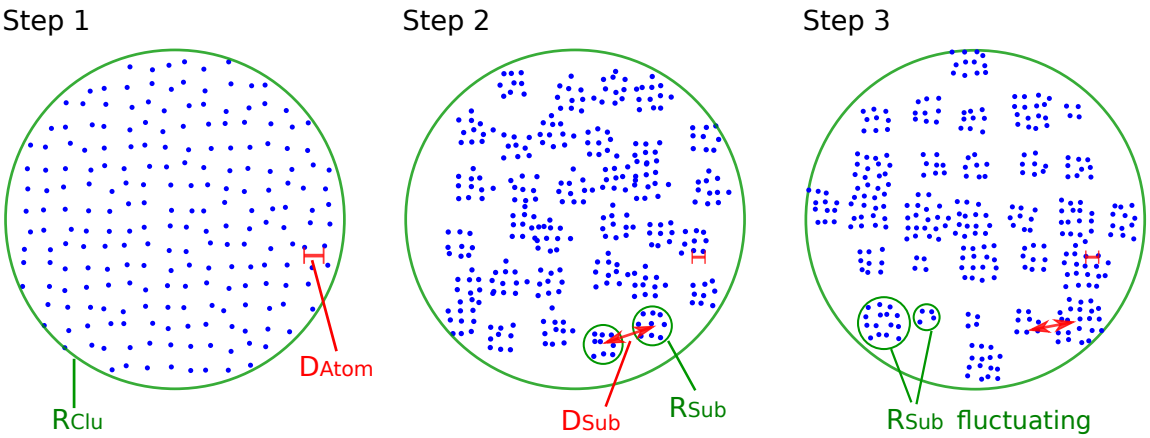

Figure 4.26: Scheme of simulated model clusters. Step 1: Clusters are modeled with amorphously distributed point scatterers of average distance d_{Atom} within a sphere of radius R_{Clu}. Step 2: The spherical cluster is subdivided in smaller sub-spheres with radius r_{Sub} and distance D_{Sub}. Step 3: A size distribution is applied on the radii of the sub-clusters.

3. In a third step, a size distribution is applied to the sub-clusters to tune this approval toward more realistic appearance.

A visualization of the model systems used in the three different steps is illustrated in figure 4.26. With the help of scattering simulations from these computed cluster geometries, it will finally become possible to understand the underlying shape of the measured xenon clusters.

Step 1: Small-angle x-ray scattering simulations from an expanding gas ball

Basic simulations with 2D-FFTs of projected sample outlines are a practical tool for fast analysis of dense objects, where the distance between the single scatterers is smaller than the impinging wavelength (as used for simulations in figure 4.21 b). Since the distance between atoms is thereby not taken into account, more sophisticated modeling is needed for dilute systems. An adequate method are small-angle scattering calculations from point-scatterers with freely tunable separation. For the simulation a MATLAB code was written based on the concept introduced in [36]. The formalism and code are described in detail in appendix A. Point-scatterers representing xenon atoms were ordered on a three-dimensional grid within a radius R_{Clu} (see fig. 4.26). The scatterer distance is denoted as d_{Atom}. In order to gain amorphous atom distribution the point-scatterer position was allowed to randomly vary from its initial position on the grid by up to $d_{Atom}/2$. The scattering signal was calculated in scalar numerical approach [36]. The experimental values of XUV wavelength $\lambda = 13.6\,\text{nm}$, detector pixel size $p = 0.069\,\text{mm}$, and distance between interaction region and detector $L = 61.64\,\text{mm}$, are used for all simulations. Therefore, simulated and measured patterns are directly comparable. The angle resolution was set to 0.2 degrees in radial and azimuthal direction respectively. All images were calculated up to 33 degrees scattering angle.

A rigid sphere with equally expanding point-scatterers was implemented as model cluster. While this model is a very basic approximation for the expansion of the neutral cluster

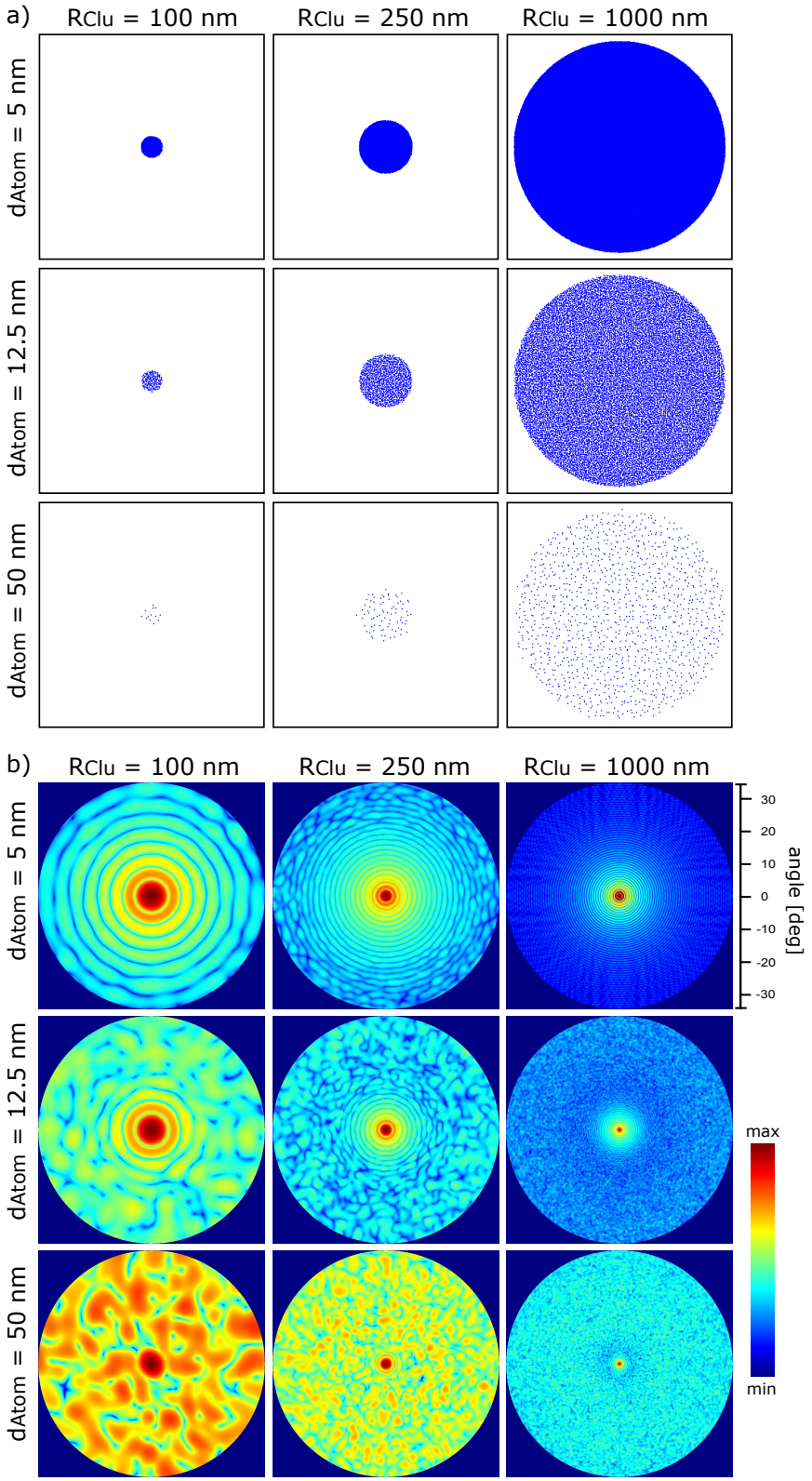

Figure 4.27: Simulation of light scattering on amorphously distributed scatterers. a) Cut through atom distribution. Atomic distances d_{Atom} are increasing from top to bottom and cluster radii R_{Clu} from left to right. b) Corresponding calculated scattering patterns. For better visibility all images are normalized to their maximum value. Therefore, absolute intensity values are not comparable. With decreasing particle density (top to bottom) the ring-patterns vanish at high angles in favor for speckles. Particle radius increase results in decrease of mean fringe spacing and speckle size respectively.

core, it provides an intuitive understanding for the underlying mechanism. In a first step the influence of cluster size and atomic distance on the diffraction image is investigated. Figure 4.27 shows central cuts through modeled clusters (a) and their corresponding simulated scattering patterns (b). From top to bottom d_{Atom} is increased from 5 to 50 nm. For dense particles (top row), coherent scattering gives pronounced interference ring patterns. For larger atomic distances (center row), fringes break up at large angles and speckles appear. Speckles arise from objects with amorphousness (for surfaces often denoted as roughness) larger than the laser wavelength. Hence, the scattered exit waves do not interfere constructively at the same scattering vector value q. In the bottom row of figure 4.27, where d_{Atom} is largest, the rings disappear almost completely towards low frequencies in the pattern center and mainly 'homogeneous' speckle patterns are visible. The angle where the ring signal transforms into speckle signal is dependent on the average distance of all point-scatterers to each other. This leads to the conclusion that the experimentally recorded speckle images result from a cluster where the density has decreased sufficiently, such that the laser wavelength becomes sensitive to the internal particle disorder and density fluctuations.

The here presented simulations mirror the detector geometry used in the experimental setup for this thesis. The maximum simulated scattering angle is 33 degrees. In the simulation the average atomic distance has to increase from $d_{Atom} = 0.48$ nm (Wigner-Seitz-radius of solid xenon: $r_W = 0.24$ nm) by one order of magnitude to $d_{Atom} = 5$ nm for speckles to become visible at maximum angles. For ring-structures to disappear completely up to 4 degrees - corresponding to the beamstop area in the detector - d_{Atom} even has to rise to 50 nm (bottom row), e.g. by two orders of magnitude.

In figure 4.27 column-wise from left to right, the size of the particle is increased from a radius of 100 to 1000 nm. While for dense targets the fringe spacing gets smaller (top row), for dilute particles analogous the speckle structure becomes finer (bottom row). The average size of the speckles is inversely proportional to the radius of the spherical cluster. Laser speckle analysis is mainly common in rough surface examination [167]. Only in the last years it gained in significance for imaging of finite target systems. From theoretical calculations on a spherical object with rough surface [168] and independently on a two-dimensional structure of spherical apertures [37] the relation between speckle and overall cluster radius can be deduced to approximately

$$R_{Clu} \approx \frac{\lambda L}{\pi p} \frac{1}{R_{Sp}} \tag{4.13}$$

with the impinging wavelength λ, the distance between detector and interaction region L, the detector pixel size p, and the mean speckle radius R_{Sp}.

For the determination of mean speckle size several approaches can be used, e.g. morphological analysis of binary images from pattern thresholding [169, 37]. This procedure is however not recommendable for patterns with an intensity modulation where lower intensity speckles might be overlooked. One of the most frequently applied methods is to extract the mean speckle size from the normalized autocovariance function[4] $C(x, y)$ of the scattering pattern intensity $I(x, y)$ [170]

$$C(x, y) = \frac{\langle I(x, y)^2 \rangle - \langle I(x, y) \rangle^2}{\sum(\langle I(x, y)^2 \rangle - \langle I(x, y) \rangle^2)}. \tag{4.14}$$

[4]The normalized autocovariance function corresponds to the autocorrelation function.

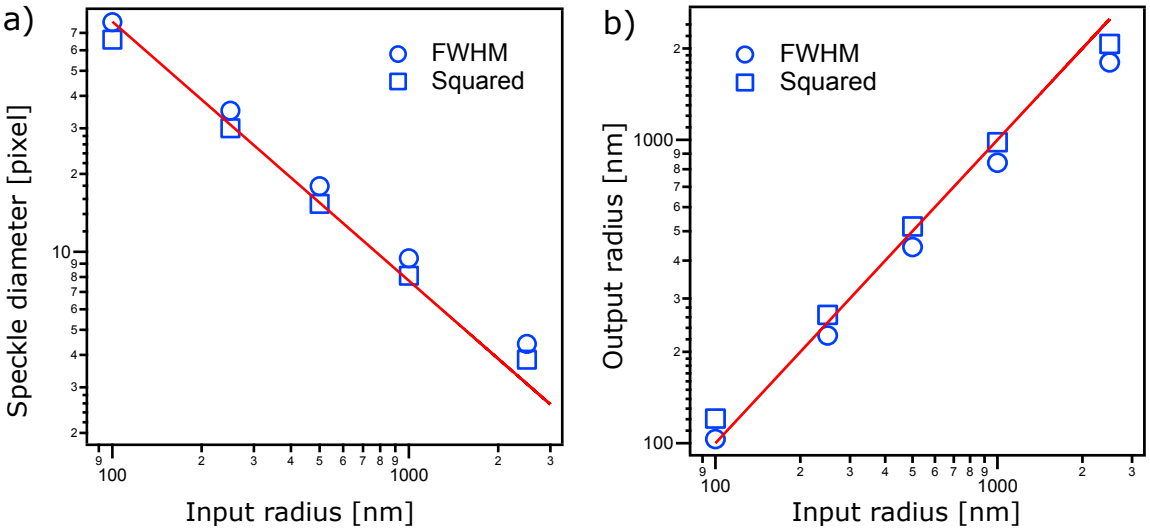

Figure 4.28: a) Full width at half maximum (FWHM, round symbols) and beam waist ($1/e^2$, squared symbol) of the mean speckle size, extracted from simulated scattering patterns plotted over radius of model clusters. b) Corresponding calculated radii over radius of model clusters. The red curve shows the dependence calculated with equation 4.13.

This technique was used here and cross-checked on simulated data. The sums of the normalized autocovariances of all rows and columns in the pattern were fitted by a Gaussian distribution. The full width at half maximum (FWHM) and the beam waist ($1/e^2$) of this Gaussian distribution were determined in pixels and converted to sphere radius with equation 4.13. It is inevitable to cross-check the reliability of the applied method and the utilized code. Therefore, the scattering patterns were calculated for several dilute gas balls with varying cluster radius. Subsequently, the values of $2R_{Sp}$ were extracted from the simulated data. In figure 4.28 mean speckle size and therefrom calculated radius are plotted over the radius that was fed in the SAXS simulations. The red curve indicates values calculated with equation 4.13. For small clusters of 100 nm radius, the extracted size is slightly overestimated and the FWHM value fits better than the $1/e^2$ value. For larger clusters from 500 nm radius onwards, the size is underestimated and the beam waist value gives a more correct result.

This method was also applied to the measured pattern presented in figure 4.29. Beamstop and dead pixels were masked before calculation of the normalized autocovariance function. A mean speckle size of $2R_{Sp} = 8.74$ FWHM and $R_{Sp} = 8.061/e^2$ was extracted from the pattern. Corresponding cluster radii of $R_{Clu} = 884.8\,\text{nm}$ and $R_{Clu} = 960.2\,\text{nm}$ are calculated with equation 4.13, with $\lambda = 13.6\,\text{nm}$, $L = 61.64\,\text{mm}$, and $p = 0.069\,\text{mm}$. A simulated speckle pattern from a gas ball of this radius $R_{Clu} = 950\,\text{nm}$ is depicted in figure 4.29 as juxtaposition to the experimental data. The speckle sizes seem to match quite well. Immediately apparent becomes the deviation of pattern intensity at high spatial frequencies between measured and simulated images. The computed image exhibits a constant average intensity distribution. In radial profiles of recorded images (see figure 4.25 b) the envelope of the amplitude exhibits a modulation. The scattering intensity shows a decline up towards around 20 degrees and stays relatively constant from this angle onwards. This behavior demonstrates that the simple model of an equally expanding sphere shows some general

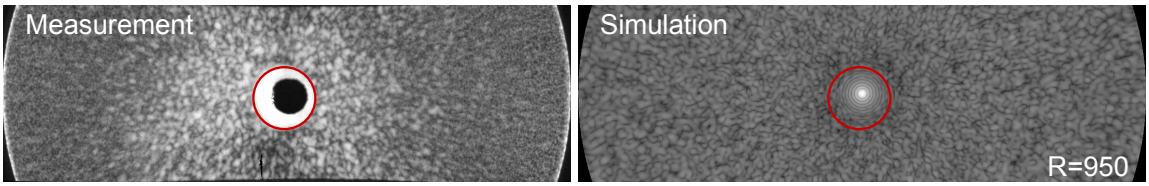

Figure 4.29: a) Diffraction pattern of a disintegrating xenon cluster imaged 1.4 ns after infrared-laser excitation. b) SAXS simulations from a sphere of equally distributed amorphous point-scatterers (as described in the text as Step 1) with $d_{Atom} = 50\,\text{nm}$ and R_{Clu} chosen to be 950 nm. The dark red circle indicates the area where the scattering signal is hidden due to stray light. The mean speckle size matches well for calculated and recorded images. However, the relative intensity distributions show clear deviations, e.g. the measured pattern exhibits an intensity modulation which is absent in the simulation.

trend, but is insufficient to describe the entire cluster evolution witnessed in the experiment.

Step 2: SAXS simulations with density division in sub-clusters

The modulated diffraction-pattern envelope implies an underlying sub-structure in the particle density distribution [166]. The above cluster model with on average equally spaced point-scatterers was refined to get a handle on this density fluctuations. The sphere was divided into several sub-clusters with internal amorphous atom distribution, as sketched in figure 4.26 step 2. In a first loop the positions of the sub-clusters were arranged with spacing D_{Sub} within a sphere of radius R_{Clu}. In a second loop the sub-spheres with radius r_{Sub} and atomic distances d_{Atom} were generated and arranged on the positions just calculated. With the overall radius R_{Clu} and the atomic distance d_{Atom} kept constant, the influence of sub-cluster size r_{Sub} and spacing D_{Sub} on the scattering pattern is demonstrated in figure 4.30. Slices through the particle center are presented in (a) and corresponding calculated scattering patterns in (b).

For all model systems in figure 4.30, the outer particle radius is kept constant at $R_{Clu} = 250\,\text{nm}$[5] and the atomic distance within a sub-cluster is held at $d_{Atom} = 5\,\text{nm}$. From top to bottom row the distance between debris centers D_{Sub} increases from 25 to 100 nm. Analogous to a change in d_{Atom} in figure 4.27, the overall particle internal disorder increases together with the surface roughness. Hence, the scattering ring pattern at large scattering angles vanishes in favor of speckles due to missing constructive interference at the same propagation vector value. The average speckle size is not affected since it is only dependent on the overall cluster radius R_{Clu}. The radius of the sub-clusters r_{sub} raises column-wise from 12.5 to 50 nm in figure 4.30. While in the left column of figure 4.30 b the simulated images do not exhibit a clear envelope modulation, it becomes prominent in the second column from a ring-shaped minimum at around 20 degrees. In the third column the first minimum is shifted to smaller angles and higher order minima appear. The angle of the first envelope minimum θ_{min} is related to the size of the mean scatterer r_{Sub} by the Airy pattern equation [32, 33]:

$$r_{Sub} = 1.22 \cdot \frac{\lambda}{2\sin(\theta_{min})}. \tag{4.15}$$

[5] For good visibility of the speckle size, a cluster radius of $R_{Clu} = 250\,\text{nm}$ was chosen for the simulations. This is not to be confused with the measured size of $R_{Clu} = 950\,\text{nm}$.

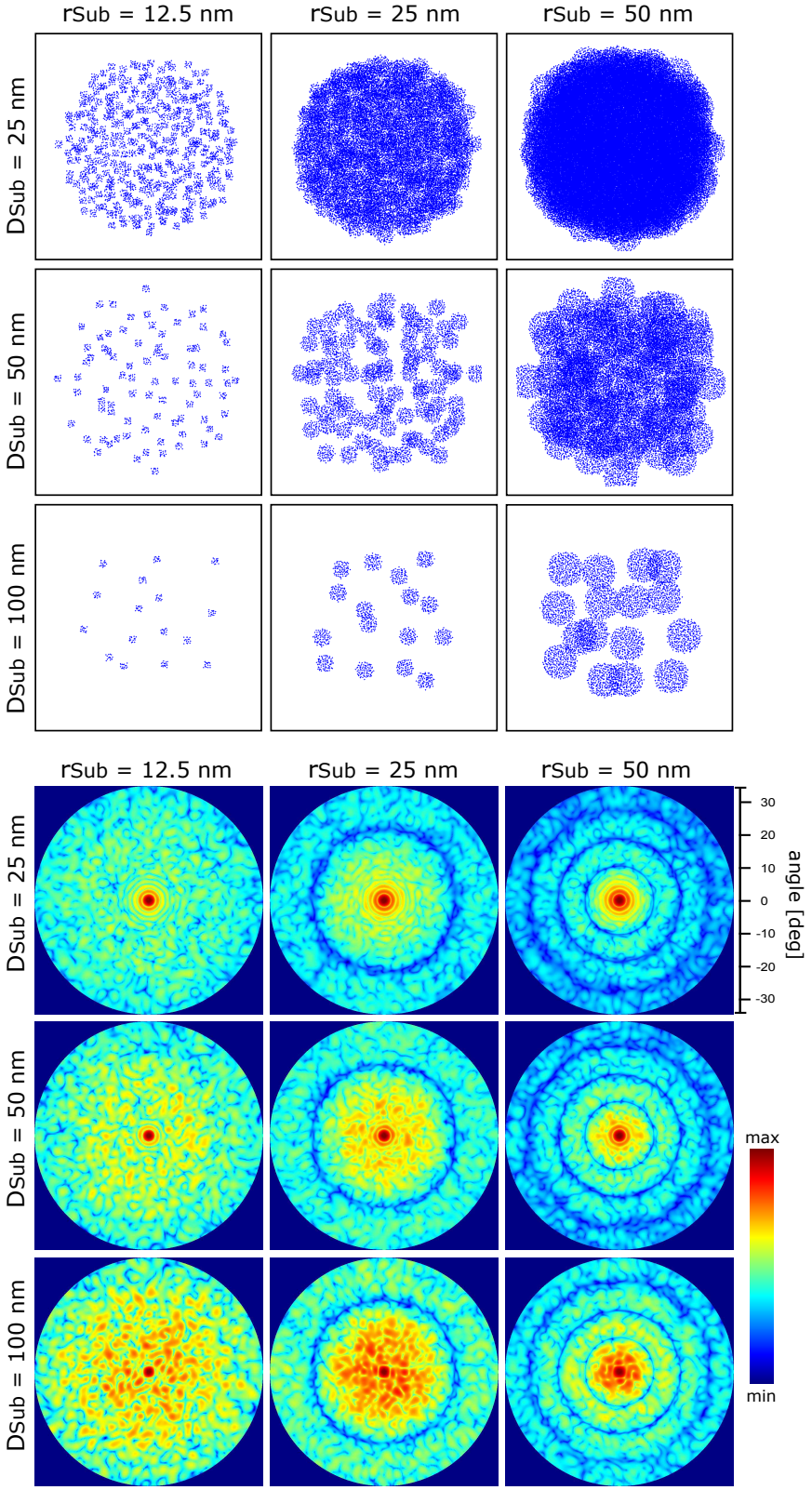

Figure 4.30: Simulation of scattering on spheres with amorphously distributed sub-spheres of scatterers. a) Slices through the particle center. The radius of the sub-spheres r_{Sub} is increased from left to right. The distance of the sub-spheres D_{Sub} in increased from top to bottom. Overall cluster radius and atom spacing are kept constant ($R_{Clu} = 250\,\text{nm}$ and $d_{Atom} = 5\,\text{nm}$). b) Corresponding scattering patterns. From top to bottom scattering rings in the pattern center break up in favor for speckles. From left to right an overmodulation with decreasing fringe spacing appears. The overmodulation's first minimum θ_{min} shifts to smaller angles with increasing sub-sphere radius.

With this relation the mean density fluctuation range can be deduced from measured patterns. From a detected angle of about 20 degrees (see radial profiles in figure 4.25) a value of $r_{Sub} \approx 25\,\text{nm}$ is calculated with an XUV wavelength of 13.6 nm.

Following equations 4.13 and 4.15, simulations of a 950 nm radius sphere with 25 nm radius sub-clusters should give a reasonable match with the measured pattern in figure 4.29. The remaining unidentified parameters are the distances d_{Atom} and D_{Sub}. The only information known up to this point is that the distance between the sub-spheres D_{Sub} significantly affects at which angle the ring pattern transforms into speckles. Since the transition is not visible in the measured pattern, it is expected that it is located at angles lower than 4 degrees, which are covered with residual light. Therefore, only an upper limit for D_{Sub} can be given.

To simulate cluster with certain density, several combinations of d_{Atom} and D_{Sub} values are applicable. The relative change in degree of density modulation, e.g. the depth of the modulation minima, is influenced by the ratio of the density of the sub-spheres to the density of the entire cluster. Several radial profiles of calculated scattering patterns with differently strong density modulation but constant number of atoms $N = 1.9 \cdot 10^6$ are depicted in figure 4.31. Note that the length scale of the fluctuations is kept constant by the sub-cluster radius $r_{Sub} = 25\,\text{nm}$ (manifested in the angle of the envelope minimum). Also the speckle size stays equal due to a constant cluster radius of $R_{Clu} = 950\,\text{nm}$. With decreasing atomic distance and correlated increasing distance between the sub-clusters, the envelope minimum becomes more pronounced due to a stronger density fluctuation. The observation that the minimum in the recorded scattering profile is rather weakly pronounced (see figure 4.25 b) points towards a weakly developed density modulation.

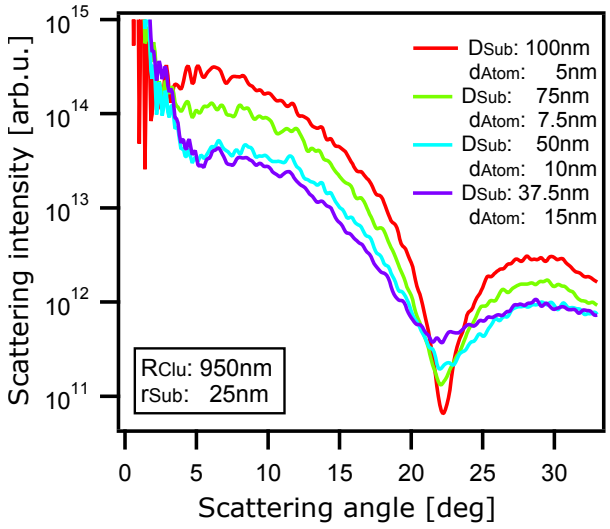

Figure 4.31: Scattering profiles from model clusters with equal size ($R_{Clu} = 950\,\text{nm}$) but of different density distributions are presented, gradually varying from systems with few dense sub-spheres (red curve) to a cluster with many dilute sub-spheres (violet curve). The amount of atoms in the system stays constant at $N = 1.9 \cdot 10^6$ atoms. Therefore, the density of the overall cluster does not change. The radial profiles of the simulated scattering patterns demonstrate a stronger pronunciation of the envelope modulation for stronger density fluctuations. The length scale of the particle fluctuation is constant for all envelopes ($r_{Sub} = 25\,\text{nm}$).

Step 3: SAXS simulations with size distribution of the sub-clusters

A different effect which makes the minimum become less deep is a size distribution of the sub-particles. The model of a cluster divided into sub-spheres is suitable to get an intuitive understanding of the influence of density modulations on diffraction patterns. However, it is certainly not appropriate to model the exact cluster internal structure. The cluster model is once more refined (see figure 4.26 step 3) by applying a size distribution on the sub-clusters to make the subject more realistic. Figure 4.32 presents several spectra from simulations with sub-particles fluctuating around 25 nm radius. With increasing size distribution the minimum in the scattering envelope becomes less pronounced (from blue to red curve). This result points towards a wide variation of density-modulation ranges inside the measured particle. However, the mean size range of the sub-clusters can be determined from the amplitude envelope outline of the recorded patterns, as evident from equation 4.15.

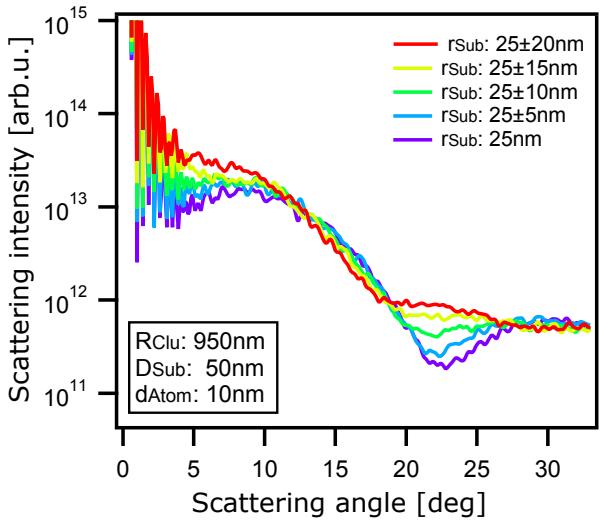

Figure 4.32: Radial profiles of simulated scattering patterns from model clusters with equal size (R_{Clu} = 950 nm) and equal internal density. Simulated scattering profiles of model systems with a sub-cluster size distribution. In step 3 of the simulation (details see text) the radius of the sub-spheres r_{Sub} is allowed to vary. While for small radius variations the minimum of the envelope modulation in the scattering profile is strong (violet curve), for a larger size distribution the envelope minimum softens (red curve).

The complexity of speckle diffraction images makes their characterization a very challenging task. Particle shape retrieval by direct comparison with theoretical calculations is often intricate. The interplay of several length scales and distributions in real space and their correlated effects on the pattern in Fourier space prevents exact determination of the object's architecture. Still the **mean particle size** and **average density fluctuation range** are well extractable from speckle analysis.

Figure 4.33 presents the juxtaposition of a measured speckle pattern (in color see figure 4.25 b) with a simulated one. As introduced above, from the means speckle size an average cluster radius of about 950 nm could be extracted from the measured pattern. The angle of the first envelope minimum in the measured scattering pattern leads to an estimated mean density fluctuation range of about 25 nm. To simulate the scattering pattern in figure 4.33 b a model cluster with the parameters R_{Clu} =950 nm, r_{Sub} =25 ± 15 nm, D_{Sub} =50 nm, and d_{Atom} = 4 nm was generated and is depicted in figure 4.33 d. The model cluster contains $N = 3.2 \cdot 10^7$ atoms. This corresponds to a cluster of $R = 75.9$ nm with solid-state density. Speckle appearances and azimuthally integrated intensity profiles are rather well matching. This simulation illustrates that despite the very approximative cluster model the main sizes are well extractable from the speckle patterns.

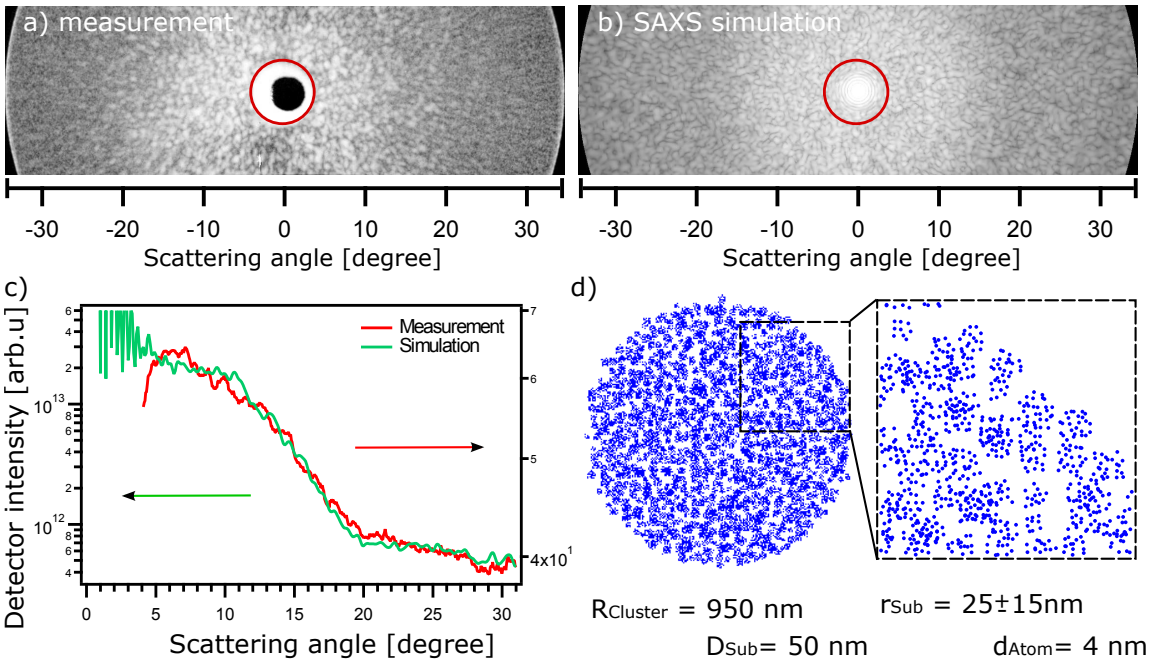

Figure 4.33: a) Typical speckle diffraction pattern recorded 1.4 ns after infrared laser impingement. See 4.25 b for color. b) Simulated pattern calculated in small angle x-ray scattering approach from a d) modeled cluster with R_{Clu} =950 nm, r_{Sub} =25 ± 15 nm, D_{Sub} =50 nm, and d_{Atom} = 4 nm. c) With this system SAXS simulations can well reproduce the measured speckle pattern in size and slope.

Conclusion

The evolution of expanding single xenon clusters was imaged. Large individual clusters were produced in supersonic expansion of 10 bar xenon at 180 K trough a conical nozzle, resulting in a log-normal size distribution between 25 and 1000 nm radius with a maximum at 34 nm radius. The particles were turned into a nanoplasma by a high power IR pulse with peak intensities of $1.1 \cdot 10^{14}$ W/cm^2. The expansion was imaged with an ultrashort FEL pulse of $4.1 \cdot 10^{14}$ W/cm^2. By snapshotting several points in time, ranging from femtoseconds up to nanoseconds, two different expansion mechanisms were identified.

- Following strong particle excitation and nanoplasma formation, quasi-free electrons migrate to the energetically preferred particle center. Efficient recombination leads to a net-neutral core embedded in a highly charged shell. At the picosecond timescale the xenon cluster gets skinned. Depending on the laser power density, a decrease of scattering signal at high detection angles with increasing time delay mirrors the accompanied softening of the cluster surface.

- The remaining net-neutral nanoplasma can efficiently recombine and stays in the interaction region up to nanoseconds. In slow motion its density decreases and internal density fluctuations build up. Diffraction images of speckle patterns are representative of this second stage of cluster expansion. Analysis of measured average speckle size and pattern intensity envelope modulation reveal the mean cluster size and range

of internal density fluctuations at the time of detection. Simulations indicate that after a nanosecond the neutral cluster core remains as expanded gas ball with measurable internal density fluctuations.

These findings from dynamic diffraction imaging extend the picture of laser-matter interaction into the nanosecond time scale. Here structural principles are discovered, which are up to date unexplored in homogeneous clusters.

Chapter 5

Summary and outlook

In this thesis, the ionization and expansion dynamics of large, single xenon clusters irradiated with highly brilliant laser pulses was studied. The method of single-shot single-cluster imaging in coincidence with ion time-of-flight (TOF) spectroscopy was applied. It enables to characterize laser-particle interaction in unprecedented detail by eliminating the influence of the laser focal volume intensity and particle size distribution. Very large clusters were produced in supersonic expansion of 180 K xenon gas with 9.8 bar backing pressure trough a conic nozzle of 200 µm orifice and 4° half opening angle. The resulting particle radius was ranging between 25 and 1000 nm. The experiments were performed at the free-electron laser in Hamburg (FLASH) at beamline 2. Ultrashort (100 fs) extreme ultraviolet (XUV) pulses delivered were focused to a spot size of 20 µm. The maximum power density in the focal volume reached about $4.1 \cdot 10^{14}\,\mathrm{W/cm^2}$. Additionally, an infrared (IR) laser with wavelength of 800 nm and pulse length of 80 fs was used. With a focal spot size of 90 µm power densities around $1.1 \cdot 10^{14}\,\mathrm{W/cm^2}$ were reached.

Three different excitation schemes were applied in order to examine different processes and timescales of laser-cluster interaction:

1) Particles were irradiated by either a single IR or a single XUV pulse only.

2) The cluster disintegration was induced by an XUV pump pulse and probed with an IR pulse in order to map the Mie resonance in the cluster nanoplasma.

3) Cluster fragmentation was initiated with an IR pulse and different disintegration states were snapshotted with a delayed XUV pulse.

In the first part, the response of the cluster was investigated in dependence on the cluster size and material, as well as the laser power density and wavelength. For clusters irradiated with IR or XUV pulses only, almost identical TOF spectra with similar charge state yields and kinetic energy distributions were found. Also xenon, argon, and silver clusters in FEL pulses resulted in similar TOF spectra.This reveals that from a certain cluster size on the cluster dynamics are universal, almost independent of laser wavelength and cluster component. This behavior leads to the conclusion that initial ionization mechanisms play a minor role and nanoplasma processes like e.g. electron collisions take the lead.

In the second part, the timescale of the experiment was extended up to one and a half nanoseconds with pump-probe technique. The XUV pulse induced cluster disintegration and therefore a lowering of the overdense particle density. The temporal delay of the IR pulse was scanned with respect to the FEL pulse arrival time in order to probe the Mie resonance. A characteristic peak delay time of 6.3 ps was found for cluster sizes ranging around 34 nm in radius. The large peak width and therefore plasmon lifetime of 5 ps is an indication for a shell-wise density decrease. By mapping the focal volume it could be shown that the characteristic delay time does not change significantly with XUV laser power density. This behavior is in agreement with calculations using the nanoplasma model. With the same model the average charge state $\langle q \rangle$ was determined to $\langle q \rangle = 2.0$, fitted to radius dependent peak delay time measurements. The delay time increases from 3.9 ps to 7.0 ps for clusters of average 28 nm radius to 40 nm radius.

In the third part, the disintegration of large xenon clusters irradiated with intense IR pulses was imaged by XUV scattering. Following strong particle excitation and nanoplasma formation, quasi-free electrons migrate to the energetically preferred particle center. Efficient recombination leads to a net-neutral core embedded in a highly charged shell. On the picosecond time scale, a major part of the xenon cluster has been skinned by a rather thin outer ionic shell in a fast expansion. This shell-ablation is mirrored in the recorded diffraction patterns by a vanishing of fringe signal and decrease in scattering signal at high scattering angles within tens of picoseconds. In basic simulations using 2D Fourier transformations of particle outlines with softened surface these changes were identified as proceeding shell ablation, leaving a shrinking cluster core behind. The remaining net-neutral nanoplasma can efficiently recombine and stays in the interaction region up to nanoseconds. Its density decreases slowly and density fluctuations occur, leading to speckle patterns with intensity modulations which appear from 500 ps on. Despite the high complexity of the speckle patterns, it was shown that the overall particle size and internal density fluctuation range can be derived by simple image analysis procedures. The findings from dynamic diffraction imaging extend the picture of laser-matter interaction in to the nanosecond time scale, where structural signatures were identified which were up to date not explored in homogeneous clusters.

In the dynamic imaging experiments of this work, which used an IR pump pulse, the initial cluster size and exposed focal flux are not well characterized since the initial image of the particle is missing. An experimental improvement could be achieved by additional imaging of the cluster at the time of pump-pulse arrival. Therefore, the IR pulse would have to be substituted by an XUV pulse in order to record an initial scattering pattern which facilitates a precise determination of the initial cluster state. The entire process of cluster dynamics could be filmed by capturing the initial and various intermediate states of the complete sample disintegration process. Up to date two major criteria limit this approach: (1) To follow the entire sample disintegration both, XUV-pump and XUV-probe beams need to be separated on an extended timescale up to nanoseconds. (2) Two separate images need to be recorded which are only separated by picoseconds. In our group, we have launched a project which addresses both limitations and will make ultrafast 'movies' of free nanoparticles feasible in future experiments.

XUV/XUV pump-probe experiments are currently possible at the FLASH facility with the autocorrelator split-and-delay unit at beamline 2 [171]. Here, one beampath can be temporally delayed from -3 ps up to $+15$ ps with respect to the other. The temporal

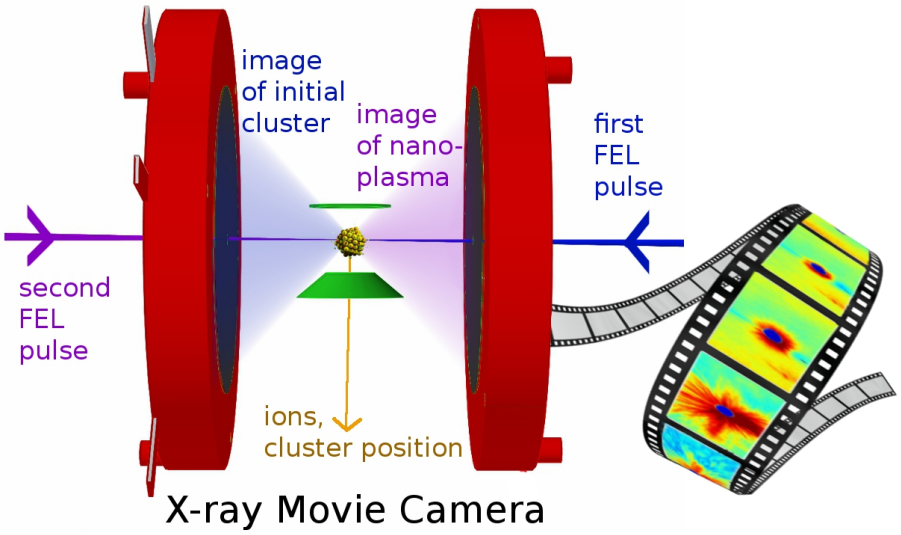

Figure 5.1: Schematic setup of the 'X-ray movie camera'. From [172]. The FEL beam is split and both beam paths are delayed with respect to each other. They are focused onto the particle from opposite sites consecutive producing separate diffraction patterns on two opposing detectors.

delay range is limited due to setup which is based on grzing incidence reflection. To push XUV/XUV experiments toward a longer timescale, a more compact split and delay unit has been developed in our group and will be installed permanently into beamline 1 at FLASH until July 2015. The DESC (**De**lay **S**tage for **C**AMP) system is based on multilayer mirrors. While multilayer mirrors only allow for a narrow wavelength range to be reflected, they effectively shorten the beampaths due to normal incidence reflection leading to a more compact geometry. With the DESC system XUV/XUV pump-probe experiments in a range up to several 100 ps will be feasible.

The second limiting criteria for the recording of molecular movies up to date is the read-out time of the scattering detector. In collinear pump-probe geometry both scattering patterns consecutively fall on the same detector where they superimpose and are recorded as one image. To circumvent this problem, in our group an 'X-ray movie camera' is envisioned and will be commissioned at FLASH in October 2015. Here, in a pump-probe setup the XUV beam is split and delayed and both pulses are focused onto the particle from opposite sites, see figure 5.1. Two separate diffraction patterns are recorded consecutively from two opposing detectors, similar as proposed in [173]. The overlay of both scattering patterns is minimized due to the geometry under 180 degrees. The knowledge about initial cluster size determined from the first image and at a later point in time from the second image would enable to determine the exact cluster disintegration process. The here presented setup will open the possibility to record a fast 'movie' from an unsupported nanoparticle in free flight.

Appendices

Appendix A

Small angle scattering code

All small angle scattering simulations in this thesis where performed in MATLAB with a code adapted from [36]. To model a xenon cluster with amorphously distributed atoms the following procedure was used: Point-scatterers were ordered at positions with coordinates r_x, r_y, and r_z on a three-dimensional grid with distance d_{Atom}. Only the atoms within a sphere of radius R_{Clu} were taken into account. To distribute the atoms amorphously they were randomly displaced by a maximum of $d_{Atom}/2$ in all three directions in space from their initial position.

```
%% IA Generate model cluster as sphere of point-scatterers on a 3D grid
clear;   clc;
RClu=35;            % radius of the core
dAtom=7;            % distance between atoms
atom=1;
box=2*RClu+1;
Cluster=zeros(box,4);
for x=(-RClu:dAtom:RClu)
    for y=(-RClu:dAtom:RClu)
        for z=(-RClu:dAtom:RClu)
            rx=x;  ry=y;  rz=z;
            R=sqrt(rx^2+ry^2+rz^2);
            if R <= RClu
                 Cluster(atom,1)=rx+(0.5-rand(1)*dAtom);
                 Cluster(atom,2)=ry+(0.5-rand(1)*dAtom);
                 Cluster(atom,3)=rz+(0.5-rand(1)*dAtom);
                 atom=atom+1;
            end
        end
    end
end
AtomInClu=atom-1;
ClusterIn=Cluster(1:AtomInClu,:);
scatter3(ClusterIn(:,1),ClusterIn(:,2),ClusterIn(:,3));
set(gca,'DataAspectRatio',[1 1 1]);
```

To model a xenon cluster with internal density fluctuations, the above model was refined by subdividing the cluster into several sub-spheres. Therefore, first the positions of the sub-spheres were ordered on a three-dimensional grid with distance D_{Sub} within the cluster of radius R_{Clu} and the positions were randomly displaced by a maximum of $D_{Sub}/2$ in all three directions in space from their initial position. Subsequently on these positions sub-spheres with radius r_{Sub} are generated with point-scatterers of distance d_{Atom} with random displacement of maximal $d_{Atom}/2$.

```
%% IB Generate sphere of point scatterers subdivided into sub-spheres
clear; clc;
RClu=35;    rSub=8;     % radius of entire cluster and of sub-sphere
dAtom=4;    dSub=20;    % distance between atoms and between sub-spheres
box=RClu*2+1;   sub=1;   Position=zeros(box,4);
for rx=(-RClu:dSub:RClu)
    for ry=(-RClu:dSub:RClu)
        for rz=(-RClu:dSub:RClu)
            R=sqrt(rx^2+ry^2+rz^2);
            if R <=RClu
                Position(sub,1)=rx+((0.5-rand(1))*dSub);
                Position(sub,2)=ry+((0.5-rand(1))*dSub);
                Position(sub,3)=rz+((0.5-rand(1))*dSub);
                sub=sub+1;
            end
        end
    end
end
SubInCluster=sub-1;   Pos=Position(1:SubInCluster,:);   clear sub
AtomInClu=zeros(SubInCluster,1);
for sub=1:SubInCluster
    atom=1;   box=RClu*2+1;   Cluster=zeros(box,4);
    PosX=Pos(sub,1); PosY=Pos(sub,2); PosZ=Pos(sub,3);
    for rx=(-rSub:dAtom:rSub)
        for ry=(-rSub:dAtom:rSub)
            for rz=(-rSub:dAtom:rSub)
                R=sqrt(rx^2+ry^2+rz^2);
                if R <= rSub
                     Cluster(atom,1)=rx+PosX+((0.5-rand(1))*dAtom);
                     Cluster(atom,2)=ry+PosY+((0.5-rand(1))*dAtom);
                     Cluster(atom,3)=rz+PosZ+((0.5-rand(1))*dAtom);
                     atom=atom+1;
                end
            end
        end
    end
    AtomInClu(sub)=atom-1;    ClusterSub=Cluster(1:AtomInClu(sub),:);
    b=sum(AtomInClu);    a=b-AtomInClu(sub)+1;
    ClusterIn(a:b,:)=ClusterSub;
end
```

To simulate the scattering from the model cluster, the scattering from each point-scatterer is calculated in azimuthal and radial direction, respectively, for a chosen angle range (N_θ, N_φ) with chosen accuracy ($\Delta\theta$, $\Delta\varphi$). The scattering vector value is wavelength and angle dependent $|\boldsymbol{q}| = 4\pi/\lambda \cdot \sin(\theta/2)$ and is in spherical coordinates composed of

$$\begin{aligned} q_x &= q \cdot \cos(\theta/2)\cos(\varphi), \\ q_y &= q \cdot \cos(\theta/2)\sin(\varphi), \\ q_z &= -q \cdot \sin(\theta/2) \quad (\pi \geq \theta \geq 0; 2\pi > \varphi \geq 0) \end{aligned} \tag{A.1}$$

The amplitude of the light scattered by a single point-scatterer is calculated in fractions of the scattering amplitude of a single free electron. The ratio of scattering amplitude of an atom to the scattering amplitude of a free electron is given by the complex atomic scattering factor. It is $f = -2.61 + i \cdot 32.92$ for xenon at 91.5 eV photon energy [**?**]. The scattering amplitude from the entire model cluster consisting of N atoms is simply calculated as the summation of the scalar electric fields from an arrangement of N point scatterers:

$$A = \sum_{\theta,\varphi}^{N_\theta,N_\varphi} A_{\theta,\varphi} = \sum_{\theta,\varphi}^{N_\theta,N_\varphi} \sum_{x,y,z=1}^{N_x,N_y,N_z} f \cdot e^{i(Q_x r_x + Q_y r_y + Q_z r_z)} \tag{A.2}$$

The intensity of the scattering signal is proportional to the squared modulus of the amplitude:

$$I = 4\pi |A|^2 \tag{A.3}$$

```
% % II Calculate scattering crossection of the model cluster
Lambda=13.5;                    % laser wavelength
FAtom=-2.61+1i*32.92;           % atomic scattering factor
DThe=2.0; The1=0; The2=33.0;    % theta increment and lower/upper bounds
DPhi=2.0; Phi1=0; Phi2=360.0;   % phi increment and lower / upper bounds
NThe=round(1+(The2-The1)/DThe);
NPhi=round(1+(Phi2-Phi1)/DPhi);
PatternAngle=zeros(3,NThe,NPhi);
for i=1:NThe
    for j=1:NPhi
        TheSc=The1+(i-1)*DThe;
        PhiSc0=Phi1+(j-1)*DPhi;
        if PhiSc0<0, PhiSc=PhiSc0+360; end
        if PhiSc0>=0, PhiSc=PhiSc0; end
        kapa=(4*pi*sin(pi*TheSc/(180*2)))/Lambda;
        Qx=kapa* cos((pi*TheSc)/(180*2))* cos((pi*PhiSc)/180);
        Qy=kapa* cos((pi*TheSc)/(180*2))* sin((pi*PhiSc)/180);
        Qz=-kapa*sin((pi*TheSc)/(180*2));
        argu=ClusterIn(:,1).*Qx+ClusterIn(:,2)*Qy+ClusterIn(:,3)*Qz;
        Amplitude=sum(FAtom.*exp(1i.*argu));
        Intensity=(4*pi*abs(Amplitude))^2;
        PatternAngle(1,i,j)=TheSc;
        PatternAngle(2,i,j)=PhiSc;
        PatternAngle(3,i,j)=Intensity;
    end
end
```

List of Figures

List of Tables

Bibliography

[1] R. Neutze, R. Wouts, D. van der Spoel, E. Weckert, and J. Hajdu. Potential for biomolecular imaging with femtosecond X-ray pulses. *Nature*, 406:752–757, 2000.

[2] J. Schneider. FLASH - from accelerator test facility to the first single-pass soft x-ray free-electron laser. *Journal of Physics B: Atomic, Molecular and Optical Physics*, 43:194001, 2010.

[3] S. Eisebitt, J. Lüning, W.F. Schlotter, M. Lörgen, O. Hellwig, W. Eberhardt, and J. Stöhr. Lensless imaging of magnetic nanostructures by X-ray. *Nature*, 432:885–888, 2004.

[4] H. N. Chapman, A. Barty, M. J. Bogan, S. Boutet, M. Frank, S. P. Hau-Riege, S. Marchesini, B. W. Woods, S. Bajt, W. H. Benner, R. A. London, E. Plonjes, M. Kuhlmann, R. Treusch, S. Düsterer, T. Tschentscher, J. R. Schneider, E. Spiller, Th. Möller, Ch. Bostedt, M. Hoener, D. A. Shapiro, K. O. Hodgson, D. van der Spoel, F. Burmeister, M. Bergh, C. Caleman, G. Huldt, M. M. Seibert, F. R. N. C. Maia, R. W. Lee, A. Szoke, N. Timneanu, and J. Hajdu. Femtosecond Diffractive Imaging with a Soft-X-ray Free-Electron Laser. *Nature Physics*, 461:839–843, 2006.

[5] H. N. Chapman, A. Barty, S. Marchesini, A. Noy, S. P. Hau-Riege, C. Cui, M. R. Howells, R. Rosen, H. He, J. C. H. Spence, U. Weierstall, T. Beetz, Ch. Jacobsen, and D. Shapiro. High-resolution ab initio three-dimensional x-ray diffraction microscopy. *Journal of the Optical Society of America. A, Optics, image science, and vision*, 23(5):1179–1200, 2006.

[6] S. Marchesini, S. Boutet, A. E. Sakdinawat, M. J. Bogan, S. Bajt, A. Barty, H. N. Chapman, M. Frank, S. P. Hau-Riege, A. Szoke, C. Cui, M. R. Howells, D. A. Shapiro, J. C. H. Spence, J. W. Shaevitz, J. Y. Lee, J. Hajdu, and M. M. Seibert. Massively parallel X-ray holography. *Nature Photonics*, 2:560–563, 2008.

[7] M. J. Bogan, W. H. Benner, S. Boulet, U. Rohner, M. Frank, A. Barty, M. M. Seibert, F. Maia, S. Marchesini, S. Bajt, B. Woods, V. Riot, S. P. Hau-Riege, M. Svenda, E. Marklund, E. Spiller, J. Hajdu, and H. N. Chapman. Single particle X-ray diffractive imaging. *Nano Letters*, 8:310–316, 2008.

[8] M. J. Bogan, D. Starodub, C. Y. Hampton, and R. G. Sierra. Single-particle coherent diffractive imaging with a soft x-ray free electron laser: towards soot aerosol morphology. *Journal of Physics B: Atomic, Molecular and Optical Physics*, 43:194013, 2010.

[9] M. M. Seibert, T. Ekeberg, F. R. N. C. Maia, M. Svenda, J. Andreasson, O. Jönsson, D. Odić, B. Iwan, A. Rocker, D. Westphal, M. Hantke, D. P. DePonte, A. Barty, J. Schulz, L. Gumprecht, N. Coppola, A. Aquila, M. Liang, T. A. White, A. Martin, C. Caleman, S. Stern, C. Abergel, V. Seltzer, J.-M. Claverie, C. Bostedt, J. D. Bozek, S. Boutet, A. A. Miahnahri, M. Messerschmidt, J. Krzywinski, G. Williams, K. O. Hodgson, M. J. Bogan, C. Y. Hampton, R. G. Sierra, D. Starodub, I. Andersson, S. Bajt, M. Barthelmess, J. C. H. Spence, P. Fromme, U. Weierstall, R. Kirian, M. Hunter, R. B. Doak, S. Marchesini, S. P. Hau-Riege, M. Frank, R. L. Shoeman, L. Lomb, S. W. Epp, R. Hartmann, D. Rolles, A. Rudenko, C. Schmidt, L. Foucar, N. Kimmel, P. Holl, B. Rudek, B. Erk, A. Hömke, C. Reich, D. Pietschner, G. Weidenspointner, L. Strüder, G. Hauser, H. Gorke, J. Ullrich, I. Schlichting, S. Herrmann, G. Schaller, F. Schopper, H. Soltau, K.-U. Kühnel, R. Andritschke, C.-D. Schröter, F. Krasniqi, M. Bott, S. Schorb, D. Rupp, M. Adolph, T. Gorkhover, H. Hirsemann, G. Potdevin, H. Graafsma, B. Nilsson, H. N. Chapman, and J. Hajdu. Single mimivirus particles intercepted and imaged with an X-ray laser. *Nature*, 470:78–81, 2011.

[10] C. Bostedt, E. Eremina, D. Rupp, M. Adolph, H. Thomas, M. Hoener, A. R. B. De Castro, J. Tiggesbäumker, K. H. Meiwes-Broer, T. Laarmann, H. Wabnitz, E. Plönjes, R. Treusch, J. R. Schneider, and T. Möller. Ultrafast x-ray scattering of xenon nanoparticles: Imaging transient states of matter. *Physical Review Letters*, 108:093401, 2012.

[11] D. Rupp, M. Adolph, T. Gorkhover, S. Schorb, D. Wolter, R. Hartmann, N. Kimmel, C. Reich, T. Feigl, A. R. B. De Castro, R. Treusch, L. Strüder, T. Möller, and C. Bostedt. Identification of twinned gas phase clusters by single-shot scattering with intense soft x-ray pulses. *New Journal of Physics*, 14:055016, 2012.

[12] I. Barke, H. Hartmann, D. Rupp, L. Flückiger, M. Sauppe, M. Adolph, S. Schorb, C. Bostedt, R. Treusch, C. Peltz, S. Bartling, T. Fennel, K.-H. Meiwes-Broer, and T. Möller. The 3D-architecture of individual free silver nanoparticles captured by X-ray scattering. *Nature Communications*, 6(6187):1–8, 2015.

[13] C. M. Günther, B. Pfau, R. Mitzner, B. Siemer, S. Roling, H. Zacharias, O. Kutz, I. Rudolph, D. Schondelmaier, R. Treusch, and S. Eisebitt. Sequential femtosecond X-ray imaging. *Nature Photonics*, 5:99–102, 2011.

[14] A. Barty, S. Boutet, M. J. Bogan, S. Hau-Riege, S. Marchesini, K. Sokolowski-Tinten, N. Stojanovic, R. Tobey, H. Ehrke, A. Cavalleri, S. Düsterer, M. Frank, S. Bajt, B. W. Woods, M. M. Seibert, J. Hajdu, R. Treusch, and H. N. Chapman. Ultrafast single-shot diffraction imaging of nanoscale dynamics. *Nature Photonics*, 2:578–578, 2008.

[15] I. Yamada, J. Matsuo, N. Toyoda, and A. Kirkpatrick. Materials processing by gas cluster ion beams. *Materials Science and Engineering: R: Reports*, 34(6):231–295, 2001.

[16] G. Scoles, D. Brassi, U. Buck, and D. Laine. *Atomic and Molecular Beam Methods: Volume 1.* Oxford University Press, New York, 1988.

[17] H. C. W. Beijerinck, R. J. F. Van Gerwen, E. R. T. Kerstel, J. F. M. Martens, E. J. W. Van Vliembergen, M. R. Th. Smits, and G. H. Kaashoek. Campargue-type supersonic beam sources: Absolute intensities, skimmer transmission and scaling laws for mono-atomic gases He, Ne and Ar. *Chemical Physics*, 96:153–173, 1985.

[18] O. F. Hagena. Cluster Formation in Expanding Supersonic Jets: Effect of Pressure, Temperature, Nozzle Size, and Test Gas. *The Journal of Chemical Physics*, 56:1793, 1972.

[19] D. Pentlehner, R. Riechers, B. Dick, A. Slenczka, U. Even, N. Lavie, R. Brown, and K. Luria. Rapidly pulsed helium droplet source. *Review of Scientific Instruments*, 80:1–9, 2009.

[20] U. Even. Pulsed Supersonic Beams from High Pressure Source: Simulation Results and Experimental Measurements. *Advances in Chemistry*, 2014(636042):1–11, 2014.

[21] C. Bobbert, S. Schütte, C. Steinbach, and U. Buck. Fragmentation and reliable size distributions of large ammonia and water clusters. *Physical Journal D*, 192:183–192, 2002.

[22] O. F. Hagena. Nucleation and growth of clusters in expanding nozzle flows. *Surface Science*, 106:101–116, 1981.

[23] O. F. Hagena. Cluster ion sources (invited). *Review of Scientific Instruments*, 63(1992):2374–2379, 1992.

[24] O. F. Hagena. Condensation in free jets: Comparison of rare gases and metals. *Zeitschrift für Physik D Atoms, Molecules and Clusters*, 4:291–299, 1987.

[25] R. Karnbach, M. Joppien, J. Stapelfeldt, J. Wörmer, and T. Möller. CLULU: An experimental setup for luminescence measurements on van der Waals clusters with synchrotron radiation. *Review of Scientific Instruments*, 64:2838–2849, 1993.

[26] U. Buck and R. Krohne. Cluster size determination from diffractive He atom scattering. *The Journal of Chemical Physics*, 105:5408, 1996.

[27] E. L. Knuth. Dimer-formation rate coefficients from measurements of terminal dimer concentrations in free-jet expansions. *The Journal of Chemical Physics*, 66(1977):3515–3525, 1977.

[28] F. Dorchies, F. Blasco, T. Caillaud, J. Stevefelt, C. Stenz, A. Boldarev, and V. Gasilov. Spatial distribution of cluster size and density in supersonic jets as targets for intense laser pulses. *Physical Review A*, 68:1–8, 2003.

[29] L. Shao-Hui, L. Bing-Chen, N. Guo-Quan, and X. Zhi-Zhan. Investigation of the time characteristics of a pulsed flow of large rare gas clusters. *Chinese Physics*, 12:856–860, 2003.

[30] D. Rupp, M. Adolph, L. Flückiger, T. Gorkhover, J. P. Müller, M. Müller, M. Sauppe, D. Wolter, S. Schorb, R. Treusch, C. Bostedt, and T. Möller. Generation and structure of extremely large clusters in pulsed jets. *Journal of Chemical Physics*, 141:044306, 2014.

[31] M. Born and E. Wolf. *Principles of optics electromagnetic theory of propagation interference and diffraction of light*. Pergamon Press, New York, 2nd edition, 1999.

[32] D. Attwood. *Soft X-Rays and Extreme Ultraviolet Radiation: Principles and Applications*. Cambridge University Press, 2000.

[33] J. Als-Nielsen and D. McMorrow. *Elements of Modern X-ray Physics*. John Wiley and Sons, New York, 2nd edition, 2011.

[34] J. D. Jackson. *Classical Electrodynamics*. John Wiley and Sons, New York, 3rd edition, 1998.

[35] S. P. Hau-Riege. *High-Intensity X-Rays - Interaction with Matter*. Wiley-VCH Verlag GmbH & Co. KGaA, Weinheim, Germany, 2011.

[36] A. R. B. De Castro, E. Eremina, C. Bostedt, M. Hoener, H. Thomas, and T. Möller. Numerical simulation of small angle scattering (SAXS) for large atomic clusters. *Journal of Electron Spectroscopy and Related Phenomena*, 166-167:21–27, 2008.

[37] Z. Ulanowski, E. Hirst, P. H. Kaye, and R. Greenaway. Retrieving the size of particles with rough and complex surfaces from two-dimensional scattering patterns. *Journal of Quantitative Spectroscopy and Radiative Transfer*, 113(18):2457–2464, 2012.

[38] G. Mie. Contributions to the optics of turbid media, particularly of colloidal metal solutions. *Annalen der Physik*, 25(3):377–445, 1908.

[39] C. F. Bohren and D. R. Huffman. *Absorption and scattering of light by small particles*. Number 6. Wiley Science Paperback Series, Chichester, UK, 1998.

[40] M. Quinten. *Optical Properties of Nanoparticle Systems: Mie and beyond*. Wiley-VCH, 2011.

[41] U. Kreibig. Hundert Jahre Mie-Theorie. Optische Eigenschaften von Nanopartikeln. *Physik in unserer Zeit*, 39(39):281–287, 2008.

[42] C. Bostedt, H. Thomas, M. Hoener, T. Möller, U. Saalmann, I. Georgescu, C. Gnodtke, and J. M. Rost. Fast electrons from multi-electron dynamics in xenon clusters induced by inner-shell ionization. *New Journal of Physics*, 12, 2010.

[43] T. Gorkhover and *et al.* Femtosecond visualization of structural dynamics in single nanoparticles. *to be published*, 2015.

[44] D. Rupp and *et al.* Explosion dynamics of single clusters resolved for particle size and laser power density. *to be published*, 2015.

[45] D. Rupp. *Ionization and plasma dynamics of single large xenon clusters in superintense XUV pulses*. PhD thesis, Technische Universität Berlin, 2013.

[46] T. Gorkhover. *Ultrafast light induced dynamics of Xe nanoparticles studied with a combination of intense infrared and x-ray pulses*. PhD thesis, Technische Universität Berlin, 2014.

[47] T. Ditmire, T. Donnelly, A. Rubenchik, R. Falcone, and M. Perry. Interaction of intense laser pulses with atomic clusters. *Physical Review A*, 53(5):3379–3402, 1996.

[48] V.P. Krainov and M.B. Smirnov. Cluster beams in the super-intense femtosecond laser pulse. *Physics Reports*, 370:237–331, 2002.

[49] U. Saalmann, C. Siedschlag, and J. M. Rost. Mechanisms of cluster ionization in strong laser pulses. *Journal of Physics B: Atomic, Molecular and Optical Physics*, 39(4):39–77, 2006.

[50] T. Fennel, K.-H. Meiwes-Broer, J. Tiggesbäumker, P. G. Reinhard, P. M. Dinh, and E. Suraud. Laser-driven nonlinear cluster dynamics. *Reviews of Modern Physics*, 82:1793–1842, 2010.

[51] U. Saalmann. Cluster nanoplasmas in strong FLASH pulses: formation, excitation and relaxation. *Journal of Physics B: Atomic, Molecular and Optical Physics*, 43:194012, 2010.

[52] M. Arbeiter and T. Fennel. Rare-gas clusters in intense VUV, XUV and soft x-ray pulses: Signatures of the transition from nanoplasma-driven cluster expansion to Coulomb explosion in ion and electron spectra. *New Journal of Physics*, 13:053022, 2011.

[53] P. G. Reinhard and E. Suraud. *Introduction to Cluster Dynamics*. Wiley-VCH Verlag, Weinheim, Germany, 2004.

[54] J. Posthumus. *Molecules and Clusters in Intense Laser Fields*. Cambridge University Press, 2009.

[55] V. Kumarappan, M. Krishnamurthy, and D. Mathur. Explosions of water clusters in intense laser fields. *Physical Journal A*, 67:063207, 2003.

[56] M. Hoener, C. Bostedt, H. Thomas, L. Landt, E. Eremina, H. Wabnitz, T. Laarmann, R. Treusch, A. R. B. De Castro, and T. Möller. Charge recombination in soft x-ray laser produced nanoplasmas. *Journal of Physics B: Atomic, Molecular and Optical Physics*, 41:181001, 2008.

[57] Y. Fukuda, Y. Kishimoto, T. Masaki, and K. Yamakawa. Structure and dynamics of cluster plasmas created by ultrashort intense laser fields. *Physical Review A - Atomic, Molecular, and Optical Physics*, 73:031201, 2006.

[58] I. Last and J. Jortner. Quasiresonance ionization of large multicharged clusters in a strong laser field. *Physical Review A*, 60(3):2215–2221, 1999.

[59] H. Wabnitz, L. Bittner, A. R. B. De Castro, R. Döhrmann, P. Gürtler, T. Laarmann, W. Laasch, J. Schulz, A. Swiderski, K. von Haeften, T. Möller, B. Faatz, A. Fateev, J. Feldhaus, C. Gerth, U. Hahn, E. Saldin, E. Schneidmiller, K. Sytchev, K. Tiedtke, R. Treusch, and M. Yurkov. Multiple ionization of atom clusters by intense soft X-rays from a free-electron laser. *Nature*, 420:482–485, 2002.

[60] I. V. Hertel and C.-P. Schulz. *Atome, Moleküle und optische Physik 1: Atomphysik und Grundlagen der Spektroskopie*. Springer, 2010.

[61] T. Ditmire. Strong Field Physics. In *Handbook of Optics: Optical Properties of Materials, Nonlinear Optics, Quantum Optics*, chapter 21. McGraw-Hill, 2009.

[62] V. P. Krainov and B. M. Smirnov. Femtosecond excitation of cluster beams. *Physics-Uspekhi*, 50:907–931, 2007.

[63] I. Georgescu. *Rare-gas clusters in intense VUV laser fields*. PhD thesis, Technische Universität Dresden, 2008.

[64] N. Bigaouette. *Computational investigation of intense short-wavelength laser interaction with rare gas clusters*. PhD thesis, University of Ottawa, 2014.

[65] L. Keldysh. Ionization in the field of a strong electromagnetic wave. *Soviet Physics Jetp*, 20(5):1307, 1964.

[66] A. Sorokin, S. V. Bobashev, T. Feigl, K. Tiedtke, H. Wabnitz, and M. Richter. Photoelectric effect at ultrahigh intensities. *Physical Review Letters*, 99:213002, 2007.

[67] A. Kramida, Y. Ralchenko, J. Reader, and NIST ASD Team. NIST Atomic Spectra Database (version 5.1) [online], 2013.

[68] M. Richter, M. Y. Amusia, S. V. Bobashev, T. Feigl, P. N. Juranić, M. Martins, A. A. Sorokin, and K. Tiedtke. Extreme ultraviolet laser excites atomic giant resonance. *Physical Review Letters*, 102:163002, 2009.

[69] A. Aguilar, J. D. Gillaspy, G. F. Gribakin, R. A. Phaneuf, M. F. Gharaibeh, M. G. Kozlov, J. D. Bozek, and A. L. D. Kilcoyne. Absolute photoionization cross sections for Xe4+, Xe5+, and Xe6+ near 13.5 nm: Experiment and theory. *Physical Review A - Atomic, Molecular, and Optical Physics*, 73(3):032717, 2006.

[70] J.-M. Bizau, J.-M. Esteva, D. Cubaynes, F. Wuilleumier, C. Blancard, A. La Fontaine, C. Couillaud, J. Lachkar, R. Marmoret, C. Rémond, J. Bruneau, D. Hitz, P. Ludwig, and M. Delaunay. Photoionization of Highly Charged Ions Using an ECR Ion Source and Undulator Radiation. *Physical Review Letters*, 84(3):435–438, 2000.

[71] S. Larochelle, A. Talebpour, and S. L. Chin. Non-sequential multiple ionization of rare gas atoms in a Ti:Sapphire laser field. *Journal of Physics B: Atomic, Molecular and Optical Physics*, 31(6):1201–1214, 1999.

[72] K. Yamakawa, Y. Akahane, Y. Fukuda, M. Aoyama, N. Inoue, H. Ueda, and T. Utsumi. Many-electron dynamics of a Xe atom in strong and superstrong laser fields. *Physical Review Letters*, 92:123001, 2004.

[73] A. McPherson, A. B. Borisov, K. Boyer, and C. K. Rhodes. Competition between multiphoton xenon cluster excitation and plasma wave Raman scattering at 248 nm. *Journal of Physics B: Atomic, Molecular and Optical Physics*, 29(7):291–297, 1999.

[74] T. Ditmire, E. Springate, J. Tisch, Y. Shao, M. Mason, N. Hay, J. Marangos, and M. Hutchinson. Explosion of atomic clusters heated by high-intensity femtosecond laser pulses. *Physical Review A*, 57(1):369–382, 1998.

[75] T. Ditmire, J. Zweiback, V. P. Yanovsky, T. E. Cowan, and G. Hays. Nuclear fusion from explosions of femtosecond laser-heated deuterium clusters. *Nature*, 398:489–492, 1999.

[76] E. Springate, S. Aseyev, S. Zamith, and M. Vrakking. Electron kinetic energy measurements from laser irradiation of clusters. *Physical Review A*, 68(5):053201, 2003.

[77] L. Ramunno, C. Jungreuthmayer, and T. Brabec. Intense laser-cluster interaction in the strong coupling regime. *Laser Physics*, 17(5):618–624, 2007.

[78] B. Ziaja, Z. Jurek, N. Medvedev, S.-K. Son, R. Thiele, and S. Toleikis. Photoelectron spectroscopy method to reveal ionization potential lowering in nanoplasmas. *Journal of Physics B: Atomic, Molecular and Optical Physics*, 46:164009, 2013.

[79] C. Varin, C. Peltz, T. Brabec, and T. Fennel. Light wave driven electron dynamics in clusters. *Annalen der Physik*, 526(3):135–156, 2014.

[80] J. Zweiback, T. Ditmire, and M. Perry. Femtosecond time-resolved studies of the dynamics of noble-gas cluster explosions. *Physical Review A*, 59(5):3166–3169, 1999.

[81] http://nanocomposix.eu/pages/plasmonics.

[82] H. M. Milchberg, S. J. McNaught, and E. Parra. Plasma hydrodynamics of the intense laser-cluster interaction. *Physical review E, Statistical, nonlinear, and soft matter physics*, 64:056402, 2001.

[83] W. Lotz. An empirical formula for the electron-impact ionization cross-section. *Zeitschrift für Physik*, 206:205–211, 1967.

[84] P. Hilse, M. Moll, M. Schlanges, and T. Bornath. Laser-Cluster-Interaction in a Nanoplasma-Model with Inclusion of Lowered Ionization Energies. *Laser Physics*, 19(3):428–436, 2008.

[85] V. P. Krainov. Inverse stimulated bremsstrahlung of slow electrons under Coulomb scattering. *Journal of Physics B: Atomic, Molecular and Optical Physics*, 33(8):31585–1595, 2000.

[86] I. Georgescu, U. Saalmann, and J. M. Rost. Attosecond resolved charging of ions in a rare-gas cluster. *Physical Review Letters*, 99:183002, 2007.

[87] C. Bostedt, H. Thomas, M. Hoener, E. Eremina, T. Fennel, K. H. Meiwes-Broer, H. Wabnitz, M. Kuhlmann, E. Plönjes, K. Tiedtke, R. Treusch, J. Feldhaus, a. R B De Castro, and T. Möller. Multistep ionization of argon clusters in intense femtosecond extreme ultraviolet pulses. *Physical Review Letters*, 100:133401, 2008.

[88] L. Flückiger, D. Rupp, M. Adolph, T. Gorkhover, M. Krikunova, M. Müller, T. Oelze, Y. Ovcharenko, M. Sauppe, S. Schorb, C. Bostedt, S. Düsterer, M. Harmand, H. Redlin, R. Treusch, and T. Möller. Infrared laser-induced cluster evolution imaged by x-ray scattering. *in preparation*, 2015.

[89] N. K. Kandadai. *Interaction of Clusters with Ultra Short X-Ray Free Electron Laser Pulses*. PhD thesis, The University of Texas at Austin, 2012.

[90] M. Lezius, S. Dobosz, D. Normand, and M. Schmidt. Explosion Dynamics of Rare Gas Clusters in Strong Laser Fields. *Physical Review Letters*, 80:261–264, 1998.

[91] M. Lebeault, J. Viallon, J. Chevaleyre, C. Ellert, D. Normand, M. Schmidt, O. Sublemontier, C. Guet, and B. Huber. Resonant coupling of small size-controlled lead clusters with an intense laser field. *European Physical Journal D*, 20:233–242, 2002.

[92] K. Ishikawa and T. Blenski. Explosion dynamics of rare-gas clusters in an intense laser field. *Physical Review A - Atomic, Molecular, and Optical Physics*, 62:063201, 2000.

[93] H. Thomas, C. Bostedt, M. Hoener, E. Eremina, H. Wabnitz, T. Laarmann, E. Plönjes, R. Treusch, A. R. B. De Castro, and T. Möller. Shell explosion and core expansion of xenon clusters irradiated with intense femtosecond soft x-ray pulses. *Journal of Physics B: Atomic, Molecular and Optical Physics*, 42:134018, 2009.

[94] B. Ziaja, F. Wang, H. Wabnitz, E. Weckert, and T. Möller. Ionization and expansion dynamics of atomic clusters irradiated with short intense VUV pulses. In *AIP Conference Proceedings*, volume 1161, pages 105–112, 2009.

[95] T. Fennel, T. Döppner, J. Passig, Ch Schaal, J. Tiggesbäumker, and K. H. Meiwes-Broer. Plasmon-enhanced electron acceleration in intense laser metal-cluster interactions. *Physical Review Letters*, 98:143401, 2007.

[96] C. Jungreuthmayer, L. Ramunno, J. Zanghellini, and T. Brabec. Intense VUV laser cluster interaction in the strong coupling regime. *Journal of Physics B: Atomic, Molecular and Optical Physics*, 38:3029–3036, 2005.

[97] E. Ackad, N. Bigaouette, S. Mack, K. Popov, and L. Ramunno. Recombination effects in soft-x-ray cluster interactions at the xenon giant resonance. *New Journal of Physics*, 15:053047, 2013.

[98] M. Arbeiter, C. Peltz, and T. Fennel. Electron-relocalization dynamics in xenon clusters in intense soft-x-ray fields. *Physical Review A*, 89:043428, 2014.

[99] M. Krikunova, M. Adolph, T. Gorkhover, D. Rupp, S. Schorb, C. Bostedt, S. Roling, B. Siemer, R. Mitzner, H. Zacharias, and T. Möller. Ionization dynamics in expanding clusters studied by XUV pumpprobe spectroscopy. *Journal of Physics B: Atomic, Molecular and Optical Physics*, 45(10):105101, 2012.

[100] L. Schroedter, M. Müller, A. Kickermann, A. Przystawik, S. Toleikis, M. Adolph, L. Flückiger, T. Gorkhover, L. Nösel, M. Krikunova, T. Oelze, Y. Ovcharenko, D. Rupp, M. Sauppe, D. Wolter, S. Schorb, C. Bostedt, T. Möller, and T. Laarmann. Hidden charge states in soft-x-ray laser-produced nanoplasmas revealed by fluorescence spectroscopy. *Physical Review Letters*, 112:183401, 2014.

[101] T. Gorkhover, M. Adolph, D. Rupp, S. Schorb, S. W. Epp, B. Erk, L. Foucar, R. Hartmann, N. Kimmel, K. U. Kühnel, D. Rolles, B. Rudek, A. Rudenko, R. Andritschke, A. Aquila, J. D. Bozek, N. Coppola, T. Erke, F. Filsinger, H. Gorke, H. Graafsma, L. Gumprecht, G. Hauser, S. Herrmann, H. Hirsemann, A. Hömke, P. Holl, C. Kaiser, F. Krasniqi, J. H. Meyer, M. Matysek, M. Messerschmidt, D. Miessner, B. Nilsson, D. Pietschner, G. Potdevin, C. Reich, G. Schaller, C. Schmidt, F. Schopper, C. D. Schröter, J. Schulz, H. Soltau, G. Weidenspointner, I. Schlichting, L. Strüder, J. Ullrich, T. Möller, and C. Bostedt. Nanoplasma dynamics of single large xenon clusters irradiated with superintense X-ray pulses from the linac coherent light source free-electron laser. *Physical Review Letters*, 108:245005, 2012.

[102] C. Varin, C. Peltz, T. Brabec, and T. Fennel. Attosecond plasma wave dynamics in laser-driven cluster nanoplasmas. *Physical Review Letters*, 108:175007, 2012.

[103] S. Sakabe, K. Shirai, M. Hashida, S. Shimizu, and S. Masuno. Skinning of argon clusters by Coulomb explosion induced with an intense femtosecond laser pulse. *Physical Review A - Atomic, Molecular, and Optical Physics*, 74:043205, 2006.

[104] T. Taguchi, T. M. Antonsen, J. Palastro, H. Milchberg, and K. Mima. Particle in cell analysis of a laser-cluster interaction including collision and ionization processes. *Optics express*, 18(3):2389–2405, 2010.

[105] M. Arbeiter and T. Fennel. Ionization heating in rare-gas clusters under intense XUV laser pulses. *Physical Review A - Atomic, Molecular, and Optical Physics*, 82:013201, 2010.

[106] M Müller, L Schroedter, T Oelze, A Przystawik, A Kickermann, M Adolph, T Gorkhover, L Flückiger, M Krikunova, M Sauppe, Y Ovcharenko, S Schorb, D Rupp, T Laarmann, and T Möller. Ionization dynamics of XUV excited clusters: the role of inelastic electron collisions. *submitted to Journal of Physics B: Atomic, Molecular and Optical Physics*, pages 1–14, 2015.

[107] R. L. Sandberg, A. Paul, D. A. Raymondson, S. Hädrich, D. M. Gaudiosi, J. Holtsnider, R. I. Tobey, O. Cohen, M. M. Murnane, H. C. Kapteyn, C. Song, J. Miao, Y. Liu, and F. Salmassi. Lensless diffractive imaging using tabletop coherent high-harmonic soft-X-ray beams. *Physical Review Letters*, 99(9):098103, 2007.

[108] R. Moshammer, Th. Pfeifer, A. Rudenko, Y. H. Jiang, L. Foucar, M. Kurka, K. U. Kühnel, C. D. Schröter, J. Ullrich, O. Herrwerth, M. F. Kling, X.-J. Liu, K. Motomura, H. Fukuzawa, A. Yamada, K. Ueda, K. L. Ishikawa, K. Nagaya, H. Iwayama, A. Sugishima, Y. Mizoguchi, S. Yase, M. Yao, N. Saito, A. Belkacem, M. Nagasono, A. Higashiya, M. Yabashi, T. Ishikawa, H. Ohashi, H. Kimura, and T. Togashi. Second-order autocorrelation of XUV FEL pulses via time resolved two-photon single ionization of He. *Optics Express*, 19(22):21698, 2011.

[109] http://flash.desy.de/.

[110] W. Ackermann and *et al.* Operation of a free-electron laser from the extreme ultraviolet to the water window. *Nature Photonics*, 1:336–342, 2007.

[111] K. Tiedtke, A. Azima, N. Von Bargen, L. Bittner, S. Bonfigt, S. Düsterer, B. Faatz, U. Frühling, M. Gensch, Ch Gerth, N. Guerassimova, U. Hahn, T. Hans, M. Hesse, K. Honkavaar, U. Jastrow, P. Juranic, S. Kapitzki, B. Keitel, T. Kracht, M. Kuhlmann, W. B. Li, M. Martins, T. Núñez, E. Plönjes, H. Redlin, E. L. Saldin, E. a. Schneidmiller, J. R. Schneider, S. Schreiber, N. Stojanovic, F. Tavella, S. Toleikis, R. Treusch, H. Weigelt, M. Wellhöfer, H. Wabnitz, M. V. Yurkov, and J. Feldhaus. The soft x-ray free-electron laser FLASH at DESY: Beamlines, diagnostics and end-stations. *New Journal of Physics*, 11:023029, 2009.

[112] R. Treusch and J. Feldhaus. FLASH: New opportunities for (time-resolved) coherent imaging of nanostructures. *New Journal of Physics*, 12:035015, 2010.

[113] P. Emma, R. Akre, J. Arthur, R. Bionta, C. Bostedt, J. Bozek, A. Brachmann, P. Bucksbaum, R. Coffee, F.-J. Decker, Y. Ding, D. Dowell, S. Edstrom, A. Fisher, J. Frisch, S. Gilevich, J. Hastings, G. Hays, Ph. Hering, Z. Huang, R. Iverson,

H. Loos, M. Messerschmidt, A. Miahnahri, S. Moeller, H.-D. Nuhn, G. Pile, D. Ratner, J. Rzepiela, D. Schultz, T. Smith, P. Stefan, H. Tompkins, J. Turner, J. Welch, W. White, J. Wu, G. Yocky, and J. Galayda. First lasing and operation of an ångstrom-wavelength free-electron laser. *Nature Photonics*, 4(9):641–647, 2010.

[114] D. Pile. X-rays: First light from SACLA. *Nature Photonics*, 5(8):456–457, 2011.

[115] E. Allaria, C. Callegari, D. Cocco, W. M. Fawley, M. Kiskinova, C. Masciovecchio, and F. Parmigiani. The FERMI@Elettra free-electron-laser source for coherent x-ray physics: Photon properties, beam transport system and applications. *New Journal of Physics*, 12:075002, 2010.

[116] M. Altarelli. The European X-ray free-electron laser facility in Hamburg. In *Nuclear Instruments and Methods in Physics Research, Section B: Beam Interactions with Materials and Atoms*, volume 269, pages 2845–2849, 2011.

[117] B. D. Patterson, R. Abela, H. H. Braun, U. Flechsig, R. Ganter, Y. Kim, E. Kirk, A. Oppelt, M. Pedrozzi, S. Reiche, L. Rivkin, T. Schmidt, B. Schmitt, V. N. Strocov, S. Tsujino, and A. F. Wrulich. Coherent science at the SwissFEL x-ray laser. *New Journal of Physics*, 12:035012, 2010.

[118] E. S. Kim and M. Yoon. Beam dynamics in a 10-GeV linear accelerator for the X-ray free electron laser at PAL. *IEEE Transactions on Nuclear Science*, 56(6):3597–3606, 2009.

[119] C. Schmüser, P. Dohlus, M. Rossbach, and J. Behrens. *Free-Electron Lasers in the Ultraviolet and X-Ray Regime*. Springer, Berlin, Germany, 2nd edition.

[120] E. L. Saldin, E. A. Schneidmiller, and M. V. Yurkov. Coherence properties of the radiation from X-ray free electron laser. *Optics Communications*, 281:1179–1188, 2008.

[121] J. Feldhaus, J. Arthur, and J. B. Hastings. X-ray free-electron lasers. *Journal of Physics B: Atomic, Molecular and Optical Physics*, 38:799–819, 2005.

[122] Z. Huang and K. J. Kim. Review of x-ray free-electron laser theory. *Physical Review Special Topics - Accelerators and Beams*, 10:034801, 2007.

[123] B. W. J. McNeil and N. R. Thompson. X-ray free-electron lasers. *Nature Photonics*, 4(12):814–821, 2010.

[124] Deutsches Elektronen-Synchrotron. *FLASH - The Free-Electron Laser in Hamburg*. 2007.

[125] I. A. Vartanyants, A. P. Mancuso, A. Singer, O. M. Yefanov, and J. Gulden. Coherence measurements and coherent diffractive imaging at FLASH. *Journal of Physics B: Atomic, Molecular and Optical Physics*, 43:194016, 2010.

[126] R. Mitzner, B. Siemer, M. Neeb, T. Noll, F. Siewert, S. Roling, M. Rutkowski, A. A. Sorokin, M. Richter, P. Juranic, K. Tiedtke, J. Feldhaus, W. Eberhardt, and H. Zacharias. Spatio-temporal coherence of free electron laser pulses in the soft x-ray regime. *Optics express*, 16(24):19909–19919, 2008.

[127] http://flash.desy.de/.

[128] H. Redlin, A. Al-Shemmary, A. Azima, N. Stojanovic, F. Tavella, I. Will, and S. Dsterer. The FLASH pumpprobe laser system: Setup, characterization and optical beamlines. *Nuclear Instruments and Methods in Physics Research, Section A: Accelerators, Spectrometers, Detectors and Associated Equipment*, 635:88–93, 2011.

[129] Private Communication with Stefan Düsterer.

[130] P. Radcliffe, S. Düsterer, A. Azima, H. Redlin, J. Feldhaus, J. Dardis, K. Kavanagh, H. Luna, J. Pedregosa Gutierrez, P. Yeates, E. T. Kennedy, J. T. Costello, A. Delserieys, C. L S Lewis, R. Taïeb, A. Maquet, D. Cubaynes, and M. Meyer. Single-shot characterization of independent femtosecond extreme ultraviolet free electron and infrared laser pulses. *Applied Physics Letters*, 90:131108, 2007.

[131] A. Azima, S. Düsterer, P. Radcliffe, H. Redlin, N. Stojanovic, W. Li, H. Schlarb, J. Feldhaus, D. Cubaynes, M. Meyer, J. Dardis, P. Hayden, P. Hough, V. V. Richardson, E. T. Kennedy, and J. T. Costello. Time-resolved pump-probe experiments beyond the jitter limitations at FLASH. *Applied Physics Letters*, 94:2009–2011, 2009.

[132] Mario Sauppe. *Untersuchung der Ionisationsdynamik von Xenonclustern mit zeitaufgelöster Massenspektroskopie und mit Streumethoden.* Master thesis, Technische Universität Berlin, 2013.

[133] J. M. Glownia, J. Cryan, J. Andreasson, A. Belkacem, N. Berrah, C. I. Blaga, C. Bostedt, J. Bozek, L. F. DiMauro, L. Fang, J. Frisch, O. Gessner, M. Gühr, J. Hajdu, M. P. Hertlein, M. Hoener, G. Huang, O. Kornilov, J. P. Marangos, A. M. March, B. K. McFarland, H. Merdji, V. S. Petrovic, C. Raman, D. Ray, D. A. Reis, M. Trigo, J. L. White, W. White, R. Wilcox, L. Young, R. N. Coffee, and P. H. Bucksbaum. Time-resolved pump-probe experiments at the LCLS. *Optics express*, 18(17):17620–17630, 2010.

[134] M. Krikunova, T. Maltezopoulos, A. Azima, M. Schlie, U. Frühling, H. Redlin, R. Kalms, S. Cunovic, N. M. Kabachnik, M. Wieland, and M. Drescher. Time-resolved ion spectrometry on xenon with the jitter-compensated soft x-ray pulses of a free-electron laser. *New Journal of Physics*, 11:123019, 2009.

[135] J. Jha. *A Study of Dynmics in Laser-cluster Interaction.* PhD thesis, Tata Institute of Fundamental Research, Mumbai, 2007.

[136] Parker General Valve Operation. Solenoid Pulsed Valve Manual.

[137] G. Chen, B. Kim, B. Ahn, and D. Kim. Pressure dependence of argon cluster size for different nozzle geometries. *Journal of Applied Physics*, 106:053507, 2009.

[138] Private Communication with Sven Toleikis.

[139] M. Adolph. *Cluster-light interaction and imaging of cluster growth processes.* PhD thesis, Technische Universität Berlin, 2014.

[140] L. Strüder, S. Epp, D. Rolles, R. Hartmann, P. Holl, G. Lutz, H. Soltau, R. Eckart, C. Reich, K. Heinzinger, C. Thamm, A. Rudenko, F. Krasniqi, K. U. Kühnel, C. Bauer, C. D. Schröter, R. Moshammer, S. Techert, D. Miessner, M. Porro,

O. Hälker, N. Meidinger, N. Kimmel, R. Andritschke, F. Schopper, G. Weidenspointner, A. Ziegler, D. Pietschner, S. Herrmann, U. Pietsch, A. Walenta, W. Leitenberger, C. Bostedt, T. Möller, D. Rupp, M. Adolph, H. Graafsma, H. Hirsemann, K. Gärtner, R. Richter, L. Foucar, R. L. Shoeman, I. Schlichting, and J. Ullrich. Large-format, high-speed, X-ray pnCCDs combined with electron and ion imaging spectrometers in a multipurpose chamber for experiments at 4th generation light sources. *Nuclear Instruments and Methods in Physics Research, Section A: Accelerators, Spectrometers, Detectors and Associated Equipment*, 614(3):483–496, 2010.

[141] E. W. Schlag. *Time-of-Flight Mass Spectrometry and its Applications.* Elsevier Science, 1st edition, 1994.

[142] W. C. Wiley and I. H. McLaren. Time-of-flight mass spectrometer with improved resolution. *Review of Scientific Instruments*, 26(12):1150–1157, 1955.

[143] J. Andreasson, A. V. Martin, M. Liang, N. Timneanu, A. Aquila, F. Wang, B. Iwan, M. Svenda, T. Ekeberg, M. Hantke, J. Bielecki, D. Rolles, A. Rudenko, L. Foucar, R. Hartmann, B. Erk, B. Rudek, H. N. Chapman, J. Hajdu, and A. Barty. Automated identification and classification of single particle serial femtosecond X-ray diffraction data. *Optics Express*, 22(3):2497, 2014.

[144] S. Das, P. M. Badani, P. Sharma, and R. K. Vatsa. Size and wavelength dependent photoionisation of xenon clusters. *Chemical Physics Letters*, 552:13–19, 2012.

[145] M. R. Islam, U. Saalmann, and J. M. Rost. Kinetic energy of ions after Coulomb explosion of clusters induced by an intense laser pulse. *Physical Review A - Atomic, Molecular, and Optical Physics*, 73:38–41, 2006.

[146] C. Bostedt, M. Adolph, E. Eremina, M. Hoener, D. Rupp, S. Schorb, H. Thomas, A. R. B. De Castro, and T. Möller. Clusters in intense FLASH pulses: ultrafast ionization dynamics and electron emission studied with spectroscopic and scattering techniques. *Journal of Physics B: Atomic, Molecular and Optical Physics*, 43:194011, 2010.

[147] D. D. Hickstein, F. Dollar, J. A. Gaffney, M. E. Foord, G. M. Petrov, B. B. Palm, K. E. Keister, J. L. Ellis, C. Ding, S. B. Libby, J. L. Jimenez, H. C. Kapteyn, M. M. Murnane, and W. Xiong. Observation and control of shock waves in individual nanoplasmas. *Physical Review Letters*, 112:115004, 2014.

[148] MATLAB, 2010.

[149] R. A. Kirian. Structure determination through correlated fluctuations in x-ray scattering. *Journal of Physics B: Atomic, Molecular and Optical Physics*, 45:223001, 2012.

[150] K. Hoffmann, B. Murphy, B. Erk, A. Helal, N. Kandadai, J. Keto, and T. Ditmire. High intensity femtosecond XUV pulse interactions with atomic clusters. *High Energy Density Physics*, 6(2):185–189, 2010.

[151] H. Iwayama, A. Sugishima, K. Nagaya, M. Yao, H. Fukuzawa, K. Motomura, X.-J. Liu, A. Yamada, C. Wang, K. Ueda, N. Saito, M. Nagasono, K. Tono, M. Yabashi,

T. Ishikawa, H. Ohashi, H. Kimura, and T. Togashi. Inhomogeneous charge redistribution in Xe clusters exposed to an intense extreme ultraviolet free electron laser. *Journal of Physics B: Atomic, Molecular and Optical Physics*, 43(16):161001, 2010.

[152] H. Thomas. *Wechselwirkung von Edelgas-Clustern mit intensiven Pulsen weicher Röntgenstrahlung vom Freie-Elektronen-Laser FLASH*. PhD thesis, Technische Universität Berlin, 2009.

[153] H. Hartmann, V. N. Popok, I. Barke, V. Von Oeynhausen, and K. H. Meiwes-Broer. Design and capabilities of an experimental setup based on magnetron sputtering for formation and deposition of size-selected metal clusters on ultra-clean surfaces. *Review of Scientific Instruments*, 83:073304, 2012.

[154] http://ulisse.elettra.trieste.it/services/elements/WebElements.html.

[155] S. Zamith, T. Martchenko, Y. Ni, S. Aseyev, H. Muller, and M. Vrakking. Control of the production of highly charged ions in femtosecond-laser cluster fragmentation. *Physical Review A*, 70:011201, 2004.

[156] T. Döppner, T. Fennel, T. Diederich, J. Tiggesbäumker, and K.-H. Meiwes-Broer. Controlling the coulomb explosion of silver clusters by femtosecond dual-pulse laser excitation. *Physical Review Letters*, 94:013401, 2005.

[157] B. N. Breizman, A. V. Arefiev, and M. V. Fomytskyi. Nonlinear physics of laser-irradiated microclusters. 12:056706, 2005.

[158] C. Siedschlag and J. M. Rost. Surface-plasma resonance in small rare-gas clusters by mixing ir and vuv laser pulses. *Physical Review A - Atomic, Molecular, and Optical Physics*, 71:031401, 2005.

[159] M. Kundu and D. Bauer. Optimizing the ionization and energy absorption of laser-irradiated clusters. *Physics of Plasmas*, 15:033303, 2008.

[160] T. Fennel, L. Ramunno, and T. Brabec. Highly charged ions from laser-cluster interactions: Local-field-enhanced impact ionization and frustrated electron-ion recombination. *Physical Review Letters*, 99:233401, 2007.

[161] A. Barty. Time-resolved imaging using x-ray free electron lasers. *Journal of Physics B: Atomic, Molecular and Optical Physics*, 43:194014, 2010.

[162] N. D. Loh, C. Y. Hampton, A. V. Martin, D. Starodub, R. G. Sierra, A. Barty, A. Aquila, J. Schulz, L. Lomb, J. Steinbrener, R. L. Shoeman, S. Kassemeyer, C. Bostedt, J. Bozek, S. W. Epp, B. Erk, R. Hartmann, D. Rolles, A. Rudenko, B. Rudek, L. Foucar, N. Kimmel, G. Weidenspointner, G. Hauser, P. Holl, E. Pedersoli, M. Liang, M. S. Hunter, L. Gumprecht, N. Coppola, C. Wunderer, H. Graafsma, F. R. N. C. Maia, T. Ekeberg, M. Hantke, H. Fleckenstein, H. Hirsemann, K. Nass, T. A. White, H. J. Tobias, G. R. Farquar, W. H. Benner, S. P. Hau-Riege, C. Reich, A. Hartmann, H. Soltau, S. Marchesini, S. Bajt, M. Barthelmess, P. Bucksbaum, K. O. Hodgson, L. Strüder, J. Ullrich, M. Frank, I. Schlichting, H. N. Chapman, and M. J. Bogan. Erratum: Fractal morphology, imaging and mass spectrometry of single aerosol particles in flight. 489(7416):460–460, 2012.

[163] C. Peltz, C. Varin, T. Brabec, and T. Fennel. Time-Resolved X-Ray Imaging of Anisotropic Nanoplasma Expansion. *Physical Review Letters*, 133401:133401, 2014.

[164] Y. V. Medvedev. Expansion of a finite plasma into a vacuum. *Plasma Physics and Controlled Fusion*, 47(7):1031–1046, 2005.

[165] P. Mora. Collisionless expansion of a Gaussian plasma into a vacuum. *Physics of Plasmas*, 12(May 2014):1–8, 2005.

[166] F. Van der Veen and F. Pfeiffer. Coherent x-ray scattering. *Journal of Physics: Condensed Matter*, 16:5003–5030, 2004.

[167] J. W. Goodman. *Speckle phenomena in optics: theory and applications*. Roberts & Company, 2007.

[168] G. Zhang, Z. Wu, and Y. Li. Speckle size of light scattered from 3D rough objects. *Optics Express*, 20(4):4726, 2012.

[169] J. C. Auger, G. E. Fernandes, K. B. Aptowicz, Y. L. Pan, and R. K. Chang. Influence of surface roughness on the elastic-light scattering patterns of micron-sized aerosol particles. *Applied Physics B: Lasers and Optics*, 99:229–234, 2010.

[170] Y. Piederrière, J. Le Meur, J. Cariou, J. Abgrall, and M. Blouch. Particle aggregation monitoring by speckle size measurement; application to blood platelets aggregation. *Optics express*, 12(19):4596–4601, 2004.

[171] M. Wöstmann, R. Mitzner, T. Noll, S. Roling, B. Siemer, F. Siewert, S. Eppenhoff, F. Wahlert, and H. Zacharias. The XUV split-and-delay unit at beamline BL2 at FLASH. *Journal of Physics B: Atomic, Molecular and Optical Physics*, 46(16):164005, 2013.

[172] D. Rupp. X-ray movie of FEL-induced dynamics in individual nanoparticles. *FLASH Beamtime Proposal*, 2014.

[173] K. E. Schmidt, J. C H Spence, U. Weierstall, R. Kirian, X. Wang, D. Starodub, H. N. Chapman, M. R. Howells, and R. B. Doak. Tomographic femtosecond X-ray diffractive imaging. *Physical Review Letters*, 101(11):1–4, 2008.

Acknowledgements

Diese Arbeit wäre nicht ohne die Hilfe und den Beistand vieler lieber Menschen entstanden. Daher möchte ich mich bedanken bei:

Thomas Möller - für die Möglichkeit unter Dir als Doktorvater zu Promovieren. Für den großzügigen Freiraum und die Unterstützung meiner Ideen aber auch die konstruktive und richtungsweisende Kritik. Für das sympathische Team das Du um Dich gesammelt hast und die angenehme Arbeitsatmosphäre die Du verbreitest.

Tim Laarmann - für die Rolle des Zweitgutachters dieser Arbeit. Für eine wunderbare Fluoreszenzmesszeit und die tollen daraus resultierenden Paper.

Dani - für Deine unerschöpfliche Energie und Deinen überbordenden Enthusiasmus. Du hast es immer wieder geschafft mich auch in frustrierenden Situationen anzuspornen und zu motivieren. Danke für all die nötigen Kopfwäschen mit viel Feingefühl und die wunderbare, unbezahlbare Betreuung. Es hat jeder Zeit viel Spass gemacht mit und von Dir zu lernen, Experimente durchzuführen, Auswertungsprogramme zu coden und zukünftige Forschungsvorhaben zu erspinnen. — Maria M. - für die herzliche Aufnahme und Einführung in die AG Möller. Für etliche lustige Stunden bei Balzac, in der Denkzelle und auf Messzeit. Für Dein Interesse, Deinen Beistand und Deine liebenswürdige Menschlichkeit. Für die richtigen Fragen zur richtigen Zeit und Dein viel zu unterschätztes Fachwissen, dass Du auf Knopfdruck mit mir geteilt hast und natürlich für die zahlreichen Stunden die Du mit der Korrektur dieser Arbeit verbracht hast.

Mario - für die gute Zusammenarbeit bei der Auswertung der XUV/IR Daten und die zahllosen Abbildungen die du mir zur Verfügung gestellt hast. Dein wunderbarer Humor hat selbst nach endlosen Nachtschichten bei mir zu Lachkrämpfen geführt. — Yevheniy - for sharing the office with me throughout my entire thesis. I really appreciate the plesant atmosphere and all the interesting discussions with you and the tons of chocolate that helped me survive the final months of my thesis. — Robert - Für jede Menge gute Ideen zu allen möglichen Komponenten wann immer ich an experimentellen Aufbauten gebastelt habe und für all die Teile die ich mir jederzeit aus deinem Labor leihen durfte. — Tais - für das Löchern mit Advocat‘s Devil Fragen, die einen selbst auf den fiesesten Referee perfekt vorbereiten. — Alex - für das Testen und die richtigen Fragen zu meinem Rekonstruktionsprogramm während Deiner Bachelorarbeit. — Marcus - für das geniale Datenausleseprogramm FoxIT. — Andre - für die Herzlichkeit die Du in der Gruppe verbreitest.

dem Rest der (Ex-)AG-Möller für die tolle Zusammenarbeit: Andrea, Bruno, Christoph, Dave, Jan, Lena, Maria K., Ramona, Schorbi, Tim, Tobi, Toli und Yussuf. — dem Team der IOAP-Werkstatt - allen voran Jörn und Fabian - für all die schönen Teile die durch Euch aus meinen Zeichnungen zur Wirklichkeit wurden. — dem FLASH-Team und allen Kollaborationspartnern für die gute und erfolgreiche Zusammenarbeit: Harald, Stefan, Marion, Rolf, Sven, Holger, Lasse, Andreas K., Andreas P., Karl-Heiz Meiwes-Broer, Thomas Fennel, Hannes, Ingo, Christian, Mathias

meiner Familie und meinen Freunden - Mama, Papa, Annette, Cori, Kathi, Marcel - die mich durch alle Höhen und Tiefen begleiten und jederzeit für mich da sind. — Veri - for proofreading in finest Oxford english — Jochen - für den endlosen mentalen Rückhalt und den nie abreißenden Klapperdraht